Engineered Colorectal Cancer Tissues Employing Patient-derived Cells for Recapitulating the Tumor Microenvironment

by

Iman Hassani

A dissertation submitted to the Graduate Faculty of
Auburn University
in partial fulfillment of the
requirements for the Degree of
Doctor of Philosophy

Auburn, Alabama
May 1, 2021

Keywords: engineered tumor model, microsphere,
PDX, CRC, colon cancer, hydrogel

Copyright 2021 by Iman Hassani

Approved by

Elizabeth A. Lipke, Chair, Mary and John H. Sanders Professor of Chemical Engineering
Michael W. Greene, Associate Professor of Nutrition, Dietetics, and Hospitality Management
Mario R. Eden, Joe T. and Billie Carole McMillan Professor of Chemical Engineering
Allan E. David, John W. Brown Associate Professor of Chemical Engineering
Robert D. Arnold, Professor of Drug Discovery and Development
Peter R. Panizzi, Associate Professor of Drug Discovery and Development

Abstract

Colorectal cancer (CRC) remains the third most prevalent cancer and the third-highest cause of cancer-related deaths among both men and women in the United States. The development of pre-clinical CRC models is vital for understanding tumor biology to identify new, effective anti-cancer therapeutics. However, the current CRC models are unable to accurately represent disease pathophysiology and the complex tumor microenvironment. Patient-derived xenografts (PDXs), an *in vivo* model, demonstrate high potential in clinical translatability due to the recapitulation of key characteristics of the patient tumor; however, the use of PDXs is costly and low-throughput. This research focuses on the establishment of an *in vitro* 3D engineered CRC model using cells isolated from CRC PDX (CRC-PDX) tumor lines to recapitulate the key attributes of the originating tumors. This study demonstrates the use of poly(ethylene glycol)-fibrinogen (PEG-Fb) hydrogels for CRC tissue engineering. Chapter 1 introduces the current preclinical CRC models and the need for better models to recapitulate the CRC tumor microenvironment. Chapter 2, as a proof of concept, demonstrates the ability of a PEG-Fb-based tissue-engineered cancer model to support the investigation of CRC cell line phenotypes. Chapter 3 describes the establishment of engineered CRC tissue that recapitulates the key attributes of a stage II CRC-PDX tumor line. In Chapter 4, two other PDX lines originated from stages III-B and IV of CRC patients were incorporated into the tissue-engineered CRC model to recapitulate patient-to-patient and/or cancer stage-to-stage variabilities. Chapter 5 describes the rapid generation of CRC tissue-engineered microspheres for high-throughput study. Overall, the robust *in vitro* tissue-engineered CRC models reported in this research demonstrate significant potential for future implementation in the study of disease progression, tumorigenic mechanisms, and drug-testing applications.

Acknowledgments

I would like to thank my advisor, Dr. Elizabeth Lipke, for her dedication, guidance, and mentorship on my Ph.D. project and her continued support throughout my academic life. I would like to thank our collaborator, Dr. Michael Greene, for his practical advice on and assistance with my project. I would like to thank former and current members of Lipke Lab; specifically, my excellent mentor, Dr. Shantanu Pradhan, for his mentorship during the first two years of my Ph.D., friendship, and continued support; Benjamin Anbiah, Nicole Habbit, Dr. Yuan Tian, and Mohammadjafar Hashemi for their friendship, assistance with research experiments, and data analysis and their advice on my research work; and Morgan Ellis, Ferdous Finklea, and Mayra Paez for their friendship and advice on the various aspects of my project. Thank you to the undergraduate students Andrew Moore and Grace Hester for their help with experiments and data analysis. I would like to thank our collaborators; specifically, Dr. Bulbul Ahmed for his assistance with animal study and gene expression experiments and Peyton Kuhlers for his help with RNA-seq data analysis. I would like to thank Dr. Michael Greene, Dr. Allan David, Dr. Mario Eden, Dr. Robert Arnold, and Dr. Peter Panizzi for their support and willingness to serve on my committee. Thank you to Michelle Aono for her assistance with tissue sectioning and H&E staining, Allison Church Bird for her constructive guidance on cell labeling and flow cytometry, Dr. Mahmoud Mansour's laboratory at Auburn University for facilitating the use of the confocal microscope, and Dr. C. Ross Ethier's laboratory at Georgia Institute of Technology for providing access to the MicroSquisher apparatus.

Last but not least, I am extremely grateful to my parents, Hamidollah and Fereshteh Hassani, my wife, Marziyeh, my son, Ryan, my brother, Ehsan, and my sister, Fatemeh for their continued support and love. Without them, this would not have been possible.

Table of Contents

Abstract 2

Acknowledgments 3

List of Tables 12

List of Figures 13

List of Abbreviations 18

Chapter 1 : Background 21

1.1 Colorectal Cancer 21

1.2 Preclinical Models to Study Cancer 22

1.2.1 *In vitro* 2D Cancer Models 23

1.2.2 *In vitro* 3D Cancer Models 23

1.2.2.1 Scaffold-free 3D Cancer Models 24

1.2.2.2 Scaffold-based 3D Cancer Models 25

1.2.3 *In vivo* cancer models 26

1.3 Cell Sources in Cancer Research 27

1.3.1 Standard Cell Lines 27

1.3.2 Patient-derived Cancer Cells 29

1.4 Patient-derived and PDX Tumor Cells in *In vitro* 3D Models 29

1.5 Characterization of and Considerations in *In vitro* 3D Cancer Model of PDX 30

Chapter 2 : An *in vitro* 3D Tissue-engineered Cancer Model for the Investigation of Colorectal Cancer Phenotypes 32

2.1 Introduction 32

2.2 Materials and Methods 35
2.2.1 Cell culture and maintenance 36
2.2.2 Hydrogel synthesis and 3D-eCRC tissues formation 36
2.2.3 Cell viability assay and image acquisition 37
2.2.4 Growth and morphological analysis of cell colonies in 3D-eCRC tissues 38
2.2.5 Flow cytometry 38
2.2.6 Immunostaining and image acquisition 39
2.2.7 Size and shape analysis of 3D-eCRC tissues 40
2.2.8 Mechanical stiffness of 3D-eCRC-PDX tissues 41
2.2.9 Cell doubling time in 2D-CRC cultures and 3D-eCRC tissues 42
2.2.10 Statistical analysis 42
2.3 Results 43
2.3.1 CRC cells remained viable in 3De-CRC tissues 43
2.3.2 CRC cells showed both region- and line-dependent growth and temporal morphological changes in 3De-CRC tissues 45
2.3.3 3D-eCRC tissues but not 2D-CRC cultures exhibited temporal changes in cell subpopulations 51
2.3.4 CRC cells showed line-, time-, and region-dependent marker positivity 55
2.3.5 3D-eCRC tissues showed line-dependent temporal changes in size and shape 57
2.3.6 3D-eCRC tissues exhibited line-dependent temporal changes in mechanical stiffness 60
2.3.7 Rates of increase in cell number in 3D-eCRC tissues were different than those in 2D-CRC cultures 61

2.4 Discussion 63
2.5 Conclusion 68
Chapter 3 : Engineered Colorectal Cancer Tissue Recapitulates Key Attributes of a Patient-derived Xenograft Tumor Line 69
3.1 Introduction 69
3.2 Materials and Methods 74
3.2.1 Synthesis of PEGDA and PEG-Fb 74
3.2.2 Propagation of CRC PDX Cells in Mice 74
3.2.3 CRC-PDX Tumor Dissociation and Cell Isolation 75
3.2.4 Formation and Culture of 3D-eCRC-PDX Tissues 75
3.2.5 2D CRC PDX Cell Culture 75
3.2.6 Cell Viability Assay and Image Acquisition and Analysis 76
3.2.7 Image Acquisition and Morphological Analysis of 3D-eCRC-PDX Tissues and 2D-CRC Cells 76
3.2.8 Cell Subpopulation Investigation by Flow Cytometry 77
3.2.9 Morphological Study of Cells by Staining 78
3.2.10 Histological Examination of 3D-eCRC-PDX Tissues and CRC-PDX Tumors 79
3.2.11 RT-qPCR Gene Expression 79
3.2.12 Morphological Analysis of 3D-eCRC-PDX Tissues 80
3.2.13 Mechanical Stiffness 80
3.2.14 Proteomics Analysis 80
3.2.15 Transcriptomic Analysis 82
3.2.16 CRC Consensus Molecular Subtype Analysis 83

3.2.17 TCGA Analysis 83
3.2.18 GSEA Analysis 83
3.2.19 Gene Ontology Analysis 84
3.2.20 Kaplan–Meier survival analysis 84
3.2.21 Statistical Analysis 84
3.3 Results 85
3.3.1 CRC-PDX Tumor Cell Viability Maintained Following 3D Encapsulation 85
3.3.2 Growth and Morphological Analysis of Tumor Cell Colonies within 3D-eCRC-PDX Tissues 88
3.3.3 3D-eCRC-PDX Tissues Maintained Cell Subpopulations 92
3.3.4 Gene Expression in CRC-PDX Tumors Was More Similar to 3D-eCRC-PDX Tissues than 2D-CRC-PDX Cells 99
3.3.5 3D-eCRC-PDX Tissues Displayed Locational Heterogeneity and Cell-induced Contraction 101
3.3.6 3D-eCRC-PDX Tissues Mimic the Mechanical Stiffness of CRC-PDX Tumors 103
3.3.7 Proteomic Analysis of CRC-PDX Tumors and 3D-eCRC-PDX Tissues 107
3.3.8 Molecular characterization of CRC-PDX Tumors and 3D-eCRC-PDX Tissues 109
3.4 Discussion 114
3.5 Conclusion 120
Chapter 4 : Engineered Colorectal Cancer Model Employing Patient-Derived Xenografts Mimics Patient-to-patient Tumor Variabilities 122
4.1 Introduction 122
4.2 Materials and Methods 126

4.2.1 Synthesis of PEGDA and PEG-Fb 126
4.2.2 Propagation of CRC PDX Cells in Mice 126
4.2.3 CRC-PDX Tumor Dissociation and Cell Isolation 127
4.2.4 Formation and Culture of 3D-eCRC-PDX Tissues 127
4.2.5 2D-CRC-PDX Cell Culture 127
4.2.6 Image Acquisition and Morphological Analysis of Cell Colonies in 3D-eCRC-PDX Tissues and 2D-CRC Cultures 128
4.2.7 Cell Subpopulation Investigation by Flow Cytometry 128
4.2.8 Morphological Analysis of 3D-eCRC-PDX Tissues 129
4.2.9 Mechanical Stiffness 129
4.2.10 Statistical Analysis 129
4.3 Results 130
4.3.1 Viable Cell Numbers Isolated from Tumors Were PDX Line-dependent 130
4.3.2 Growth and Morphological Changes of Tumor Cell Colonies Were Both PDX Line- and Culture Platform-dependent 130
4.3.3 3D-eCRC-PDX Tissues Better Maintained Cell Subpopulations as Compared to 2D-CRC-PDX Cultures 135
4.3.4 3D-eCRC-PDX Tissues Exhibited Cell-induced Contraction 140
4.3.5 3D-eCRC-PDX Tissues Mimicked the Mechanical Stiffness of CRC-PDX Tumors 142
4.4 Discussion 144
4.5 Conclusion 148

Chapter 5 : Rapid Generation of Colorectal Cancer Tissue-Engineered Microspheres Based on Patient-derived Xenograft Tumor Cells 149
5.1 Introduction 149
5.2 Materials and Methods 151
5.2.1 Synthesis of PEGDA and PEG-Fb 151
5.2.2 HT-29 CRC Cell Culture and Maintenance 152
5.2.3 Propagation of CRC PDX Cells in Mice 152
5.2.4 CRC-PDX Tumor Dissociation and Cell Isolation 152
5.2.5 Production of Microspheres Using Microfluidic Platform 153
5.2.6 2D-CRC-PDX Cell Culture 154
5.2.7 Cell Viability Assay and Image Acquisition and Analysis 154
5.2.8 Image Acquisition and Morphological Analysis of Cell Colonies in HT-29 and 3D-eCRC-PDX Microspheres 154
5.2.9 Cell Subpopulation Investigation by Flow Cytometry 155
5.2.10 Morphological Study of Cells by Staining 155
5.2.11 Analysis of Changes in Size and Shape of Microspheres 156
5.2.12 Statistical Analysis 156
5.3 Results 156
5.3.1 HT-29 Cells Remained Viable in Microspheres 156
5.3.2 HT-29 Cell Colonies Grew in Microspheres 157
5.3.3 HT-29 Microspheres Grew Over Time 159
5.3.4 HT-29 Cell Colonies Maintained Uniform Distribution in Microspheres 160
5.3.5 CRC-PDX Cell Colonies Grew in Microspheres 161

5.3.6 Microspheres Better Maintained CRC-PDX Cell Subpopulations as Compared to 2D-eCRC-PDX Cultures 162
5.4 Discussion 165
5.5 Conclusion 167
Chapter 6 : Summary and Conclusion 169
References 174
Appendix A : Method Details 208
A.1 Fabrication of PDMS Molds 208
A.2 CRC-PDX Tumor Dissociation and Cell Isolation 208
A.3 Formation and Culture of 3D-eCRC-PDX Tissues 209
A.4 2D CRC PDX Cell Culture 210
A.5 Cell Viability Assay and Image Analysis 210
A.6 Flow Cytometry 211
A.7 Immunostaining for Examination of Cell Morphology 217
A.8 Histological Examination of CRC-PDX Tumors and 3D-eCRC-PDX Tissues 218
A.9 Mechanical Stiffness 218
A.10 Proteomics Analysis 219
A.11 Method Validation 222
Appendix B : Supporting Information for Chapter 2 225
Appendix C : Supporting Information for Chapter 3 234
C.1 Data 234
Appendix D : Supporting Information for Chapter 4 255
Appendix E : Supporting Information for Chapter 5 265

Appendix F : Supporting Information for Figure 3.3 266

Appendix G : Reagent Table..... 274

List of Tables

Table 1.1. Major risk factors for colorectal cancer 22

Table 2.1. Specifications of CRC cell lines and their culture media 36

Table 2.2. Specifications of primary and secondary antibodies 39

Table C.1. Summary of the sequencing reads alignment to the reference genomes for the CRC-PDX 254

Table G.1. Reagents 274

List of Figures

Figure 2.1. CRC cells were encapsulated in PEG-Fb 44

Figure 2.2. CRC cells remained viable in the 3D-eCRC tissues 44

Figure 2.3. CRC cells showed temporal, region- and line-dependent growth and morphology in 3De-CRC tissues 47

Figure 2.4. 3D-eCRC tissues, but not 2D-CRC cultures, demonstrated line-dependent temporal changes in cell subpopulations 52

Figure 2.5. CRC cells showed line-, time-, and region-dependent marker positivity..... 56

Figure 2.6. 3D-eCRC tissues showed line-dependent temporal changes in size and shape. 59

Figure 2.7. Changes in mechanical stiffness of the 3D-eCRC tissues over time were cell line-dependent..... 61

Figure 2.8. Direct cell count for the 3D-eCRC tissues correlated with calculated cell numbers . 62

Figure 3.1. Following encapsulation in PEG-Fb, CRC-PDX tumor cells were viable during long-term culture..... 86

Figure 3.2. Morphological analysis of cell colonies within 3D-eCRC-PDX tissues and in 2D-CRC-PDX cultures 90

Figure 3.3. 3D-eCRC-PDX tissues maintained the CRC-PDX tumor cell subpopulations during long-term culture, whereas the 2D-CRC-PDX cells did not 94

Figure 3.4. Gene expression of epithelial to mesenchymal transition (EMT), stem cell, and angiogenesis markers in CRC-PDX tumors was more similar to 3D-eCRC-PDX tissues than 2D-CRC-PDX cells 101

Figure 3.5. 3D-eCRC-PDX tissues showed locational heterogeneity and whole-tissue contraction over time..... 102

Figure 3.6. 3D-eCRC-PDX tissues and CRC-PDX tumors showed similar Young's moduli and ECM proteins 105
Figure 3.7. Transcriptomic characterization of 3D-eCRC-PDX tissues demonstrated that 3D-eCRC-PDX tissues recapitulated key molecular characteristics of CRC-PDX tumors 110
Figure 4.1. Growth and morphological changes of tumor cell colonies were both PDX line- and culture platform-dependent 132
Figure 4.2. The 3D-eCRC-PDX tissues better maintained cell subpopulations as compared to 2D-eCRC-PDX cultures 136
Figure 4.3. 3D-eCRC-PDX tissues exhibited cell-induced contraction 141
Figure 4.4. The 3D-eCRC-PDX tissues mimicked the mechanical stiffness of CRC-PDX tumors 143
Figure 5.1. HT-29 cells remained viable in microspheres 157
Figure 5.2. HT-29 cell colonies grew in microspheres 158
Figure 5.3. HT-29 microspheres grew over time 159
Figure 5.4. HT-29 cell colonies maintained uniform distribution in microspheres 160
Figure 5.5. CRC-PDX cell colonies grew in microspheres 162
Figure 5.6. Microspheres better maintained CRC-PDX cell subpopulations as compared to 2D-eCRC-PDX cultures 164
Figure A.1. Representative images of (A) the PDMS mold used to generate 3D-eCRC-PDX tissues, (B) the generated 3D-eCRC-PDX tissues, and (C) 2D-CRC-PDX cells.. 222
Figure A.2. Representative fluorescent images of cell viability assay for the 3D-eCRC-PDX tissues 223

Figure A.3. Quantification of cell subpopulations 223
Figure A.4. Immunostaining of the CRC-PDX cells within the 3D-eCRC-PDX tissues 224
Figure A.5. Mechanical stiffness measurements 224
Figure B.1. Cell viability was similar in the core, midpoint, and periphery regions 225
Figure B.2. Temporal changes in the cell colony area were both region- and line-dependent... 226
Figure B.3. Total colony area per tissue volume was both region- and line-dependents 227
Figure B.4. Temporal changes in cell colony aspect ratio were both line- and region-dependent 228
Figure B.5. 3D-eCRC tissues demonstrated line-dependent changes in cell subpopulations 229
Figure B.6. Changes in mechanical stiffness of the 3D-eCRC tissues over time were cell line-dependent..... 229
Figure B.7. Doubling time of the cell lines in 2D-CRC cultures and 3D-eCRC tissues 230
Figure B.8. Calculated cell numbers for the 3D-eCRC correlated with direct cell count 231
Figure B.9. Forward Scatter (FSC) and Side Scatter (SSC) were line- and time-dependent 232
Figure C.1. Live/Dead assay quantification of cell viability 235
Figure C.2. CRC-PDX cell growth rate in 2D-CRC-PDX cultures without cell passaging 236
Figure C.3. Viable CRC-PDX cell numbers within the 3D-eCRC-PDX tissues 236
Figure C.4. Examination of human ($B2M^+$), mouse ($H2Db^+$), and $CK20^+$ cell subpopulations 237
Figure C.5. Quantification of CRC PDX cell subpopulations through flow cytometry 238
Figure C.6. Cell subpopulations within the CRC-PDX tumors, 3D-eCRC-PDX tissues, and 2D-CRC-PDX cultures 240
Figure C.7. Cluster analysis of the cell subpopulations obtained from flow cytometry results . 241
Figure C.8. Staining of cells within the 3D-eCRC-PDX tissues 243

Figure C.9. Staining of 2D-CRC-PDX cells 244
Figure C.10. Size and shape of acellular PEG-Fb hydrogels over time 245
Figure C.11. Mechanical stiffness of the acellular hydrogels 246
Figure C.12. Comparison of identified extracellular matrix (ECM) proteins in CRC-PDX tumors and 3D-eCRC-PDX tissues 247
Figure C.13. Protein batch-to-batch consistency between CRC-PDX tumors or 3D-eCRC-PDX tissues 248
Figure C.14. Comparison between the identified ECM proteins in CRC-PDX tumors and 3D-eCRC-PDX tissues from Batch 1 (B1), Batch 2 (B2), and Batch 3 (B3) 249
Figure C.15. Gene ontology analysis of molecular functions enriched in CRC-PDX tumor and 3D-eCRC-PDX tissue samples 250
Figure C.16. Gene Set Enrichment Analysis (GSEA) 252
Figure C.17. Prognostic Kaplan–Meier survival analysis 253
Figure D.1. Viable cell numbers isolated from CRC-PDX tumors were line-dependent 255
Figure D.2. Quantification of growth and morphological changes of tumor cell colonies in 3D-eCRC-PDX tissues for 3 separate batches of cultures 256
Figure D.3. Quantification of growth and morphological changes of tumor cell colonies in 2D-CRC-PDX cultures for 3 separate batches of cultures 257
Figure D.4. Quantification of growth and morphological changes of tumor cell colonies in 3D-eCRC-PDX tissues for 3 separate batches of cultures 258
Figure D.5. Quantification of growth and morphological changes of tumor cell colonies in 3D-eCRC-PDX tissues 259
Figure D.6. Quantification of CRC-PDX tumor growth 260

Figure D.7. CRC-PDX cell growth rate in 2D-CRC-PDX cultures without cell passaging..... 260
Figure D.8. The 3D-eCRC-PDX tissues better maintained the originating CRC-PDX tumor cell subpopulations as compared to 2D-CRC-PDX cultures 261
Figure D.9. Quantification of size and shape of the 3D-eCRC-PDX tissues for a minimum of two separate batches of cultures 263
Figure D.10. The 3D-eCRC-PDX tissues mimicked the stage-dependent mechanical stiffness of CRC-PDX tumors 264
Figure E.1. HT-29 cells in microspheres were positive for CK20 marker 265

List of Abbreviations

2D	Two-dimensional
2D-CRC	Two-dimensional Colorectal Cancer
2D-CRC-PDX	Two-dimensional Colorectal Cancer Patient-derived Xenograft
3D	Three-dimensional
3D-eCRC	Three-dimensional Engineered Colorectal Cancer
3D-eCRC-PDX	Three-dimensional Engineered Colorectal Cancer Patient-derived Xenograft
ANOVA	One-way Analysis of Variance
ATCC	American Type Culture Collection
B2M	β2-microglobulin
BSA	Bovine Serum Albumin
CI	Confidence Interval
CK20	Cytokeratin 20
CMS	Consensus Molecular Subtype
CRC	Colorectal Cancer
DEG	Differentially Expressed Gene
DMEM	Dulbecco's Modified Eagle's Medium
DNA	Deoxyribonucleic Acid
DNase I	Deoxyribonuclease I
ECM	Extracellular Matrix
EMT	Epithelial to Mesenchymal Transition
EthD-1	Ethidium Homodimer-1

FBS	Fetal Bovine serum
FDR	False Discovery Rate
FSC	Forward Scattering
FSC-A	Forward Scattering-area
GO	Gene Ontology
GSEA	Gene Set Enrichment Analysis
GSL	Genomic Services Laboratory
H2Db	MHC Class I H-2 Db
HBSS	Hank's Buffered Saline Solution
MMPs	Matrix Metalloproteases
MSigDB	Molecular Signature Database
NCAD	N-Cadherin
NEAA	Non-essential Amino Acid
NES	Normalized Enrichment Score
nL	Nanoliter
NVP	1-Vinyl-2-Pyrrolidinone
PBS	Phosphate Buffered Saline
PDMS	Poly(dimethyl siloxane)
PDX	Patient-derived Xenograft
PE	R-phycoerythrin
PEG	Poly(ethylene glycol)
PEG-Fb	Poly(ethylene glycol)-fibrinogen
PEGDA	Poly(ethylene glycol) Diacrylate

pen/strep	Penicillin/Streptomycin
PF	Poly(ethylene glycol) Diacrylate-fibrinogen
qPCR	Quantitative Polymerase Chain Reaction
SCID	Severe Combined Immunodeficient
SSC	Side Scattering
SSC-A	Side Scattering-area
TCGA-COAD	The Cancer Genome Atlas Colon Adenocarcinoma
TEOA	Triethanolamine
TS	Tumor Spheroids
α-SMA	alpha-Smooth Muscle Actin

Chapter 1: Background

1.1 Colorectal Cancer

Colorectal cancer (CRC) remains the third most prevalent cancer and the third-highest cause of cancer-related deaths among both men and women in the United States, with approximately 145,600 new cases and 51,020 deaths in 2019 (American Cancer Society 2019; Libutti et al. 2015; Schaeybroeck et al. 2014). It has been estimated that there are currently more than a million people with CRC living in the United States (Gonzalez-Pons and Cruz-Correa 2015). Globally, CRC is the third most common cancer in men and the second in women (Font-Burgada, Sun, and Karin 2016). In 2015, 814,000 cases of CRC in men and 664,000 cases in women were reported which make CRC 9.7% of all cancer cases (Aran et al. 2016). Although there has been an overall decreasing trend in CRC rates over the past several decades, the incidence in individuals under the age of 55 has increased (American Cancer Society 2019; Libutti et al. 2015; Schaeybroeck et al. 2014). Additionally, despite advances in early CRC detection and targeted treatment strategies, the 5-year relative survival rates of patients with distant-stage CRC (malignant CRC metastasized to distal regions of the body) is only 14% (American Cancer Society 2019; Libutti et al. 2015; Schaeybroeck et al. 2014).

The CRC risk factors include two major categories—hereditary and non-hereditary factors (Table 1.1 (Aran et al. 2016)). Studies suggest that some cancer types occur in certain families; however, only 5% of CRC cases have been diagnosed as inherited patients (Aran et al. 2016). The majority of CRC cases are caused by non-hereditary factors, including the environment and lifestyle (Aran et al. 2016). Diet is one of the major lifestyle factors which showed a significant impact on CRC incidence. It has been demonstrated that a vegetarian diet reduces the risk of this disease as compared to a meat diet, mainly due to genome instability initiated by epigenetic and

genetic changes resulted from meat and fat consumption (Aran et al. 2016). In addition, increasing evidence from epidemiological studies suggests that obesity is associated with a 30% to 70% greater risk of CRC (Calle and Kaaks 2004; Bardou, Barkun, and Martel 2013). Moreover, studies have shown that the impact of obesity on cancer can be different based on gender, cancer sites, adipocytes sites, and age, to name a few (Riondino et al. 2014). For instance, it has been indicated that there is a higher risk for colon cancer than rectum cancer in an obese individual; men are more prone to cancer compared to woman; and central obesity (as defined by excessive abdominal fat around the stomach) make individuals more susceptible to colon cancer compared to fat accumulation in different locations of the body (Riondino et al. 2014).

Table 1.1. Major risk factors for colorectal cancer

Hereditary	**Non-hereditary**
Family history	Hereditary syndromes
Hereditary syndromes	Smoking
	High alcohol intake
	Obesity
	Age ≥ 50
	Diet rich in meat, fat, and low fiber

1.2 Preclinical Models to Study Cancer

Despite the tremendous effort and investment in understanding cancer over the last few decades, it is still the second leading cause of death in the united states (Siegel, Miller, and Jemal 2020). Development of preclinical cancer models, including both *in vitro* and *in vivo* models, has

been of great value to study tumor biology and investigate anti-cancer therapeutics. The following sections will discuss these models.

1.2.1 *In vitro* 2D Cancer Models

The most common *in vitro* cancer cell culture model relies on two-dimensional (2D) culture of cells which has advantages in terms of simplicity and ease of analysis; yet, there are many inherent differences between the microenvironmental cues present in 2D *in vitro* and *in vivo* cancer models. For example, in 2D models, the cells are not surrounded by a supporting matrix, and the mechanical properties of tissue culture substrates are much stiffer than *in vivo* tumor tissue. Both of these differences are known to impact cellular morphology, polarity, and proliferation rate. The culture of patient cells in 2D monolayers also results in substantial changes in the ratios of cell types present in the overall population, thereby resulting in a cancer cell *in vitro* model that no longer mimics the parental cell subpopulations (Okada, Vaeteewoottacharn, and Kariya 2019; Kodack et al. 2017). Furthermore, tumors often contain subpopulations that do not adhere to the surface of the culture flask, preventing direct contact between non-anchorage and anchorage-dependent cell types that are able to be maintained and thereby hindering cell-cell interactions important for preserving *in vivo* cellular phenotypes. Moreover, the absence of a supporting matrix in 2D models precludes multi-dimensional cell-matrix interactions that modulate tumor pathophysiology.

1.2.2 *In vitro* 3D Cancer Models

For several decades, *in vitro* 2D cancer models have facilitated the understanding of tumor biology and the testing of anti-cancer drug candidates. However, these models are inherently

unable to mimic many pathophysiological complexities of the native tumor milieu. To overcome this limitation, *in vitro* 3D cancer models have been introduced to more closely recapitulate the key attributes of the native tumors. *In vitro* 3D cancer models have bridged the gap between 2D *in vitro* models and *in vivo* models and offer several advantages over 2D models, including cell-matrix and cell-cell interactions, facilitation of use of other cell types (e.g., fibroblasts, endothelial cells, immune cells, and others) to fabricate the tumor-stromal microenvironment, activation of specific 3D cell-signaling mechanisms and subsequent drug targets, tumor heterogeneity, and increase in drug resistance due to diffusion mechanism. All these advantages of 3D over 2D models play crucial roles in mimicking tumor microenvironments. The *in vitro* 3D cancer models can be divided into two major categories—scaffold-free and scaffold-based models. The use of 3D cancer cell culture, including both scaffold-free and scaffold-based 3D models, has been reported for breast cancer (D. Truong et al. 2016; Pradhan, Clary, et al. 2017; Pradhan, Hassani, et al. 2017; Pradhan and Slater 2019), prostate cancer (Hsiao et al. 2009; Gao et al. 2014; Gurski et al. 2009; E.L. Fong et al. 2014; E.L. Fong, Wan, et al. 2016), lung cancer (Gill et al. 2012; Simon et al. 2016), CRC (Luca et al. 2013; Hoshiba and Tanaka 2016; Devarasetty et al. 2017; Dolznig et al. 2011; Stadler et al. 2018; Magdeldin et al. 2014), and melanoma (D.H. Kim et al. 2018) among others.

1.2.2.1 Scaffold-free 3D Cancer Models

Scaffold-free 3D cancer models, including self-aggregated tumor spheroids (TS) and organoids, have been successfully employed in CRC research (Luca et al. 2013). However, TS- and organoids-based models have several limitations. Some cell lines form irregular-sized TS or organoids, whereas some do not self-aggregate and form them at all. Even for cancer cell lines that

can self-aggregate, it has been shown that some subsets of the cell population are unable to adhere and integrate into TS. Specifically, for CRC cells, Stadler et al. (Stadler et al. 2018) demonstrated that a small proportion of HCT 116, DLD, and SW620 CRC cells lost their adhesion phenotype through TS formation and did not integrate into the TS. In addition, self-aggregated cancer cells lack the support of a surrounding extracellular matrix (ECM) as they form these 3D structures. Cell-matrix interactions play an important role in cancer progression, invasion, and metastasis, as well as cell responses to anti-cancer drugs (Quail and Joyce 2013; Nguyen, Bos, and Massague 2009). The lack of 3D matrix results in the loss of many physiological complexities of *in vivo* tumors, including tissue architecture, tumor heterogeneity, necrotic tumor regions, mechanical properties, and cell-matrix interactions, to name a few. Thus, having a matrix to support cell adhesion and expansion and provide the cells with a microenvironment recapitulating patient tumor ECM is vital.

1.2.2.2 Scaffold-based 3D Cancer Models

Tissue engineering as a tool for 3D cell culture utilizes polymeric biomaterials to provide cancer cells with matrix support. Biomaterials employed in cancer tissue engineering include natural materials such as Matrigel, collagen, and agarose, synthetic materials such as poly(ethylene glycol) and poly(lactic-co-glycolic acid), and hybrid materials, which are a combination of natural ECM proteins and synthetic polymer components (Pradhan et al. 2016). Although the use of both natural and synthetic biomaterials has enhanced cancer research, these biomaterials have a number of inherent limitations. For instance, natural biomaterials have shown batch-to-batch inconsistency and low elastic modulus as compared to patient tumors (Pradhan et al. 2016). Although synthetic biomaterials overcome these limitations, they are unable to provide biochemical cues for cells to

closely mimic the way they function in the native tumor milieu (Pradhan et al. 2016). Therefore, the use of hybrid materials in cancer tissue engineering has become prevalent as an appropriate scaffold that overcomes the limitations associated with both natural and synthetic biomaterials (Pradhan et al. 2016).

One important type of biomaterials is hydrogels, which are cross-linked networks of chains of natural or synthetic polymers and offer distinct advantages over other biomaterials. Hydrogels are capable of maintaining high water content and providing nutrient and cellular metabolite exchange. Mechanical and biochemical characteristics of hydrogels can be modulated by modifying either the individual polymer chains of the network or the cross-linking properties of the polymer chains in general (Pradhan et al. 2016). Other advantages of hydrogels are their capabilities for the inclusion of adhesive sites, growth factors, and matrix metalloproteases (MMPs)-sensitive cleavage sites, thereby influencing phenotype and growth of cells *in vitro*. Overall, biomimetic hydrogels can be engineered chemically, mechanically, and structurally to modify cellular behavior with time and provide critical physiological context to 3D cultured cancer cells (Pradhan et al. 2016).

1.2.3 *In vivo* cancer models

In vivo models are a useful tool to examine tumor biology and anti-cancer therapeutic response with a higher degree of physiological relevance compared to *in vitro* cancer models (Cree, Glaysher, and Harvey 2010). Several studies have shown that immunocompromised mice-based cancer models can maintain patient tumor molecular characteristics, gene expression, and mutations (Brown et al. 2016; Lee et al. 2014; Cho et al. 2014). Other studies generated genetic models of cancer *in vivo* (L. Yang et al. 2019; Walrath et al. 2010). However, the use of animal

models requires special facilities and typically is costly, time-consuming, and labor-intensive, thereby resulting in low throughput platforms (Day, Merlino, and Van Dyke 2015; McIntyre et al. 2015; Murayama and Gotoh 2019). Furthermore, it is difficult to visualize real-time cell-cell, cell-matrix, and cell-drug interactions in *in vivo* models, and the number of experimental conditions that can be tested is limited. Thus, development of *in vitro* 3D models to study cancer is needed.

1.3 Cell Sources in Cancer Research

1.3.1 Standard Cell Lines

Although over the last two decades, cancer therapy for colorectal tumors has significantly been improved, almost half of the patients with this disease experience recurrence (relapse) after undergoing cancer therapy (Lee et al. 2014). This recurrence is partly due to poor correlations between clinical responses to therapeutic agents in experimental models and responses to the identical agents in patients(Hidalgo et al. 2014). Preclinical trials of anti-cancer drugs mostly rely on *in vivo* and *in vitro* models using standard tumor cell lines. However, the molecular characteristics of these cell lines have been altered over time due to the prolonged *in vitro* cell culturing (Lee et al. 2014). In addition, as cell lines are typically composed of one cell subpopulation and selectively isolated during establishment, they lack the extensive heterogeneity observed in patients' tumors (Cree, Glaysher, and Harvey 2010; Fernando et al. 2006).

Cancer cell lines can be used in animals to generate tumor xenograft models. The generated xenografts in *in vivo* models show different gene expression and heterogeneity from those of patient tumors. These differences in gene expression and heterogeneity caused the cells to be a poor prediction for the translation of preclinical drug testing into the clinical outcome (Lee et al. 2014).

The majority of the current 3D models have focused on the use of standard cell lines (Pradhan, Clary, et al. 2017; Rios de la Rosa et al. 2018; Dolznig et al. 2011; Hoshiba and Tanaka 2016; Magdeldin et al. 2014; Dainiak et al. 2008; Shakibaei et al. 2015; Nyga et al. 2013). Self-aggregated tumor spheroids (TS) and organoids, as scaffold-free 3D cancer models, have been successfully employed in CRC research (Luca et al. 2013; Stadler et al. 2018). A few studies have also focused on utilizing CRC cell lines in different types of biomaterials for tissue engineering (Hoshiba and Tanaka 2016; Dainiak et al. 2008; Magdeldin et al. 2014; Shakibaei et al. 2015; Nyga et al. 2013; Dolznig et al. 2011). Most of these studies are aimed at developing tissue-engineered CRC models using natural biomaterials such as collagen and alginate for drug testing applications. For instance, Magdeldin et al. (Magdeldin et al. 2014) developed a tissue-engineered CRC model using collagen I hydrogel and HCT 116 and HT-29 cell lines to study the anti-proliferative effects of the antineoplastic agent, cetuximab, on the 3D cultured cells in comparison to 2D culture. Shakibaei et al. (Shakibaei et al. 2015) cultured HCT 116 cell line in alginate to investigate the activity of 5-FU chemotherapeutic agent. Apart from the model development for drug testing applications, one study (Dolznig et al. 2011) established a 3D culture model using LS 174T CRC cells. The authors embedded either normal colon or CRC-associated fibroblasts with pre-formed CRC spheroids in collagen I to examine fibroblast-cancer cell interactions phenotypically and at the molecular level. Another study (Nyga et al. 2013) developed a 3D engineered CRC model using HT-29 in collagen I to study cancer cell phenotypes such as cell morphology, growth rate, and migration in 3D in comparison to 2D cell culture. The tissue-engineered models in these studies were created with a relatively low cell density ($0.2\text{-}2 \times 10^6$) compared to patients' tumors. In addition, in most of these studies, the engineered tissues were

maintained in culture for up to 15 days, thereby limiting the investigation of changes to cancer cell phenotypes in long-term culture.

1.3.2 Patient-derived Cancer Cells

To address the shortcomings of standard cell lines, patient-derived cancer cells can be utilized in cancer research. One application of these cancer cells is an *in vivo* cancer model of patient-derived xenograft (PDX). PDX tumors are established when a human tumor is implanted directly into an animal, typically mice (Hidalgo et al. 2014). The major histological and genetic characteristics of PDX tumor models may be identical to their donor tumors and PDX tumors are significantly more predictive of clinical outcomes compared to standard cell lines (Hidalgo et al. 2014). These physiologically relevant pre-clinical PDX tumor models are useful platforms to understand tumor biology and for identifying anti-cancer therapeutics (Cree, Glaysher, and Harvey 2010). However, as an animal model, the use of PDX tumor models requires special facilities and typically is associated with a high cost of care (Day, Merlino, and Van Dyke 2015; McIntyre et al. 2015; Murayama and Gotoh 2019). Furthermore, experimental assays are usually low throughput in animals, thereby resulting in hurdles in anti-cancer drug development (Day, Merlino, and Van Dyke 2015; McIntyre et al. 2015; Murayama and Gotoh 2019).

1.4 Patient-derived and PDX Tumor Cells in *In vitro* 3D Models

Several studies have utilized PDX cells, including CRC PDX cells, in *in vitro* platforms to overcome challenges associated with animal models. Kondo et al. (Kondo et al. 2019) isolated CRC PDX cells and produced self-aggregated clusters of pure cancer cells to screen over 2400 drugs. Other studies also reported the generation of high-throughput cancer models from patient-

derived or PDX cells for understanding tumor biology and drug screening (Boehnke et al. 2016; Verissimo et al. 2016). However, the models developed in these studies were matrix-free in the initial tissue formation and selectively incorporated only some of the cell types from the PDX or primary tumor. Both matrix support and inclusion of all cellular subpopulations may be advantageous in recapitulating the parental tumor microenvironment more fully.

Recent studies have begun to employ patient-derived cells to form engineered cancer tissues, including prostate and glioblastoma tissues (E.L. Fong, Wan, et al. 2016; Pedron et al. 2019; Pedron, Hanselman, et al. 2017; Pedron, Polishetty, et al. 2017) and create *in vitro* platforms that provide an ECM for patient-derived cells. Fong et al. (E.L. Fong, Wan, et al. 2016) engineered a 3D *in vitro* prostate cancer model by separating and encapsulating aggregates of pure cancer cells to monitor tumor-stromal interactions involved in prostate cancer bone metastasis. Pedron et al. (Pedron et al. 2019) utilized gelatin methacrylamide and hyaluronic acid methacrylate hydrogels for the culture of patient-derived glioblastoma cells. In these studies, 3D scaffolds have been utilized to mimic tumor microenvironmental cues with high relevance and produce a higher throughput platform as compared to PDX tumor models for cancer study.

1.5 Characterization of and Considerations in *In vitro* 3D Cancer Model of PDX

In vitro 3D models of PDX can be characterized through experimental assays and compared to prenatal tumors. Important aspects to consider include tumor heterogeneity, cell subpopulations, gene expression, mutation, to name a few. Arguably, one of the most advantageous characteristics of PDX tumor models is that they can maintain intratumor heterogeneity and histological features of their parental tumors (Kopetz, Lemos, and Powis 2012). It is known that human tumor is heterogeneous and heterogeneity plays an important role in cancer

treatment (Dobbin et al. 2014; McGranahan and Swanton 2015; Cassidy, Caldas, and Bruna 2015; Marusyk and Polyak 2010); however, it is still unclear which aspects of tumor heterogeneity are important to therapeutics and clinical treatment (Alizadeh et al. 2015). To better understand this complexity, researchers try to define various types of heterogeneity which exist within a tumor. Tumor heterogeneity can generally be caused by two factors; cell-intrinsic and cell-extrinsic (P. R. Prasetyanti and Medema 2017). Examples of cell-intrinsic factors are genetic mutations, epigenetic alterations, gene expression, cell surface markers, and cellular morphology, among others. Fong et al. (E.L.S. Fong et al. 2018) considered the characterization of their *in vitro* 3D model of PDX tumors based on studying these phenotypes and genotypes. The authors reported a similar tumor heterogeneity in 3D microporous hydrogels and the originating Hepatocellular carcinoma in SCID mice, suggesting that 3D *in vitro* model using PDX lines may maintain heterogeneity of the parental tumor. The authors also observed similar gene expression and mutational profile for the 3D microporous hydrogels and Hepatocellular carcinoma in SCID mice (E.L.S. Fong et al. 2018). Considering these methods of characterization are essential for validation of the 3D *in vitro* model based on PDX tumor cells.

Chapter 2: An *in vitro* 3D Tissue-engineered Cancer Model for the Investigation of Colorectal Cancer Phenotypes

2.1 Introduction

Despite the tremendous effort and investment in understanding cancer over the last few decades, it is still the second leading cause of death in the united states (Siegel, Miller, and Jemal 2020). Development of *in vitro* cancer models has been of great value to study tumor biology and investigate anti-cancer therapeutics. To develop these *in vitro* models, cancer cells were traditionally cultured on plastic substrates as 2D monolayer cell cultures. Although 2D cancer models have provided many insights into cancer cell biology and facilitated anti-cancer drug development, these models are intrinsically unable to mimic many pathophysiological cues of the native tumor milieu. Furthermore, these models can cause alteration in cellular functions such as growth and proliferation due to culture conditions (Okada, Vaeteewoottacharn, and Kariya 2019; Kodack et al. 2017). To overcome these challenges, *in vitro* 3D cell cultures emerged as a valuable technique to improve cancer modeling. *In vitro* 3D cell cultures have recently gained a lot of attention in cancer research as they better resemble human tumors and have longer lifespans.

The use of 3D cancer cell culture, including both scaffold-free and scaffold-based 3D models, has been reported for breast cancer (D. Truong et al. 2016; Pradhan, Clary, et al. 2017; Pradhan, Hassani, et al. 2017; Pradhan and Slater 2019), prostate cancer (Hsiao et al. 2009; Gao et al. 2014; Gurski et al. 2009; E.L. Fong et al. 2014; E.L. Fong, Wan, et al. 2016), lung cancer (Gill et al. 2012; Simon et al. 2016), colorectal cancer (Luca et al. 2013; Hoshiba and Tanaka 2016; Devarasetty et al. 2017; Dolznig et al. 2011; Stadler et al. 2018; Magdeldin et al. 2014), and melanoma (D.H. Kim et al. 2018) among others. Self-aggregated tumor spheroids (TS) and organoids, valuable scaffold-free 3D cancer models, have been successfully employed in

colorectal cancer research (Luca et al. 2013). However, TS- and organoids-based models have several limitations; some cell lines form irregular-sized TS or organoids, whereas some do not self-aggregate and form them at all. Even for cancer cell lines that can self-aggregate, it has been shown that some subsets of the cell population are unable to adhere and integrate to TS. Specifically, for colorectal cancer cells, Stadler et al. (Stadler et al. 2018) demonstrated that a small proportion of HCT 116, DLD, and SW620 colorectal cancer cell lines lost their adhesion phenotype through TS formation and did not integrate into the TS. In addition, self-aggregated cancer cells lack the support of a surrounding extracellular matrix (ECM) as they form these 3D structures. Cell-matrix interactions play an important role in cancer progression, invasion, and metastasis, as well as cell responses to anti-cancer drugs (Quail and Joyce 2013; Nguyen, Bos, and Massague 2009). The lack of 3D matrix results in the loss of many physiological hallmarks of *in vivo* tumors, including tissue architecture, tumor heterogeneity, necrotic tumor regions, mechanical properties, and cell-matrix interactions, to name a few. Thus, having a matrix to support cell adhesion and expansion and provide the cells with a microenvironment recapitulating patient tumor ECM is vital.

Tissue engineering as a tool for 3D cell culture utilizes polymeric biomaterials to provide cancer cells with matrix support. Biomaterials employed in cancer tissue engineering include natural materials such as Matrigel, collagen, and agarose, synthetic materials such as poly(ethylene glycol) and poly(lactic-co-glycolic acid), and hybrid materials which are a combination of natural ECM proteins and synthetic polymer components (Pradhan et al. 2016). Although the use of both natural and synthetic biomaterials has enhanced cancer research, these biomaterials have a number of inherent limitations. For instance, natural biomaterials have shown batch-to-batch inconsistency and low elastic modulus as compared to patients' tumors (Pradhan et al. 2016). Although synthetic

biomaterials overcome these limitations, they are unable to provide biochemical cues for cells to closely mimic the way they function in the native tumor milieu (Pradhan et al. 2016). Therefore, the use of hybrid materials in cancer tissue engineering has become prevalent as an appropriate scaffold that overcomes the limitations associated with both natural and synthetic biomaterials (Pradhan et al. 2016) .

A few studies have also focused on utilizing different types of biomaterials for CRC tissue engineering (Hoshiba and Tanaka 2016; Dainiak et al. 2008; Magdeldin et al. 2014; Shakibaei et al. 2015; Nyga et al. 2013; Dolznig et al. 2011). Most of these studies are aimed at developing tissue-engineered CRC models using natural biomaterials such as collagen and alginate for drug testing applications. For instance, Magdeldin et al. (Magdeldin et al. 2014) developed a tissue-engineered CRC model using collagen I hydrogel and HCT 116 and HT-29 cell lines to study the anti-proliferative effects of the antineoplastic agent, cetuximab, on the 3D cultured cells in comparison to 2D culture. Shakibaei et al. (Shakibaei et al. 2015) cultured HCT 116 cell line in alginate to investigate the activity of 5-FU chemotherapeutic agent. Apart from the model development for drug testing applications, one study (Dolznig et al. 2011) established a 3D culture model using LS 174T CRC cells. The authors embedded either normal colon or CRC-associated fibroblasts with pre-formed CRC spheroids in collagen I to examine fibroblast-cancer cell interactions phenotypically and at the molecular level. Another study (Nyga et al. 2013) developed a 3D engineered CRC model using HT-29 in collagen I to study cancer cell phenotypes such as cell morphology, growth rate, and migration in 3D in comparison to 2D cell culture. The tissue-engineered models in these studies were created with a relatively low cell density ($0.2\text{-}2 \times 10^6$) compared to patients' tumors. In addition, in most of these studies, the engineered tissues were

maintained in culture for up to 15 days, thereby limiting the investigation of changes to cancer cell phenotypes in long-term culture.

3D engineered tissue models have shown the ability to recapitulate line-to-line differences in phenotype for several cancers, including breast (Pradhan, Hassani, et al. 2017; D. Truong et al. 2016) and prostate (Xu et al. 2019; Long et al. 2013) cancers. However, the recapitulation of phenotypic differences in CRC cell lines within a 3D engineered matrix has not been investigated systematically. Here, we have developed an *in vitro* 3D engineered tumor model of colorectal cancer to systematically investigate the phenotypic differences of three commonly used colorectal cancer cells, HCT 116, HT-29, and SW480, using the hybrid biomaterial, poly(ethylene glycol) fibrinogen (PEG-Fb). These 3D engineered colorectal cancer (3D-eCRC) tissues were created by encapsulating each CRC line within PEG-Fb hydrogels at substantially higher cell density (20×10^6) as compared to those reported in the literature. In addition, we maintained these 3D-eCRC tissues in long-term culture (29 days) to investigated changes in cell phenotypes over time as well as line-to-line differences. We have then examined and compared the cell growth, cellular morphology, changes in cell subpopulations, and tissue mechanical stiffness for these cell lines. Overall, our findings are extremely useful for understating the biology of CRC cell lines in 3D matrices. This 3D *in vitro* model could also be further extended for the examination of CRC progression, cell migration and metastasis, and cancer drugs to mitigate the impact of the disease.

2.2 Materials and Methods

2.2.1 Cell culture and maintenance

HCT 116, HT-29, and SW480 CRC cell lines were cultured and passaged in tissue culture flasks using the media specified in Table 2.1. All cultured cells (2D-CRC cells) were maintained in a standard incubator with a temperature of 37 °C and 5% CO2. The cell culture media was changed every 2 days for all cells.

Table 2.1. Specifications of CRC cell lines and their culture media

Cell Line	CRC Stage	Source	Media
HCT 116	Dukes' D	Lipke Lab*	McCoy's 5A Modified Medium 10% (v/v) FBS‡ 1% (v/v) penicillin-streptomycin
HT-29	Dukes' C	ATCC†	Same as HCT 116 media
SW480	Dukes' B	Greene Lab*	DMEM§ 10% (v/v) FBS 1% (v/v) penicillin-streptomycin 12 mM glutagro™ Supplement 1% (v/v) NEAA| solution

*Auburn University (Auburn, AL), †American Type Culture Collection (Manassas, VA), ‡fetal bovine serum, §Dulbecco's Modified Eagle Medium, |non-essential amino acid

2.2.2 Hydrogel synthesis and 3D-eCRC tissues formation

Poly(ethylene glycol) diacrylate (PEGDA) (Pradhan, Hassani, et al. 2017; DeLong, Gobin, and West 2005) and poly(ethylene glycol)-fibrinogen (PEG-Fb) (Almany and Seliktar 2005) were synthesized following established methods. The poly(dimethyl siloxane) (PDMS) molds were made according to methods described in Appendix A. To create the 3D-eCRC tissues, each CRC cell line was mixed with a polymer precursor solution at a density of 20×10^6 cells/mL. The precursor solution contained PEG-Fb with a final concentration of 1.5% (v/v) triethanolamine (TEOA) (Acros Organics), 37 mM 1-vinyl-2-pyrrolidinone (NVP) (Sigma-Aldrich), and 0.1 mM Eosin Y in PBS. A volume of 10 µl of the cell-laden precursor solution was pipetted into each PDMS mold well placed in a 6-well plate. The cell-laden precursor solution was exposed to visible

light for 2 minutes to crosslink. Molds were then removed, and 3 mL cell culture media was added. The 3D-eCRC tissues were maintained in culture for 29 days in a standard incubator with a temperature of 37 °C and 5% CO_2. Similar to 2D cell culture, the cell culture media was changed every 2 days for all cells.

2.2.3 Cell viability assay and image acquisition

To determine whether the CRC cells maintained their viability in the 3D-eCRC tissues both post-encapsulation and over timer, the cell viability was assessed for core, midpoint, and periphery regions of 3D-eCRC tissues using LIVE/DEAD® Viability/Cytotoxicity Kit (ThermoFisher Scientific) and according to the manufacturer's protocol. Briefly, a viability solution containing 2 μM calcein AM, 4 mM ethidium homodimer-1 (EthD-1), and Hoechst 33342 (Calbiochem) (20 μg/mL) was added to the tissue to mark live cells, dead cells, and all cell nuclei. The fluorescently labeled cells were imaged using an inverted Nikon Eclipse Ti microscope equipped with an Andor Luca S camera and a fluorescence light source to obtain Z-stacks. ImageJ software (version: 2.0.0-rc-68/1.52e) was employed to analyze the Z-stacks of the core, midpoint, and periphery of the 3D-eCRC tissue and calculate the cell viability. The number of both viable and dead cells (cell nuclei count) and the number of dead cells were manually quantified, and the viability percentage was calculated using Equation 2.1. Statistical analysis for cell viability assay was performed using two-way ANOVA followed by the Tukey post *hoc* test.

$$\text{Viability (\%)} = \frac{\text{No. of cell nuclei} - \text{No. of dead cells}}{\text{No. of cell nuclei}} \qquad \text{Equation 2.1}$$

2.2.4 Growth and morphological analysis of cell colonies in 3D-eCRC tissues

The 3D-eCRC tissues were maintained in long-term culture (29 days). The core, midpoint, and periphery of the tissues were imaged every 7 days using the aforementioned microscope to obtain phase-contrast Z-stacks (100 μm thickness). The Z-stack images were analyzed using ImageJ software to quantify the area and aspect ratio of the cancer cell colonies within 3D-eCRC tissues. At least 100 cancer cell colonies in regions of interest from 3D-eCRC tissues were analyzed.

2.2.5 Flow cytometry

Cell labeling and quantification by flow cytometry were carried out according to the protocols described in Appendix A. Briefly, the 2D-CRC cells and 3D-eCRC tissues were dissociated to obtain single cells, and the number of viable cells was counted post-dissociation using a hemocytometer and trypan blue staining. To identify CD44 positive ($CD44^+$) cells, proliferating cells, differentiated epithelial cells, and N-Cadherin positive ($NCAD^+$) cells, the antibodies listed in Table 2.2 were used, respectively. Zombie Green™ Fixable Viability Kit (BioLegend) was used to gate out the dead cells. Nonspecific binding sites on the cell surface were blocked using cold blocking buffer (0.5% (w/v) Bovine Serum Albumin (BSA) (Sigma-Aldrich) and 10% (v/v) FBS in 1X PBS) containing 12 μg/mL of Human BD Fc Block™ (BD Biosciences) and 5 μg/mL of Mouse BD Fc Block™ (BD Biosciences). The cells were fixed and permeabilized using cold Foxp3 Fixation/Permeabilization (eBioscience™) working solution. Nonspecific binding sites inside the cells were blocked using FACS buffer (0.5% (w/v) BSA and 10% (v/v) FBS in 1X Permeabilization Buffer). The absence of cell autofluorescence was confirmed using unstained cells. Compensation beads (ThermoFisher Scientific) and dead cell control were used to

compensate for fluorochrome overlaps. A CytoFLEX LX Flow Cytometer (Beckman Coulter) was utilized to quantify the labeled cells, and subsequently, FlowJo software (version 10.0.7) was employed for data analysis. The cell populations within the 3D-eCRC tissues were investigated on Days 1, 8, 15, 22, and 29, and two separately prepared cell cultures of 2D-CRC were used as control. In addition to investigating the percentage of cell subpopulations within the 3D-eCRC tissues over time, the number of cells in each subpopulation (the population percentage quantified via flow cytometry multiplied by the total number of viable cells counted post tissue dissociation) was tracked over time. Forward Scatter (FSC) and Side Scatter (SSC) of the cells were also obtained by flow cytometry. FSC and SSC are proportional to cell size and granularity, respectively.

Table 2.2. Specifications of primary and secondary antibodies

Primary antibody	Host species	Isotype	Clonality	Secondary antibodies	Reactivity	Isotype
CD44	Mouse	IgG2a	Monoclonal	Zenon™ PE[‡]	Mouse	IgG2a
Ki-67	Rabbit	IgG	Polyclonal	Zenon™ A647[§]	Rabbit	IgG
CK20[*]	Rabbit	IgG	Monoclonal	Zenon™ A647[§]	Rabbit	IgG
NCAD[†]	Sheep	IgG	Polyclonal	NL557[|]	Sheep	IgG

[*]Cytokeratin 20, [†]N-Cadherin, [‡]R-phycoerythrin, [§]Alexa Fluor™ 647, [|]NorthernLights™ NL557

2.2.6 Immunostaining and image acquisition

To investigate the cell morphology and locational heterogeneity within the 3D-eCRC tissues, the cells were labeled according to the protocol described in Appendix A. The following antibodies combinations were used; 1) Hoechst 33342, Ki-67 rabbit IgG pAb with Alexa Fluor 488 anti-rabbit IgG secondary antibody (ThermoFisher Scientific cat. # A11008), and CD44 mouse IgG2a mAb with Alexa Fluor 568 anti-mouse IgG secondary antibody (ThermoFisher Scientific cat. # A11004), or 2) Hoechst 33342, N-Cadherin sheep IgG labeled with

NorthernLights™ NL557 anti-sheep IgG secondary antibody, and alpha-smooth muscle actin (α-SMA) mouse IgG2a mAb with Alexa Fluor 647 anti-mouse IgG secondary antibody (ThermoFisher Scientific cat. #A-21235). The core, midpoint, and periphery of the 3D-eCRC tissues were imaged using a Nikon confocal microscope. (Nikon AI Confocal Scanning Laser Microscope) to obtain Z-stacks. The fluorescence Z-stacks were processed using ImageJ software.

The Z-stack images were also used to count the number of all cell colonies per each field of view of the core, midpoint, and periphery regions of the 3D-eCRC tissues. The number of colonies per nanoliter (nL) tissue volume was calculated for each region by dividing the counted number of cell colonies by the volume of each Z-stack. The number of colonies per each region was calculated by multiplying the number of colonies per nL tissue volume by the total volume of each region. The number of colonies per tissue was calculated by summing up the number of colonies per each region for all regions. Total colony area per nL tissue volume was calculated by multiplying the number of colonies per nL tissue volume by the average colony area for each region. Total colony area per each region was calculated by multiplying the total colony area per nL tissue volume by the total volume of each region. Total colony area per tissue, proportional to the total cell number in the 3De-CRC tissues, was calculated by summing up the total colony area per each region for all regions. Furthermore, the Z-stack images were used to quantify the area of each cell in the 3D-eCRC tissues.

2.2.7 Size and shape analysis of 3D-eCRC tissues

The changes in whole 3D-eCRC tissue morphology were investigated over time using the images obtained from a CellScale MicroSquisher system (side view of the tissues) and phase-contrast images taken by the Nikon microscope (top view of the tissues). These images were used

to quantify the volume (top and side views), mean geometric diameter (top view using Equation 2.2), thickness (side view), circularity (side view using Equation 2.3), aspect ratio (side view using Equation 2.4), and protrusiveness (top view using Equation 2.5) of the 3D-eCRC tissues using ImageJ software. A minimum of three 3D-eCRC tissues per time point were analyzed.

$$\text{Geometric Diameter} = \sqrt{\text{major axis} \times \text{minor axis}} \quad \text{Equation 2.2}$$

$$\text{Circularity} = \frac{4\pi \times \text{area}}{\text{perimeter}^2} \quad \text{Equation 2.3}$$

$$\text{Aspect ratio} = \frac{\text{major axis}}{\text{minor axis}} \quad \text{Equation 2.4}$$

$$\text{Protrusiveness} = \frac{1}{\text{solidity}} = \frac{\text{convex area}}{\text{area}} \quad \text{Equation 2.5}$$

2.2.8 Mechanical stiffness of 3D-eCRC-PDX tissues

To track the change in the mechanical stiffness of the 3D-eCRC tissues over the course of 29 days, the tissues were subjected to parallel-plate compression testing using a CellScale MicroSquisher system. The compression system was equipped with a 558.8 μm gauge cantilever beam and a square microplate. The 3D-eCRC tissues were placed onto the Microsquisher stage in PBS at 37°C and preconditioned by being compressed three times. The force versus displacement data were collected by SquisherJoy software with compression and relaxation cycles at a rate of 10 μm/s to 30% deformation. The data were then converted to stress-strain curves using Microsoft Excel. The Young's moduli were calculated by selecting the linear portion of the curve and obtaining the slope for the selected line. Three samples were measured for each time point for each of the three cell lines.

2.2.9 Cell doubling time in 2D-CRC cultures and 3D-eCRC tissues

For 2D-CRC cultures, approximately 5×10^6 viable cells were seeded to each tissue culture flask. After 4 to 8 days of culture, the CRC cells were dissociated using trypsin and counted using a hemocytometer and trypan blue staining. The doubling time was calculated based on the number of seeded and harvested viable cells. For 3D-eCRC tissues, following tissue dissociation for flow cytometry analysis, the total number of viable cells in each 3De-CRC tissue was counted on Day 1 and Day 15 using a hemocytometer and trypan blue staining. The doubling time was calculated based on the total number of viable cells (direct cell count) in each 3De-CRC tissue on Day1 and Day 15. The total cell numbers in 3D-eCRC tissues were also calculated based on the number of colonies per tissue, cell colony area, single-cell area, and cell viability and compared to the direct cell count

2.2.10 Statistical analysis

GraphPad Prism 8.0 (GraphPad Software, San Diego, California USA, www.graphpad.com) was used for the following analysis. The outliers were removed using the ROUT method with coefficient Q = 1%. The normality of distribution and equality of variance were then checked. Either one-way or two-way ANOVA followed by Tukey *post hoc* test was performed to determine statistical significance. The rates of change over time (slopes) were found and compared using linear regression analysis followed by an F-test to determine statistically significant differences. Correlation matrix was calculated based on Spearman's correlation analysis. p value ≤ 0.05 was considered statistically significant unless otherwise stated.

2.3 Results

2.3.1 CRC cells remained viable in 3De-CRC tissues

HCT 116, HT-29, SW480 CRC cell lines were individually encapsulated within PEG-Fb hydrogel to create 3D-eCRC tissues. Schematic of the encapsulation process is presented in Figure 2.1. Having assessed the cell viability in 3De-CRC tissues over time, it was found that a high percentage of the cells remained viable both post-encapsulation and over long-term culture. On Day 1, approximately 94±1%, 97±1%, and 95±1% of cells were found to be viable in HCT 116, HT-29, and SW480 tissues, respectively (Figure 2.2). Although, from Day 1 to Day 29, HCT 116, HT29, and SW480 showed approximately 4%, 7%, and 3% decrease in cell viability, respectively ($p < 0.005$), the viability was approximately higher than 90% for all cells on all time points (Figure 2.2 and Figure B.1). Furthermore, the viability was found to be region-independent as the core, midpoint, and periphery of 3D-eCRC tissues showed similar cell viability for each cell line with no significant difference (Figure B.1).

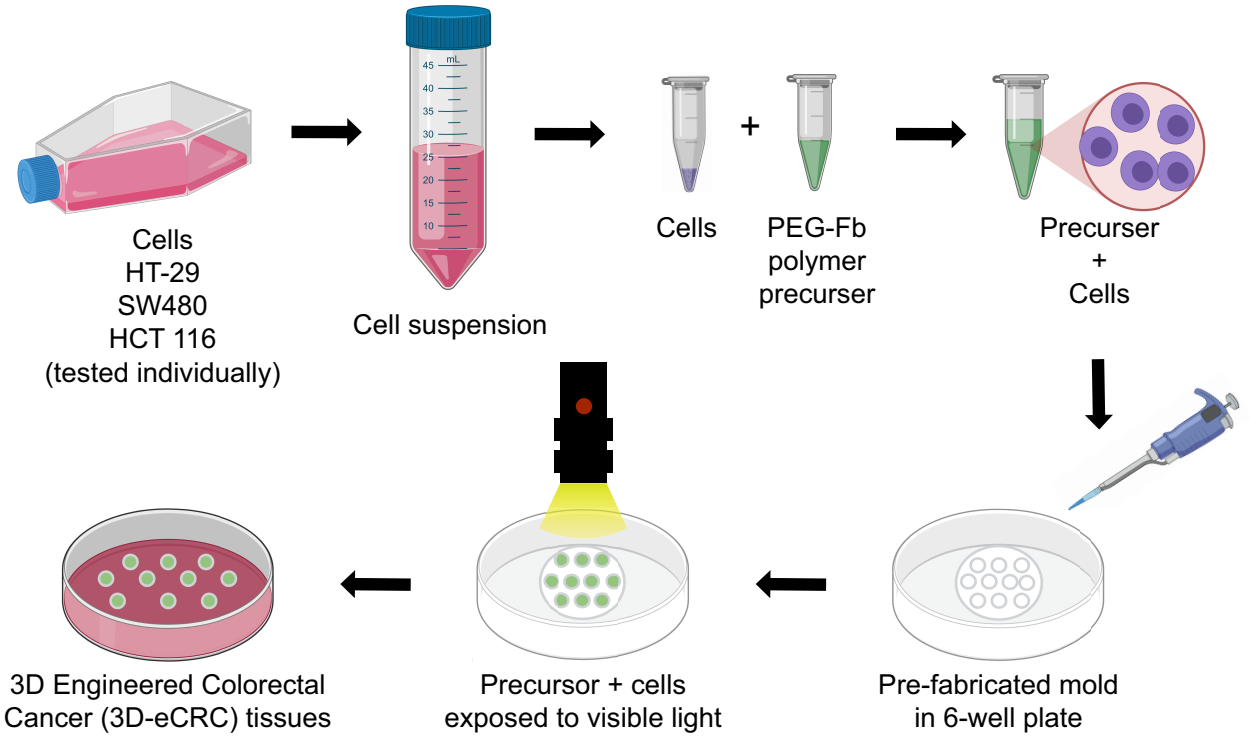

Figure 2.1. CRC cells were encapsulated in PEG-Fb. HCT 116, HT-29, and SW480 CRC cell lines were individually encapsulated in PEG-Fb to form 3D-eCRC tissue and cultured over 29 days.

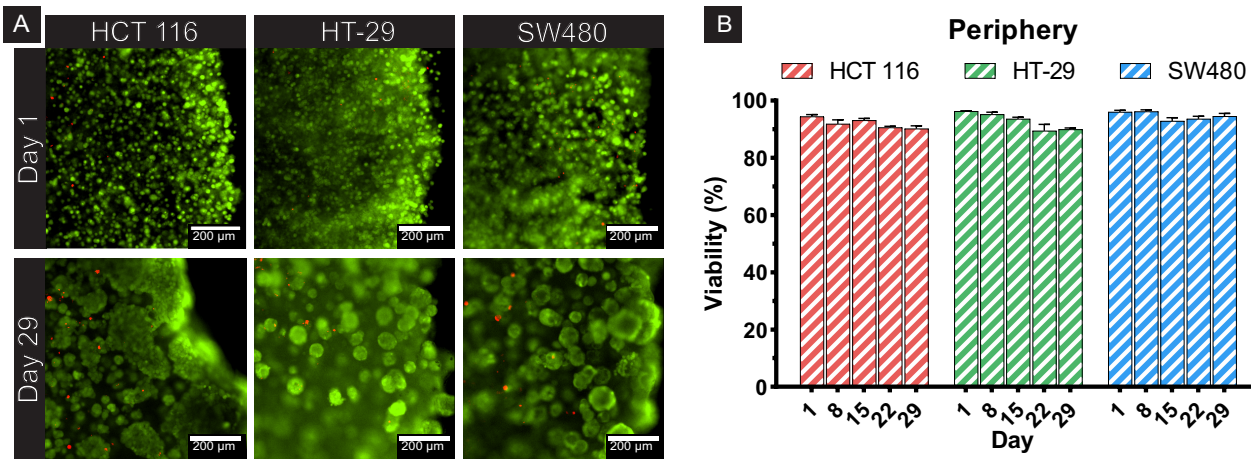

Figure 2.2. CRC cells remained viable in the 3D-eCRC tissues. (A) Representative confocal images of live (green) and dead (red) cells in the periphery region of 3D-eCRC tissues (scale bar

= 200 μm). (B) Cell viability quantification. The percentage of viable cells in the periphery region of 3D-eCRC tissues decreased significantly over 29 days of culture; however, the viability was approximately higher than 90% for all CRC cells at all time points. Bar = mean ± SD. Means that do not share a letter are significantly different ($p \leq 0.05$; n = 3 tissues).

2.3.2 CRC cells showed both region- and line-dependent growth and temporal morphological changes in 3De-CRC tissues

To investigate the growth and morphological changes of CRC cells within the 3De-CRC tissues, Z-stack images of the cells in the core, midpoint, and periphery of the 3De-CRC tissues were taken and analyzed over time (Figure 2.3 A-C). Growth and morphological changes of the cells were found to be highly dependent on both tissue regions and cell lines. The cell colony area increased significantly over 29 days of culture for all cell lines and all regions ($p < 0.0001$); however, the rates of increase in colony area were found to be the highest for the periphery, followed by midpoint and core regions ($p<0.0001$) (Figure 2.3 D-F and Figure B.2 A-C). For instance, the rates of increase in colony area for the periphery region were approximately 139%, 85%, and 106% higher than those for the core regions for HCT 116, HT-29, and SW480, respectively. Similarly, the rates of increase in colony area for the midpoint region were approximately 71%, 25%, and 45% higher than those for the core regions for HCT 116, HT-29, and SW480, respectively. In addition to region dependency, the CRC cell colonies in HT-29 and SW480 tissues were found to grow at significantly higher rates than those in HCT-116 tissues for all regions ($p<0.0001$) (Figure 2.3 G and Figure B.2 D). For instance, for the periphery region, the rates of increase in colony area of HT-29 and SW480 tissues were approximately 94% and 118%

higher than that of HCT 116 tissues, respectively; no significant difference was observed between the rates of change in colony area for HT-29 and SW480 tissues ($p = 0.1097$).

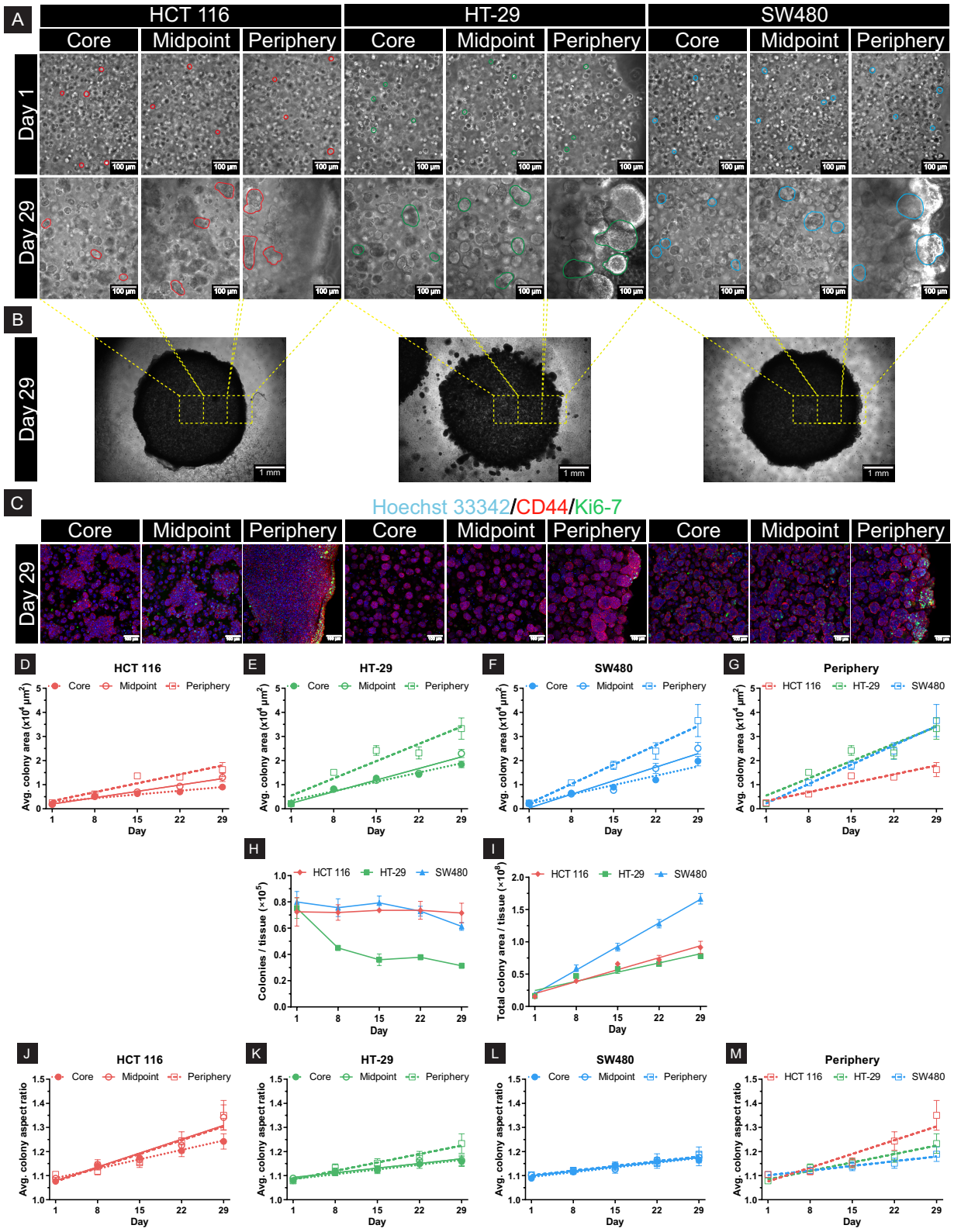

Figure 2.3. CRC cells showed temporal, region- and line-dependent growth and morphology in 3De-CRC tissues. (A) Representative phase-contrast images of CRC cell colonies in the 3D-

eCRC tissues on Day 1 and Day 29. Although on Day 1, the size of the CRC cell colonies for a given cell line was region-independent, on Day 29, larger cell colonies were observed in the periphery, followed by midpoint and core regions (scale bar = 200 μm). (B) Representative phase-contrast images of the 3D-eCRC tissues on Day 29. Many HT-29 cell colonies were anchoring to the tissues as blebs along with existing in the culture media as cell aggregates, which is indicative of collective cell migration from inside the tissues toward the surrounding culture media. HCT 116 and SW480 tissues did not show such a migration pattern. (C) Representative confocal images of CRC cells in the 3D-eCRC tissues labeled with Hoechst 33342 (blue) and CD44 (red) on Day 29. HCT 116 cells formed cell monolayers on the top and bottom of the 3D-eCRC tissues, apart from growing as colonies inside the tissues. No such a cell monolayer formation was observed for HT-29 and SW480 tissues. (D-G) Cell colony area quantification. (D-F) The rate of increase in colony area was significantly higher for the periphery, followed by midpoint and core regions for all CRC cell lines. (G) The cell colonies in HCT-116 tissues grew at a significantly lower rate than those in HT-29 and SW480 tissues; no significant difference was found between the rates of increase in colony area for HT-29 and SW480 tissues. The Data are mean (95% CI) ($p \leq 0.05$; n ≥ 100 cell colonies from at least 3 tissues). (H) the number of colonies per tissue for HT-29 decreased over time and was significantly lower than those for HCT-116 and SW480 tissues. Data are mean ± SD ($p \leq 0.05$; n = 3 tissues). (I) The rate of increase in total colony area for SW480 tissues was significantly higher, followed by those for HCT 116 and HT-29 tissues. Data are mean ± SD ($p \leq 0.05$; n = 3 tissues). (J-M) Cell colony aspect ratio quantification. (J) In the periphery region, the rate of increase in cell colony aspect ratio was significantly higher for HCT 116, followed by those for HT-29 and SW480 tissues. (K-M) For HCT 116, the rates of increase in cell colony aspect ratio for both midpoint and peripety regions were significantly higher than that for the core region. For

HT-29, the periphery region showed a significantly higher rate of increase compared to midpoint and core regions. For SW480, no significant difference between rates of increase for the core, midpoint, and periphery regions was observed. The Data are mean (95% CI) ($p \leq 0.05$; $n \geq 100$ cell colonies from at least 3 tissues).

The numbers of colonies per tissue were also counted for HCT-116, HT-29, and SW480 over 29 days of culture. Although on Day 1, the numbers of colonies per tissue were equivalent for all CRC cell lines, these numbers varied for each cell line as the days progressed. For HCT-116 and SW480, the numbers of colonies per tissue remained fairly constant over time; however, the number of colonies per tissue for HT-29 decreased over time and was significantly lower than those for HCT-116 and SW480 tissues ($p<0.0001$) (Figure 2.3 H). Moreover, the rate of increase in total colony area per tissue was cell line-dependent as the rates of increase for SW480 and HCT 116 were approximately 97% ($p < 0.0001$) and 30% ($p < 0.03$) higher than that for HT-29, respectively (Figure 2.3 I). In addition, the increase in total colony area per nL tissue volume was found to be both cell line- and region-dependent (Figure B.3). Having investigated the underlying reasons, we found that the differences in the number of colonies per tissue and total colony area of the CRC cell lines were partially attributed to the varied migration patterns. For HT-29, many cancer cell colonies were found to be anchoring to the tissues as blebs along with existing in the culture media as cell aggregates, which is indicative of collective cell migration from inside the tissues toward the surrounding culture media (Figure 2.3 B). HCT 116 tissues did not show such a migration pattern, and instead, the cells formed cell sheets on the top and bottom of the 3D-eCRC tissues, apart from growing as colonies inside the tissues (Figure 2.3 C). These cell sheets occupied

a larger area on the tissue periphery as compared to the core and midpoint regions. No pattern of migration (blebbing or cell sheet formation) was observed for SW480 tissues.

The aspect ratio of CRC cell colonies within the 3D-eCRC tissues was also investigated for the core, midpoint, and periphery regions over 29 days of culture. It has been shown that a higher aspect ratio of cancer cell colonies is associated with invasiveness (D. Truong et al. 2016; D.D. Truong et al. 2019; Lyons et al. 2016). Consistent with the metastatic phenotype of the CRC cell lines, the rate of increase in colony aspect ratio for periphery region was the highest for HCT 116 tissues, followed by HT-29 and SW480 ($p < 0.005$) (Figure 2.3 J and Figure B.4 A). The increase in colony aspect ratio over time was also found to be region-dependent (Figure 2.3 K-M and Figure B.4 B-D). For HCT 116 tissues, the increases in colony aspect ratio for both periphery and midpoint regions were approximately 43% higher than that for the core region ($p < 0.002$); no significant difference was observed between the midpoint and periphery regions ($p = 0.9509$). For HT-29 tissues, the increase in colony aspect ratio for the periphery region was approximately 79% higher than those for midpoint and core regions ($p < 0.0003$); no significant difference was observed between the midpoint and core regions ($p = 0.9137$). Interestingly, for SW480 which were the least metastatic among all three cell lines, the rate of increase in colony aspect ratio displayed no significant difference between the core, midpoint, and periphery regions. Taken together, the colony aspect ratio increased over time, and the rate of increase for each CRC cell line was consistent with its metastatic phenotype.

2.3.3 3D-eCRC tissues but not 2D-CRC cultures exhibited temporal changes in cell subpopulations

To identify the temporal changes in cell subpopulations, the cells were labeled with CD44, Ki-67, NCAD, and CK20 antibodies and quantified using flow cytometry. The changes in cell subpopulations within the 3D-eCRC tissues were investigated over 29 days and, as a control, compared to two 2D-CRC cultures that were four cell passage number apart (P_i and P_{i+4}). For 2D-CRC cultures of HCT 116, approximately 70±1 and 73±4 percent of P_i and P_{i+4} cells were found to be $CD44^+$, respectively, with no significant difference between the two cell passages (p = 0.8701) (Figure 2.4 A). This cell subpopulation remained relatively constant over 29 days of culture within the HCT 116 tissues. For HT-29, all cells in both 2D-CRC cultures and 3D-eCRC tissues were positive for CD44 with no temporal changes (Figure 2.4 A). For 2D-CRC cultures of SW480, the P_i and P_{i+4} cells were approximately 93±2 and 94±2 percent $CD44^+$, respectively, with no significant difference between the two cell passages (p = 0.9996). However, in contrast to HCT 116 and HT-29 tissues, this $CD44^+$ cell subpopulation exhibited a significantly decreasing trend within the SW480 tissues, from 90±4 on Day 1 to 81±2 percent on Day 29 ($p < 0.0001$) (Figure 2.4 A). Overall, HT-29 tissues had the highest average percentage of $CD44^+$ cell subpopulation (100%; from Day 1 to Day 29), followed by SW480 (85±4%), and then HCT 116 tissues (71±5%) ($p < 0.0001$) (Figure B.5 A).

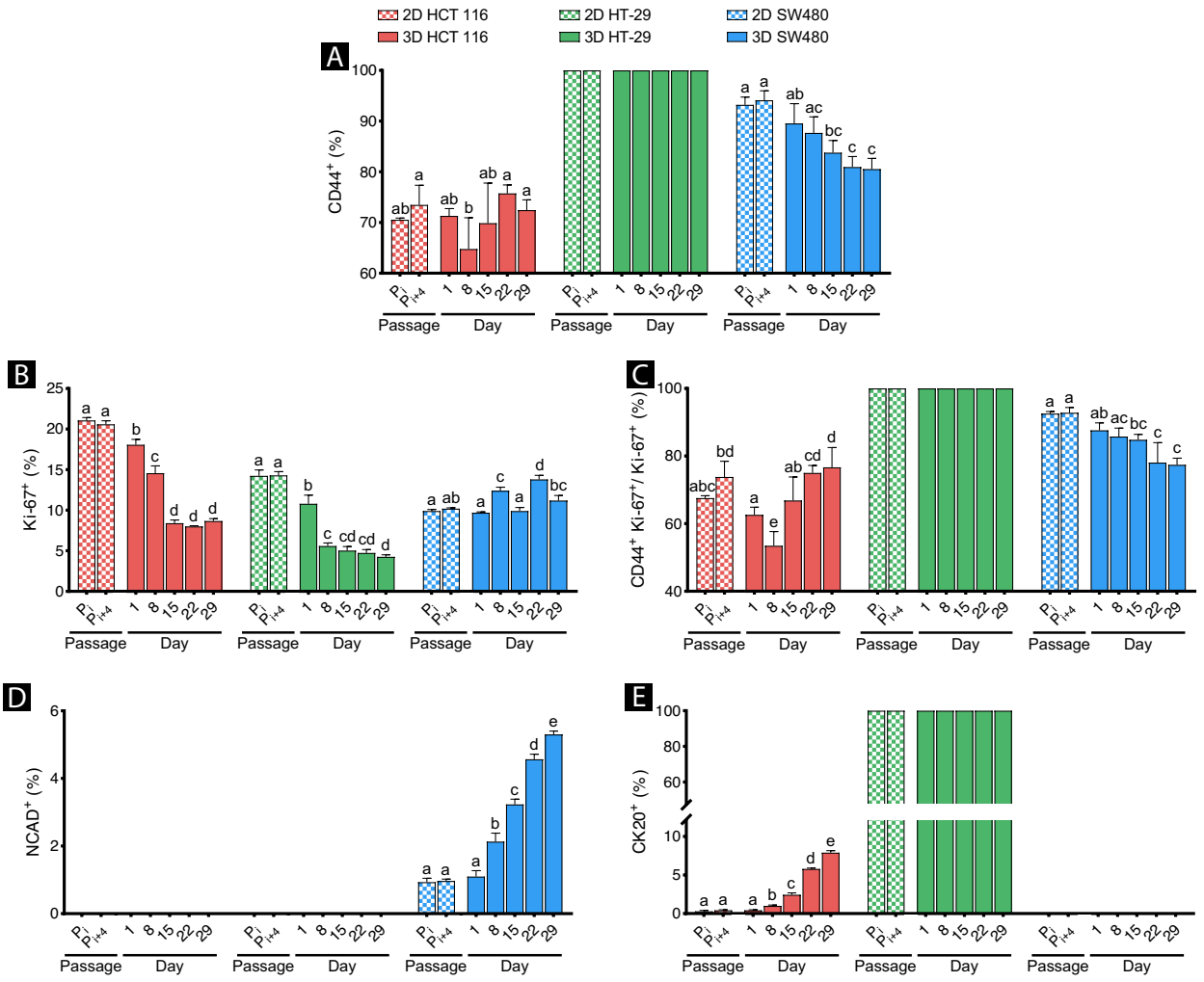

Figure 2.4. 3D-eCRC tissues, but not 2D-CRC cultures, demonstrated line-dependent temporal changes in cell subpopulations. The CRC cells were labeled with CD44, Ki-67, NCAD, and CK20 markers and were quantified using flow cytometry. For individual cell lines, 2D-CRC cultures showed similar cell subpopulations between cell passages (P_i = initial passages; P_{i+4} = four passages after the initial). (A) For HCT 116 tissues, the percentage of $CD44^+$ cell subpopulation was relatively constant over time, whereas this percentage decreased significantly over time for SW480 tissues. All HT-29 cells were positive for CD44. (B) Both HCT 116 and HT-29 tissues exhibited a decreasing percentage of Ki-67 over time, whereas for SW480 tissues, it remained relatively constant. (C) The ratio of proliferative $CD44^+$ cells over the total proliferative

cell subpopulation for HCT 116 first decreased significantly and then increased. For HT-29 tissues, this ratio was 100% at all times as all the cells were positive for CD44. However, a significant decreasing trend in that ratio was observed for SW480 tissues over time. (D) All HCT 116 and HT-29 tissues were negative for NCAD. Interestingly, a minuscule percentage of SW480 cells in 2D-CRC cultures were positive for NCAD; however, when cultured in 3D-eCRC tissues, the $NCAD^+$ cell percentage increased over time. (E) Although HCT 116 cells were negative for CK20 when cultured in 2D, the cells showed an increasing $CK20^+$ cell percentage over time when cultured in 3D-eCRC tissues ($p \leq 0.05$, n = 3 tissue culture flasks for 2D or tissues for 3D. Bar = mean ± SD. Means that do not share a letter are significantly different).

The percentage of proliferative cell subpopulation was quantified by labeling the cells with the Ki-67 marker. HCT 116 and HT-29 cells demonstrated significantly lower percentages of proliferative cells in 3D-eCRC tissues as compared to their 2D counterparts ($p < 0.0001$). Whereas the percentages of proliferative SW480 cells in 3D-eCRC were either not significantly different ($p > 0.2175$) or significantly higher ($p < 0.0001$) as compared to their 2D counterparts (Figure 2.4 B). The percentage of proliferative cell subpopulation was found to show a decreasing trend within the HCT 116 tissues from 18±1% on Day 1 to 8±1% on Day 15 ($p < 0.0001$) and remained constant thereafter (Figure 2.4 B). In HT-29 tissues, a continuous decreasing trend in this cell subpopulation from 7±1% to 4±1% was observed over 29 days ($p < 0.0001$), whereas SW480 tissues had significantly higher proliferative cells at several later time points compared to Day 1 (ranging from 10±1% to 14±1%) ($p \leq 0.0127$) (Figure 2.4 B). Overall, average percentages of proliferative cell subpopulation (from Day 1 to Day 29) in HCT 116 and SW480 tissues were equivalent (11±2%

and 11±4%, respectively; $p = 0.9910$), whereas HT-29 tissues had a significantly lower value ($p < 0.0001$)(6±3%) (Figure B.5 B).

Ki-67 was employed in tandem with CD44 marker to quantify both proliferative and $CD44^+$ cells and calculate the ratio of proliferative $CD44^+$ over total proliferative cell subpopulation. For 2D-CRC cultures, the above-mentioned ratio percentage exhibited no significant difference between P_i and P_{i+4} for a given cell line (Figure 2.4 C). For HCT 116 tissues, the above-mentioned ratio percentage decreased significantly from 62±2% on Day 1 to 53±4% on Day 8 ($p = 0.0091$) and increased from Day 8 to Day 29 (76±6%) ($p < 0.0001$), whereas SW480 tissues demonstrated a decreasing trend in that ratio over 29 days of culture (86±2% to 77±2%) ($p = 0.0025$) (Figure 2.4 C). Since all HT-29 cells were positive for CD44, as expected, the above-mentioned ratio percentage was always 100%.

The percentage of NCAD+ and CK20+ cell subpopulations were also quantified using flow cytometry. All HCT 116 and HT-29 cells in both 2D-CRC cultures and 3D-eCRC tissues were negative for NCAD (Figure 2.4 D). For SW480, only 1 percent of the cells were positive for this marker in the 2D-CRC cultures with no significant difference between P_i and P_{i+4} ($p = 0.9992$). Interestingly, in SW480 tissues, a 4-fold increase from Day 1 to Day 29 (from 1±0% to 5±0%) was observed in this cell subpopulation ($p < 0.0001$) (Figure 2.4 D). In contrast to NCAD, CK20 was found to be negative for all SW480 cells and positive for all HT-29 cells (Figure 2.4 E). Interestingly, HCT 116 cells were negative for CK20 when cultured in 2D; however, these cells showed a significantly increasing trend from 0% to 8±0% for CK20 positivity over time when cultured in 3D-eCRC tissues ($p < 0.0001$).

2.3.4 CRC cells showed line-, time-, and region-dependent marker positivity

The CRC cells in the 3D-eCRC tissues were immunostained with Hoechst 33342, CD44, Ki-67, NCAD, and α-SMA to visualize different cell subpopulations. The immunostaining of the CRC cells in the 3D-eCRC tissues demonstrated that the proliferative ($Ki\text{-}67^{+}$) cells were primarily located in the periphery as compared to the core and midpoint regions for all cell lines (Figure 2.5 A). Moreover, the CRC cells in HCT 116 and HT-29 tissues were verified to be negative for NCAD throughout long-term culture as found in flow cytometry analysis (Figure 2.5 B). In SW480 tissues, although the CRC cells were negative for NCAD on Day 1, immunostaining confirmed that a small quantity of these cells was positive for this marker on Day 29, consistent with the flow cytometry results. Importantly, the NCAD-positive cells were located only in the periphery of the SW480 tissues (Figure 2.5 B). Furthermore, all 3D-eCRC tissues were immunostained using α-smooth muscle actin (α-SMA). Although all CRC cells in HCT 116 tissues were negative for α-SMA on Day 1, independent of regions, they were found to be partially positive for this marker on Day 29 (Figure 2.5 B). For HT-29 and SW480 tissues, all CRC cells were found to be negative for α-SMA throughout the long-term culture. Overall, each CRC cell line in the 3D-eCRC tissues exhibited different markers which were also contingent upon culture time.

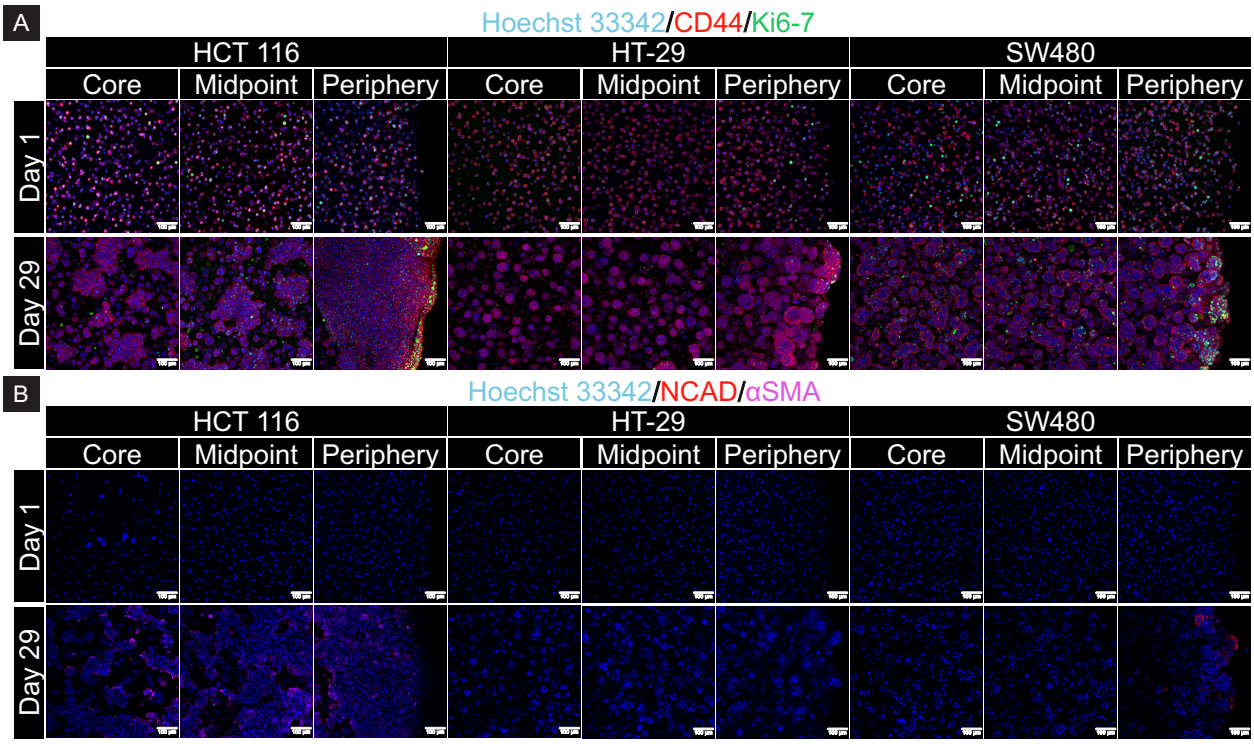

Figure 2.5. CRC cells showed line-, time-, and region-dependent marker positivity. Representative confocal images of CRC cells in the 3D-eCRC tissues labeled with either (A) Hoechst 33342 (blue), Ki-67 (green), and CD44 (red) or (B) Hoechst 33342 (blue), NCAD (red), and α-SMA (magenta). (A) Independent of cell lines, the majority of Ki-67^{+} cells were located in the periphery as compared to midpoint and core regions, thereby causing the cells to grow in larger colonies in the periphery. (B) Although on Day 1, all HCT 116 cells in the 3D-eCRC tissues were negative for α-SMA, the cells were partially positive on Day 29, independent of region. All HT-29 and SW480 cells were negative for this maker at all times. Similarly, all HCT 116 and HT-29 cells were found to be negative for NCAD, independent of time. Although SW480 cells were negative for this marker on Day 1, consistent with flow cytometry data, the cells were partially positive on Day 29. Interestingly, these NCAD^{+} cells were located only in the periphery region.

2.3.5 3D-eCRC tissues showed line-dependent temporal changes in size and shape

To further investigate the phenotypic differences of the CRC cell lines in 3D culture and the effect of cell lines on changes in the tissues' size and shape, parameters such as volume (top and side views), diameter (top view), thickness (side view), circularity (side view), aspect ratio (side view), and protrusiveness (top view) of the 3D-eCRC tissues were quantified over time (Figure 2.6 A). The rate of increase in volume was the highest for HCT 116 (0.15±0.02 nL/day; p < <0.0001), followed by that for SW480 (0.08±0.02 nL/day; $p \leq 0.0004$) which was approximately half of that for HCT-116, whereas HT-29 tissue volume remained constant over time ($p = 0.1165$) (Figure 2.6 B). The diameter of the HCT 116, HT-29, and SW480 tissues remained constant over time based on one-way ANOVA with a post-test for linear trend ($p \geq 0.4597$) (Figure 2.6 C). Although the thickness of the HCT 116, HT-29, and SW480 tissues remained constant over the initial 15 days of culture ($p \geq 0.3142$), it increased significantly from Day 15 to Day 29 for all cell lines ($p \leq 0.02$). The rate of increase for HCT 116 tissues was significantly higher (20.5±2.5 μm/day) than those for SW480 (10.5±1.7 μm/day) and HT-29 (8±2.4 μm/day) tissues ($p \leq 0.005$) (Figure 2.6 D). Therefore, the increase in tissue volumes was a result of the increase in thickness rather than the diameter. The circularity of HCT 116 tissues remained constant from Day 1 to Day 15 and increased significantly from Day 15 to Day 29 (rate = 0.014±0.003 per day, $p = 0.0028$), whereas it remained constant for HT-29 and SW480 tissues over 29 days of culture ($p \geq 0.0642$) (Figure 2.6 E). The aspect ratio of HCT 116 tissues remained constant from Day 1 to Day 15 and increased significantly from Day 15 to Day 29 (rate = – 0.16±0.03 per day, $p = 0.0009$), whereas it remained constant for HT-29 and SW480 tissues over 29 days of culture ($p \geq 0.05$) (Figure 2.6 F). The protrusiveness of the HCT 116, HT-29, and SW480 tissues increased significantly over time ($p < 0.0001$) (Figure 2.6 G). Importantly, these increases in the protrusiveness were found to

be more evident after Day 15, especially for HT-29 tissues. From Day 15 to Day 29, the rate of increase in HT-29 tissue protrusiveness, occurring due to colony outgrowth, was approximately 207% and 1126% higher than those for SW480 and HCT 116 tissues, respectively. Taken together, the temporal changes in tissue size and shape were line-dependent and occurred with a higher rate from Day 15 to Day 29 as compared to the initial 15 days of culture.

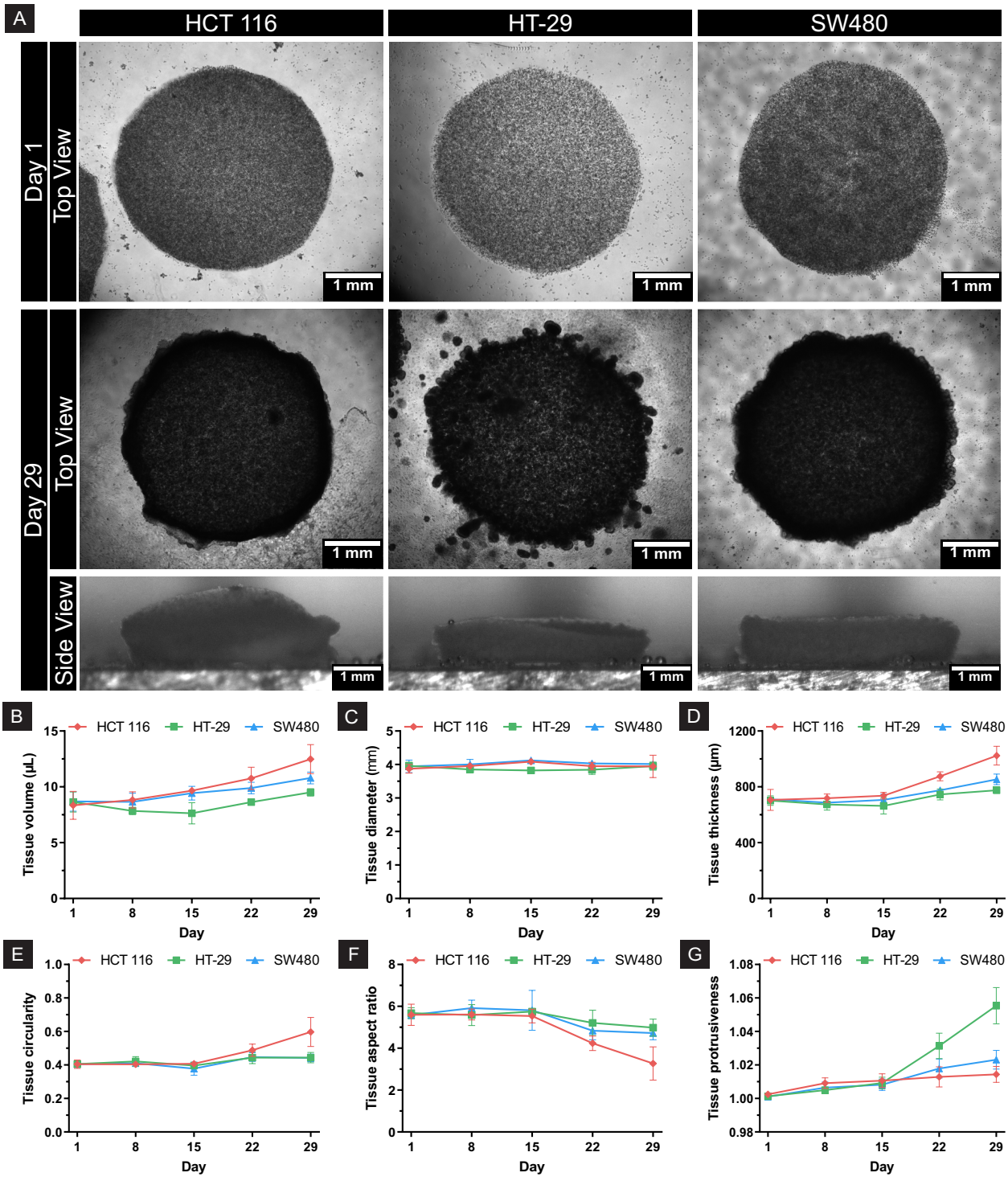

Figure 2.6. 3D-eCRC tissues showed line-dependent temporal changes in size and shape. (A) Representative phase-contrast images of the 3D-eCRC tissues on Day 1 and Day 29 (scale bar = 200 µm). These phase-contrast images were used to quantify the volume (top and side views),

diameter (top view), thickness (side view), circularity (side view), aspect ratio (side view), and protrusiveness (top view) of the 3D-eCRC tissues. (B-G) 3D-eCRC tissue size and shape quantification. (B) The rate of increase in volume was the highest for HCT 116, followed by that for SW480, whereas HT-29 tissue volume remained constant over time. (C) The diameter of the HCT 116, HT-29, and SW480 tissues remained constant. (D-G) Changes in tissue thickness, circularity, aspect ratio, and protrusiveness were line-dependent and more evident from Day 15 to Day 29 as compared to the initial 15 days of culture. Data are mean ± SD ($p \leq 0.05$; n ≥ 3 tissues).

2.3.6 3D-eCRC tissues exhibited line-dependent temporal changes in mechanical stiffness

To understand the differences in mechanical properties of CRC cell lines, Young's modulus of the 3D-eCRC tissues was calculated based on obtained data from the MicroSquisher apparatus. The stiffness of the 3D-eCRC tissues was found to vary significantly depending on the cell line. HCT 116 tissues showed a decreasing trend in stiffness over time, ranging from 227±18 Pa to 134±20 Pa (Figure 2.7). In contrast, an increasing trend in stiffness of both HT-29 and SW480 tissues was observed from Day 1 to Day 29 (Figure 2.7). The stiffness of HT-29 and SW480 tissues ranged from 218±25 Pa to 340±34 Pa and 218±12 Pa to 441±20 Pa, respectively (Figure 2.7). Although, as expected, the stiffness of 3D-eCRC tissues from the three cells was similar on Day 1, temporal changes resulted in significantly higher stiffness for SW480 and HT-29 compared to HCT 116 beginning from Day 15 ($p < 0001$) (Figure B.6). On Day 29, SW480 tissues showed the highest stiffness which was approximately 30% and 230% higher than those for HT-29 and HCT 116 tissues ($p < 0001$) (Figure B.6).

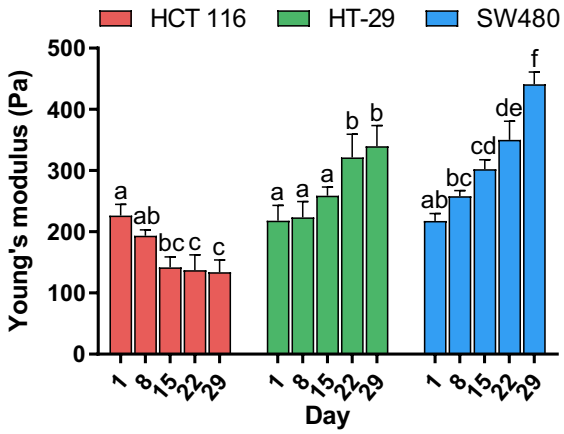

Figure 2.7. Changes in mechanical stiffness of the 3D-eCRC tissues over time were cell line-dependent. Stiffness of HCT 116 tissues was found to decrease significantly over time, whereas for HT 29 and SW480 tissues, an opposite trend was observed. ($p \leq 0.05$, n = 3 tissues of 3D-eCRC per time point. Bar = mean ± SD. Means that do not share a letter are significantly different. Statistical significance was calculated between time points for a given cell line).

2.3.7 Rates of increase in cell number in 3D-eCRC tissues were different than those in 2D-CRC cultures

The total number of viable cells in each 3De-CRC tissue was counted over time (direct cell count) using a hemocytometer following tissue dissociation and trypan blue staining. This number increased significantly over the initial 15 days of culture ($p < 0.0001$) and remained relatively constant thereafter (Figure 2.8 A). Interestingly, the rates of increase in direct cell count differed for 2D-CRC cultures and 3D-eCRC tissues, which were quantified as doubling times. For 2D-CRC cultures, the doubling times for HCT 116 and HT-29 were equivalent (21±1 and 23±1 hours; $p = 0.0924$), whereas that for SW480 was significantly higher (40±2 hours; $p < 0.0001$), which was consistent with ATCC (Manassas, VA) protocols for each cell line (Figure B.7). However, in 3D-eCRC tissues, the doubling times for HCT-116 and SW480 were equivalent (105±8 and

119±14 hours; $p = 0.6505$), whereas that for HT-29 was significantly higher (190±28 hours; $p \leq 0.0081$) over 15 days of culture (Figure B.7). For validation, the total cell numbers in 3D-eCRC tissues were also calculated based on the number of colonies per tissue, cell colony area, single-cell area, and cell viability and compared to the direct cell count. Interestingly, the calculated cell numbers per tissue showed increasing trends similar to direct cell count (Figure 2.8 A and Figure B.8). For investigating the mechanism behind differences in cell number increase in 3D-eCRC tissues, a correlation analysis was performed on Day 15 between the following quantities: total cell number per tissue, number of colonies per tissue, colony area, Forward Scatter (FSC), Side Scatter (SSC) (Figure B.9), cell proliferation (percentage of Ki-67), and tissue volume. It was found that the total cell number per tissue had a significantly positive correlation with the number of colonies per tissue, cell proliferation, and tissue volume and negative correlation with FSC ($p \leq 0.05$). Accordingly, lower values of the number of colonies per tissue, cell proliferation, and tissue volume and higher FSC values (proportional to cell size) for HT-29 tissues resulted in the lower cell number as compared to HCT 116 and SW480 tissues.

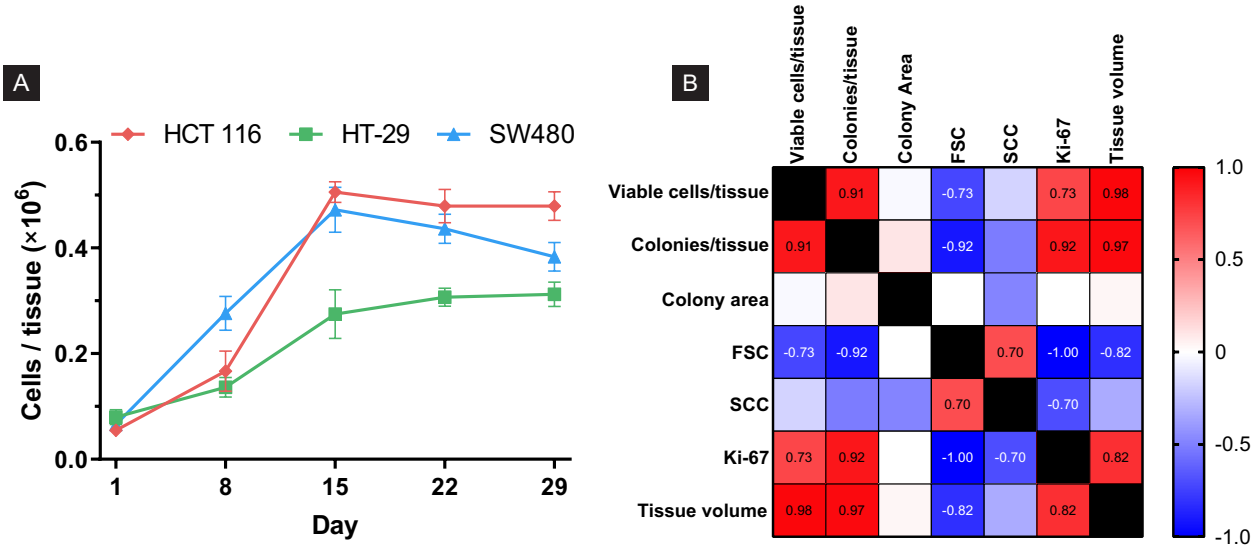

Figure 2.8. Direct cell count for the 3D-eCRC tissues correlated with calculated cell numbers. (A) The total number of viable cells in each 3De-CRC tissue was counted over time (direct cell

count) following tissue dissociation for flow cytometry analysis. It was found that the rate of increase in total cell number in HT-29 tissues was significantly lower than those in HCT 116 and SW480 tissues, whereas HCT 116 and SW480 showed equivalent rates of increase. These changes in total cell numbers were consistent with the calculated cell numbers for each cell line (Figure B.8). Data are mean ± SD. (B) A correlation matrix analysis showed that the total cell numbers in the 3D-eCRC tissues had significantly positive correlations with the number of colonies per tissue, cell proliferation, and tissue volume and negative correlation with FSC. Number in each square represent Spearman's correlation coefficient ($p \leq 0.05$; n = 3 tissues).

2.4 Discussion

For several decades, *in vitro* 2D cancer models have facilitated the understanding of tumor biology. However, these models inadequately mimic many pathophysiological complexities of the native tumor milieu due to their dimensions. Recently, 3D tissue-engineered cancer models have been developed to better recapitulate the key attributes of the native tumors. Specifically, a few studies have reported the development of engineered CRC tissues for drug testing applications and tumor cells and stromal fibroblasts interactions (Hoshiba and Tanaka 2016; Dainiak et al. 2008; Magdeldin et al. 2014; Shakibaei et al. 2015; Nyga et al. 2013; Dolznig et al. 2011). One less explored area in the development of 3D tissue-engineered CRC models is the investigation of the phenotypic differences between CRC cell lines. To this end, we have developed 3D engineered CRC (3D-eCRC) tissues by individually encapsulating three CRC cell lines, HCT 116, HT-29, and SW480, in PEG-fibrinogen (PEG-Fb) biomaterial. Compared to studies reported in the literature, our 3D tissue-engineered model provided an appropriate platform to encapsulate CRC cell lines with at least 10 times higher cell density (20×10^6 cells/mL for our model vs. 0.2-2 ×

10^6 for models found in literature) and maintain the cells in culture for substantially longer time (29 days vs. 11-15 days) to better recapitulate the native tumor conditions. We found significant differences in phenotypes of the cell lines such as cellular growth and morphology, cell subpopulations, cell size and granularity, migration patterns, tissue growth, and tissue stiffness. Importantly, these differences were found to be most prominent from Day 22 to Day 29, thereby indicating the importance of long-term culture for investigation of cancer phenotypes. Furthermore, these phenotypes of the cell lines within the 3D-eCRC tissues were found to differ from their 2D-CRC counterpart.

The presence of extracellular matrix (ECM) can greatly impact many cancer cell phenotypes such as growth, morphology, and proliferation (Riedl et al. 2017; Okada, Vaeteewoottacharn, and Kariya 2019; Kodack et al. 2017). The tumor ECM establishes a mass transfer gradient from the periphery to the core of the tumor which significantly affects the accessibly of each cell to the surrounding nutrition, oxygen, and CO_2 (Thomlinson and Gray 1955; Forster et al. 2017). This results in locational heterogeneity, with the core of tumor tissues being hypoxic and necrotic and the periphery being proliferative (Daster et al. 2017). This locational heterogeneity can be recapitulated *in vitro* when cancer tissues have a thickness > 200 μm (Khaitan et al. 2006; Daster et al. 2017). In addition, higher cell density helps the recapitulation of this locational heterogeneity as the cells are barriers to nutrition and oxygen diffusion (Pradhan, Chaudhury, and Lipke 2014). In our experience, the 3D-eCRC tissues which had a thickness of 800 μm and cell density of 20×10^6, demonstrated significantly larger cell colonies with significantly higher proliferation in the tissue periphery compared to the core for all CRC cell lines, thereby recapitulating locational heterogeneity of the native tumors.

In addition to the impact on cellular growth and proliferation, cell-cell and cell-matrix interactions play a crucial role in cancer cell invasion, migration, and dissemination (Schrader et al. 2011; J.S. Park et al. 2011; Swaminathan et al. 2011; Zaman et al. 2006; Marquez et al. 2006; Jin et al. 2015; Bell, Ivarsson, and Merrill 1979; Godbout et al. 2013; Marquez, Elson, and Genin 2010; Jansen et al. 2013; Hinz et al. 2001; Pradhan, Hassani, et al. 2017; Kraning-Rush and Reinhart-King 2012; Chen, Pedron, and Harley 2017; Holt et al. 2017). Cancer cells invade and migrate either individually when cell-cell junctions are lacking or collectively when cell-cell adhesions are present (Pandya, Orgaz, and Sanz-Moreno 2017; Friedl and Alexander 2011). For CRC, collective invasion and migration have been reported in several studies (Pape et al. 2019; Magdeldin et al. 2017; Pandya, Orgaz, and Sanz-Moreno 2017; Nabeshima et al. 1999; Prall, Nizze, and Barten 2005; Carr, Levy, and Watson 1986; Bronsert et al. 2014; Brabletz et al. 2001). Specifically, Pape et al. (Pape et al. 2019) observed that HCT 116 cells exhibited cell sheet formation when invading the surrounding microenvironment, whereas HT-29 cells demonstrated invasive blebbing on tumoroids and migrated detached bodies in the media. In our 3D-eCRC model, while all CRC cell lines form colonies inside the tissues, HCT 116 and HT-29 cells demonstrated migration patterns similar to those reported by Pape et al. (Pape et al. 2019); HCT 116 cells formed cell sheets on the top and bottom of the 3D-eCRC tissues whereas HT-29 cell colonies were found to be anchoring to the tissues as blebs along with existing in the culture media as cell aggregates. No pattern of migration (blebbing or cell sheet formation) was observed for SW480 tissues. This pattern of migration resulted in a significantly ($p < 0.0001$) lower number of colonies remaining inside the HT-29 tissues as compared to HCT 116 and SW480 tissues as the HT-29 cell colonies would migrate from inside the tissues toward the surrounding culture media.

The presence of 3D matrix also impacted the rates of cell number increase over time and doubling times. Whereas in 2D-eCRC cultures, the doubling times for HCT 116 and HT-29 were equivalent and that for SW480 was significantly higher ($p < 0.0001$), within the 3D-eCRC tissues, HCT-116 and SW480 showed equivalent doubling times, and HT-29 had a significantly higher value ($p \leq 0.0081$). These discrepancies between 2D-CRC cultures and 3D-3CRC tissues were further investigated using correlation analysis. Based on the analysis, the rates of change in total cell numbers within the 3D-eCRC tissues were attributed to the different migration patterns, percentages of proliferative cells, tissue volumes, and cell sizes. Since HT-29 cells migrated from the inside of 3D-eCRC tissues toward the surrounding culture media, the rate of increase in the number of colonies and subsequently the number of cells in HT-29 tissues were significantly lower as compared to HCT 116 and SW480 tissues ($p < 0.0001$). Furthermore, the cells in HT-29 tissues were found to be less proliferative than those in HCT 116 and SW480 tissues. In addition, since HT-29 tissues and cells were significantly smaller and larger ($p < 0.05$), respectively, the tissues were unable to accommodate as many cells as those found in HCT 116 and SW480 tissues. Therefore, lower values for the number of colonies per tissue, cell proliferation, and tissue volume and higher values of cell size for HT-29 resulted in the lower cell number in HT-29 tissues as compared to HCT 116 and SW480 tissues.

As cell-cell and cell-matrix interactions impact the growth, morphology, proliferation, and migration of cells, changes in both distinct cell subpopulations and protein expression may arise during cell culture (Riedl et al. 2017; Okada, Vaeteewoottacharn, and Kariya 2019; Kodack et al. 2017; Han et al. 2013; Wei et al. 2012). For CRC, it has been demonstrated that whereas all HCT 116 and HT-29 cells were positive for CK20 when cultured as a 2D monolayer, all HCT 116 cells were negative, and only a small HT-29 cell subpopulation was positive for this marker when

cultured as spheroids. In addition, all HCT 116 and HT-29 cells were negative for α-SMA when cultured as a 2D monolayer and positive for this marker when cultured as spheroids. Furthermore, the percentage of CD133+ cell subpopulations increased significantly for both HCT 116 and HT-29 cells when cultured as spheroids as compared to the 2D cultured cells (Han et al. 2013). In our 3D-eCRC tissues, we tracked the changes in distinct cell subpopulations over time and compared them with those in the 2D-CRC cultures. Consistent with the literature, we observed discrepancies in the percentage of cell subpopulations between 3D-eCRC tissues and their 2D counterparts. The presence of the 3D matrix in our model resulted in the decrease in $CD44^+$ and increase in $NCAD^+$ cell subpopulations in only SW480 tissues and increase in both $CK20^+$ and $\alpha\text{-}SMA^+$ cell subpopulations in only HCT 116 tissues as compared to their 2D counterparts; HT-29 tissues showed no change in these cell subpopulations as compared to their 2D counterparts.

Our efforts in this study were focused on the development of an *in vitro* 3D platform for CRC cells. Although we demonstrated the ability of our tissue-engineered model to support the investigation of phenotypic differences between CRC cell lines, the current study had limitations. The 3D-eCRC tissues exhibited two different patterns of migration; HCT 116 cells formed cell sheets on the tissues, whereas HT-29 cells migrated from inside the tissues to the surrounding culture media. Further investigation is warranted to clarify the mechanism behind each migration pattern. Whereas three CRC cell lines with different metastatic phenotypes were employed in this study, future work can include more cell lines to examine the metastatic mechanisms and their correlation with other cancer cell phenotypes.

2.5 Conclusion

In this study, we have developed an *in vitro* 3D engineered CRC (3D-eCRC) tissue model to investigate the phenotypic differences between three cell lines. We have demonstrated that our 3D-eCRC tissue model supported both high-density cell encapsulation (20×10^6 cells/mL) and long-term cell culture (29 days). Introducing the ability to culture CRC cells long-term in an *in vitro* 3D model revealed both phenotypic changes over time and differences between cell lines that cannot be investigated in 2D cancer models due to the limitation of the cell culture period. Our 3D-eCRC tissue model showed a high potential to study disease progression, metastatic mechanisms, and anti-cancer drug candidates to mitigate the impact of CRC.

Chapter 3: Engineered Colorectal Cancer Tissue Recapitulates Key Attributes of a Patient-derived Xenograft Tumor Line

3.1 Introduction

Colorectal cancer (CRC) remains the third most prevalent cancer and the third-highest cause of cancer-related deaths among both men and women in the United States, with approximately 145,600 new cases and 51,020 deaths in 2019 (American Cancer Society 2019; Libutti et al. 2015; Schaeybroeck et al. 2014). Although there has been an overall decreasing trend in CRC rates over the past several decades, the incidence in individuals under the age of 55 has increased (American Cancer Society 2019; Libutti et al. 2015; Schaeybroeck et al. 2014). Additionally, despite advances in early CRC detection and targeted treatment strategies, the 5-year relative survival rates of patients with distant-stage CRC (malignant CRC metastasized to distal regions of the body) is only 14% (American Cancer Society 2019; Libutti et al. 2015; Schaeybroeck et al. 2014).

To investigate tumor biology and assess anti-cancer therapeutics, *in vivo* and *in vitro* models are utilized to mimic the patient tumor milieu. However, deficiencies in existing models have impeded the success of clinical trials. In part, this deficiency can be attributed to the inability of pre-clinical models to accurately represent disease pathophysiology and the complex tumor microenvironment (Mazzoleni, Di Lorenzo, and Steimberg 2009). Tumors are heterogeneous neoplastic tissues composed of multiple cell types such as tumor cells, cancer stem cells, endothelial cells, immune cells, cancer-associated fibroblasts, and other stromal cells, within and surrounded by extracellular matrix (ECM) (P. R. Prasetyanti and Medema 2017; Easwaran, Tsai, and Baylin 2014; Nagle 2004). The intratumoral cell-cell and cell-matrix interactions play crucial roles in tumor progression, cancer cell invasion and migration, and tumor metastasis, as well as in

anti-cancer therapeutic response (Quail and Joyce 2013; Nguyen, Bos, and Massague 2009; Kraning-Rush et al. 2013; Kraning-Rush and Reinhart-King 2012; Balzer et al. 2012; Paul, Mistriotis, and Konstantopoulos 2017; D.H. Kim et al. 2018; J. Park et al. 2016). Therefore, the presence of cancer-associated cells together with cancer cells within a matrix is essential to more accurately modeling the tumor microenvironment.

Improved recapitulation of the patient tumor microenvironment in *in vitro* and *in vivo* models can be achieved in part through consideration of the model cellular components. Standard cell lines lack the extensive heterogeneity observed in patient tumors. Furthermore, the phenotype, genetics, and molecular characteristics of standard cell lines have been changed due to extended culture *in vitro*, thus resulting in poor correspondence to patient tumors (Cree, Glaysher, and Harvey 2010; Fernando et al. 2006). Patient-derived xenograft (PDX) models more accurately mimic patient tumors both genotypically and phenotypically (Cree, Glaysher, and Harvey 2010; Chou et al. 2013). In most cases, it has been shown that PDX line propagation in immunocompromised mice maintains patient tumor molecular characteristics, gene expression, and mutations (Brown et al. 2016; Lee et al. 2014; Cho et al. 2014). These PDX models are a useful tool to examine tumor biology and anti-cancer therapeutic response with a higher degree of physiological relevance compared to cell lines (Cree, Glaysher, and Harvey 2010). However, employing PDX models is costly and time-consuming due to the low throughput nature of expansion and testing in mice (Day, Merlino, and Van Dyke 2015; McIntyre et al. 2015; Murayama and Gotoh 2019). Furthermore, the number of experimental conditions that can be tested using *in vivo* PDX models is limited, and the complexity of these *in vivo* models limits the ability to probe real-time cell-cell, cell-matrix, and cell-drug interactions.

The most common *in vitro* cancer cell culture model relies on two-dimensional (2D) culture of cells which has advantages in terms of simplicity and ease of analysis; yet, there are many inherent differences between the microenvironmental cues present in 2D *in vitro* and *in vivo* cancer models. For example, in 2D models, the cells are not surrounded by a supporting matrix, and the mechanical properties of tissue culture substrates are much stiffer than *in vivo* tumor tissue; both of these differences are known to impact cellular morphology, polarity, and proliferation rate. The culture of PDX cells in 2D monolayers also results in substantial changes in the ratios of cell types present in the overall population, thereby resulting in a cancer cell *in vitro* model that no longer mimics the *in vivo* PDX cell subpopulations (Okada, Vaeteewoottacharn, and Kariya 2019; Kodack et al. 2017). Furthermore, tumors often contain subpopulations that do not adhere to the surface of the culture flask, preventing direct contact between non-anchorage and anchorage-dependent cell types that are able to be maintained and thereby hindering cell-cell interactions important for preserving *in vivo* cellular phenotypes. Moreover, the absence of a supporting matrix in 2D models precludes multi-dimensional cell-matrix interactions which modulate tumor pathophysiology.

To overcome the inherent limitations of 2D models, scaffold-free three-dimensional (3D) platforms for the culture of PDX cells have been developed, including those for CRC PDX cells. For instance, Kondo et al. (Kondo et al. 2019) generated cancer tissue-originated spheroids, formed from isolated aggregates of human CRC PDX cells. Other studies have developed organoids from either primary CRC obtained directly from patients or CRC PDX as novel models for high-throughput drug screening and investigation of disease mechanisms (Boehnke et al. 2016; Verissimo et al. 2016). In all of these cancer models, however, aggregates or spheroids selectively incorporated only some of the cell types from the primary or PDX tumor. Inclusion of all cellular

subpopulations may be advantageous in recapitulating the parental tumor microenvironment more fully.

Formation of 3D engineered tissues using biomimetic scaffolds has emerged as an important tool for mimicking the native tumor tissue microenvironment. In comparison to 2D and aggregate cell culture, engineered cancer tissue models can more closely recapitulate *in vivo* tumor dimensionality and cell-cell and cell-matrix interactions (Cox et al. 2015; Gu and Mooney 2016; Carvalho et al. 2015). Most of the research in cancer tissue engineering, including for CRC, currently employs standard cancer cell lines; CRC cancer tissue models have been developed using HCT 116 and HT-29 cell lines and alginate, collagen I, and poly(ethylene glycol)-fibrinogen (PEG-Fb) materials (Pradhan, Clary, et al. 2017; Rios de la Rosa et al. 2018; Dolznig et al. 2011; Hoshiba and Tanaka 2016; Magdeldin et al. 2014; Dainiak et al. 2008; Shakibaei et al. 2015; Nyga et al. 2013). Recent studies have begun to employ patient-derived cells to form engineered cancer tissues, including prostate and glioblastoma tissues (E.L. Fong, Wan, et al. 2016; Pedron et al. 2019; Pedron, Hanselman, et al. 2017; Pedron, Polishetty, et al. 2017). Fong et al. (E.L. Fong, Wan, et al. 2016) engineered a 3D *in vitro* prostate cancer model by separating and encapsulating aggregates of pure cancer cells to monitor tumor-stromal interactions involved in prostate cancer bone metastasis. Pedron et al. (Pedron et al. 2019) utilized gelatin methacrylamide and hyaluronic acid methacrylate hydrogels for the culture of patient-derived glioblastoma cells. In these studies, 3D scaffolds have been utilized to mimic tumor microenvironmental cues with high relevance; however, there is a need to examine the potential of 3D scaffold-based *in vitro* models to support maintenance and expansion of mixed CRC-PDX tumor cell subpopulations, including both human cancer and mouse stromal cells, and investigate the extent to which such 3D *in vitro* models mimic the parental CRC-PDX tumor.

Here we examine the ability of CRC-PDX tumor cells to be encapsulated and maintained within poly(ethylene glycol)-fibrinogen (PEG-Fb) hydrogels and investigate the extent to which this 3D engineered CRC tissue model recapitulates the originating *in vivo* PDX tumor, including comparison of gene expression profiles through transcriptomic analysis. Our group has recently shown that PEG-Fb supports the formation of engineered breast cancer tissues (Pradhan, Hassani, et al. 2017; Pradhan et al. 2018; Pradhan, Clary, et al. 2017). Capable of being remodeled by encapsulated cells, PEG-Fb provides cell adhesion sites and facilitates the incorporation of the heterogeneous cell types, including fibroblasts co-cultured with cancer cell lines (Pradhan et al. 2018). To construct the 3D engineered CRC PDX (3D-eCRC-PDX) tissue model, PDX cells propagated *in vivo* from a patient diagnosed with stage II CRC adenocarcinoma were dissociated and encapsulated within the PEG-Fb matrix. To assess the ability of this 3D-eCRC-PDX tissue model to maintain parental tumor cell subpopulations throughout long-term culture, we monitored temporal variations in cell subpopulations in comparison to 2D CRC PDX (2D-CRC-PDX) cell culture. Due to recent findings that tumor tissue mechanical stiffness plays an important role in cell phenotype and genotype, as well as cell-cell, cell-matrix, and cell-drug interactions (Pradhan, Hassani, et al. 2017; Schrader et al. 2011; J.S. Park et al. 2011; Swaminathan et al. 2011; Zaman et al. 2006; Jabbari et al. 2015; X. Yang et al. 2013), we quantified the mechanical stiffness of the 3D-eCRC-PDX tissues and compared it to that of CRC-PDX tumors. Most notably, we found that 3D-eCRC-PDX tissues not only support the growth of CRC PDX cells from this patient line in long-term culture, but also mimic the originating CRC-PDX tumors in terms of cell subpopulation proportions, gene expression, and mechanical stiffness, providing evidence that these engineered tissues may be capable of supporting the culture of CRC PDX cells *in vitro*.

3.2 Materials and Methods

3.2.1 Synthesis of PEGDA and PEG-Fb

Poly(ethylene glycol) diacrylate (PEGDA) was synthesized following previously established methods (Pradhan, Hassani, et al. 2017; DeLong, Gobin, and West 2005). The conjugation of fibrinogen to PEG was also carried out according to previously described methods (Almany and Seliktar 2005). The characterization of PEG-Fb was performed by evaluating PEGylation efficiency and the ability of PEG-Fb to photocrosslink and form 3D hydrogels (Dikovsky, Bianco-Peled, and Seliktar 2006).

3.2.2 Propagation of CRC PDX Cells in Mice

All experimental procedures were approved by the Auburn University Animal Care and Use Committee. A frozen stage II CRC adenocarcinoma PDX line from a white female patient pre-treatment was kindly provided by BioConversant, LLC. To establish xenografts from frozen PDX cells, approximately 1.4 x 10^6 tumor cells were mixed at a 1:1 ratio with Matrix High Concentration, Phenol-Red free Matrigel (Corning) and injected into the flank of a NOD.Cg-Prkdc^{scid} Il2rg^{tm1Wjl}/SzJ (NOD-SCID) mouse (The Jackson Laboratory). To propagate the PDX line, the freshly excised tumor (~0.8 g) was washed in sterile PBS, minced in approximately 2.5 mL DMEM with 100 U/mL penicillin and 100 µg/mL streptomycin, and approximately 200 µL of the minced tumor suspension was injected into the flank of a NOD-SCID mouse. Experiments discussed in this study were performed using CRC-PDX tumors that were propagated in the absence of Matrigel and were passaged 3-4 times in mice.

3.2.3 CRC-PDX Tumor Dissociation and Cell Isolation

Excised CRC-PDX tumors were dissociated according to the methods described in Appendix A, and all PDX cells, including both human cancer cells and mouse stromal cells, were isolated for subsequent *in vitro* culture as 2D-CRC-PDX cells and 3D-eCRC-PDX tissues.

3.2.4 Formation and Culture of 3D-eCRC-PDX Tissues

To create the 3D-eCRC-PDX tissues, the isolated CRC PDX cells were mixed with the PEG-Fb polymer precursor solution (see Appendix A for formulation). The cell-laden precursor solution was pipetted into a pre-fabricated PDMS mold and photocrosslinked with visible light for 2 minutes. The 3D-eCRC-PDX tissues were maintained in long-term culture (29 days) in a standard incubator with a temperature of 37 °C and 5% CO_2 with media refreshes every 2-3 days.

3.2.5 2D CRC PDX Cell Culture

CRC cells isolated from the CRC-PDX tumors were cultured in T-75 standard cell culture flasks according to the method described in Appendix A. These 2D cultured CRC PDX (2D-CRC-PDX) cells were passaged after 8 days of culture and subsequently passaged every 7 days up to a total of 29 days. All of the cultured cells were maintained in a standard incubator with a temperature of 37 °C and 5% CO_2, with media changes every 2-3 days.

To investigate the cell growth curve or the increase in the total number of 2D-CRC-PDX cells over time, 2×10^5 cells/cm^2 were seeded into ten T-25 standard cell culture flasks, one of which was used for cell counting every 24 hours (Days 1-11) using 0.25% Trypsin-EDTA (Corning) to detach the cells. The spent media containing the 2D-CRC-PDX non-adherent cells was also collected and included in cell counting. Following staining with trypan blue, the live cells

were then counted using a hemocytometer. Additionally, 2×10^5 cells/cm^2 were seeded onto a 24-well plate to investigate the viability of cells in 2D-CRC-PDX culture on Day 1 by Live/Dead staining.

3.2.6 Cell Viability Assay and Image Acquisition and Analysis

A cell viability assay was performed using the LIVE/DEAD® Viability/Cytotoxicity Kit (ThermoFisher Scientific) according to the manufacturer's protocol. To quantify the percentage of live cells, Hoechst 33342 (Calbiochem) (20 µg/mL) was used to counterstain the cell nuclei. The fluorescently labeled cells were observed, and images and Z-stacks were obtained using a Nikon Eclipse TE2000 Inverted Microscopes equipped with a Nikon A1 plus Confocal Microscope System. The confocal microscopic images of the 2D-CRC-PDX cells and Z-stacks of the 3D-eCRC-PDX tissues were analyzed using ImageJ software (version: 2.0.0-rc-68/1.52e). The percentage of viable cells was calculated by dividing the manually quantified number of viable cells (total cell nuclei count minus dead cells) by the total number of cell nuclei (total number of cells). Further details on the staining and imaging procedures are provided in Appendix A.

3.2.7 Image Acquisition and Morphological Analysis of 3D-eCRC-PDX Tissues and 2D-CRC Cells

The 3D-eCRC-PDX tissues were cultured *in vitro* over a 29-day period and imaged every 7 days. Phase-contrast images and Z-stacks of 3D-eCRC-PDX tissues were obtained using an inverted Nikon Eclipse Ti microscope equipped with an Andor Luca S camera and analyzed using ImageJ software (version: 2.0.0-rc-68/1.52e) to quantify the area, major axis, minor axis,

circularity, and aspect ratio of the tumor cell colonies within 3D-eCRC-PDX tissues. For 2D-CRC-PDX cells, phase-contrast images were obtained prior to cell passaging.

By selecting random regions from phase-contrast images or Z-stacks, three 3D-eCRC-PDX tissue batches with at least 50 tumor cell colonies from each batch, were analyzed and the data exported to MS Excel. The diameter represented in the Results section is the mean geometric diameter, which was calculated using Equation 2.2.

3.2.8 Cell Subpopulation Investigation by Flow Cytometry

To investigate the cell subpopulations using flow cytometry, the CRC-PDX tumors, 3D-eCRC-PDX tissues, and 2D-CRC-PDX cells were dissociated to obtain single cells, and the numbers of viable cells were manually counted post-dissociation as described above. Detailed cell staining and flow cytometry protocols are provided in Appendix A. Briefly, to identify human-derived cells, mouse-derived cells, CRC cells, and proliferating cells the following antibodies were used, respectively: β-2-microglobulin (B2M) mouse IgG2a mAb (OriGene Technologies) conjugated to Zenon™ R-phycoerythrin (PE) mouse IgG2a (ThermoFisher Scientific), MHC Class I H-2 Db antibody (H2Db) mouse IgG2a mAb (OriGene Technologies) conjugated to the Zenon™ PE mouse IgG2a, cytokeratin 20 (CK20) rabbit IgG mAb (Cell Signaling Technology) conjugated to Zenon™ Alexa Fluor™ 647 rabbit IgG (ThermoFisher Scientific), and Ki-67 rabbit IgG pAb (abcam) conjugated to the Zenon™ Alexa Fluor™ 647 rabbit IgG.

To exclude dead cells and debris from the analysis, cells were labeled with Zombie Green™ dye (Zombie Green™ Fixable Viability Kit, BioLegend). To block nonspecific binding on the cell surface, cold blocking buffer (0.5 % (w/v) Bovine Serum Albumin (BSA) (Sigma-Aldrich) and 10 % (v/v) FBS in 1X PBS) containing Human BD Fc Block™ (BD Biosciences)

(12 µg/mL) and Mouse BD Fc Block™ (BD Biosciences) (5 µg/mL) was used. To fix and permeabilize the cells, 0.5 mL of cold Foxp3 Fixation/Permeabilization (eBioscience™) working solution (prepared according to manufacturer protocol) was used for each sample tube. To block nonspecific binding for intracellular staining, FACS buffer (0.5 % (w/v) BSA and 10 % (v/v) FBS in 1X Permeabilization Buffer) was used. Compensation beads (ThermoFisher Scientific) were used according to the manufacturer protocol to accurately set the compensation in the event of fluorochrome overlap. To monitor for cell autofluorescence, unstained cell controls were also used. To set an accurate compensation for Zombie Green™ dye, a dead control cell population was used. A BD Accuri C6 cytometer was used to quantify labeled cells and subsequently, FlowJo software (version 10.0.7) was employed for data analysis.

In addition to investigating the percentage of cell subpopulations in culture over time, we also assessed the change in the total number of cells and the number of cells in each subpopulation. To calculate the number of cells in each subpopulation, the population percentage quantified via flow cytometry was multiplied by the total number of viable cells counted as described above. To account for obligatory cell passaging required for maintenance in the 2D-CRC-PDX culture, total numbers of 2D-CRC-PDX cells were calculated based on cell counts at each time point and the number of cells seeded at each passage.

3.2.9 Morphological Study of Cells by Staining

To study the cell morphology within both 3D-eCRC-PDX tissues and 2D-CRC-PDX cultures, the cells were labeled with Hoechst 33342, B2M mouse IgG2a mAb with goat anti-mouse IgG Alexa Fluor™ 488 (ThermoFisher Scientific), Alexa Fluor™ 568 Phalloidin (ThermoFisher Scientific), and CK20 rabbit IgG mAb conjugated to Zenon™ Alexa Fluor™ 647 rabbit IgG to

observe the cell nuclei, human-derived cells, f-Actin filaments, and CRC cells, respectively. The cells were imaged using a Nikon confocal microscope. Further detail is provided in Appendix A.

3.2.10 Histological Examination of 3D-eCRC-PDX Tissues and CRC-PDX Tumors

To visualize both cellular and tissue microanatomy, a portion of the CRC-PDX tumors and entire 3D-eCRC-PDX tissues were sequentially sectioned and embedded in paraffin. The paraffin-embedded sections of CRC-PDX tumors and 3D-eCRC-PDX tissues were stained using hematoxylin and eosin (H&E). The stained sections were scanned using an Aperio CS2 scanner (Leica Biosystems) at 40x magnification. The digital images were viewed using Aperio ImageScope (Ver. 12.3.2.8013). Further details on the H&E staining protocol are provided in Appendix A.

3.2.11 RT-qPCR Gene Expression

Total RNA was extracted from CRC-PDX tumors, 2D-CRC-PDX cells, and 3D-eCRC-PDX tissues using the RNeasy Plus Micro Kit (Qiagen). The analysis was carried out for 3-4 separately obtained tumors and the corresponding batches of 3D-eCRC-PDX tissues and 2D-CRC-PDX cultures. Total RNA (50 ng) was used for cDNA synthesis using SuperScript™ IV First-Strand Synthesis System (Invitrogen). Quantitative polymerase chain reaction (qPCR) amplifications were performed using RT2 SYBR Green qPCR Mastermix (Qiagen) with amplification conditions: 40 cycles of 15 seconds of denaturation at 95 °C followed by 1-minute annealing. Reactions were performed in triplicate, and data were calculated using the ΔΔCt method. Gene expression was normalized by using *B2M* and *GAPDH* as reference genes.

3.2.12 Morphological Analysis of 3D-eCRC-PDX Tissues

To study whole-tissue morphological changes of 3D-eCRC-PDX tissues over time, images were obtained from a CellScale MicroSquisher system (side view of the tissues) and through phase-contrast microscopy (top view of the tissues) and used to quantify the volume (top and side views of the tissues), mean geometric diameter (top view of the tissues using Equation 2.2), circularity (side view of the tissues using Equation 2.3), and aspect ratio (side view of the tissues using Equation 2.4) of the 3D-eCRC-PDX tissues using ImageJ software. A minimum of 3 samples per time point per batch were analyzed.

3.2.13 Mechanical Stiffness

The mechanical stiffness of CRC-PDX tumors and 3D-eCRC-PDX tissues was evaluated using a CellScale MicroSquisher system and the associated SquisherJoy software according to the previously published protocol (Pradhan, Hassani, et al. 2017). For 3D-eCRC-PDX tissue samples, the mechanical stiffness was quantified on Days 1, 8, 15, 22, and 29 post-encapsulation. A minimum of three samples were measured per batch for each condition. Further details on mechanical stiffness measurement are provided in Appendix A.

3.2.14 Proteomics Analysis

To isolate ECM enriched fractions of protein CRC-PDX tumors and 3D-eCRC-PDX tissues were processed via Millipore Compartmental Protein Extraction Kit following the manufacturer's instruction. Of note, samples were weighed prior to processing, and buffer volume was adjusted appropriately based on the sample weight. Following sequential extraction of cytoplasmic, nuclear, membrane, and cytoskeletal proteins via the kit (Naba et al. 2012; Naba,

Clauser, and Hynes 2015), the remaining pellet was washed once with 500 µL of PBS and reconstituted in 2x Novex NuPAGE LDS sample buffer (Invitrogen) supplemented with 2x NuPAGE sample reducing agent (Invitrogen). ECM-enriched fractions were then sonicated in an ultrasonic water bath for 20min. at ambient temperature. Debris was removed by centrifugation for 20 min. at 16,000 ×g, 4°C. Proteomics workup was carried out as previously reported (Ludwig et al. 2016). Briefly, the protein fractions were quantified; ~20 µg of protein per sample was then reduced with DTT and denatured at 70°C for 10min. prior to loading onto 10% Bis-Tris Protein gels and separating as a short stack run. The gels were stained overnight with colloidal Coomassie for visualization purposes, each lane was cut into 6-MW fractions and equilibrated in 100 mM ammonium bicarbonate (AmBc), and each gel plug was then digested overnight with Trypsin Gold, Mass Spectrometry Grade (Promega) following manufacturer's instruction. Peptide extracts were reconstituted in 0.1% Formic Acid/ ddH_2O at 0.1 µg/µL. Mass spectrometry was carried out, and the data were processed, searched, filtered, grouped, and quantified using normalized spectral counting as previously reported in detail (Ludwig et al. 2016).

All identified proteins were converted from UniProtKB AC/ID to UniProtKB using the Retrieve/ID Mapping feature in UniProt to obtain primary gene names. The primary gene names were processed using MatrisomeAnnotator (http://matrisome.org/) (Naba et al. 2017) to identify ECM and ECM-associated proteins and subsequently categorized into ECM glycoproteins, collagens, proteoglycans, ECM regulators, ECM-affiliated proteins and secreted factors. The categorized proteins detected in only one out of six samples (CRC-PDX tumors and 3D-eCRC-PDX tissues) were removed from the analysis. The proteins were then employed to plot Euler diagrams using the *eulerr* package in RStudio (Version 1.2.1335) for each sample. Moreover, the categorized proteins from three samples (CRC-PDX tumors or 3D-eCRC-PDX tissues) were

pooled and presented for the comparison between CRC-PDX tumors and 3D-eCRC-PDX tissues. For the pooled data, a protein was indicated as present when the protein was detected in at least two out three samples. Further details on the proteomics analysis protocol are provided in Appendix A.

3.2.15 Transcriptomic Analysis

RNeasy Plus Micro Kits (Qiagen) were used to isolate total RNA from frozen CRC-PDX tumors (obtained after 31-42 days of tumor growth) and 3D-eCRC-PDX tissues (obtained on the 15th day of *in vitro* culture) following the manufacturer's protocol. Procedures for RNA-seq were performed at the Genomic Services Laboratory (GSL), HudsonAlpha Institute for Biotechnology. Extracted total RNA initial QC quantification was done using a Qubit Fluorometer (Invitrogen), and the quality of the extracted RNA was evaluated using an Agilent 2100 Bioanalyzer. RNA with a RIN score of 7.0 or higher was used for RNA-seq library preparation using an Illumina TruSeq Stranded RNA Kit with Ribo-Zero Gold and sequenced on NovaSeq sequencers at 100PE.

Sequencing reads were aligned to both the human GRCh38 and mouse GRCm38 reference genomes and counted with STAR (Dobin et al. 2013) using aRNApipe, a RNA-seq analysis pipeline developed at the HusdonAlpha Institute for Biotechnology (Alonso et al. 2017). Approximately 62%-65% of the reads uniquely mapped to the human GRCh38 reference genome, while approximately 12%-21% of the reads uniquely mapped to the mouse GRCm38 reference genome (Table C.1). Human mapped raw counts obtained from STAR were used for differential expression analysis with the R package *DESeq2* (Love, Huber, and Anders 2014). False discovery rates (FDR) *p* value less than 0.05 were considered significantly differentially expressed and genes with $\log_2$ fold change greater than 1.5 were used for downstream gene set analyses.

3.2.16 CRC Consensus Molecular Subtype Analysis

Human mapped raw counts were used for consensus molecular subtype analysis with the R package *CMScaller* (Eide et al. 2017), with default RNA-seq settings. *CMScaller* uses the nearest template prediction algorithm (Hoshida 2010) to assign each sample to a consensus molecular subtype (CMS) (Guinney et al. 2015). In brief, *CMScaller* computes cosine distances for each sample and assigns it to a CMS based on the smallest distance to the CMS template. Prediction FDR *p* value greater than 0.05 resulted in no classification.

3.2.17 TCGA Analysis

The R package *TCGAbiolinks (Colaprico et al. 2015)* was used to obtain HT-Seq gene counts from the Genomic Data Commons for CRC tumor and tumor-adjacent tissue as a part of the TCGA-COAD (Peng et al. 2015) project. CRC-PDX tumor and 3D-eCRC-PDX tissue HT-Seq gene counts and TCGA counts were merged by Ensembl gene ID's and processed as described above with *DESeq2*. The combined sequence data were variance stabilized using the *DESeq* method.

3.2.18 GSEA Analysis

GSEA was performed using the desktop GSEA program (version 4.0.3) (Subramanian et al. 2005) and the Molecular Signature Database (MSigDB) Hallmarks v7.0 gene sets. GSEA analysis was performed using 1000 permutations and the phenotype permutation type. Annotations of human ensemble gene ID to MSigDB.v7.0 were performed. Enrichment plots and a heatmap were presented to visualize the data. Normalized enrichment score (NES) and the false discovery

rate (FDR) q-value which presents that the estimated probability that the NES represents a false positive finding were reported in the Enrichment plots.

3.2.19 Gene Ontology Analysis

The web-based application *GOrilla* (Eden et al. 2009) was used to identify enriched gene molecular function ontologies between CRC-PDX tumor and 3D-eCRC-PDX tissue samples and TCGA CRC tumor-adjacent tissue. The application REViGO (Supek et al. 2011) was used to eliminate redundant GO terms and visualize the enriched terms using the TreeMap function which shows a two-level hierarchy of GO terms. The following REViGO settings were used: allowed similarity, (0.5, small); and semantic similarity measure, Resnik (normalized).

3.2.20 Kaplan–Meier survival analysis

To examine expression of the top 16 significantly upregulated genes between CRC-PDX tumors and 3D-eCRC-PDX tissues in the precomputed GEO datasets GSE17536, GSE14333, GSE17537, and TCGA-COAD, the PROGgeneV2 tool was used (Goswami and Nakshatri 2013, 2014). All cohorts were adjusted for age, stage, and gender covariates and bifurcated based on median expression. The hazard ratios, 95% confidence intervals, and *p* values were reported.

3.2.21 Statistical Analysis

The outliers were removed using the ROUT method with coefficient Q = 1%. The normality of distribution and equality of variance were then checked. T-test was performed when comparing the means of two groups. One-way ANOVA followed by Tukey *post hoc* test was performed when comparing the means of more than two groups. Two-way ANOVA followed by

Tukey was performed for Morphological Analysis and Mechanical Stiffness. Two-way ANOVA followed by Bonferroni-Šídák *post hoc* test was performed when comparing groups to a control group (Flow Cytometry). Linear trend analysis was performed using one-way ANOVA with a post-test for linear trend. The rates of increase or decrease (slopes) were found using linear regression analysis. p value ≤ 0.05 was considered statistically significant unless otherwise stated. GraphPad Prism 7.0 (GraphPad Software, San Diego, California USA, www.graphpad.com) was used for the above analysis. Hierarchical cluster analysis was carried out using *heatmap.plus* package in RStudio (Version 1.2.1335).

3.3 Results

3.3.1 CRC-PDX Tumor Cell Viability Maintained Following 3D Encapsulation

Using an optimized tumor dissociation method, we obtained 14.6 ± 0.6 million viable cells/gram of initial tissue (n = 5 CRC-PDX tumors). The isolated cells were then employed to create the 3D-eCRC-PDX tissues and separately cultured as 2D-CRC-PDX cells. A schematic of the process is shown in Figure 3.1.

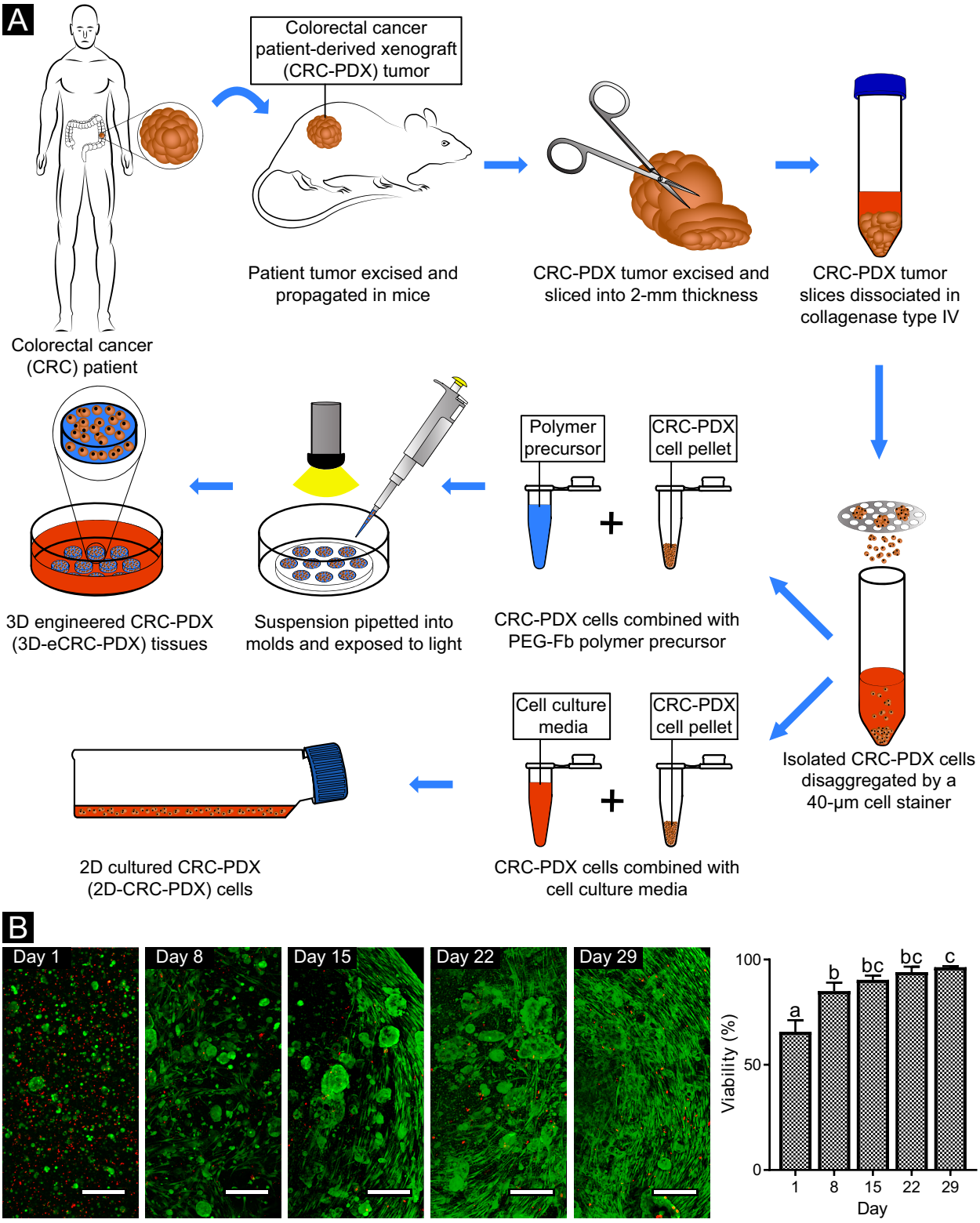

Figure 3.1. Following encapsulation in PEG-Fb, CRC-PDX tumor cells were viable during long-term culture. (A) All PDX cells, including both human cancer cells and mouse stromal cells,

were isolated from CRC-PDX tumors and used to create 3D-eCRC-PDX tissues and cultured as 2D-CRC-PDX cells. (B) Representative confocal images of live (green) and dead (red) cells within 3D-eCRC-PDX tissues (scale bar = 200 μm). Day 1 cell viability was equivalent to that of non-encapsulated cells (Figure C.1). Cell elongation and increasing cell colony size were observed from Day 1 to Day 29 post-encapsulation. As a result of cell growth, the percentage of viable cells within the 3D-eCRC-PDX tissues increased significantly during *in vitro* culture. Bar = mean ± SD. Means that do not share a letter are significantly different ($p \leq 0.05$; n = 3 tissues).

To evaluate cell viability, the encapsulated cells within the 3D-eCRC-PDX tissues were labeled with Live/Dead dye and counterstained with Hoechst 33342. Based on confocal z-stack analysis, 67 ± 4% of encapsulated cells within the 3D-eCRC-PDX tissues were viable on Day 1 (Figure 3.1 B). To examine whether cell viability was reduced due to the tumor dissociation process, the cell encapsulation process, or a combination of both procedures, we performed viability assays on 2D-CRC-PDX cells on Day 1 post-tumor dissociation. Image analysis revealed that approximately 66 ± 6% of the cells were viable (Figure C.1) with no significant difference between 2D-CRC-PDX cells and the cells encapsulated within the 3D-eCRC-PDX tissues. Therefore, the lower viability of tumor cells observed within the 3D-eCRC-PDX tissues on Day 1 was primarily a result of the tumor dissociation process, as expected. Prior investigation of CRC-PDX tumor dissociation by Petit et al. reported similar post-dissociation cell viability (Petit et al. 2013).

Long-term viability was also examined to determine the temporal impact of *in vitro* culture on cell survival in the 3D-eCRC-PDX tissues. The percentage of viable cells on Day 8, 15, 22, and 29 was 85 ± 6%, 90 ± 2%, 94 ± 3%, and 96 ± 1%, respectively (Figure 3.1 B), which was

significantly higher than Day 1 ($p \leq 0.0003$). Furthermore, the cell viability was significantly higher on Day 29, as compared to Day 8 ($p = 0.0149$). The high viability at the later time points is a result of cell proliferation and a subsequent overall increase in the total number of viable cells throughout the long-term culture, as can be seen in the confocal images (Figure 3.1 B). The cells encapsulated within the 3D-eCRC-PDX tissues proliferated (quantified via flow cytometry, as reported in detail below) and altered their morphological characteristics, with some cells forming colonies and others elongating within the biomaterial matrix (Figure 3.1 B). Elongated cells were first observed on Day 8 and increased in abundance over time, as visualized on Day 29.

3.3.2 Growth and Morphological Analysis of Tumor Cell Colonies within 3D-eCRC-PDX Tissues

To assess the colony-forming ability of the tumor cells in the 3D-eCRC-PDX tissues and temporal changes in the colony size and morphology, cells within the 3D-eCRC-PDX tissues and in 2D-CRC-PDX culture were imaged over a period of 29 days. Three batches of 3D-eCRC-PDX tissues and 2D-CRC-PDX cultures were separately prepared, each from separate tumors, and analyzed. Phase-contrast z-stacks showed that the cell colony area and diameter within the 3D-eCRC-PDX tissues ranged from approximately 70 to 850 μm^2 and 10 to 40 μm on Day 1, respectively (Figure 3.2 A-E, K, L). However, for 2D-CRC-PDX cells, the cell colony area and diameter ranged from approximately 300 to 1,300 μm^2 and 20 to 50 μm on Day 1, respectively (Figure 3.2 F-J, O, P). Cell colony area and diameter within 3D-eCRC-PDX tissues increased from Day 1 to Day 29 for each batch based on one-way ANOVA with a post-test for linear trend ($p < 0.0001$); observed increases were consistent between batches with no significant difference between the slopes based on linear regression analysis. Within the 3D-eCRC-PDX tissues on Day

29, the cell colony area and diameter ranged from approximately 3,500 to 35,000 μm^2 and from approximately 70 to 220 μm, respectively (Figure 3.2 A-E, K, L). This increase in the size of CRC PDX cell colonies within the 3D-eCRC-PDX tissues over time was also observed using H&E staining (Figure 3.2 S-V). For 2D-CRC-PDX cells, passaging was necessary after 8 days of *in vitro* culture to prevent cell death (Figure C.2). The 2D-CRC-PDX cell colonies increased in size from Day 1 to Day 8; however, following passaging, the subsequent colonies did not grow as large as those quantified on Day 8 (Figure 3.2 F-J, O, P).

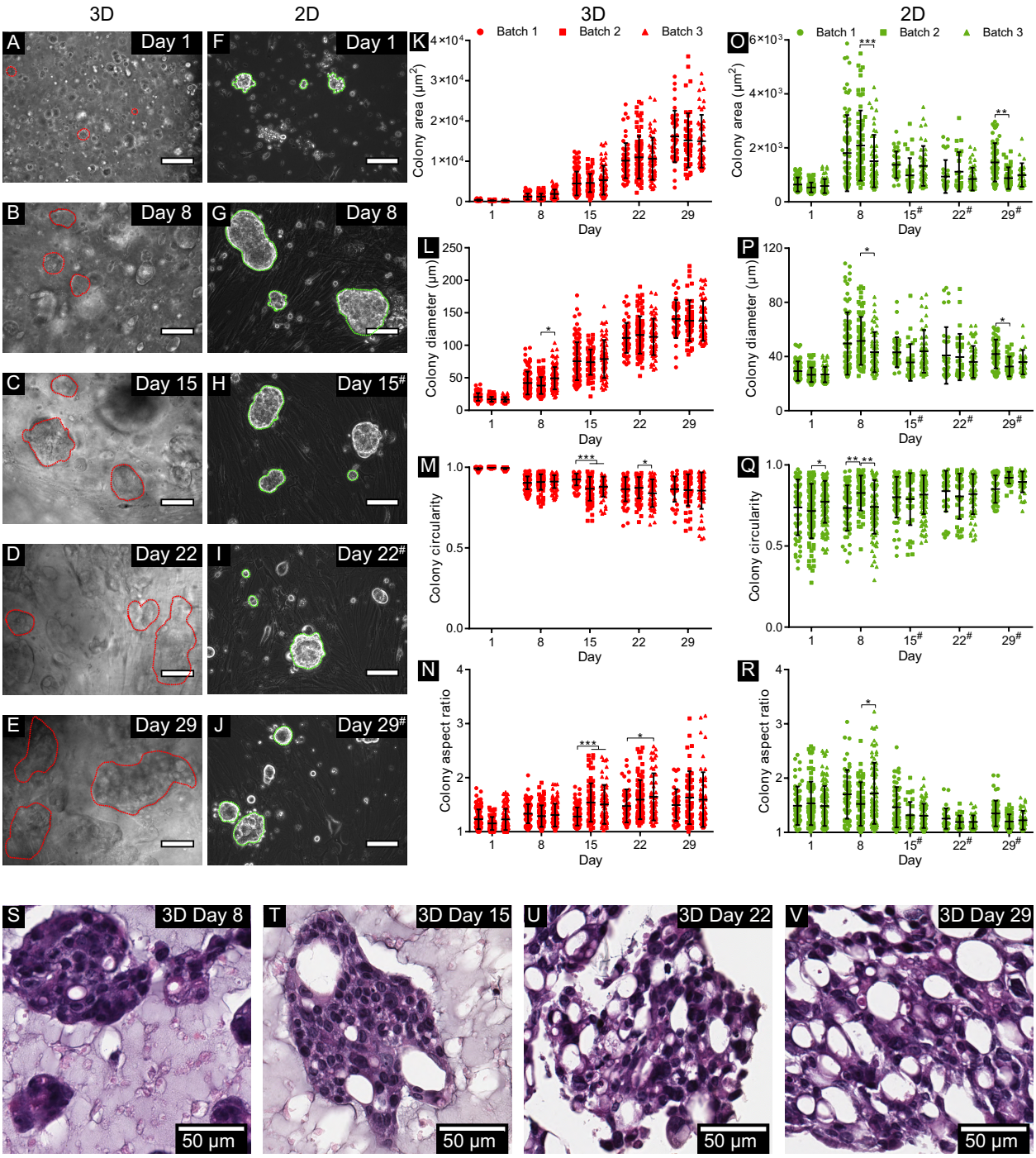

Figure 3.2. Morphological analysis of cell colonies within 3D-eCRC-PDX tissues and in 2D-CRC-PDX cultures. Representative phase-contrast images of cell colonies (A-E) within the 3D-eCRC-PDX tissues (outlined by red dotted lines) and (F-J) in the 2D-CRC-PDX cultures (outlined by green dotted lines) over 29 days of culture (scale bar = 100 µm). Within the 3D-eCRC-PDX

tissues, an increase in (K) cell colony area and (L) colony diameter, a (M) decrease in colony circularity, and an (N) increase in cell colony aspect ratio were observed from Day 1 to Day 29; these changes were generally consistent between batches. (O-P) 2D-CRC-PDX cell colony area and diameter increased from Day 1 to Day 8; however, following passaging on Day 8 the subsequent colonies did not grow as large as prior to passaging. For 2D-CRC-PDX cells, (Q) colony circularity increased and (R) colony aspect ratio decreased from Day 1 to Day 29. (S-V) Increasing CRC PDX colony size was also observed in histological sections of 3D-eCRC-PDX tissues over time. Data are mean ± SD, and each dot represents one colony. At least 50 cell colonies within 3D-eCRC-PDX tissues or in 2D-CRC-PDX cultures were examined for each of 3 separately prepared batches. *$p \leq 0.05$, **$p \leq 0.01$, ***$p \leq 0.001$. # indicates that the 2D-CRC-PDX cells were passaged at the previous time point.

Cell growth and morphology within the 3D-eCRC-PDX tissues were consistent between batches. No significant differences in 3D-eCRC-PDX tissue mean cell colony area were observed between batches at any time point; the only significant difference between batches in mean colony diameter occurred on Day 8 between batches 2 and 3 ($p = 0.0017$) (Figure 3.2 K, L). Furthermore, the number of viable cells within each 3D-eCRC-PDX tissue was counted after dissociation for flow cytometry analysis. The total number of viable cells increased linearly from Day 1 to Day 29 based on one-way ANOVA with a post-test for linear trend ($p < 0.0001$); the data showed that this increase did not differ significantly between batches based on linear regression analysis (Figure C.3). In contrast, for 2D-CRC-PDX cells, significant differences were observed between batches, including differences in both cell colony area and diameter on Day 8 and Day 29 ($p = 0.0121$ and $p = 0.0187$, respectively) (Figure 3.2 O, P). In 2D-CRC-PDX cell culture, the total number of

viable cells for all three batches was found to increase from Day 1 to Day 29 based on one-way ANOVA with a post-test for linear trend ($p < 0.0001$); however, in contrast with 3D-eCRC-PDX tissues, the slopes differed significantly for the 2D-CRC-PDX cells ($p = 0.0274$).

Circularity and aspect ratio of the cells and cell colonies, which are indicators of invasiveness (D. Truong et al. 2016; D.D. Truong et al. 2019; Lyons et al. 2016), were also analyzed. Within the 3D-eCRC-PDX tissues, circularity of the cell colonies decreased and aspect ratio increased from Day 1 to Day 29 based on one-way ANOVA with a post-test for linear trend ($p < 0.0001$) (Figure 3.2 M, N). Circularity ranged from 0.97 to 1.00 on Day 1 and from 0.55 to 0.97 on Day 29; the aspect ratio ranged from 1.00 to 1.80 on Day 1 and from 1.00 to 3.15 on Day 29. However, for 2D-CRC-PDX cells, circularity increased, and aspect ratio decreased from Day 1 to Day 29 (one-way ANOVA, post-test for linear trend, $p < 0.0001$) (Figure 3.2 Q, R). Circularity ranged from 0.27 to 0.97 on Day 1 and from 0.72 to 0.98 on Day 29, while the aspect ratio ranged from 1.00 to 2.58 on Day 8 and between 1.00 to 2.00 on Day 29. Significant differences in cell colony circularity and aspect ratio were not consistently observed between batches (Figure 3.2 M, N, Q, R).

3.3.3 3D-eCRC-PDX Tissues Maintained Cell Subpopulations

Using flow cytometry, we quantified both the human and mouse cell subpopulations from the CRC-PDX tumor, 3D-eCRC-PDX tissues, and 2D-CRC-PDX cultures; PDX models contain mouse stromal components in addition to the human malignant cells (Okada, Vaeteewoottacharn, and Kariya 2019; Maykel et al. 2014) and maintaining both subpopulations is important for recapitulation of the tumor microenvironment. Human cells were identified using the cell marker β-2 microglobulin (B2M); the cells were also labeled with a mouse cell marker, H2Db, to confirm

that those cells which were negative for B2M were the mouse cell subpopulation (Figure C.4). For dissociated CRC-PDX tumor cells, 71±3% of the cell population was positive for the B2M human marker (3 separately dissociated tumors, Figure 3.3 A). Importantly, as the cells grew within the 3D-eCRC-PDX tissues, the human cell subpopulation ($B2M^+$) percentage remained constant during long-term culture (through Day 22); there was an average percentage of 68±6% $B2M^+$ cells (Days 8,15, 22) with no significant difference between the 3D-eCRC-PDX tissues and dissociated CRC-PDX tumors (n = 3 separately prepared batches). On Day 29, the percentage of $B2M^+$ cells (53±12%) was significantly lower than that on Days 1 and 8 (71±3% and 74±7%, respectively, $p < 0.003$, Figure 3.3 A). In sharp contrast to the 3D-eCRC-PDX tissues, the percentage of $B2M^+$ cells in 2D-CRC-PDX cultures had already decreased by over 80 percent after 8 days of culture (from 71±3% to 13±11%, n = 3 separate batches, $p < 0.0001$)) and then remained constant over 29 days. It is important to note that whereas the 3D-eCRC-PDX tissues were maintained in continuous culture for 29 days, it was necessary to passage the 2D-CRC-PDX cells every 7 days starting on Day 8 to avoid cell confluence; data presented are prior to each passage for 2D-CRC-PDX cells.

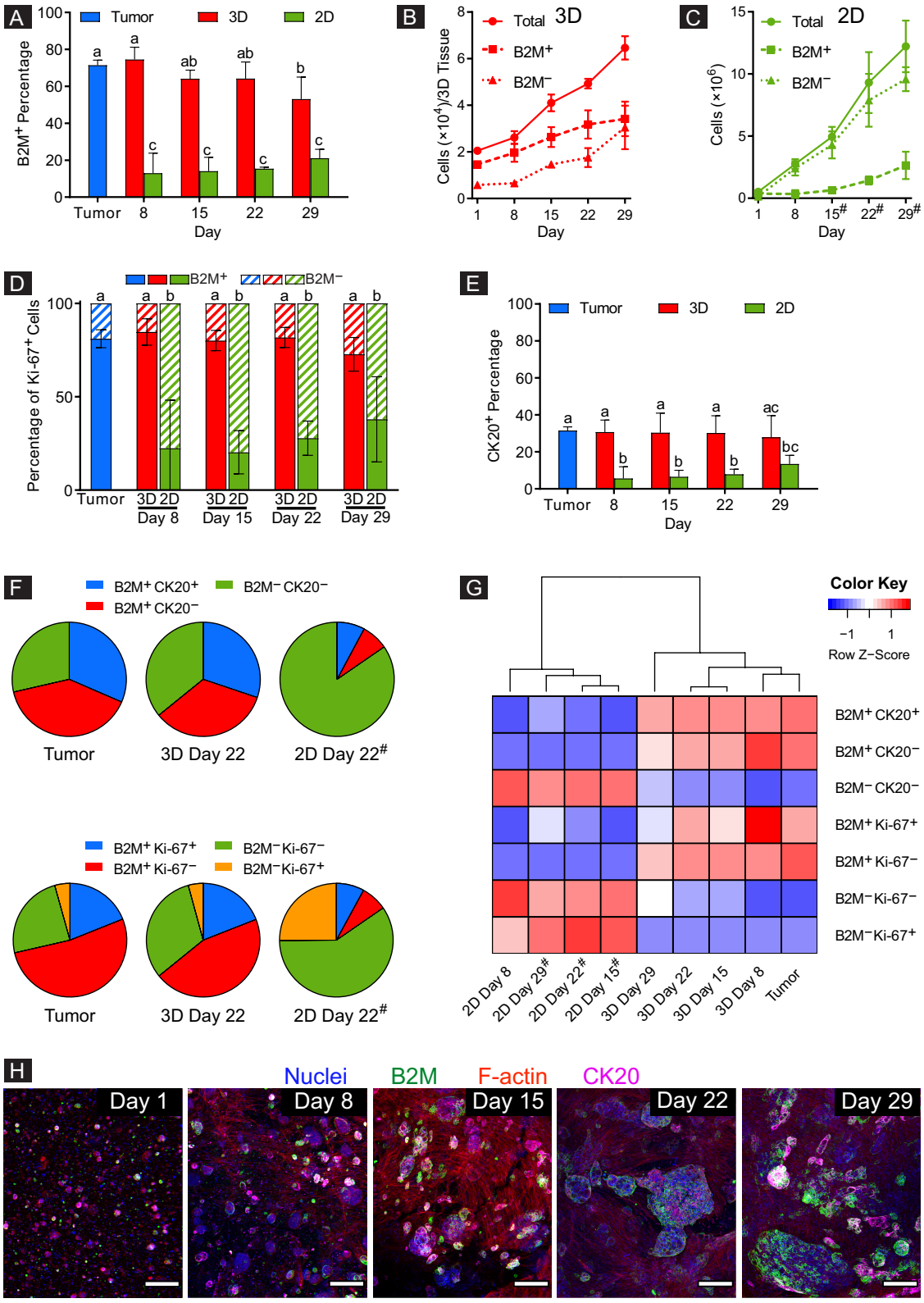

Figure 3.3. 3D-eCRC-PDX tissues maintained the CRC-PDX tumor cell subpopulations during long-term culture, whereas the 2D-CRC-PDX cells did not. (A) The percentage of

human ($B2M^+$) cells within the 3D-eCRC-PDX tissues remained constant during long-term culture (through Day 22), maintaining the originating CRC-PDX tumor composition. However, for 2D-CRC-PDX cells, the percentage of human cells decreased by over 80% after 8 days of culture. While the cell numbers increased over time, (B) the 3D-eCRC-PDX tissues maintained similar ratios of human cancer and mouse stromal cells to those of the originating CRC-PDX tumor, whereas in (C) 2D-CRC-PDX culture, mouse ($B2M^-$) cells outgrew the human cells. The 3D-eCRC-PDX tissues maintained the percentages of (D) human proliferative ($B2M^+$ $Ki67^+$) and (E) $CK20^+$ cells over 29 days of culture, whereas in 2D-CRC-PDX cultures, these percentages decreased significantly after 8 days of culture and remained low thereafter. (F) In sharp contrast to the 2D-CRC-PDX cultures, cell subpopulations within the 3D-eCRC-PDX tissues were similar to the originating CRC-PDX tumors. (G) The 3D-eCRC-PDX tissue cell subpopulations clustered with the CRC-PDX tumors whereas the 2D-CRC-PDX cells clustered separately from both the 3D-eCRC-PDX tissues and CRC-PDX tumors. (H) Colony-forming cells within the 3D-eCRC-PDX tissues were all $B2M^+$ and partially $CK20^+$, thereby being human cells. Conversely, the elongated cells were neither $B2M^+$ nor $CK20^+$, thereby being mouse stromal cells (scale bar = 200 μm). Data are mean ± SD. Means that do not share a letter are significantly different ($p \leq 0.05$, n = 3 separate batches of cell culture). # indicates that the 2D-CRC-PDX cells were passaged at the previous time point.

In both the 3D-eCRC-PDX tissues and 2D-CRC-PDX cultures, the total number of viable cells, human cells, and mouse cells increased over time (Figure 3.3 B, C). However, which cell subpopulations contributed to this increase differed drastically. In the 3D-eCRC-PDX tissues, both human and mouse cell subpopulations increased in number, maintaining similar ratios to those of

the original CRC-PDX tumor over time; no significant difference was observed between the rates of increase for the 3D-eCRC-PDX tissue $B2M^+$ and $B2M^-$ subpopulations (based on linear regression analysis, $p = 0.4695$, Figure 3.3 B). In sharp contrast, the mouse cells were the major contributor to the increase in total cell number in 2D-CRC-PDX cultures; although numbers of human cells increased over time, the rate was significantly lower (0.23±0.04 fold, $p < 0.0001$) than that for the mouse cell subpopulations.

To further investigate temporal cell subpopulation changes, Ki-67 was employed as a proliferative marker in tandem with B2M to identify human proliferative cells. Although only 23±4% of all cells harvested from the CRC-PDX tumor were Ki-67 positive (Figure C.5 A), 81±5% of these Ki-67^+ cells were human cells ($B2M^+$) (Figure 3.3 D). Remarkably, the 3D-eCRC-PDX tissues maintained this human proliferative cell subpopulation over 29 days of culture with no significant changes (85±7%, 80±5%, 82±5%, and 73±9% on Day 8, Day 15, Day 22, and Day 29, respectively), whereas in 2D-CRC-PDX cultures, a significant decrease ($p = 0.0113$) in the percentage of human proliferative cells was observed after 8 days of culture (from 81±5% to 22±26%) with the percentage remaining low thereafter.

For both 2D-CRC-PDX cultures and 3D-CRC-PDX tissues, approximately 20-30% of all cells (human and mouse) were Ki-67^+ over the 29 days of culture (Figure C.5 A). The lower human cell proliferation in 2D-CRC-PDX cultures was offset by higher mouse cell proliferation; therefore, less than 25% of 2D-CRC-PDX cells were B2M positive after a week of *in vitro* culture (Figure 3.3 A). Moreover, total proliferative (Ki-67^+) and non-proliferative (Ki-67^-) cell numbers increased over time for both the 3D-eCRC-PDX tissues and 2D-CRC-PDX cultures; however, the major contributors to these increases differed. For 3D-eCRC-PDX tissues the rates of increase in human proliferative ($B2M^+$ $Ki67^+$) and mouse proliferative ($B2M^-$ Ki-67^+) and human non-

proliferative ($B2M^+$ $Ki\text{-}67^-$) and mouse non-proliferative ($B2M^-$ $Ki\text{-}67^-$) cell numbers were similar (no significant difference), maintaining ratios equivalent to the original tumor. In sharp contrast, for 2D-CRC-PDX cultures, mouse cells were the major contributor to both the total proliferative and non-proliferative cell number increases, whereas human proliferative and non-proliferative cell numbers increased at significantly lower rates (0.53±0.07 and 0.12±0.01 fold, respectively, $p \leq 0.05$) (Figure C.5 B-E). Taken together, these results indicate that the maintenance of human CRC PDX cells and equivalent rates of increase in human and mouse cell subpopulations in the 3D-eCRC-PDX tissues throughout long-term culture was a result of maintenance of these proliferative cell subpopulations, whereas proliferative subpopulation changes in 2D-CRC-PDX cultures resulted in domination by the mouse cells over time.

To examine temporal changes in cancer cell subpopulations in the CRC-PDX tumor, 3D-eCRC-PDX tissues, and 2D-CRC-PDX cultures, cytokeratin 20 (CK20) was used to examine a CRC positive ($CK20^+$) cell subpopulation. Even though CK20 is a CRC marker, not all CRC cells express the CK20 protein; the CK20 negative cell subpopulation may include other CRC cells (J.H. Kim et al. 2013; Imai et al. 2014; Shin et al. 2010; Toyoshima et al. 2016; Bayrak, Haltas, and Yenidunya 2012). As expected, the $CK20^+$ cells were a subpopulation of the $B2M^+$ cells while all mouse cells were negative for B2M as well as CK20 (Figure C.4). The number of cells in both $B2M^+$ $CK20^+$ and $B2M^+$ $CK20^-$ subpopulations within the 3D-eCRC-PDX tissues and 2D-CRC-PDX cultures increased over time (Figure C.5 H, I). For the dissociated CRC-PDX tumors, 32±2% of cells were positive for CK20 (Figure 3.3 E). Importantly, 3D-eCRC-PDX tissues were able to maintain a subpopulation of 32±2% $CK20^+$ cells over 29 days of culture, whereas a significant decrease ($p = 0.0001$) in the percentage of $CK20^+$ cells was observed by Day 8 in 2D-CRC-PDX

cultures in relation to the CRC-PDX tumor (from 32±2% to 6±6%). This trend was also observed for the dual-labeled $B2M^+$ and $CK20^-$ cell subpopulation (Figure C.5 G).

Overall, we found that the percentages of key cell subpopulations within the 3D-eCRC-PDX tissues were maintained over time with no significant changes through Day 22 of culture as compared to the CRC-PDX tumors. Conversely, 2D-CRC-PDX cells exhibited significant changes within the initial days of culture (Figure 3.3 F and Figure C.6). Moreover, cluster analysis of these cell subpopulations revealed that the 3D-eCRC-PDX tissues from all time points clustered in a group with the CRC-PDX tumors, with Day 8 of the 3D-eCRC-PDX tissues clustering closest (Figure 3.3 G and Figure C.7). In contrast, the 2D-CRC-PDX cells clustered separately from both the 3D-eCRC-PDX tissues and CRC-PDX tumors.

Morphological study of the distinct cell types supported the results found using flow cytometry. To visualize the cells within the 3D-eCRC-PDX tissues and in 2D-CRC-PDX cultures, immunostaining for nuclei, B2M, F-actin, and CK20 was carried out using Hoechst 33342, anti-B2M (human marker), phalloidin, and anti-CK20, respectively. Two distinct subpopulations were noted—a subpopulation of colony-forming cells and another of elongated cells. All of the colony-forming cells were positive for B2M and a portion was positive for CK20, whereas none of the elongated cells were positive for either B2M or CK20. Therefore, we can infer that the elongated cell subpopulation was comprised of mouse stromal cells (Figure 3.3 H and Figure C.8) which is consistent with observations that human stromal cells are replaced by mouse-derived cells in cancer xenografts (Okada, Vaeteewoottacharn, and Kariya 2019; Maykel et al. 2014). Consistent with these findings, labeled 2D-CRC-PDX cells also demonstrated that colony-forming cells were positive for CK20 and B2M, whereas the elongated cells were not positive for either maker (Figure C.9).

3.3.4 Gene Expression in CRC-PDX Tumors Was More Similar to 3D-eCRC-PDX Tissues than 2D-CRC-PDX Cells

To examine gene expression of colon cancer markers of the epithelial to mesenchymal transition (EMT), stem cells, and angiogenesis, we performed RT-qPCR on total RNA isolated from CRC-PDX tumors, 3D-eCRC-PDX tissues, and 2D-CRC-PDX cells. We compared the expression of the colon cancer markers in the 3D-eCRC-PDX tissues and 2D-CRC-PDX cells to that in the CRC-PDX tumors. The expression of the EMT markers *SNAI1* and *TWIST1*, which play a role in tumor metastasis, were 8.15 ± 0.71 and 4.91 ± 0.66 fold higher, respectively, in the 2D-CRC-PDX cells as compared to the CRC-PDX tumors (p = 0.001 and p = 0.005, respectively) (Figure 3.4 A). However, no significant differences were found between the 3D-eCRC-PDX tissues and CRC-PDX tumors. The expression of the EMT marker *TGFβ1* in both the 2D-CRC-PDX cells and 3D-eCRC-PDX tissues significantly increased by 3.85 ± 0.16 and 4.82 ± 0.51 fold, respectively, (p = 0.009 and p = 0.003, respectively). Next, we examined the expression of the stem cell marker genes *ALDH1A1*, *GPX2, LGR5*, and *OLFM4*. We observed a reduction in expression of *ALDH1A1* (0.49 ± 0.7 fold), *LGR5* (0.43 ± 0.11 fold) and *OLFM4* (0.18 ± 0.14 fold) in the 2D-CRC-PDX cells (p = 0.016, p = 0.022, and p = 0.001, respectively) (Figure 3.4 B). However, in the 3D-eCRC-PDX tissues, *ALDH1A1* expression increased by 1.61 ± 0.17 fold (p = 0.006) and *OLFM4* expression decreased by 0.14 ± 0.03 fold (p = 0.001). No significant difference in the expression of *GPX2* was observed in the 2D-CRC-PDX cells and the 3D-eCRC-PDX tissues. Lastly, we examined the expression of the angiogenesis marker genes *KDR* and *VEGFA* (Figure 3.4 C). We observed that *KDR* expression increased by 11.42 ± 3.95 fold in 2D-CRC-PDX cells (p = 0.028), while the *VEGFA* expression also increased but did not reach statistical significance

(Figure 3.4 C). In contrast, the expression of *KDR* and *VEGFA* was similar between the 3D-eCRC-PDX tissues and the CRC-PDX tumors. Taken together, our investigation into the expression of EMT, stem cell, and angiogenesis markers suggests that gene expression is more similar between the 3D-eCRC-PDX tissues and the CRC-PDX tumors, whereas significant differences were observed between 2D-CRC-PDX cells and the CRC-PDX tumors.

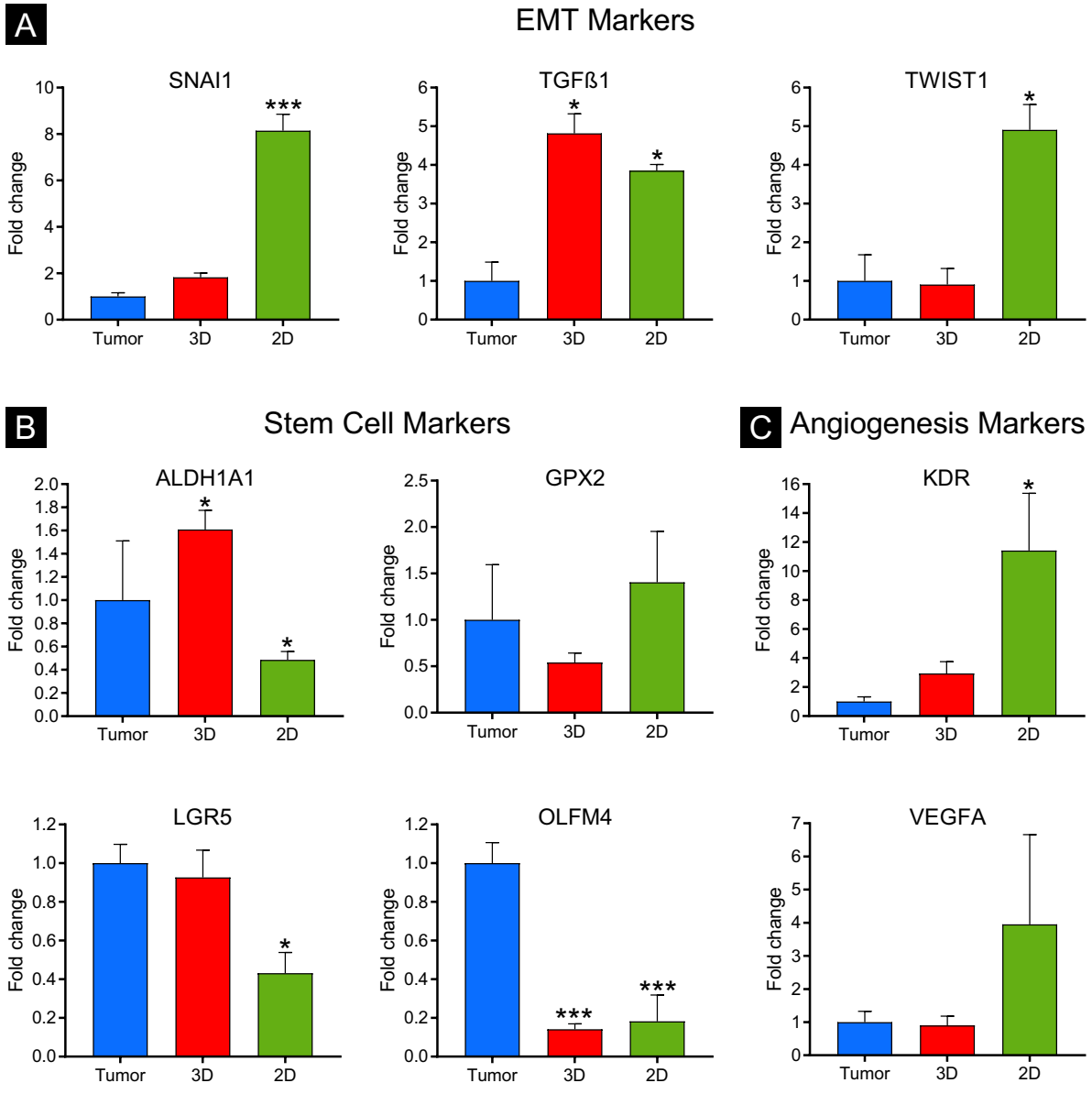

Figure 3.4. Gene expression of epithelial to mesenchymal transition (EMT), stem cell, and angiogenesis markers in CRC-PDX tumors was more similar to 3D-eCRC-PDX tissues than 2D-CRC-PDX cells. Gene expression of (A) EMT markers, *SNAI1* and *TWIST1*, (B) stem cell markers, *GPX2* and *LGR5*, and (C) angiogenesis markers, *KDR* and *VEGFA*, in the 3De-CRC-PDX tissues was not significantly different compared to the CRC PDX tumors. In 2D-CRC-PDX cultures, however, gene expression of four out of these six markers (*SNAI1*, *TWIST1*, *LGR5*, and *KDR*) was significantly different compared to the CRC PDX tumors. Data are mean ± SE (*$p \leq$ 0.05 and ***$p \leq 0.001$ compared to the CRC-PDX tumors. n = 3-4 separately obtained tumors and the corresponding batches of 3D-eCRC-PDX tissues and 2D-CRC-PDX cultures).

3.3.5 3D-eCRC-PDX Tissues Displayed Locational Heterogeneity and Cell-induced Contraction

Locational heterogeneity within the 3D-eCRC-PDX tissues was observed through immunostaining and confocal imaging. Elongated cells were primarily located on the outer layer (periphery) of the 3D-eCRC-PDX tissues, while the colony-forming cells were more prevalent within the 3D-eCRC-PDX tissues (Figure 3.5 A). Similar locational heterogeneity of cell morphology was also observed in the H&E stained 3D-eCRC-PDX tissues (Figure 3.5 C). Furthermore, H&E staining illustrated that the colony size within the 3D-eCRC-PDX tissues increased over time and displayed similar cellular morphology to the CRC-PDX tumor on Days 22 and 29 (Figure 3.5 C and see Figure 3.2 S-V). As the density of elongated cells increased on the periphery of the 3D-eCRC-PDX tissues, the 3D-eCRC-PDX tissues remodeled themselves from a disk shape on Days 1 and 8 to a near-spherical tissue by Day 29 (Figure 3.5 A, B).

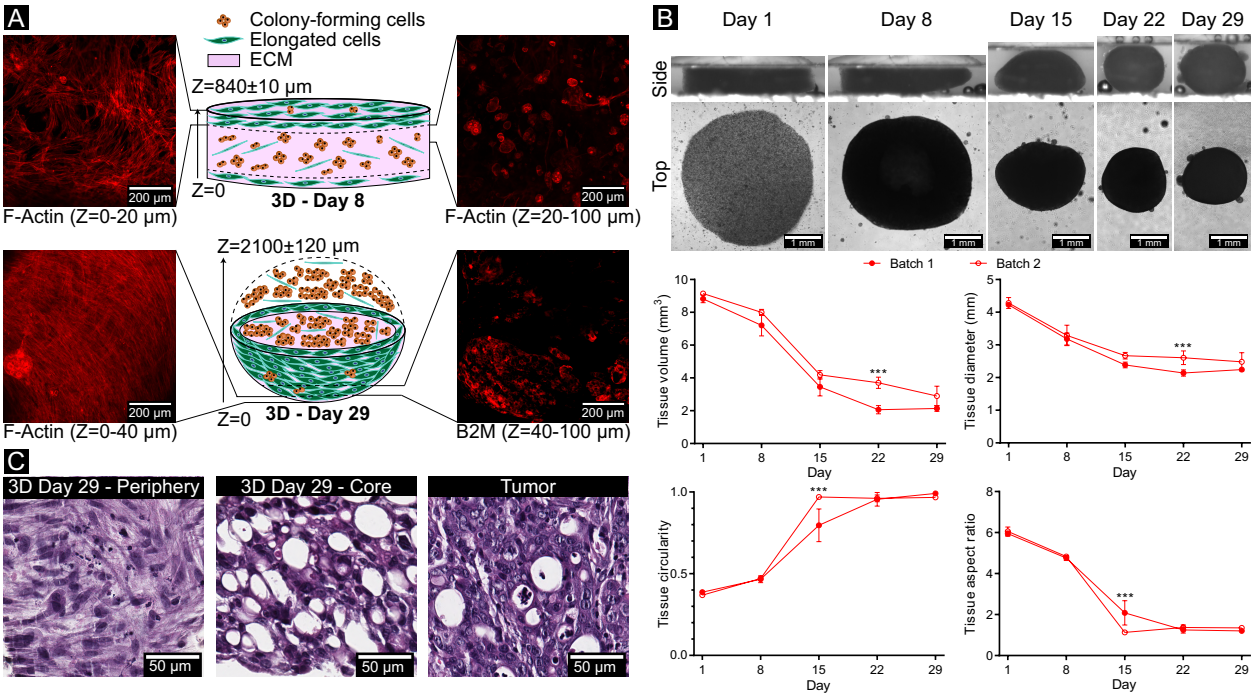

Figure 3.5. 3D-eCRC-PDX tissues showed locational heterogeneity and whole-tissue contraction over time. (A) Locational heterogeneity was observed in the 3D-eCRC-PDX tissues through immunostaining and confocal imaging. A Z-stack projection of sequential images showed that elongated cells were predominantly located on the periphery of the 3D-eCRC-PDX tissues, whereas the colony-forming cells were present mostly inside the tissue. (B) Side views of the 3D-eCRC-PDX tissues demonstrated that the 3D-eCRC-PDX tissues were remodeled from a disk shape on Day 1 to a near-spherical tissue by Day 29 where the diameter of the disk decreased as the height increased. Top views of the 3D-eCRC-PDX tissues illustrate the cell-mediated contraction of 3D-eCRC-PDX tissues over 29 days of culture. The decrease in volume and diameter of the 3D-eCRC-PDX tissues, increase in circularity, and decrease in aspect ratio was associated with the morphological change from disk-like to a spherical shape. Data are mean ± SD (***$p \leq 0.001$. n = at least 3 separate 3D-eCRC-PDX tissues). (C) Similar locational heterogeneity was observed in H&E stained 3D-eCRC-PDX tissues with elongated cells present primarily at the periphery and colony-forming cells present primarily at the core.

To examine the contraction of the 3D-eCRC-PDX tissues, which plays an important role in ECM remodeling, mechanical stiffness and cell phenotype, the size and dimensions of the 3D-eCRC-PDX tissues were investigated over 29 days in 2 separate batches. The 3D-eCRC-PDX tissue volume and diameter decreased significantly from Day 1 to Day 29 (Figure 3.5 B). The volume of acellular control hydrogels increased (8.8±0.2%, $p < 0.0001$) from Day 1 to Day 8 and remained constant after Day 8 over 29 days of incubation at 37 °C and 5% CO_2 (Figure C.10); this change in volume was a result of an increase in the acellular tissue thickness, whereas diameter remained constant. Thus, the 3D-eCRC-PDX tissue contraction and matrix remodeling were cell-mediated. Furthermore, tissue circularity and tissue aspect ratio were examined over time to quantify changes in tissue morphology. As the volume and diameter decreased, the 3D-eCRC-PDX tissue circularity increased and aspect ratio of the lateral surface (side view) decreased from Day 1 to Day 29, which was consistent with the change from the initial disk-like shape to a spherical shape; importantly, this result was consistent between batches (Figure 3.5 B).

3.3.6 3D-eCRC-PDX Tissues Mimic the Mechanical Stiffness of CRC-PDX Tumors

To assess tissue mechanical stiffness, two CRC-PDX tumors and two paired batches of 3D-eCRC-PDX tissues were subjected to parallel plate compression testing. CRC-PDX tumor stiffness was found to vary significantly depending on the geometric region of the tumor from which the sample was taken. An increasing trend ($p < 000.1$) in stiffness was observed from the core to the periphery of the tumor for both tumors (Figure 3.6 A). The core region of the CRC-PDX tumor was the least stiff (average of ~0.5 kPa), while the periphery region had the highest

stiffness (average of ~2.8 kPa), with no significant difference between Tumor 1 and Tumor 2 for a given region.

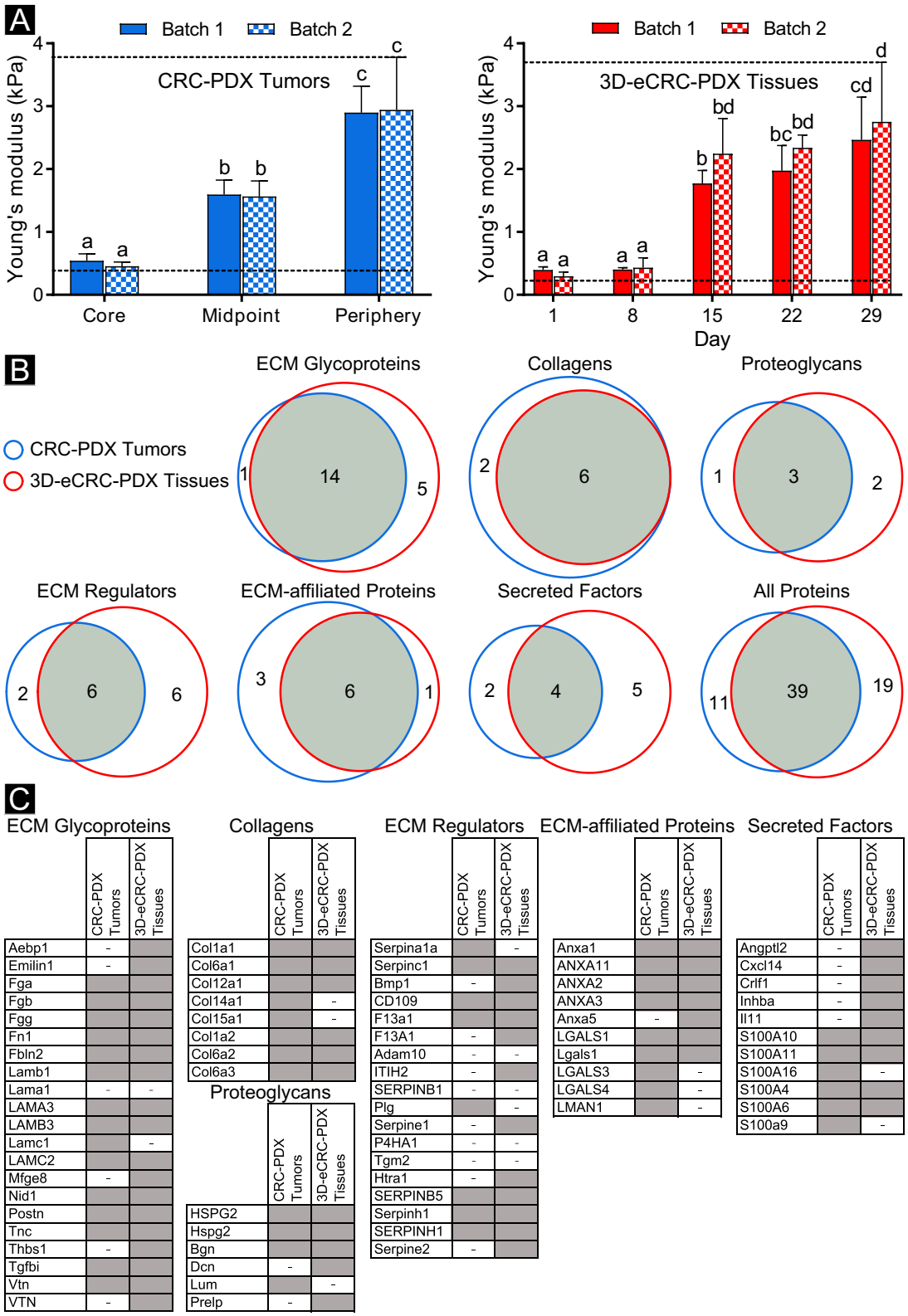

Figure 3.6. 3D-eCRC-PDX tissues and CRC-PDX tumors showed similar Young's moduli and ECM proteins. (A) CRC-PDX tumor stiffness differed regionally with the core of the tumor

having the lowest stiffness and the periphery having the highest stiffness, based on parallel plate compression testing. For two CRC-PDX tumors no statistical difference was found between samples taken from the same tumor region ($p \leq 0.05$, n = 3 tissues per region per tumor). The stiffness of 3D-eCRC-PDX tissues increased over 29 days of culture with a significant increase from Day 8 to Day 15. No significant difference was found between two separate batches of 3D-eCRC-PDX tissues ($p \leq 0.05$, n = 3 tissues per timepoint per batch). Interestingly, the range of stiffness of the 3D-eCRC-PDX tissues was within that of the CRC-PDX tumors. Bar =mean ± SD. Means that do not share a letter are significantly different. The dashed lines show the ranges of stiffness. (B, C) ECM proteins from CRC-PDX tumors and 3D-eCRC-PDX tissues were identified using proteomics; 39 proteins (approximately 57%) were observed in both the CRC-PDX tumors and the 3D-eCRC-PDX tissues. ECM glycoproteins and collagens showed the highest overlap among all subtypes, whereas ECM regulators and secreted factors contained the least common proteins. A protein was indicated as present (gray cell) when detected in at least two out of three samples and as absent (cell with a minus sign) when detected in only one sample or not detected. Proteins presented in uppercase and lowercase letters are from human and mouse databases, respectively.

The average stiffness of the 3D-eCRC-PDX tissues increased temporally from Day 1 to Day 29, where stiffness of ~0.4 kPa was quantified on Day 1 and ~2.8 kPa on Day 29, with no significant difference between Batch 1 and Batch 2 for a given time point (Figure 3.6 A). Most notably, the range of stiffness of the 3D-eCRC-PDX tissues was similar to that of the CRC-PDX tumors, while the time-dependent stiffness of the 3D-eCRC-PDX tissues mimicked the region-dependent stiffness of the CRC-PDX tumor. To determine if the PEG-Fb biomaterial contributed

to the increase in stiffness, acellular hydrogels were created and maintained in similar conditions to the cell-laden tissues. In contrast to the mechanical stiffness of 3D-eCRC-PDX tissues, we found that the stiffness of acellular hydrogels decreased from Day 1 to Day 8, primarily due to swelling, and then remained constant from Day 8 to Day 29 (Figure C.11). Therefore, the observed temporal increase in 3D-eCRC-PDX tissue stiffness is consistent with a cell-mediated mechanism.

3.3.7 Proteomic Analysis of CRC-PDX Tumors and 3D-eCRC-PDX Tissues

To compare the ECM compositions of CRC-PDX tumors and 3D-eCRC-PDX tissues, proteomic analysis using ECM protein enrichment and mass spectroscopy characterization was performed on three separate batches of paired CRC-PDX tumors and 3D-eCRC-PDX tissues. Between all samples, 872 unique proteins were identified, 74 of which were identified as matrisome (Naba et al. 2017). Correlation in ECM proteins observed in CRC-PDX tumors and paired 3D-eCRC-PDX tissues was first examined on a batch-by-batch basis. Approximately 61% of identified ECM proteins (38 out of 62) were observed in both the batch 1 CRC-PDX tumor and its paired 3D-eCRC-PDX tissues, while approximately 10% were only identified in the CRC-PDX tumor and 29% only identified in the 3D-eCRC-PDX tissues (Figure C.12 A). Similarly, in batch 2 approximately 54% of identified proteins (38 out of 70) were observed in both the CRC-PDX tumor and the 3D-eCRC-PDX tissues, whereas in batch 3, approximately 47% of proteins were found in both CRC-PDX tumors and 3D-eCRC-PDX tissues (Figure C.12 B, C). Overall, when comparing the pooled ECM proteins identified, there were 39 proteins (approximately 57%) observed in both the CRC-PDX tumors and the 3D-eCRC-PDX tissues, whereas 11 proteins (approximately 16%) were only identified in the CRC-PDX tumors and 19 proteins (approximately 27%) were only identified in the 3D-eCRC-PDX tissues (Figure 3.6 B). In addition, we evaluated

the similarity between CRC-PDX tumors; approximately 60% of ECM proteins within CRC-PDX tumors were the same for all three batches, 28% of the ECM proteins were present in at least two batches, and 12% of the ECM proteins were specific to each batch (Figure C.13 A). Similarly, within 3D-eCRC-PDX tissues, 60% of ECM proteins were found to be the same among all batches, 25% were present in at least two batches, and 15% were batch-specific (Figure C.13 B). Therefore, batch-to-batch consistency of the ECM proteins from the 3D-eCRC-PDX tissues was similar to those from the CRC-PDX tumors.

We further categorized the ECM proteins into ECM glycoproteins, collagens, proteoglycans, ECM regulators, ECM-affiliated proteins, and secreted factors. The number of ECM proteins per each subtype (e.g. ECM Glycoproteins) found in the CRC-PDX tumors and 3D-eCRC-PDX tissues are presented in Figure 3.6 B and Figure C.13 A, B. Identified ECM proteins for all CRC-PDX tumors and 3D-eCRC-PDX tissues from all batches are also reported by subtype in a table (Figure 3.6 C and Figure C.14). We found that ECM glycoproteins, collagens, proteoglycans, and ECM-affiliated proteins exhibited the most ECM proteins shared between CRC-PDX tumors and 3D-eCRC-PDX tissues. ECM glycoproteins and Collagens showed the highest overlap among all subtypes, whereas ECM regulators and secreted factors contained the least common proteins. In general, a higher total number of ECM proteins were identified in the 3D-eCRC-PDX tissues, thereby resulting in a higher number of proteins that were specific to the 3D-eCRC-PDX tissues.

3.3.8 Molecular characterization of CRC-PDX Tumors and 3D-eCRC-PDX Tissues

Transcriptome analysis using RNA seq was performed to undertake a molecular characterization of the CRC-PDX tumors and the 3D-eCRC-PDX tissues. To assess the CRC molecular subtype (Guinney et al. 2015) we classified the CRC-PDX tumors and the 3D-eCRC-PDX tissues together with 478 primary CRC tumors from the Cancer Genome Atlas Colon Adenocarcinoma (TCGA-COAD) cohort (Muzny et al. 2012). Our classification of TCGA-COAD cohort tumors resulted in the majority of tumors being classified as consensus molecular subtypes (CMS) 2 and 4 which is consistent with previous classifications of CRC tumors (Guinney et al. 2015; Pramudita R Prasetyanti et al. 2019) (Figure 3.7 A). We observed that both the CRC-PDX tumors and the 3D-eCRC-PDX tissues classified as CMS1. Thus, the process of engineering our CRC PDX tissue did not alter the CRC molecular subtype.

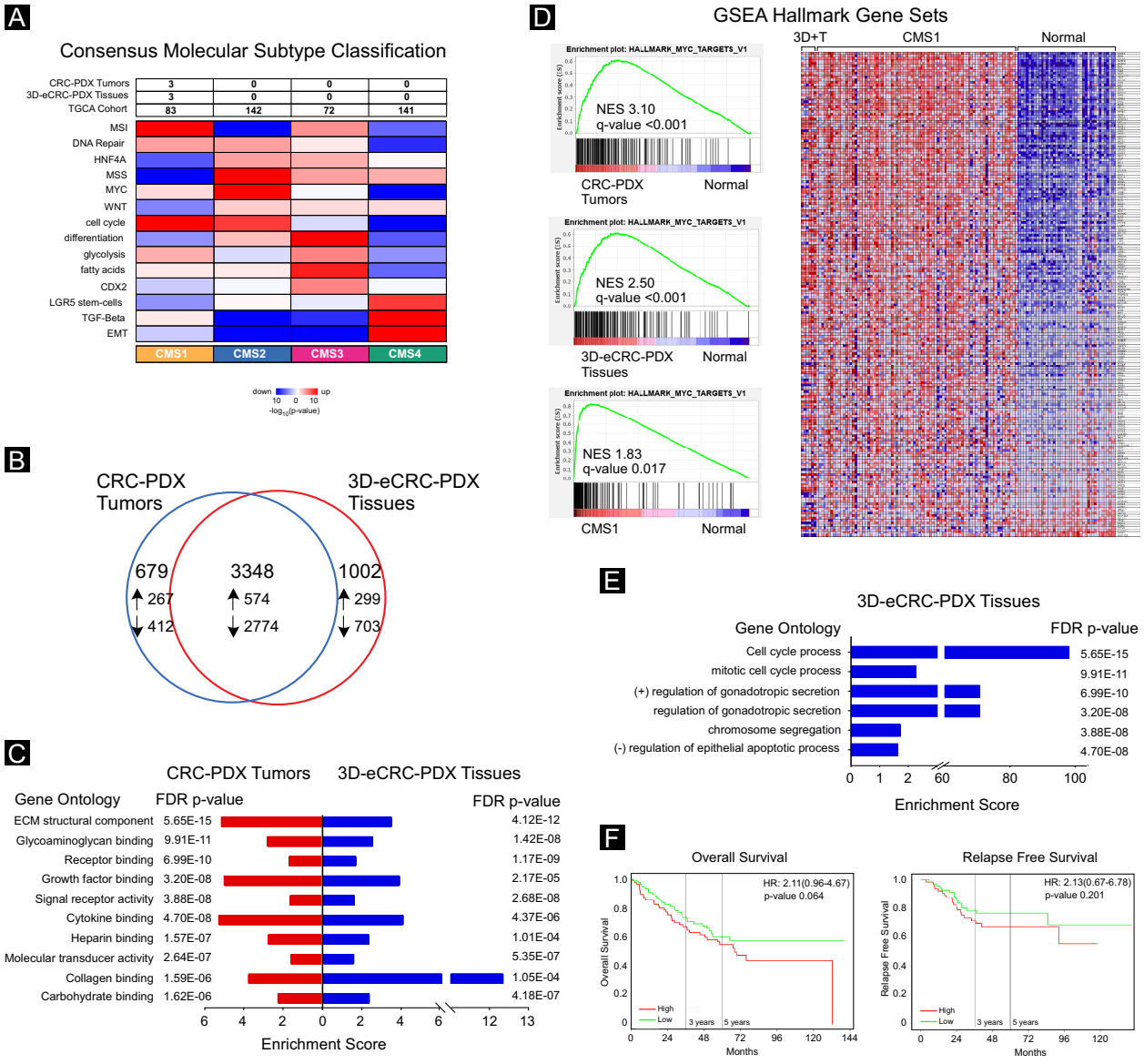

Figure 3.7. Transcriptomic characterization of 3D-eCRC-PDX tissues demonstrated that 3D-eCRC-PDX tissues recapitulated key molecular characteristics of CRC-PDX tumors. (A) CRC Consensus Molecular Subtype Analysis. CRC-PDX tumor (n = 3) and 3D-eCRC-PDX tissue (n = 3) HT-Seq gene counts and TCGA-COAD counts were used to assess CRC consensus molecular subtype. (B) DEGs in CRC-PDX tumor and 3D-eCRC-PDX tissue compared to normal colon tissue (n = 41) from the TCGA-COAD. The number of DEGs that were downregulated (down arrow) or upregulated (up arrow) is shown. (C) Enriched gene molecular function

ontologies between CRC-PDX tumors and 3D-eCRC-PDX tissues and normal colon tissue (n = 41) are shown. (D) GSEA Analysis. The top enriched Hallmarks gene sets in CRC-PDX tumors (*upper left panel*), 3D-eCRC-PDX tissues (*middle left panel*) and patient CRC tumor TCGA-COAD samples (n = 84) (*lower left panel*) compared to normal colon tissue (n = 41). Normalized enrichment score (NES) and the FDR q-value are shown. Heatmap of CRC-PDX tumors, 3D-eCRC-PDX tissues, and patient CRC tumors (n = 84) and normal colon tissue (*right panel*). (E) Gene ontology analysis of molecular functions enriched in DEGs between CRC-PDX tumors and 3D-eCRC-PDX tissues. (F) Prognostic Kaplan–Meier survival analysis using DEGs upregulated between CRC-PDX tumors and 3D-eCRC-PDX tissues in the precomputed GEO dataset GSE17536 (n = 87) adjusted for age, stage, and gender covariates and bifurcated based on median expression was examined for overall survival (*left panel*) and relapse-free survival (*right panel*). The hazard ratios, 95% confidence intervals, and *p* values are shown.

To assess cancer-specific differentially expressed genes and gene ontology functions in the CRC-PDX tumors and the 3D-eCRC-PDX tissues, we determined differentially expressed genes (DEGs) in the CRC-PDX tumors and the 3D-eCRC-PDX tissues compared to tumor-adjacent normal colon tissue in the TGCA-COAD patient cohort. Approximately 66% of the DEGs were overlapping when the samples were compared (Figure 3.7 B). ECM structural component (GO:000521) was the top significantly enriched gene ontology function term observed in both the CRC-PDX tumors (5.65E-15 FDR *p* value, 5.05 enrichment) and 3D-eCRC-PDX tissues (4.12E-12 FDR *p* value, 3.41 enrichment) (Figure 3.7 C). Further, the top ten significantly (FDR *p* value < 0.05) enriched gene ontology function terms observed in the CRC-PDX tumors were also significantly enriched in the 3D-eCRC-PDX tissues. Because there is overlap between gene

ontology terms, a REViGO analysis (Supek et al. 2011) was performed to remove redundant terms from the significantly enriched gene ontology function terms identified in the CRC-PDX tumors and the 3D-eCRC-PDX tissues. As shown in the TreeMaps in Figure C.15, enrichment in receptor binding, signaling receptor activity, extracellular matrix structural constituents were observed in both the CRC-PDX tumors and the 3D-eCRC-PDX tissues.

To gain cancer-related biological insight into gene expression in the CRC-PDX tumors and 3D-eCRC-PDX tissues, we performed gene set enrichment analysis (GSEA) using the Hallmark gene sets (Liberzon et al. 2015) from the Molecular Signatures Database (Broad Institute) (Subramanian et al. 2005). The most enriched gene set (Myc targets v1, Normalized enrichment score 3.10, q-value < 0.001) in the CRC-PDX tumors (Figure 3.7 D, *upper left panel*) was also the most enriched (Normalized enrichment score 2.50, q-value < 0.001) in the 3D-eCRC-PDX tissues (Figure 3.7 D, *middle left panel*). We also observed that 8 of the top 10 Hallmark gene sets (Myc_Targets v1, E2F_Targets, Myc_Targets v2, DNA_Repair, Unfolded_Protein_Response, P53_Pathway, and MTORC1) significantly enriched in the CRC-PDX tumors were also significantly enriched in the 3D-eCRC-PDX tissues (Figure C.16, *left and middle panels*). To assess whether the Hallmark gene sets are also enriched in patient tumors, we next examined whether CMS1 classified primary tumors in the TCGA-COAD cohort were enriched for the 10 significantly enriched Hallmark gene sets in the CRC-PDX tumors and the 3D-eCRC-PDX tissues. The top enriched gene set in the CRC-PDX tumors and the 3D-eCRC-PDX tissues, Myc_Targets v1 gene set, was also significantly enriched (Normalized enrichment score 1.83, q-value < 0.017) in the CMS1 patient CRC tumors (Figure 3.7 D, *lower left panel*). Indeed, 9 of the top 10 Hallmark gene sets significantly enriched in the CRC-PDX tumors were also significantly enriched in CMS1 patient CRC tumors (Figure C.16, *right panel*); only the P53_Pathway gene set was not

significantly (q-value 0.174) enriched in the CMS1 patient CRC tumors (Figure C.16, *right panel*). To visualize the enrichment of the Myc targets v1 gene set in the CRC-PDX tumors, 3D-eCRC-PDX tissues, CMS1 patient CRC tumors, and tumor-adjacent normal colon tissue in the TGCA-COAD patient cohort, a heatmap was generated using the GSEA software. As shown in Figure 3.7 D, *right panel*, tumor-adjacent normal colon tissue differentially expresses genes in the Myc targets v1 gene set compared to CRC-PDX tumors, 3D-eCRC-PDX tissues, and CMS1 patient CRC tumors.

To determine transcriptomic differences between the CRC-PDX tumors and the 3D-eCRC-PDX tissues, differential expression analysis was performed. We observed 2193 DEGs (adj p value < 0.05, baseMean > 10, Log_2-fold > 1.5). Gene ontology was performed to assess potential function differences between the CRC-PDX tumors and the 3D-eCRC-PDX tissues. The significantly (FDR p value < 0.05) regulated gene ontology function terms enriched in the 3D-eCRC-PDX tissues were cell cycle processes (Figure 3.7 E). To examine the prognostic relevance of the top 16 upregulated DEGs in the 3D-eCRC-PDX tissues compared to the CRC-PDX tumors on overall survival and relapse-free survival in CRC patients, we generated Kaplan-Meier plots (Goswami and Nakshatri 2013). In the CRC cohort GSE17536, there was not a significant difference in overall survival ($p = 0.064$) and relapse-free survival ($p = 0.201$) in CRC patients with high expression of the 16 DEGs in the 3D-eCRC-PDX tissues (Figure 3.7 F). We also did not observe significant differences in overall survival ($p = 0.246$) in the CRC cohort GSE17537 and the TGCA-COAD cohort ($p = 0.697$) and with relapse-free survival ($p = 0.112$) in the CRC cohort GSE14333 (Figure C.17).

3.4 Discussion

In vitro 3D cancer tissues created using tissue engineering tools represent one of the new cancer disease models needed to advance our understanding of cancer biology and therapeutic development. For CRC, 3D tissue-engineered platforms using biomaterials such as PEG-Fb (Pradhan, Clary, et al. 2017), collagen I (Magdeldin et al. 2014; Dolznig et al. 2011; Nyga et al. 2013; Dainiak et al. 2008), alginate (Shakibaei et al. 2015), and decellularized matrices (Hoshiba and Tanaka 2016) have been used to study cell morphology, growth rate, and migration, cell-cell interactions, and drug testing. In each of these studies, however, standard cancer cell lines such as HCT 116, HT-29, LS 174T, and SW480 were used to create the *in vitro* disease model. While standard cancer cell lines provide valuable information in the field of cancer research, cell heterogeneity and molecular characteristics of standard cancer cell lines do not represent patient tumors (Cree, Glaysher, and Harvey 2010; Fernando et al. 2006). In contrast, the PDX models are more advanced cancer models of the patient tumor which demonstrate high potential in clinical translatability due to the maintenance of key characteristics of the patient tumor (Brown et al. 2016).

Here we developed a new cancer model for CRC combining the clinical translatability of PDX lines and the more high-throughput capacity of *in vitro* culture. We described the generation of the 3D-eCRC-PDX tissues as an *in vitro* tumor model and investigated the extent to which this *in vitro* model recapitulated the originating *in vivo* CRC-PDX tumors with a parallel comparison to 2D-CRC-PDX cultures. We found that, in contrast to 2D-CRC-PDX cultures, the 3D-eCRC-PDX tissues maintained the originating CRC-PDX tumor cell compositions during long-term culture, with the total cell numbers for each subpopulation increasing over time. Importantly, the

3D-eCRC-PDX tissues recapitulated key transcriptomic characteristics, ECM proteins, and mechanical stiffness of the CRC-PDX tumors.

Cell-cell and cell-matrix interactions can impact the cellular growth rate and thus, changes in distinct cell subpopulations may arise as the cells respond to their environment (Riedl et al. 2017; Okada, Vaeteewoottacharn, and Kariya 2019; Kodack et al. 2017). As PDXs are maintained and propagated *in vivo*, the resultant tumors are composed of both human and mouse cells. The inclusion of cancer and stromal PDX cell subpopulations is necessary for accurate recapitulation of the PDX tumor microenvironment. However, in the few studies that have reported the culture of PDX cells *in vitro* in a 3D microenvironment, the adherent cell subpopulation was selectively removed from the PDX cell population (E.L. Fong et al. 2014; E.L. Fong, Wan, et al. 2016). None of these studies investigated whether the original PDX cell subpopulations could be maintained in a 3D engineered tissue model over time. Therefore, here we examined changes in distinct cell subpopulations using β-2 microglobulin (B2M) as a human cell marker, Ki-67 as a proliferative cell marker, and cytokeratin 20 (CK20) as a CRC cell marker. Importantly, we demonstrated that even as cell number increased during long-term culture, the 3D-eCRC-PDX tissues maintained the key cell subpopulations at ratios similar to the originating CRC-PDX tumor, whereas 2D-CRC-PDX cultures did not. The changes in cell subpopulations of 2D-CRC-PDX cultures were consistent with the observations reported by Kodack et al. (Kodack et al. 2017) as they attempted to establish cancer cell lines from multiple primary patient-derived tumors; in some cases, the stromal cells, primarily fibroblasts, outgrew the cancer cells, thereby hindering the tumor cell growth and resulting in the failure of cell line generation.

Taken together, our results indicated that the 3D-eCRC-PDX tissues not only mimicked the cellular heterogeneity and cell population composition of the CRC-PDX tumors but were also

able to maintain the cell populations in long-term *in vitro* culture. Notably, this maintenance of cell subpopulation ratios occurred simultaneously with temporal increases in cell numbers, an increase in the size of cell colonies, and an observed increasing presence of elongated cells over time within the 3D-eCRC-PDX tissues labeled with $B2M^+$, $CK20^+$, and phalloidin. Furthermore, consistent with flow cytometry results, gene expression analysis suggests that EMT, stem cell, and angiogenesis marker expression was more similar to the CRC-PDX tumors in the 3D-eCRC-PDX tissues than the 2D-CRC-PDX cells. -

In addition, it must be noted that immunostaining revealed two distinct cell subpopulations in the *in vitro* cultures, colony-forming cells ($B2M^+$) and elongated cells ($B2M^-$). Since human stromal cells are replaced by mouse-derived cells in cancer xenografts [25, 78], our data suggest that all human cells (colony-forming cells) were CRC cells despite the fact that only a portion (~ 40%) of them positively expressed CK20. This result is consistent with immunohistochemical findings that 78% of stage II colon cancer patients had partial positivity for CK20 (Vaz et al. 2014). Importantly the CK20 protein is linked to metastasis and invasiveness, microsatellite instability, differentiation, and stage of CRC (J.H. Kim et al. 2013; Imai et al. 2014; Shin et al. 2010; Toyoshima et al. 2016).

Transcriptomic analysis was performed to examine molecular similarities and differences between our CRC-PDX tumors and 3D-eCRC-PDX tissues. We first observed that the CRC-PDX tumors and 3D-eCRC-PDX tissues were classified as CMS1 tumors which is a molecular subtype associated with worse survival after relapse (Guinney et al. 2015). Even though we observed approximately 2000 DEGs between the CRC-PDX tumors and 3D-eCRC-PDX tissues, there was not a significant difference in prognostic Kaplan-Meier plots for overall survival and relapse free survival using the top 16 DEGs between the CRC-PDX tumors and 3D-eCRC-PDX tissues,

suggesting that the top DEGs between the two models are not clinically relevant. Our observation of differential enrichment in the cell cycle molecular function between the CRC-PDX tumors and 3D-eCRC-PDX tissues is consistent with differential growth between *in vivo* tumors and *in vitro* tissues (Sachs and Clevers 2014).

To further assess transcriptomic similarities between our CRC-PDX tumors and 3D-eCRC-PDX tissues, we identified enriched gene ontology molecular functions and Hallmark gene sets in the CRC-PDX tumors and the 3D-eCRC-PDX tissues compared to tumor-adjacent normal colon tissue. We observed congruence in the enriched gene ontology molecular functions (top ten GO terms in CRC-PDX tumors were also significantly enriched in 3D-eCRC-PDX tissues) and Hallmark gene sets (eight of the top ten enriched gene sets in CRC-PDX tumors were also significantly enriched in 3D-eCRC-PDX tissues). Taken together, our molecular characterization results suggest that 3D-eCRC-PDX tissues transcriptionally resemble CRC-PDX tumors.

We next sought to identify and compare ECM proteins from both CRC-PDX tumors and 3D-eCRC-PDX tissues from three separate batches. Although the ECM compositions of engineered CRC-PDX tissues have not been previously investigated, the ECM proteins of CRC tumors from patients have been reported. Naba et al. (Naba et al. 2014) demonstrated that there was consistency in ECM proteins between two samples from each patient as well as among three patients. Similar to our results, ECM regulators were the least common identified proteins between the two samples from each patient. In our model, the similarity of identified ECM proteins between CRC-PDX tumors and 3D-eCRC-PDX tissues, as well as the consistency among separately prepared batches, was relatively high; however, the number of ECM proteins identified in our *in vitro* and *in vivo* CRC-PDX tissues was lower compared to that identified in the patient CRC tissues by Naba et al. (Naba et al. 2014). For CRC-PDX line employed here, patient tumor tissue

for ECM analysis was not available; future work to examine the correlation between the *in vitro* model established here and patients' ECM compositions is warranted.

Cancer progression leads to remodeling of the tumor microenvironment (Yuan et al. 2016; Bager et al. 2016). A driver of microenvironmental remodeling is fibroblast-derived ECM components (Alkasalias et al. 2018); fibroblasts also interact with the surrounding ECM proteins and contract the tumor tissue which affects the mechanobiological properties of the tissue (Yuan et al. 2016; Alkasalias et al. 2018; Marquez et al. 2006). Consistent with prior findings (Marquez et al. 2006; Jin et al. 2015; Bell, Ivarsson, and Merrill 1979; Godbout et al. 2013; Marquez, Elson, and Genin 2010; Jansen et al. 2013; Hinz et al. 2001; Dolznig et al. 2011), we observed that the 3D-eCRC-PDX tissues displayed tissue contraction over time as the mouse stromal cells elongated. We additionally found that the 3D-eCRC-PDX tissue volume decreased temporally, which was not observed in acellular PEG-Fb hydrogels and is, therefore, not intrinsic to the biomaterial properties under our cell culture conditions. This observation suggests that the change in 3D-eCRC-PDX tissue morphology was a result of cell-matrix interactions. Fibroblast-induced contraction and remodeling of ECM, which play roles in matrix stiffening and cell signaling, division, and migration, have been widely investigated (Schrader et al. 2011; J.S. Park et al. 2011; Swaminathan et al. 2011; Zaman et al. 2006; Marquez et al. 2006; Jin et al. 2015; Bell, Ivarsson, and Merrill 1979; Godbout et al. 2013; Marquez, Elson, and Genin 2010; Jansen et al. 2013; Hinz et al. 2001). Marquez et al. (Marquez et al. 2006) demonstrated higher fibroblast density increased ECM contraction and stiffness in collagen I hydrogels. Consistent with the previously reported observation (Marquez et al. 2006; Jin et al. 2015; Bell, Ivarsson, and Merrill 1979; Godbout et al. 2013; Marquez, Elson, and Genin 2010; Jansen et al. 2013; Hinz et al. 2001), our data suggest that

the increase in stiffness of the 3D-eCRC-PDX tissue could be partially a result of the increasing number of elongated cells over time.

Tumor tissue stiffness impacts tumor cell proliferation, dormancy, migration and metastasis, and chemotherapeutic response while simultaneously affecting cell-matrix interactions; thus, stiffness is widely recognized as an important factor for cancer cell behavior (Pradhan, Hassani, et al. 2017; Schrader et al. 2011; J.S. Park et al. 2011; Swaminathan et al. 2011; Zaman et al. 2006; Kraning-Rush and Reinhart-King 2012; Chen, Pedron, and Harley 2017; Holt et al. 2017). In CRC, tumor stiffness correlates to a higher stage, as well as metastatic phenotypes (Kawano et al. 2015). The bulk elastic modulus was 1.08-12.2 kPa (median = 3.49 kPa) for stage II CRC while the normal tissue presented a stiffness range of 0.37-7.33 kPa (median = 0.936 kPa). Our CRC-PDX tumors fell within the reported stiffness range for the stage II CRC patient tumors. Specifically, we found that CRC-PDX tumor stiffness increased from the core to the periphery, with regional stiffness ranges of 0.4-0.6 kPa, 1.3-1.9 kPa, 2.4-3.4 kPa at the core, midpoint, and periphery regions, respectively. Interestingly, the time-dependent bulk stiffness of our 3D-eCRC-PDX tissues (ranging from 0.3-3.5 kPa) recapitulated the full range of regional stiffnesses observed in the CRC-PDX tumors.

Although we demonstrated the ability of CRC PDX cells to be maintained in long-term *in vitro* culture using tissue engineering tools, the current study had limitations. Our efforts in this study were focused on the engineered CRC-PDX tissue model development, in-depth characterization and comparison between *in vitro* tissues and *in vivo* tumors, and batch-to-batch reproducibility. Future work in our laboratory will investigate the applicability of this *in vitro* 3D model for other CRC PDX lines from multiple patients. Whereas this study employed patient-derived cells, the patient tumor tissue used to initiate the PDX CRC line employed was not

available for direct comparison with the *in vivo* tumors or *in vitro* tissues. Furthermore, we were not able to include human stromal cells in our *in vitro* model as these cells are replaced by mouse stromal cells in PDX tumors. Whereas directly using patient tumor cells to create this engineered CRC tissue model and including patient-specific tumor stromal cells such as cancer-associated fibroblasts and immune cells could potentially result in a better recapitulation of the patient tumor, this approach only allows cells to be obtained once from each patient; given the high level of heterogeneity between patient tumors, using patient tumor cells directly, rather than PDX lines, would not have provided the ability to directly assess and refine model reproducibility. To test the clinical translatability of our model in predicting individual patient drug response, further studies are needed. Furthermore, the use of this *in vitro* 3D model could be extended to examine the potential to support PDX or patient cells from other types of cancer.

3.5 Conclusion

In this study, we have developed a new *in vitro* 3D engineered tissue model (3D-eCRC-PDX tissues) using cells isolated from a CRC-PDX tumor. During long-term culture, the 3D-eCRC-PDX tissues maintained the cell populations observed in the originating CRC-PDX tumor, whereas in 2D-CRC-PDX cultures, mouse stromal cells grew at a much faster rate and overtook the human CRC cells, thereby leading to cell population compositions that deviated from the CRC-PDX tumor. The cells within the 3D-eCRC-PDX tissues demonstrated locational heterogeneity in terms of cell subpopulations; elongated mouse cells were primarily present on the surface of the 3D-eCRC-PDX tissues and human colony-forming CRC cells were present throughout the 3D-eCRC-PDX tissues. Furthermore, cellular morphology within the 3D-eCRC-PDX tissues was similar to that observed in CRC-PDX tumors. CRC-PDX tumor stiffness varied regionally; 3D-

eCRC-PDX tissues increased in stiffness over time in culture, providing recapitulation of the full CRC-PDX tumor stiffness range. Moreover, results from our transcriptomic analysis of CRC-PDX tumors and 3D-eCRC-PDX tissues indicate similarity in enriched gene ontology molecular functions and Hallmark gene sets. Importantly, prognostic Kaplan-Meier plots for overall survival and relapse free survival did not reveal significant differences between CRC-PDX tumors and 3D-eCRC-PDX tissues.

Culturing CRC-PDX tumor-derived cells *in vitro* through the use of our 3D-eCRC-PDX tissues was found to be mutually beneficial to (1) the advancement of *in vitro* CRC-PDX tumor-derived cell culture and (2) the capacity of 3D engineered cancer tissue models to recapitulate patient tumors. Introducing the ability to culture PDX cells long-term (29 days) in an *in vitro* biomimetic environment that preserves native cell behavior overcoming 2D culture and *in vivo* testing limitations, whereas implementing a more pathophysiologically relevant cell source improves 3D engineered cancer tissue model recapitulation of patient tumors, thus overcoming limitations imposed by the use of cancer cell lines. The cell encapsulation and subsequent tissue formation were robust as no significant differences were observed between multiple batches of 3D-eCRC-PDX tissues prepared from separate CRC-PDX tumors. In conclusion, our novel *in vitro* CRC model exhibits high potential for the examination of CRC disease progression, elucidation of tumorigenic mechanisms, and therapeutic development to mitigate the impact of CRC.

Chapter 4: Engineered Colorectal Cancer Model Employing Patient-Derived Xenografts Mimics Patient-to-patient Tumor Variabilities

4.1 Introduction

Currently, colorectal cancer (CRC) is the third most common cancer and the third-highest cause of cancer-related deaths among both men and women in the United States (American Cancer Society 2019; Libutti et al. 2015; Schaeybroeck et al. 2014). To understand CRC biology and address relevant research questions, development of cancer models that better recapitulate the tumor heterogeneity is needed. Although significant insights of CRC have been achieved through the use of modeling, the majority of the current models have focused on the use of standard cell lines (Pradhan, Clary, et al. 2017; Rios de la Rosa et al. 2018; Dolznig et al. 2011; Hoshiba and Tanaka 2016; Magdeldin et al. 2014; Dainiak et al. 2008; Shakibaei et al. 2015; Nyga et al. 2013). As cell lines are typically compromised of one cell subpopulation and selectively isolated during establishment, they lack the extensive heterogeneity observed in patients' tumors (Cree, Glaysher, and Harvey 2010; Fernando et al. 2006).

To overcome this deficiency, the use of patient-derived cells in animals has first been utilized as patient-derived xenograft models. PDX models more accurately recapitulate the heterogeneity of patients' tumors as compared to standard cell lines (Cree, Glaysher, and Harvey 2010; Chou et al. 2013). In most cases, it has been shown that PDX tumor in immunocompromised mice maintains patient tumor molecular characteristics, gene expression, and mutations (Brown et al. 2016; Lee et al. 2014; Cho et al. 2014). Although these PDX models are a useful tool to examine tumor biology, the use of PDX models involved extensive animal handling, thereby resulting in a costly, time-consuming, and low throughput platform (Day, Merlino, and Van Dyke 2015; McIntyre et al. 2015; Murayama and Gotoh 2019). To address these limitations, several research

groups have attempted to culture PDX cells in in vitro 2D models (Okada, Vaeteewoottacharn, and Kariya 2019; Kodack et al. 2017). However, the culture of PDX cells in 2D monolayers results in substantial changes in the ratios of cell types present in the overall population, thereby resulting in a cancer cell *in vitro* model that no longer mimics the *in vivo* PDX cell subpopulations (Okada, Vaeteewoottacharn, and Kariya 2019; Kodack et al. 2017). Other groups utilized patient-derived cells in *in vitro* 3D CRC models (Kondo et al. 2019; Boehnke et al. 2016; Verissimo et al. 2016). In all of these studies, however, the resulting cancer models selectively incorporated only some of the cell types from the PDX or primary tumor. The inclusion of all cellular subpopulations is advantageous in recapitulating the parental tumor heterogeneity more fully.

Tissue engineering of CRC has the capacity to support tumor heterogeneity and more closely mimic patients' tumor as compared traditional 2D models by providing an architecture that better represent the native tumor microenvironment (Estrada et al. 2016; Szot et al. 2011; Bray et al. 2015; Kondo et al. 2019; Boehnke et al. 2016; Verissimo et al. 2016; E.L. Fong, Wan, et al. 2016; Pedron et al. 2019; Pedron, Hanselman, et al. 2017; Pedron, Polishetty, et al. 2017). The use of patient-derived cells in biomimetic materials such as hydrogels to create *in vitro* 3D tissue-engineered models has been proposed for several types of cancers, including prostate (E.L. Fong, Wan, et al. 2016) and glioblastoma tissues (Pedron et al. 2019; Pedron, Hanselman, et al. 2017; Pedron, Polishetty, et al. 2017). Fong et al. (E.L. Fong, Wan, et al. 2016) employed a hyaluronan-based hydrogel to engineer a 3D *in vitro* prostate cancer model of patient-derived xenograft (PDX). Pedron et al. (Pedron et al. 2019) utilized gelatin methacrylamide and hyaluronic acid methacrylate hydrogels for the culture of patient-derived glioblastoma cells. In these studies, the synergic use of 3D scaffolds and patient-derived cells has enhanced the recapitulation of the native tumor

microenvironmental cues. Yet, it is unclear whether tissue engineering is able to support patient-to-patient and/or cancer stage-to-stage tumor heterogeneity.

Experimental tests need to be carried out to assess whether tissue engineering platforms can support in vitro culture of PDX cells and recapitulate the key attributes of the originating PDX tumors. Prior to such experimental testing, it is essential to examine whether PDX tumor cells can maintain viability and grow in engineered tissues (E.L. Fong, Wan, et al. 2016; E.L. Fong et al. 2014; E.L.S. Fong et al. 2018). To validate an engineered cancer PDX model, the investigation of distinct cell subpopulation growth (E.L. Fong, Harrington, et al. 2016; Pedron et al. 2019; E.L. Fong, Wan, et al. 2016; E.L. Fong et al. 2014; E.L.S. Fong et al. 2018), stromal cell-matrix interaction (Alkasalias et al. 2018; Yuan et al. 2016; Bager et al. 2016; Marquez et al. 2006; Jin et al. 2015; Bell, Ivarsson, and Merrill 1979; Godbout et al. 2013; Marquez, Elson, and Genin 2010; Jansen et al. 2013; Hinz et al. 2001; Dolznig et al. 2011), mechanical stiffness (Pradhan, Hassani, et al. 2017; Schrader et al. 2011; J.S. Park et al. 2011; Swaminathan et al. 2011; Zaman et al. 2006; Kraning-Rush and Reinhart-King 2012; Chen, Pedron, and Harley 2017; Holt et al. 2017), gene expression, and molecular characteristics and transcriptomics (E.L.S. Fong et al. 2018; Guinney et al. 2015; Sachs and Clevers 2014) is of importance. Cell-matrix interactions can impact the cellular growth rate, and thus, changes in distinct cell subpopulations may arise as the cells respond to their environment (Riedl et al. 2017; Okada, Vaeteewoottacharn, and Kariya 2019; Kodack et al. 2017). Pedron et al. (Pedron et al. 2019) have quantified CD133+ (glioblastoma stem cell) and CD68+ (tumor-associated microglia/macrophage) subpopulations for patient-derived glioblastoma; however, investigation of changes in cell subpopulations of patient-derived and PDX tumor cells in engineered tissues has not been reported in the literature. The stiffness of tumor tissues has been demonstrated to have significant impacts on tumor cell phenotypes such as

proliferation, dormancy, migration, and metastasis. Therefore, stiffness is an important factor for cancer cell behavior (Pradhan, Hassani, et al. 2017; Schrader et al. 2011; J.S. Park et al. 2011; Swaminathan et al. 2011; Zaman et al. 2006; Kraning-Rush and Reinhart-King 2012; Chen, Pedron, and Harley 2017; Holt et al. 2017). Fong et al. (E.L.S. Fong et al. 2018) reported the mechanical stiffness for liver cancer PDX cells in macroporous hydrogels; however, no comparison of mechanical stiffness between engineered PDX tissue and the originating PDX tumors has been reported before. This research group also performed transcriptomic analysis for 3D liver cancer PDX tissues (E.L.S. Fong et al. 2018); however, there is a need to examine molecular characteristics and transcriptomics for 3D engineered CRC-PDX tissues. Besides, it is of great importance to separate these molecular characteristics and transcriptomics for mouse stromal cells and human cells in PDX tumor-based models.

To this end, we employed three PDX tumor lines, originated from stages II, III-B, and IV of CRC patients, in the PEG-Fb hydrogels to examine to which extent this biomimetic material is able to recapitulate the patient-to-patient and/or cancer stage-to-stage heterogeneity. We assessed the rates of change in CRC PDX cell colony sizes and cell numbers in 3D-eCRC-PDX tissues over time and compared them to the growth rates of the originating CRC-PDX tumors. To assess the ability of these 3D-eCRC-PDX tissues to maintain parental tumor cell subpopulations throughout the long-term culture, we monitored temporal variations in cell subpopulations in comparison to 2D-CRC-PDX cell cultures for all CRC-PDX lines. We also quantified the mechanical stiffness of the 3D-eCRC-PDX tissues and compared it to those of CRC-PDX tumors. Most notably, we found that 3D-eCRC-PDX tissues recapitulated the key attributes of the originating CRC-PDX tumors such as growth rates, cell subpopulation proportions, and mechanical stiffness, providing evidence

that these engineered tissues may be capable of mimicking patient-to-patient and/or cancer stage-to-stage variabilities.

4.2 Materials and Methods

4.2.1 Synthesis of PEGDA and PEG-Fb

Poly(ethylene glycol) diacrylate (PEGDA) was synthesized following previously established methods (Pradhan, Hassani, et al. 2017; DeLong, Gobin, and West 2005). The conjugation of fibrinogen to PEG was also carried out according to previously described methods (Almany and Seliktar 2005). The characterization of PEG-Fb was performed by evaluating PEGylation efficiency and the ability of PEG-Fb to photocrosslink and form 3D hydrogels (Dikovsky, Bianco-Peled, and Seliktar 2006).

4.2.2 Propagation of CRC PDX Cells in Mice

All experimental procedures were approved by the Auburn University Animal Care and Use Committee. Frozen stage II, III-B, and IV CRC adenocarcinoma PDX lines were kindly provided by BioConversant, LLC. Xenografts from frozen PDX cells were established and propagated in NOD.Cg-Prkdc^{scid} Il2rg^{tm1Wjl}/SzJ (NOD-SCID) mice (The Jackson Laboratory) according to the methods described in Chapter 3. Experiments discussed in this study were performed using CRC-PDX tumors that were propagated in the absence of Matrigel and were passaged 3-4 times in mice.

4.2.3 CRC-PDX Tumor Dissociation and Cell Isolation

Stage II, III-B, and IV CRC-PDX tumors were excised and dissociated according to the methods described in Appendix A. The PDX cells were isolated from each CRC-PDX tumor line for subsequent *in vitro* cultures as 2D-CRC-PDX cells and 3D-eCRC-PDX tissues.

4.2.4 Formation and Culture of 3D-eCRC-PDX Tissues

The isolated CRC-PDX cells from each CRC-PDX tumor line were encapsulated in PEG-Fb hydrogels to create the 3D-eCRC-PDX tissues according to the previously established methods (Appendix A). All 3D-eCRC-PDX tissues were maintained in culture for 29 days in a standard incubator with a temperature of 37 °C and 5% CO_2. The culture media were changed every 2-3 days. Media for all experiments was composed of DMEM (Lonza) containing 10% (v/v) fetal bovine serum (FBS) (Atlanta Biologicals™), 1% (v/v) penicillin:streptomycin solution (pen/strep) (HyClone™), and 2 mM glutagro™ Supplement (Corning).

4.2.5 2D-CRC-PDX Cell Culture

CRC cells isolated from each CRC-PDX tumor line were individually cultured in T-75 standard cell culture flasks according to the methods described in Appendix A. The 2D-CRC-PDX cells were passaged after 8 days of culture and subsequently passaged every 7 days up to a total of 29 days. All of the cultured cells were maintained in a standard incubator with a temperature of 37 °C and 5% CO_2, with media changes every 2-3 days. To investigate the cell growth curve or the increase in the total number of 2D-CRC-PDX cells over time, the CRC cells isolated from each CRC-PDX tumor line were also seeded into ten T-25 standard cell culture flasks according to

methods described in Appendix A, and one of which was used for cell counting every 24 hours (Days 1-11).

4.2.6 Image Acquisition and Morphological Analysis of Cell Colonies in 3D-eCRC-PDX Tissues and 2D-CRC Cultures

The 3D-eCRC-PDX tissues from each CRC-PDX tumor line were cultured *in vitro* over a 29-day period and imaged every 7 days. Phase-contrast images and Z-stacks of 3D-eCRC-PDX tissues were obtained. The area, major axis, minor axis, circularity, and aspect ratio of the tumor cell colonies were analyzed according to the methods described in Chapter 3. For 2D-CRC-PDX cells, phase-contrast images were obtained prior to cell passaging.

4.2.7 Cell Subpopulation Investigation by Flow Cytometry

To investigate the cell subpopulations using flow cytometry, the CRC-PDX tumors, 3D-eCRC-PDX tissues, and 2D-CRC-PDX cells from each CRC-PDX tumor line were dissociated to obtain single cells, and the numbers of viable cells were manually counted post-dissociation as described above. To identify human-derived cells, mouse-derived cells, CRC cells, and proliferating cells, the following antibodies were used, respectively: β-2-microglobulin (B2M) mouse IgG2a mAb (OriGene Technologies) conjugated to Zenon™ R-phycoerythrin (PE) mouse IgG2a (ThermoFisher Scientific), MHC Class I H-2 Db antibody (H2Db) mouse IgG2a mAb (OriGene Technologies) conjugated to the Zenon™ PE mouse IgG2a, cytokeratin 20 (CK20) rabbit IgG mAb (Cell Signaling Technology) conjugated to Zenon™ Alexa Fluor™ 647 rabbit IgG (ThermoFisher Scientific), and Ki-67 rabbit IgG pAb (abcam) conjugated to the Zenon™ Alexa Fluor™ 647 rabbit IgG. All staining procedures, including unstained cell, isotype, and dead

cells controls and cell subpopulation quantifications were performed according to the methods described in Appendix A.

4.2.8 Morphological Analysis of 3D-eCRC-PDX Tissues

To study whole-tissue morphological changes of 3D-eCRC-PDX tissues over time, images were obtained from a CellScale MicroSquisher system (side view of the tissues) and through phase-contrast microscopy (top view of the tissues) and used to quantify the volume (top and side views of the tissues), mean geometric diameter (top view of the tissues using Equation 2.2), circularity (side view of the tissues using Equation 2.3), and aspect ratio (side view of the tissues using Equation 2.4) of the 3D-eCRC-PDX tissues using ImageJ software. A minimum of 3 samples per time point per batch were analyzed.

4.2.9 Mechanical Stiffness

The mechanical stiffness of CRC-PDX tumors and 3D-eCRC-PDX tissues was evaluated using a CellScale MicroSquisher system and the associated SquisherJoy software according to the protocols described in Appendix A. For 3D-eCRC-PDX tissue samples, the mechanical stiffness was quantified on Days 1, 8, 15, 22, and 29 post-encapsulation. A minimum of three samples were measured per batch for each condition.

4.2.10 Statistical Analysis

GraphPad Prism 8.0 (GraphPad Software, San Diego, California USA, www.graphpad.com) was used for the following analysis. The outliers were removed using the ROUT method with coefficient Q = 1%. The normality of distribution and equality of variance

were then checked. Either one-way or two-way ANOVA followed by Tukey *post hoc* test was performed to determine statistical significance. The rates of change over time (slopes) were found and compared using linear regression analysis followed by an F-test to determine statistically significant differences. p value ≤ 0.05 was considered statistically significant unless otherwise stated.

4.3 Results

4.3.1 Viable Cell Numbers Isolated from Tumors Were PDX Line-dependent

We previously established a method to maintain cells from CRC-PDX cells in culture for one PDX line. Here, we expanded our methodology to incorporated two more patients. To isolate and encapsulate the cells from each CRC-PDX tumor line, the CRC-PDX tumors were dissociated using an optimized protocol (see Appendix A), and the number of viable cells was counted using trypan blue and hemocytometer. The numbers of viable cells isolated from CRC-PDX tumors were dependent on the PDX line (Figure D.1). Stage III-B CRC-PDX tumors yielded the highest cell number (35.9±5.3 million per gr tumor), followed by stage IV (27.1±5.3 million per gr tumor), and then stage II (15.2±1.7 million per gr tumor) ($p < 0.0208$).

4.3.2 Growth and Morphological Changes of Tumor Cell Colonies Were Both PDX Line- and Culture Platform-dependent

To assess the growth and temporal morphological changes of cancer cell colonies in the 3D-eCRC-PDX tissues and 2D-CRC-PDX cultures, phase-contrast Z-stacks and images were taken over 29 days of cell culture (Figure 4.1 A, B). For each CRC-PDX tumor line, three separate batches, each from separate tumors, were prepared and analyzed. The analyzed data from all three

batches were pooled for each CRC-PDX tumor line and are presented in Figure 4.1 (see Figure D.2, Figure D.3, and Figure D.4 for data from each batch). The data showed that the changes in area and diameter of cell colonies were both PDX line- and culture platform-dependent (Figure 4.1 C-J and Figure D.5). Within the 3D-eCRC-PDX, the area and diameter of both stage II and stage III-B CRC-PDX cell colonies increased significantly from Day 1 to Day 29 ($p < 0.0001$); however, the rates of increase in area and diameter of stage II cell colonies were approximately 60-fold and 16-fold higher than those of stage III-B cell colonies, respectively ($p < 0.0001$) (Figure 4.1 C, E and Figure D.5 A, B). Interestingly, these significantly higher increases in colony and diameter of cell colonies for stage II 3D-eCRC-PDX tissues were consistent with the *in vivo* growth rates of CRC-PDX tumors (Figure 4.1 C, E, Figure D.5 A, B and Figure D.6). On the other hand, the area and diameter of stage IV cell colonies increased significantly from Day 1 to Day 8 and decreased thereafter ($p < 0.0001$) (Figure 4.1 C, E and Figure D.5 A, B). For 2D-CRC-PDX cells, passaging was necessary after 8 days of *in vitro* culture as the increase in cell number was not observed thereafter (Figure D.7). In 2D-CRC-PDX cultures, the area and diameter of CRC-PDX cell colonies increased significantly from Day 1 to Day 8 for all CRC-PDX tumor lines ($p < 0.0001$); however, stage IV CRC-PDX cells demonstrated the largest colony area and diameter, followed by stage III-B, and then stage II ($p < 0.0001$) (Figure 4.1 D, F). Following cell passaging, although the colonies reformed in stage II 2D-CRC-PDX cultures over 29 days, they did not grow as large as those quantified on Day 8. In both stage III-B and stage IV 2D-CRC-PDX cultures, few colonies reformed after the first cell passaging (from Day 8 to Day 15), and no colonies reformed thereafter.

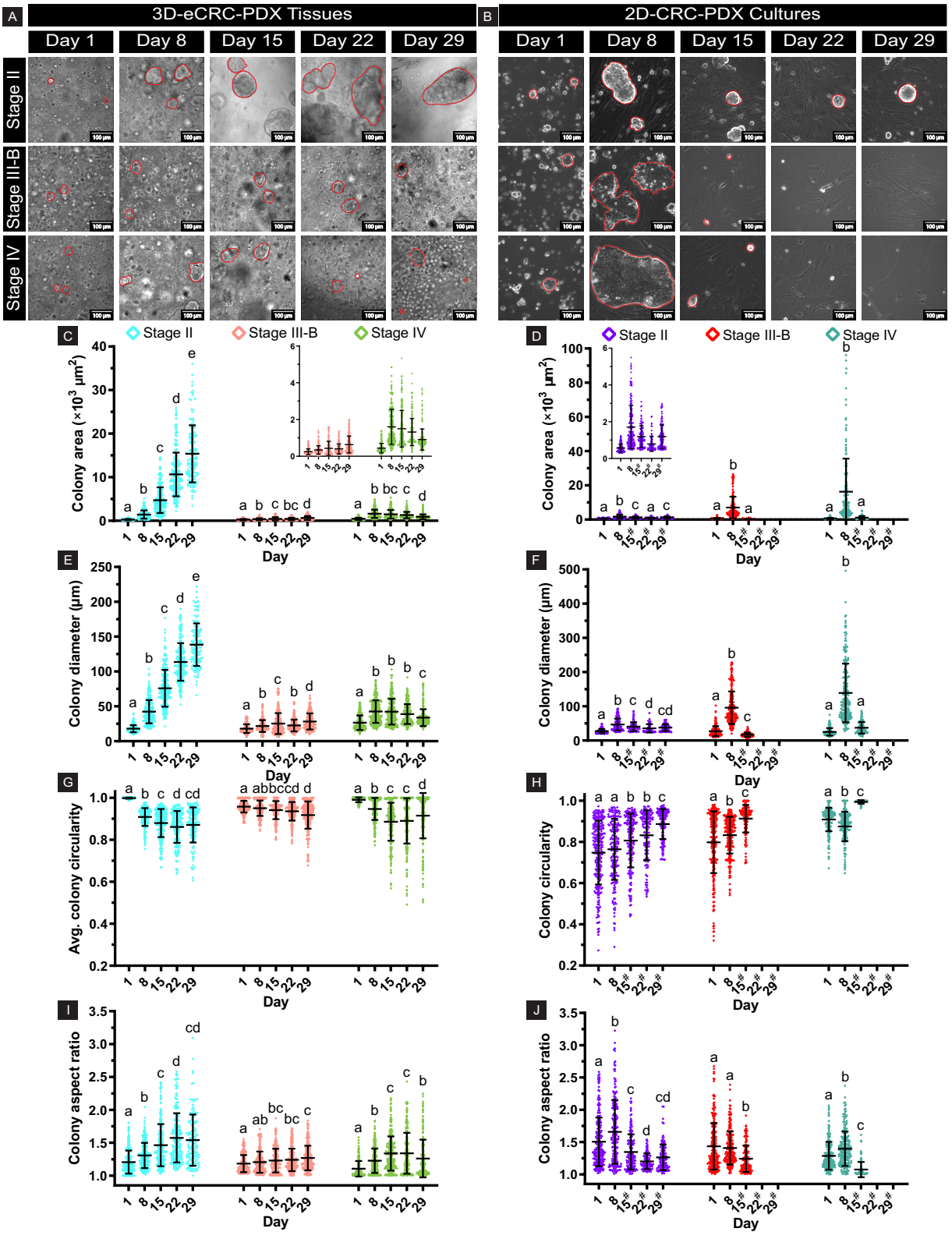

Figure 4.1. Growth and morphological changes of tumor cell colonies were both PDX line- and culture platform-dependent. Representative phase-contrast images of cell colonies

(outlined) in the (A) 3D-eCRC-PDX tissues and (B) 2D-CRC-PDX culture over 29 days for all CRC stages. Within 3D-eCRC-PDX tissues, the rates of increase in (C) area and (E) diameter of stage II CRC cell colonies of stage II CRC were significantly higher than those of stage III-B CRC cell colonies; the area and diameter of stage IV CRC cell colonies increased significantly from Day 1 to Day 8 and decreased thereafter. In 2D-CRC-PDX cultures, the (D) area and (F) diameter of cell colonies increased significantly from Day 1 to Day 8 for all CRC-PDX tumor lines; however, stage IV CRC cells demonstrated the largest colony area and diameter. Following cell passaging on Day 15, no colonies reformed in stage III-B and stage IV 2D-CRC-PDX cultures. Within the 3D-eCRC-PDX, the rates of decrease in (G) circularity and increase in (I) aspect ratio of stage II CRC cell colonies were significantly higher than those of stage III-B CRC cell colonies; the circularity of stage IV CRC cell colonies decreased, and aspect ratio increased significantly from Day 1 to Day 15 with opposite trends thereafter. In 2D CRC-PDX cultures, the (H) circularity increased and (J) aspect ratio decreased over time for both stage II and stage III-B CRC cell colonies, whereas the circularity of stage IV CRC cell colonies decreased and the aspect ratio increased from Day 1 to Day 8 with opposite trends from Day 8 to Day 15. Data are mean ± SD, and each data point represents one colony. At least 80 CRC cell colonies per CRC-PDX tumor line per time point per culture platform were examined for each of 3 separately prepared batches. Means that do not share a letter are significantly different (statistical significance was calculated between time points for a given PDX line). # indicates that the 2D-CRC-PDX cells were passaged at the previous time point.

Cell colony circularity and aspect ratio were also assessed over 29 days of culture. Within the 3D-eCRC-PDX, the circularity of both stage II and stage III-B CRC-PDX cell colonies

decreased and the aspect ratio of those increased significantly from Day 1 to Day 29 ($p < 0.0001$); however, the rates of change for stage II and stage III-B CRC-PDX cell colonies were significantly different ($p < 0.0001$) (Figure 4.1 G, I and Figure D.5 C, D). The rate of decrease in circularity and increase in aspect ratio of stage II cell colonies was approximately 2.4-fold and 3.9-fold higher than those of stage III-B cell colonies, respectively. On the other hand, the circularity of stage IV cell colonies decreased and aspect ratio increased significantly from Day 1 to Day 15 ($p < 0.0001$); after Day 15, the circularity increased and aspect ratio decreased ($p < 0.0045$) (Figure 4.1 G, I and Figure D.5 C, D). For 2D CRC-PDX cultures, stage II cell colonies showed significant increasing and decreasing trends for circularity and aspect ratio, respectively, from Day 1 to Day 29 ($p < 0.0001$) (Figure 4.1 H, J). Similar to stage II CRC-PDX tumor line, the stage III-B exhibited increasing and decreasing trends for circularity and aspect ratio, respectively, from Day 1 to Day 15 ($p < 0.0001$) (no colonies reformed after Day 15), whereas the circularity of stage IV cell colonies decreased and the aspect ratio increased from Day 1 to Day 8 ($p < 0.005$) with opposite trends from Day 8 to Day 15 ($p < 0.0001$).

Overall, both 3D-eCRC-PDX tissues and 2D-CRC-PDX cultures for all PDX lines showed similar growth patterns and morphological changes between three separate batches; thus, these models demonstrated a high degree of reproducibility. However, in sharp contrast to 2D-CRC-PDX cultures, 3D-eCRC-PDX tissues were able to mimic the *in vivo* CRC-PDX tumor growth rates.

4.3.3 3D-eCRC-PDX Tissues Better Maintained Cell Subpopulations as Compared to 2D-CRC-PDX Cultures

As PDX tumors contain both human-derived and mouse-derived cells, maintaining these cell subpopulations in *in vitro* cultures is vital for recapitulating the originating *in vivo* tumors. To assess the ability of both 3D-eCRC-PDX tissues and 2D-eCRC-PDX cultures to maintain different cell subpopulations of the originating CRC-PDX tumors in *in vitro* cultures over 29 days, flow cytometry was used. To prepare single cells for flow cytometry cell quantification, we first dissociated and counted the viable cells in both 3D-eCRC-PDX tissues and 2D-CRC-PDX cultures at each time point using trypan blue and a hemocytometer. The cell counts showed that the rates of change in viable cell number were different between 3D-eCRC-PDX tissues and 2D-CRC-PDX cultures and were dependent on each CRC-PDX tumor line (Figure 4.2 A, B). In 3D-eCRC-PDX tissues, the viable cell number increased significantly for all stages of CRC-PDX cells ($p < 0.05$); however, the rate of increase for stage II 3D-eCRC-PDX tissues was significantly higher than those for stage III-B and stage IV 3D-eCRC-PDX tissues (approximately 3.4-fold and 17.5-fold, respectively, $p < 0.0001$). Interestingly, these rates of increase in 3D-eCRC-PDX tissues were consistent with *in vivo* growth rates of the originating CRC-PDX tumors (Figure 4.2 A and Figure D.6). In sharp contrast, the rate of increase in viable cell number from Day 1 to Day 15 for stage III-B 2D-CRC-PDX cultures was significantly higher than those for stage II and stage IV (2.1-fold and 2.0-fold, respectively, $p < 0.0165$), with no significant difference between stage II and stage IV (Figure 4.2 B). The stage II 2D-CRC-PDX cell number continued to increase over 29 days, whereas the cell numbers in stage III-B and stage IV 2D-CRC-PDX cultures decreased from Day 15 to Day 29 due to cell death.

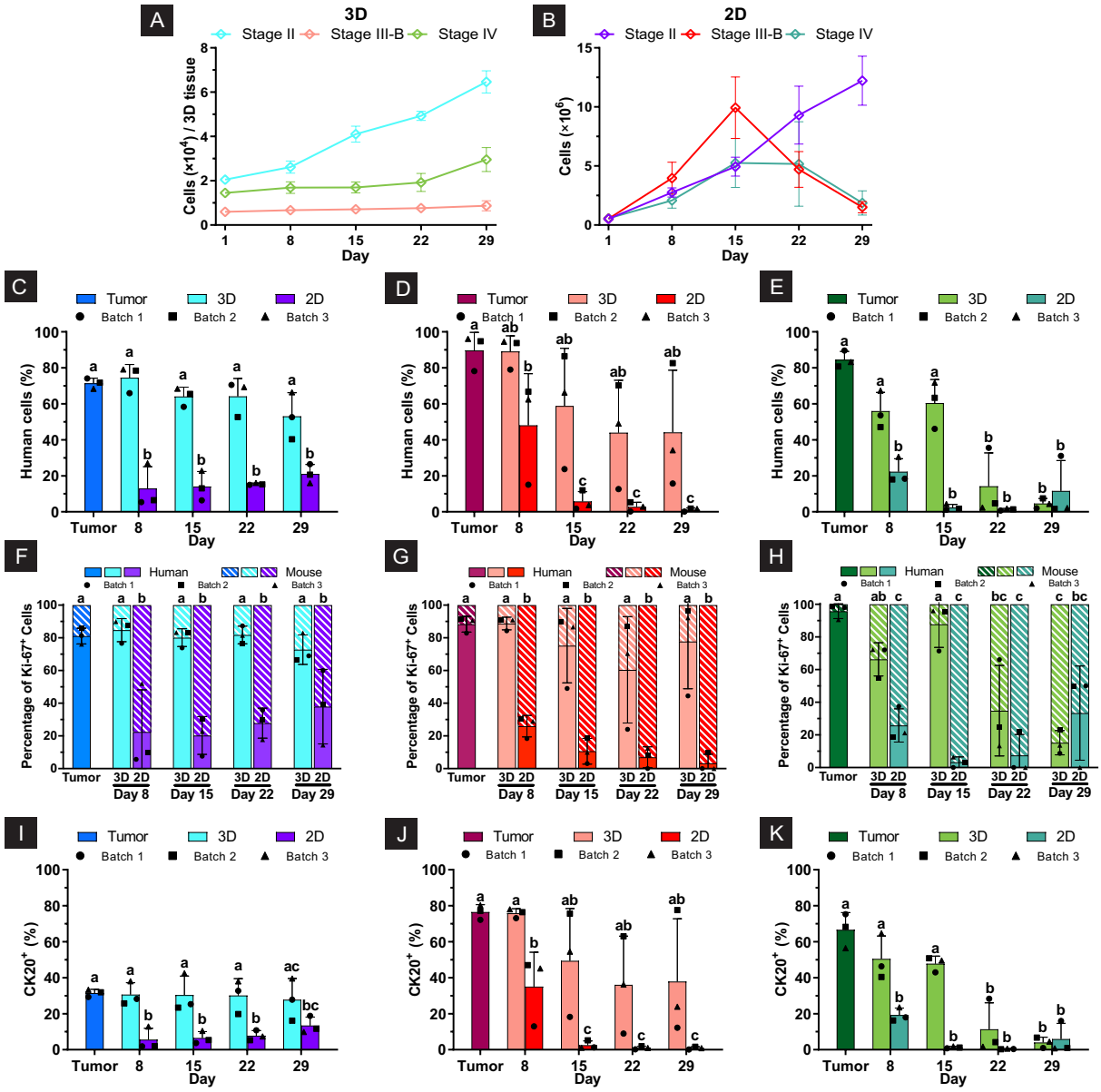

Figure 4.2. The 3D-eCRC-PDX tissues better maintained cell subpopulations as compared to 2D-eCRC-PDX cultures. (A) In 3D-eCRC-PDX tissues, the rate of increase in viable cell number for stage II 3D-eCRC-PDX tissues was significantly higher than those for stage III-B and stage IV 3D-eCRC-PDX tissues which were consistent with *in vivo* growth rates (Figure D.6). In sharp contrast, (B) for 2D-CRC-PDX cultures, the rate of increase in viable cell number from Day 1 to Day 15 was significantly higher for stage III-B as compared to those for stage II and stage with no significant difference between stage II and stage IV. The stage II 2D-CRC-PDX cell

number continued to increase over 29 days, whereas the cell numbers in stage III-B and stage IV 2D-CRC-PDX cultures decreased from Day 15 to Day 29 due to cell death. Approximately 71±3%, 90±10%, and 85±5% of all cells were human cells for (C) stage II, (D) stage III-B, and (E) stage IV CRC-PDX tumors, respectively. Interestingly, no significant difference was found between the percentages of human cell subpopulations in both stage II and III-B 3D-eCRC-PDX tissues at each time point and the originating CRC-PDX tumor cells. The stage IV 3D-eCRC-PDX tissues were able to maintain these cell subpopulations over 15 days of culture ($p > 0.0551$). In sharp contrast, in 2D-CRC-PDX cultures, the percentages of human cell subpopulations decreased significantly after 8 days of culture. Furthermore, both (F) stage II and (G) stage III-B 3D-eCRC-PDX tissues maintained proliferative human cell subpopulations over 29 days of culture; the (H) stage IV 3D-eCRC-PDX tissues could maintain this proliferative human cell subpopulation over 15 days. In sharp contrast, in 2D-CRC-PDX cells, a significant decrease in this cell subpopulation was found after 8 days of culture with the percentages remaining low thereafter. Similar trends to (C-E) human cell populations were also observed for the (I-K) CK20 marker. Data are mean ± SD. Means that do not share a letter are significantly different ($p \leq 0.05$, n = 3 separate batches of cell culture).

To quantify the percentage of human-derived cells (human cells) and mouse-derived cells (mouse cells), B2M and H2Db markers were used, respectively. The percentage of human cell subpopulation in CRC-PDX tumors was found to be PDX line-dependent. Approximately 71±3%, 90±10%, and 85±5% of all cells were human cells for stage II, stage III-B, and stage IV CRC-PDX tumors, respectively (Figure 4.2 C-E). Interestingly, the stage II and III-B 3D-eCRC-PDX tissues maintained these cell subpopulations over 29 days of culture; no significant difference was found between the percentages of human cell subpopulation in the 3D-eCRC-PDX tissues at each time point and the originating CRC-PDX tumor cells ($p > 0.0649$) (Figure 4.2 C, D). The stage IV

3D-eCRC-PDX tissues were able to maintain the human cell subpopulations over 15 days of culture ($p > 0.0551$); however, the human cell subpopulation decreased by over 60% on Days 22 and 29 as compared to the originating CRC-PDX tumors (Figure 4.2 E). In sharp contrast, in 2D-CRC-PDX cultures, the percentages of human cell subpopulations decreased significantly after 8 days of culture from 71±3% to 13±12% for stage II, from 90±10% to 48±29% for III-B, and 85±5% to 22±7% for stage IV ($p < 0.0001$) (Figure 4.2 C-E). In stage II and stage IV 2D-CRC-PDX cultures, these percentages remained constant after Day 8, whereas in III-B 2D-CRC-PDX cultures, the percentage of human cells decreased significantly from Day 8 to Day 15 (from 48±29% 6±5%, $p < 0.05$) and remained constant thereafter. It is important to note that whereas the 3D-eCRC-PDX tissues were maintained in continuous culture for 29 days, it was necessary to passage the 2D-CRC-PDX cells every 7 days starting on Day 8 to avoid cell confluence; data presented are prior to each passage for 2D-CRC-PDX cells.

To further investigate the reason why 3D-eCRC-PDX tissues better maintained human cell subpopulations than 2D-CRC-PDX cultures, we used Ki-67 as a proliferative marker in tandem with B2M or H2Db to identify human proliferative and mouse proliferative cell subpopulations. Although only 23±4% of cells in stage II CRC-PDX tumors were proliferative ($Ki\text{-}67^{+}$), 81±5% of these proliferative cells were human cells (Figure 4.2 F and Figure D.8 A). Notably, the stage II 3D-eCRC-PDX tissues maintained this proliferative human cell subpopulations over 29 days of culture, whereas in 2D-CRC-PDX cells, a significant decrease in this cell subpopulation was found after 8 days of culture (from 81±5% to 22±26%, $p = 0.0002$) with the percentages remaining low thereafter (Figure 4.2 F). Similar to stage II 3D-eCRC-PDX tissues, no significant difference was found between the percentages of proliferative human cell subpopulation in the stage III-B 3D-eCRC-PDX tissues and originating CRC-PDX tumors (88±5%, $p > 0.2571$), whereas stage III-B

2D-CRC-PDX cultures showed significantly lower percentages on all time points as compared to that for the originating CRC-PDX tumors ($p < 0.0013$) (Figure 4.2 G and Figure D.8 B). For stage IV CRC-PDX tumors, although only 6±2% of cells were proliferative, 95±4% of these proliferative cells were human cells (Figure 4.2 H and Figure D.8 C). The stage IV 3D-eCRC-PDX tissues maintained this proliferative human cell subpopulation over 15 days; however, a significant decrease in the percentages of this subpopulation was observed on Day 22 (from 95±4% to 35±28%, $p < 0.0008$) and Day 29 (from 95±4% to 15±7%, $p < 0.0001$) (Figure 4.2 H). Similar to stage II and stage III-B 2D-CRC-PDX cultures, the percentage of proliferative human cell subpopulation in stage IV 2D-CRC-PDX cultures decreased significantly after 8 days of culture (from 95±4% to 26±10%, $p < 0.0001$) and remained low thereafter (Figure 4.2 H).

To investigate the temporal changes in CRC cell subpopulations, cytokeratin 20 (CK20) was used in tandem with B2M or H2Db. In Chapter 3, we showed that not all CRC cells express CK20, and $CK20^-$ cells may include other CRC cell subpopulations. Stage II, stage III-B, and stage IV CRC-PDX tumors had 32±2%, 77±4%, and 67±10% $CK20^+$ cells, respectively (Figure 4.2 I-K). Both stage II and stage III-B 3D-eCRC-PDX tissues maintained this cell subpopulation over 29 days of culture (Figure 4.2 I, J), whereas stage IV 3D-eCRC-PDX tissues maintained it over 15 days of culture with a significant decrease on Day 22 (from 67±10% to 11±15%, $p < 0.0001$) and Day 29 (from 67±10% to 4±3%, $p < 0.0001$) (Figure 4.2 K). In sharp contrast, this cell subpopulation decreased significantly from Day 1 to Day 8 in all stages of 2D-eCRC-PDX cultures (from 32±2% to 6±6% for stage II, 77±4% to 35±19% for stage III-B, and 67±10% to 19±4% for Stage IV, $p < 0.05$) and remained low thereafter (Figure 4.2 I-K). These trends were also observed for the dual-labeled $B2M^+$ (or $H2Db^-$) and $CK20^-$ cell subpopulations (Figure D.8 D-F). In addition, as expected for all stages of CRC, the percentages of $CK20^+$ and human $CK20^+$

cell subpopulations were equivalent (Figure 4.2 I-K and Figure D.8 G-I), meaning that the $CK20^+$ cells were a subpopulation of the human cells while all mouse cells were $B2M^-$ (or $H2Db^+$) as well as $CK20^-$.

Overall, we found that the percentage of key cell subpopulations within the 3D-eCRC-PDX tissues were maintained over time with no significant changes over 29 days for both stage II and II-B and over 15 days for stage IV as compared to the originating CRC-PDX tumors. Conversely, 2D-CRC-PDX cells exhibited significant changes after 8 days of culture. For key cell subpopulations within the 3D-eCRC-PDX tissues, batch-to-batch variabilities were found to be higher for the stage III-B PDX line as compared to stage II and IV lines; thus, the stage II and IV 3D-eCRC-PDX tissues were more reproducible.

4.3.4 3D-eCRC-PDX Tissues Exhibited Cell-induced Contraction

Since tissue contraction plays an important role in ECM remodeling, mechanical stiffness, and cell phenotype, we investigated the changes in size and shapes of the 3D-eCRC-PDX tissues over 29 days for at least 2 separate batches of cell culture. The analyzed data from all batches were pooled for each CRC-PDX tumor line and are presented in Figure 4.3 (see Figure D.9 for data from each batch). It was found that for all stages of CRC, the volume, diameter, and aspect ratio (side view) of the 3D-eCRC-PDX tissues decreased, and circularity (side view) increased significantly from Day 1 to Day 29 ($p < 0.0001$); however, the rates of change were PDX line-dependent (Figure 4.3 B-E). For instance, the rates of decrease in volume, diameter, and aspect ratio of stage II 3D-eCRC-PDX tissues were significantly higher (approximately 50%, 35%, and 30% for volume, diameter, and aspect ratio, respectively, $p \leq 0.05$) than those of stage III-B and stage IV 3D-eCRC-PDX tissues (Figure 4.3 B, C, E); the rate of increase in circularity of stage II

3D-eCRC-PDX tissues was significantly higher (60%, $p < 0.0001$) than those of stage III-B and stage IV 3D-eCRC-PDX tissues (Figure 4.3 D). The rates of change in volume, diameter, circularity, and aspect ratio of stage III-B and stage IV 3D-eCRC-PDX tissues were equivalent ($p > 0.1971$) (Figure 4.3 B-E). The changes in circularity and aspect ratio of the 3D-eCRC-PDX tissues were consistent with the changes of tissues from the initial disk-like shape to a spherical shape (Figure 4.3 A).

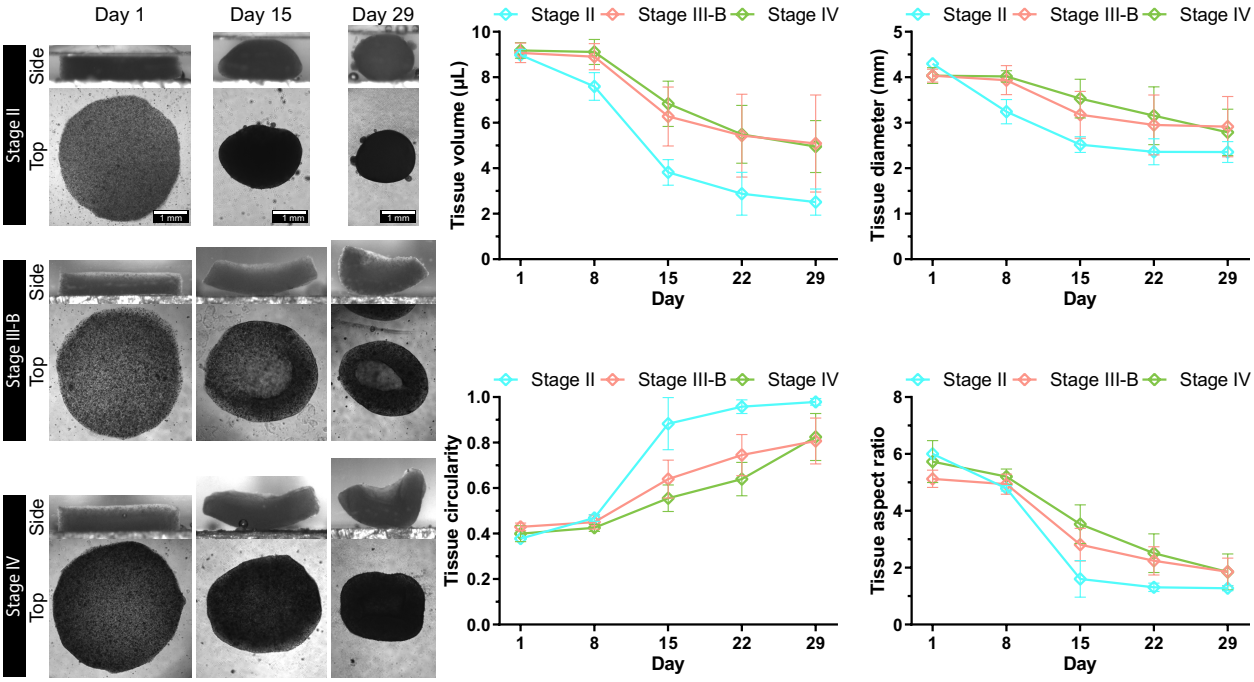

Figure 4.3. 3D-eCRC-PDX tissues exhibited cell-induced contraction. (A) Representative phase-contrast images of the 3D-eCRC-PDX tissues over 29 days for all CRC stages. The rates of decrease in (B) volume, (C) diameter, and (E) aspect ratio (side view) and increase in (D) circularity (side view) of stage II 3D-eCRC-PDX tissues were significantly higher than those of stage III-B and stage IV 3D-eCRC-PDX tissues. The rates of change in volume, diameter, circularity, and aspect ratio of stage III-B and stage IV 3D-eCRC-PDX tissues were equivalent. The decrease in volume, diameter, and aspect ratio and increase in circularity of the 3D-eCRC-

PDX tissues were associated with the morphological change from disk-like to a round shape. Data are mean ± SD ($p \leq 0.05$, n = a minimum of 6 tissues from at least 2 separate batches of cell culture).

4.3.5 3D-eCRC-PDX Tissues Mimicked the Mechanical Stiffness of CRC-PDX Tumors

To assess tissue mechanical stiffness, at least two separate CRC-PDX tumors and two paired batches of 3D-eCRC-PDX tissues for each CRC stage were subjected to parallel plate compression testing. For all CRC stages, CRC-PDX tumor stiffness was found to vary significantly depending on the geometric region of the tumor from which the sample was taken; the periphery of each CRC-PDX tumor showed the highest stiffness, followed by the midpoint, and then the core ($p < 0.05$) (Figure 4.4 A-C). The stiffness consistency among batches (tumors) of a given CRC stage was also found to be PDX line-dependent. Whereas the stiffness values of a given region were equivalent for batch 1 and batch 2 of stage II CRC-PDX tumors ($p = 0.9928$) (Figure 4.4 A), significant variations among batches were observed for both midpoint and periphery of both stage III-B and stage IVCRC-PDX tumors ($p < 0.0338$); no significant difference among batches was found for the core ($p > 0.8253$) (Figure 4.4 B, C). Furthermore, the average stiffness of all batches (pooled data of all batches) was found to be CRC stage-dependent. Although the average stiffness values for the core were equivalent for all CRC stages (0.49±0.08, 0.46±0.06, and 0.41±0.07 kPa for stage II, III-B, and IV, respectively, $p > 0.8849$), the periphery of stage II CRC-PDX tumors had the highest stiffness (2.95±0.55 kPa), followed by those of stage III-B (1.94±0.54 kPa), and then stage IV (1.24±0.27 kPa) ($p < 0.0001$) (Figure D.10 A).

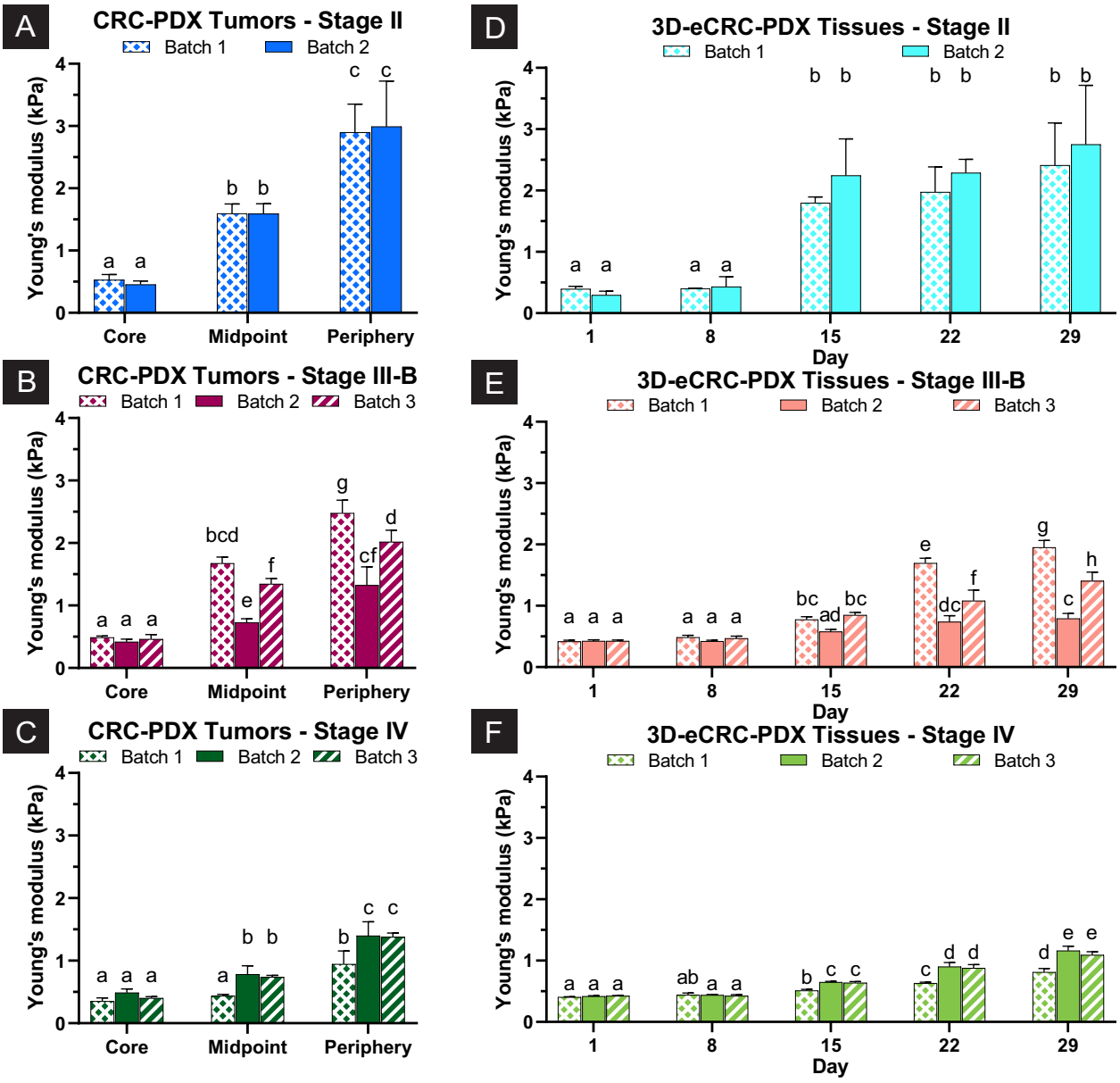

Figure 4.4. The 3D-eCRC-PDX tissues mimicked the mechanical stiffness of CRC-PDX tumors. (A-C) For all CRC stages, CRC-PDX tumor stiffness varied regionally with an increasing trend from the core to the periphery. Whereas the stiffness values of a given region were equivalent for batch 1 and batch 2 of (A) stage II CRC-PDX tumors, significant variations among batches were observed for both midpoint and periphery of both (B) stage III-B and (C) stage IVCRC-PDX tumors; no significant difference among batches was found for the core. (D-F) The stiffness of 3D-eCRC-PDX tissues increased significantly over time for all CRC stages. Interestingly, the time-

dependent stiffness of the 3D-eCRC-PDX tissues mimicked both region-dependent and batch-dependent stiffness of the originating CRC-PDX tumors for a given CRC stage (D vs. A, E vs. B, and F vs. C). Bar =mean ± SD. Means that do not share a letter are significantly different ($p \leq 0.05$, n = 3 tissues per region or time point per batch).

The stiffness of 3D-eCRC-PDX tissues increased significantly over time ($p < 0.0001$) for all CRC stages (Figure 4.4 D-F). Remarkably, the time-dependent stiffness of the 3D-eCRC-PDX tissues mimicked both region-dependent and batch-dependent stiffness of the originating CRC-PDX tumors for a given CRC stage (Figure 4.4 D vs. A, E vs. B, and F vs. C). In addition, the average stiffness of all batches of 3D-eCRC-PDX tissues mimicked the stage-dependent average stiffness of the CRC-PDX tumors (Figure D.10 B vs. A). Whereas the average stiffness values for 3D-eCRC-PDX tissues on Day 1 were equivalent for all CRC stages (0.35±0.07, 0.42±0.02, and 0.42±0.01 kPa for stage II, III-B, and IV, respectively, $p > 0.8681$), on Day 29, stage II CRC-PDX tumors showed the highest stiffness (2.58±0.78 kPa), followed by stage III-B (1.38±0.51 kPa), and then stage IV (1.02±0.17 kPa) ($p < 0.0258$) (Figure D.10 B).

4.4 Discussion

To understand tumor biology and investigate the mechanism of the disease, preclinical cancer models that mimic patients' tumors with high physiological relevance are needed. PDX tumors have shown high clinical translatability (Cree, Glaysher, and Harvey 2010; Chou et al. 2013; Brown et al. 2016; Lee et al. 2014; Cho et al. 2014); however, the use of PDX tumors, as an animal model, is typically time-consuming, labor-intensive, and low throughput (Day, Merlino, and Van Dyke 2015; McIntyre et al. 2015; Murayama and Gotoh 2019). The creation of 2D cancer

models using PDX tumor cells typically results in a faster growth rate of mouse-derived cells as compared to human-derived cells and, subsequently, a model that no longer mimics the originating PDX tumors (Okada, Vaeteewoottacharn, and Kariya 2019; Kodack et al. 2017). To overcome these challenges, a few groups have employed PDX tumor cells in 3D *in vitro* models (Boehnke et al. 2016; Verissimo et al. 2016). However, the models developed in these studies did not include all cell types from the PDX tumors—only one or some types of PDX cells were maintained in the resultant 3D culture. We previously showed that a 3D tissue-engineered tumor model based on PEG-Fb hydrogels was able to encapsulate and maintain all cell types from a stage II CRC-PDX tumor line; the model was also able to recapitulate the key attribute of the originating CRC-PDX tumors (see Chapter 3).

Here, we sought to use CRC-PDX cells from two other patients, a stage III-B and stage IV CRC adenocarcinoma, in our previously developed tissue-engineered model and investigate the ability of our model to recapitulate the patient-to-patient PDX tumor variabilities in comparison to their 2D cultured cell counterparts. We demonstrated that CRC-PDX cell colony sizes and cell numbers in 3D-eCRC-PDX tissues increased over time with similar growth rates of the originating CRC-PDX tumors, whereas 2D-CRC-PDX cultures did not. These 3D-eCRC-PDX tissues much better maintained cell subpopulations of the originating CRC-PDX tumors throughout long-term culture in comparison to 2D-CRC-PDX cell cultures. In addition, the mechanical stiffness of the 3D-eCRC-PDX tissues mimicked those of CRC-PDX tumors.

Cell-cell and cell-matrix interactions play a vital role in cell growth and proliferation and can affect changes in distinct cell subpopulations (Riedl et al. 2017; Okada, Vaeteewoottacharn, and Kariya 2019; Kodack et al. 2017). To mimic the cell-cell and cell-matrix interactions of a PDX tumor in an in vitro model, all cell types from that originating PDX should be incorporated in the

in vitro tumor microenvironment. A few studies have reported the culture of PDX cells *in vitro* in a 3D matrix; however, these models did not include all cell types of the PDX cell population (E.L. Fong et al. 2014; E.L. Fong, Wan, et al. 2016). Therefore, here we examined changes in distinct cell subpopulations using markers and investigated patient-to-patient tumor cell composition variabilities. Notably, we showed that the 3D-eCRC-PDX tissues maintained the key cell subpopulations of the originating stage II and stage III-B CRC-PDX tumors in long-term culture; these cell subpopulations were also maintained this stage IV 3D-eCRC-PDX tissues over at least 15 days of culture. This maintenance of distinct cell subpopulations occurred simultaneously with an increase in the total cell number in all stages of 3D-eCRC-PDX tissues. In sharp contrast, significant changes in all cell subpopulations occurred in 2D-CRC-PDX cultures. Kodack et al. (Kodack et al. 2017) also reported a similar observation for 2D cultures of primary patient-derived tumors; they show that the stromal cells outgrew the cancer cells in 2D cultures, thereby impeding the cancer cell growth and resulting in the failure of cell line generation. In brief, our results demonstrated that the 3D-eCRC-PDX tissues for all stages mimicked the cell subpopulations of the originating CRC-PDX tumors.

The stiffness of tumor tissues has been demonstrated to have significant impacts on tumor cell phenotypes such as proliferation, dormancy, migration, and metastasis. Therefore, stiffness is an important factor for cancer cell behavior (Pradhan, Hassani, et al. 2017; Schrader et al. 2011; J.S. Park et al. 2011; Swaminathan et al. 2011; Zaman et al. 2006; Kraning-Rush and Reinhart-King 2012; Chen, Pedron, and Harley 2017; Holt et al. 2017). Although previous studies have not shown a comparison between in vivo and in vitro tissue stiffness, the stiffness of CRC tumors from patients is reported in the literature. For CRC samples directly taken from patients, tumor stiffness correlates to a higher stage, as well as metastatic phenotypes (Kawano et al. 2015). The bulk elastic

modulus ranges of 1.91-3.96 kPa (median = 2.81 kPa), 1.08-12.2 kPa (median = 3.49 kPa), 2.60-43.2 (median = 8.89 kPa), and 5.58-68.0 kPa (median = 13.8 kPa) were observed for CRC of stages of I, II, III, and IV, respectively. However, both our CRC-PDX tumors and 3D-eCRC-PDX tissues demonstrated a reciprocal correlation between tissue stiffness and tumor stages. Possible reasons for this discrepancy between our result and those reported in literature could be the following: 1) the numbers of patients were small in both our studies and those in the literature; 2) the method of stiffness measurement used in the literature was not optimized; and 3) our PDX tumors were propagated subcutaneously whereas the literature reports the stiffness of the tumors taken directly from patients. Nonetheless, in our models, the average stiffness of all batches of 3D-eCRC-PDX tissues mimicked the stage-dependent average stiffness of the CRC-PDX tumors. Besides, the stiffness of our PDX tumors is in the same order of magnitude as those reported in the literature.

Although we demonstrated the ability of the 3D-eCRC-PDX tissues to mimic tumor-to-tumor variabilities, the current study had limitations. Our efforts in this study were focused on the engineered CRC-PDX tissue model development and generation of a robust model to mimic PDX tumor variabilities with high batch-to-batch reproducibility. Although employing CRC tumors taken directly from patients in 3D engineered tissues could lead to better tumor recapitulation, this approach could potentially result in high batch-to-batch variabilities, given the high level of heterogeneity between patient tumors. Future work could directly utilize CRC patient tumor cells in 3D engineered tumor tissues to model reproducibility. Moreover, our *in vitro* 3D model could be employed to examine the support of PDX or patient cells from other types of cancer.

4.5 Conclusion

In this study, we employed three PDX tumor lines, originated from stages II, III-B, and IV of CRC patients, in the PEG-Fb hydrogels to examine to which extent this biomimetic material is able to recapitulate key attributes of the originating CRC-PDX tumors. For all CRC stages, we demonstrated that the rates of change in CRC PDX cell colony sizes and cell numbers in 3D-eCRC-PDX tissues over time mimicked the growth rates of the originating CRC-PDX tumors. We monitored temporal variations in cell subpopulations of the 3D-eCRC-PDX tissues in comparison to 2D-CRC-PDX cell cultures. In sharp contrast to 2D-CRC-PDX cultures, the 3D-eCRC-PDX tissues were able to maintain all cell subpopulations of the originating CRC-PDX tumors for all CRC stages. Furthermore, the time-dependent stiffness of the 3D-eCRC-PDX tissues mimicked both region-dependent and batch-dependent stiffness of the originating CRC-PDX tumors for a given CRC stage. In addition, the average stiffness of all batches of 3D-eCRC-PDX tissues mimicked the stage-dependent average stiffness of the CRC-PDX tumors. The ability of these 3D-eCRC-PDX tissues to recapitulate the key attributes of the originating CRC-PDX tumors provides evidence that these engineered tissues are capable of mimicking patient-to-patient and/or cancer stage-to-stage variabilities. In the future, this model can be extended to include other types of cancer for investigation of the disease mechanism and drug testing application.

Chapter 5: Rapid Generation of Colorectal Cancer Tissue-Engineered Microspheres Based on Patient-derived Xenograft Tumor Cells

5.1 Introduction

Despite the tremendous efforts to develop new strategies for cancer detection and treatment, colorectal cancer (CRC) is still the third most common cancer among both men and women in the United States (American Cancer Society 2019; Libutti et al. 2015; Schaeybroeck et al. 2014). A large number of preclinically approved anti-cancer drug candidates fail to pass both clinical efficacy and safety tests in the human body (Wong, Siah, and Lo 2019). Resulting in the loss of hundreds of millions of dollars, this poor translatability is partially due to patient-to-patient variability in response to therapeutics and the inaccuracy of preclinical CRC models to recapitulate the key attributes of the patient's tumor (Rodenhizer et al. 2018; Larson 2015; Mazzoleni, Di Lorenzo, and Steimberg 2009). Therefore, enhanced CRC models that better mimic the complexity of tumor from each patient is needed.

CRC are heterogeneous neoplastic tissues composed of distinct cell types such as tumor cells, cancer stem cells, cancer-associated fibroblasts, and other stromal cells in an extensive macromolecule network called extracellular matrix (ECM) (P. R. Prasetyanti and Medema 2017; Easwaran, Tsai, and Baylin 2014; Nagle 2004). The CRC intratumoral cell-cell and cell-ECM interactions have a great impact on cellular behaviors such as dissemination, invasion, migration, and metastatic and can determine the tumor fates (Quail and Joyce 2013; Nguyen, Bos, and Massague 2009; Kraning-Rush et al. 2013; Kraning-Rush and Reinhart-King 2012; Balzer et al. 2012; Paul, Mistriotis, and Konstantopoulos 2017; D.H. Kim et al. 2018; J. Park et al. 2016). Thus, the generation of preclinical CRC models that more accurately recapitulate the tumor microenvironment requires the incorporation of all cell types from the patient tumor.

Patient-derived xenografts (PDXs) have demonstrated high potential in clinical translatability and are able to more accurately recapitulate the key attributes of patients' tumors such as gene expression, molecular characteristics, and cancer cell mutation(Cree, Glaysher, and Harvey 2010; Chou et al. 2013; Brown et al. 2016; Lee et al. 2014; Cho et al. 2014). These physiologically relevant pre-clinical PDX tumor models are useful platforms to understand tumor biology and for identifying anti-cancer therapeutics (Cree, Glaysher, and Harvey 2010). However, as an animal model, the use of PDX tumor models requires special facilities and typically is associated with a high cost of care (Day, Merlino, and Van Dyke 2015; McIntyre et al. 2015; Murayama and Gotoh 2019). Furthermore, experimental assays are usually low throughput in animals, thereby resulting in hurdles in anti-cancer drug development (Day, Merlino, and Van Dyke 2015; McIntyre et al. 2015; Murayama and Gotoh 2019).

Several studies have utilized PDX cells, including CRC PDX cells, in *in vitro* platforms to overcome challenges associated with animal models. Kondo et al. (Kondo et al. 2019) isolated CRC PDX cells and produced self-aggregated clusters of pure cancer cells to screen over 2400 drugs. Other studies also reported the generation of high-throughput cancer models from patient-derived or PDX cells for understanding tumor biology and drug screening (Boehnke et al. 2016; Verissimo et al. 2016). However, the models developed in these studies were matrix-free in the initial tissue formation and selectively incorporated only some of the cell types from the PDX or primary tumor. To address these shortcomings, other studies employed tissue engineering techniques for prostate and glioblastoma tissues (E.L. Fong, Wan, et al. 2016; Pedron et al. 2019; Pedron, Hanselman, et al. 2017; Pedron, Polishetty, et al. 2017) to create *in vitro* platforms that provide an ECM for patient-derived cells. Although promising, these platforms were low-throughput and typically time-consuming, thereby hindering their use in high-throughput studies.

Thus, faster systems that can create a large number of engineered tissues for high-throughput studies are needed.

Based on this need, we have developed a microfluidic platform to rapidly generate a large number of uniform microspheres composed of a biomimetic material, poly(ethylene glycol)-fibrinogen (PEG-Fb), as an ECM for CRC Cells. First, we examined the ability of our microspheres to support the culture of HT-29 CRC cell line. Next, we generated microspheres using the CRC-PDX cells from a stage II patient and assessed the ability of the model to support the maintenance and expansion of mixed CRC-PDX tumor cell subpopulations. Interestingly, we demonstrated the ability of our microfluidic platform to generate a large number of microspheres that not only support the growth of the CRC-PDX cells but also mimic the originating CRC-PDX tumor in terms of cell subpopulation proportions. These CRC-PDX microspheres incorporate all the cells from the originating tumor and have a high potential for future use in high-throughput drug screening.

5.2 Materials and Methods

5.2.1 Synthesis of PEGDA and PEG-Fb

Following previously established methods (Pradhan, Hassani, et al. 2017; DeLong, Gobin, and West 2005; Almany and Seliktar 2005), poly(ethylene glycol) diacrylate (PEGDA) was first synthesized and then conjugated to fibrinogen to produce PEG-Fb. To characterize PEG-Fb, we quantified PEGylation efficiency and examined the ability of PEG-Fb to photocrosslink and form 3D hydrogels (Dikovsky, Bianco-Peled, and Seliktar 2006).

5.2.2 HT-29 CRC Cell Culture and Maintenance

HT-29 CRC cells were purchased from the American Type Culture Collection (Manassas, VA). The cells were cultured and passaged in T-25 tissue culture flasks using the media composed of McCoy's 5A Modified Medium, 10% (v/v) fetal bovine serum (FBS) (Atlanta Biologicals™), 1% (v/v) penicillin-streptomycin (pen/strep) (HyClone™). All cultured cells (2D-CRC cells) were maintained in a standard incubator with a temperature of 37 °C and 5% CO_2. The cell culture media was changed every 2 days.

5.2.3 Propagation of CRC PDX Cells in Mice

All experimental protocols involved animals were pre-approved by the Auburn University Animal Care and Use Committee. Frozen adenocarcinoma PDX line established from a stage II white female patient pre-treatment was kindly provided by BioConversant, LLC. We utilized NOD.Cg-Prkdc^{scid} Il2rg^{tm1Wjl}/SzJ (NOD-SCID) mice (The Jackson Laboratory) to established and propagate xenografts from frozen PDX cells according to methods described in Chapter 3. All CRC-PDX tumors utilized in subsequent experiments were propagated in the absence of Matrigel and were passaged 3-4 times in NOD-SCID mice.

5.2.4 CRC-PDX Tumor Dissociation and Cell Isolation

Excision and dissociation of the Stage II CRC-PDX tumors were carried out according to the previously described methods (Appendix A). Following dissociation, the cells were isolated from the CRC-PDX tumors and employed for subsequent *in vitro* cultures as 2D-CRC-PDX cells and 3D-eCRC-PDX microspheres.

5.2.5 Production of Microspheres Using Microfluidic Platform

A custom-made microfluidic platform was employed to generate HT-29 and 3D-eCRC-PDX microspheres. The microfluid platform composed of a PDMS microfluidic device, syringe pumps, and a light source was set up according to the previously published description (Tian and Lipke 2020). Briefly, a PDMS microfluidic device with a T-junction pattern was created using the SYLGARD® 184 Silicone Elastomer Kit (Dow Corning) and molding techniques. To create the microspheres, either HT29 CRC cells or isolated CRC PDX cells were mixed with a polymer precursor solution containing poly(ethylene glycol)-fibrinogen (PEG-Fb) with a final concentration of 1.5% (v/v) triethanolamine (TEOA) (Acros Organics), 37 mM 1-vinyl-2-pyrrolidinone (NVP) (Sigma-Aldrich), and 0.1 mM Eosin Y in PBS at a density of 20×10^6 cells/mL. The syringe pumps were used to drive the cell-laden precursor solution into one of the microfluidic device inlets and mineral oil into the other inlet. The microspheres were formed at the T-junction, photocrosslinked in the outlet channel using a 2.7W visible light source (Prior Lumen 200), and collected at the end of the outlet channel using cell culture media. The collected microspheres were centrifuged to remove the mineral oil and consumed media and resuspend in fresh culture media. The HT-29 microspheres were cultured in McCoy's 5A Modified Medium containing 10% (v/v) FBS and 1% (v/v) pen/strep. The 3D-eCRC-PDX microspheres were cultured in DMEM (Lonza) containing 10% (v/v) FBS, 1% (v/v) pen/strep, and 2 mM glutagro™ Supplement (Corning). All microspheres were maintained in culture for 29 days in a standard incubator with a temperature of 37 °C and 5% CO_2. The culture media were changed every 2-3 days.

5.2.6 2D-CRC-PDX Cell Culture

The isolated CRC-PDX cells were also cultured in T-75 standard cell culture flasks to create 2D-CRC-PDX cell cultures according to the method described in Appendix A. The 2D-CRC-PDX cells were passaged after 8 days of culture and subsequently passaged every 7 days up to a total of 29 days. All 2D-CRC-PDX cells were maintained in the same culture media and incubator used to culture 3D-eCRC-PDX microspheres. Similar to 3D-eCRC-PDX microspheres, the media were changed every 2-3 days for 2D-CRC-PDX cells.

5.2.7 Cell Viability Assay and Image Acquisition and Analysis

To assess the ability of PEG-Fb-based microspheres in maintaining the CRC cells viable post-encapsulation, cell viability assay for HT-29 microspheres was performed using LIVE/DEAD® Viability/Cytotoxicity Kit (ThermoFisher Scientific) and according to previously described methods Appendix A. The fluorescently labeled CRC cells were imaged using an inverted Nikon Eclipse Ti microscope equipped with an Andor Luca S camera and a fluorescence light source. Image processing and viability quantification were carried out according to the methods described in Appendix A. At least three microspheres per time point were used for quantification.

5.2.8 Image Acquisition and Morphological Analysis of Cell Colonies in HT-29 and 3D-eCRC-PDX Microspheres

The HT-29 and 3D-eCRC-PDX microspheres were cultured *in vitro* over a 29-day period and imaged every 7 days. Phase-contrast and confocal images and Z-stacks of microspheres were employed to quantify the area, major axis, minor axis, circularity, and aspect ratio of the tumor

cell colonies according to the previously described methods (Chapter 3). The diameter of the cell colonies was calculated based on Equation 2.2.

5.2.9 Cell Subpopulation Investigation by Flow Cytometry

To quantify the temporal changes in cell subpopulations of PDX cells, flow cytometry was used. The CRC-PDX tumors, 3D-eCRC-PDX microspheres, and 2D-CRC-PDX cells were dissociated to obtain single cells. The numbers of viable cells were manually counted post-dissociation using trypan blue dead cell exclusion and a hemocytometer. To identify human-derived cells, CRC cells, and proliferating cells, the following antibodies were used, respectively: β-2-microglobulin (B2M) mouse IgG2a mAb (OriGene Technologies) conjugated to Zenon™ R-phycoerythrin (PE) mouse IgG2a (ThermoFisher Scientific), cytokeratin 20 (CK20) rabbit IgG mAb (Cell Signaling Technology) conjugated to Zenon™ Alexa Fluor™ 647 rabbit IgG (ThermoFisher Scientific), and Ki-67 rabbit IgG pAb (abcam) conjugated to the Zenon™ Alexa Fluor™ 647 rabbit IgG. All experimental procedures for flow cytometry, including unstained cell, isotype, and dead cell controls and cell subpopulation quantifications, were performed according to the previously described methods (Appendix A).

5.2.10 Morphological Study of Cells by Staining

To study the cellular morphology, HT-29 microspheres were labeled with the primary and secondary antibodies combinations; Ki-67 rabbit IgG pAb with Alexa Fluor 488 anti-rabbit IgG secondary antibody (ThermoFisher Scientific cat. # A11008), CD44 mouse IgG2a mAb with Alexa Fluor 568 anti-mouse IgG secondary antibody (ThermoFisher Scientific cat. # A11004), and CK20 rabbit IgG mAb with Alexa Fluor 488 anti-rabbit IgG secondary antibody. Hoechst

33342 was used to counterstain the cell nuclei. The staining and imaging were performed according to the previously described methods (Appendix A).

5.2.11 Analysis of Changes in Size and Shape of Microspheres

To investigate the changes in HT-29 microspheres over time, images were obtained through phase-contrast microscopy and used to quantify the volume, diameter, circularity (Equation 2.3), and aspect ratio (Equation 2.4) of the HT-29 microspheres using ImageJ software. A minimum of 3 samples per time point per batch were analyzed.

5.2.12 Statistical Analysis

Hierarchical cluster analysis was carried out using *heatmap.plus* package in RStudio (Version 1.2.1335). GraphPad Prism 8.0 (GraphPad Software, San Diego, California USA, www.graphpad.com) was used for the following analysis. The outliers were removed using the ROUT method with coefficient Q = 1%. The normality of distribution and equality of variance were then checked. Either one-way ANOVA followed by Tukey *post hoc* test was performed to determine statistical significance. p value ≤ 0.05 was considered statistically significant unless otherwise stated.

5.3 Results

5.3.1 HT-29 Cells Remained Viable in Microspheres

HT-29 CRC cells were encapsulated in microspheres using a custom-designed microfluidic platform. A representative phase-contrast image of HT-29 microspheres is shown in Figure 5.1 A. To examine whether HT-29 CRC cells maintain their viability post-encapsulation and over long-

term culture, a viability assay was performed. Approximately 98±1% of HT-29 cells were viable in microspheres post-encapsulation (Day 1) (Figure 5.1 B, C). There was a 6±1% decrease in HT-29 cell viability from Day 1 to Day 29 ($p < 0.0001$); however, the viability was over 90% at all time points (Figure 5.1 C). Thus, HT-29 cells maintained their viability in microspheres in long-term culture.

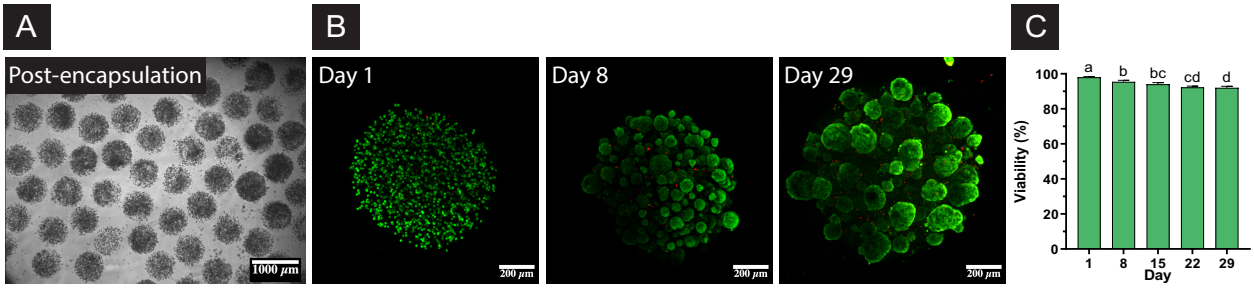

Figure 5.1. HT-29 cells remained viable in microspheres. (A) A representative phase-contrast image of HT-29 microspheres with uniform size and shape. (B) Representative confocal images of live (green) and dead (red) HT-29 cells in microspheres on Days 1, 8, and 29. (C) HT-29 cells maintained their viability post-encapsulation and in long-term culture as the viability was over 90% on all time points. Bar = mean ± SD. Means that do not share a letter are significantly different ($p \leq 0.05$; n = 3 tissues).

5.3.2 HT-29 Cell Colonies Grew in Microspheres

To assess the growth and morphological changes of HT-29 CRC cell colonies in the microspheres, Z-stack images were taken and analyzed over time (Figure 5.2 A). Both cell colony area and diameter of HT-29 cells in microspheres increased significantly over time ($p < 0.0001$)—from Day 1 to Day 29, the colony area and diameter increased from approximately 160±38 to 21117±16535 μm^2 and 14±2 to 154±72 μm, respectively (Figure 5.2 B). Colony circularity

exhibited an approximately 5% significant decrease ($p < 0.0001$) from Day 1 to Day 8 and remained relatively constant thereafter (Figure 5.2 B). The colony aspect ratio showed an approximately 6% significant increase ($p < 0.0001$) from Day 1 to Day 8 and remained relatively constant thereafter (Figure 5.2 B). The colony protrusiveness did not change significantly over 29 days of culture (Figure 5.2 B).

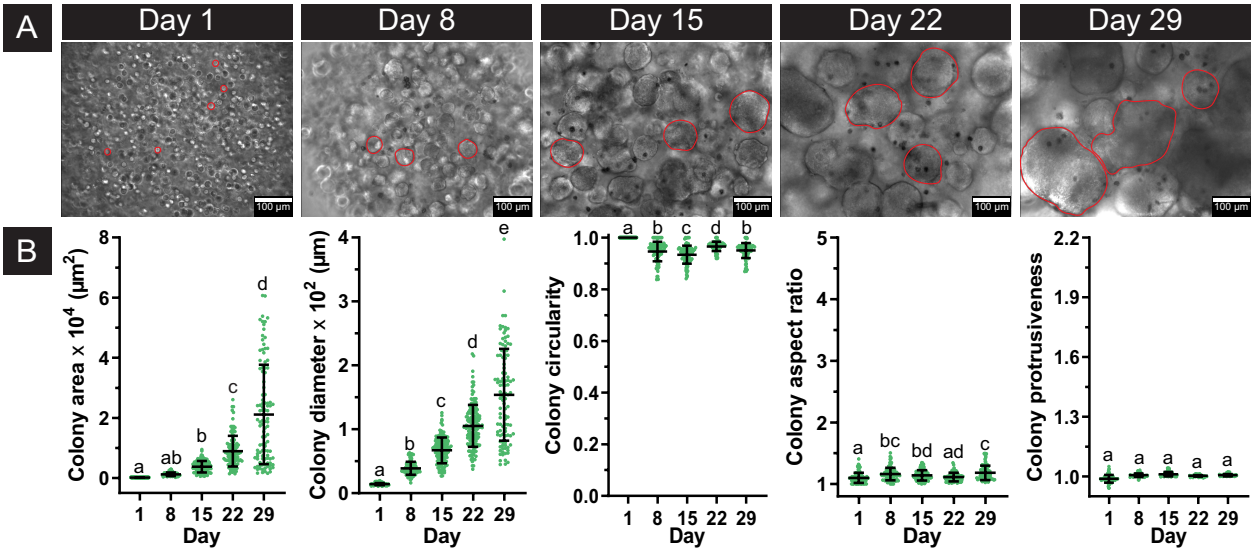

Figure 5.2. HT-29 cell colonies grew in microspheres. (A) Representative phase-contrast image of HT-29 cell colonies in microspheres over 29 days of culture. (B) Both cell colony area and diameter of HT-29 cells in microspheres increased significantly over time. Colony circularity exhibited an approximately 5% significant decrease from Day 1 to Day 8 and remained relatively constant thereafter. The colony aspect ratio showed an approximately 6% significant increase from Day 1 to Day 8 and remained relatively constant thereafter. The colony protrusiveness did not change significantly over 29 days of culture. Data are mean ± SD, and each dot represents one colony. Means that do not share a letter are significantly different ($p \leq 0.05$; n ≥ 100 colonies per time point).

5.3.3 HT-29 Microspheres Grew Over Time

To examine the growth and morphological changes of HT-29 microspheres, phase-contrast images of tissues were taken and analyzed over time (Figure 5.3 A). Both microsphere area and diameter increased significantly over time ($p < 0.0001$)—approximately 155% and 58% increase in the area and dimeter from Day 1 to Day 29, respectively (Figure 5.3 B). The microsphere circularity exhibited an approximately 42% significant decrease, whereas aspect ratio demonstrated an approximately 54% significant increase from Day 1 to Day 29 ($p < 0.0001$) (Figure 5.3 B). An approximately 14% increase was also observed for the microsphere protrusiveness over 29 days of culture ($p < 0.0001$) (Figure 5.3 B).

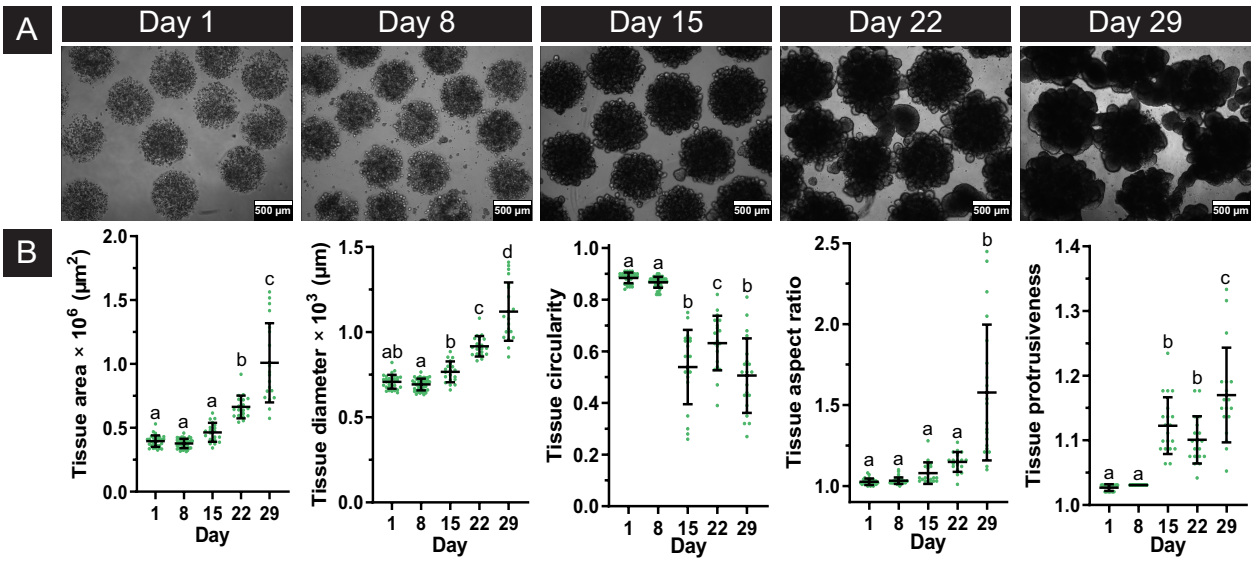

Figure 5.3. HT-29 microspheres grew over time. (A) Representative phase-contrast image of HT-29 microspheres over 29 days of culture. (B) Both microsphere area and diameter increased significantly over time. The microsphere circularity exhibited an approximately 42% significant decrease whereas aspect ratio demonstrated an approximately 54% significant increase from Day 1 to Day 29. An approximately 14% increase was also observed for the microsphere protrusiveness

over 29 days of culture. Changes in the circularity, aspect ratio, and protrusiveness of microspheres were the result of HT-29 cell colonies migrating from inside of the microspheres to the periphery and protruding from the perimeter of the tissues. Data are mean ± SD, and each dot represents one microsphere. Means that do not share a letter are significantly different ($p \leq 0.05$; $n \geq 20$ microspheres per time point).

5.3.4 HT-29 Cell Colonies Maintained Uniform Distribution in Microspheres

To visualize the localization of both HT-29 cell colonies and proliferative cells, Hoechst 33342, CD44, Ki-67, and CK20 markers were employed. Hoechst 33342 labeled the cell nuclei while CD44 marked the membrane of all HT-29 cells. The cell labeling with Hoechst 33342 and CD44 demonstrated that the HT-29 cell colonies were uniformly distributed throughout the microspheres (Figure 5.4) over 29 days of culture. The Ki-67 marker also showed that the proliferative cells were uniformly distributed around the microspheres (Figure 5.4). All HT-29 cells were also positive for CK20 marker, indicative of their ability to express this CRC-specific protein in the microspheres (Figure E.1).

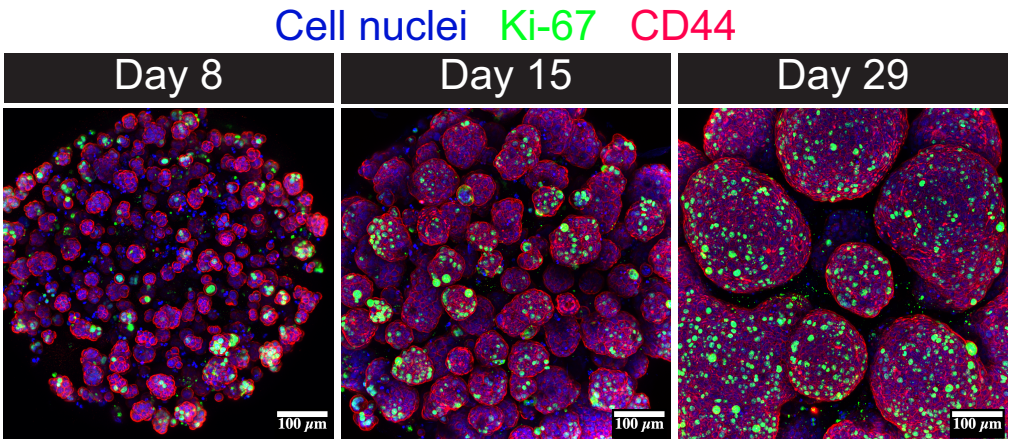

Figure 5.4. HT-29 cell colonies maintained uniform distribution in microspheres. Representative confocal images of cell nuclei (blue), CD44 (red), Ki-67 (green) in HT-29

microspheres on Days 8, 15, and 29. Both HT-29 cell colonies and Ki-67^{+} cells were uniformly distributed throughout the microspheres over 29 days of culture.

5.3.5 CRC-PDX Cell Colonies Grew in Microspheres

To investigate the growth and morphological changes of CRC-PDX cell colonies in the microspheres, Z-stack images were taken and analyzed over time (Figure 5.5 A). Both cell colony area and diameter of CRC-PDX cells in microspheres increased significantly over time ($p < 0.0001$)—from Day 1 to Day 29, the colony area and diameter increased from approximately 239±132 to 29683±16916 μm^2 and 18±6 to 188±52 μm, respectively (Figure 5.5 B). Colony circularity exhibited an approximately 64% significant decrease, whereas colony aspect ratio showed an approximately 98% significant increase ($p < 0.0001$) from Day 1 to Day 29 (Figure 5.5 B). The colony protrusiveness also demonstrated an approximately 50% significant increase over 29 days of culture (Figure 5.5 B).

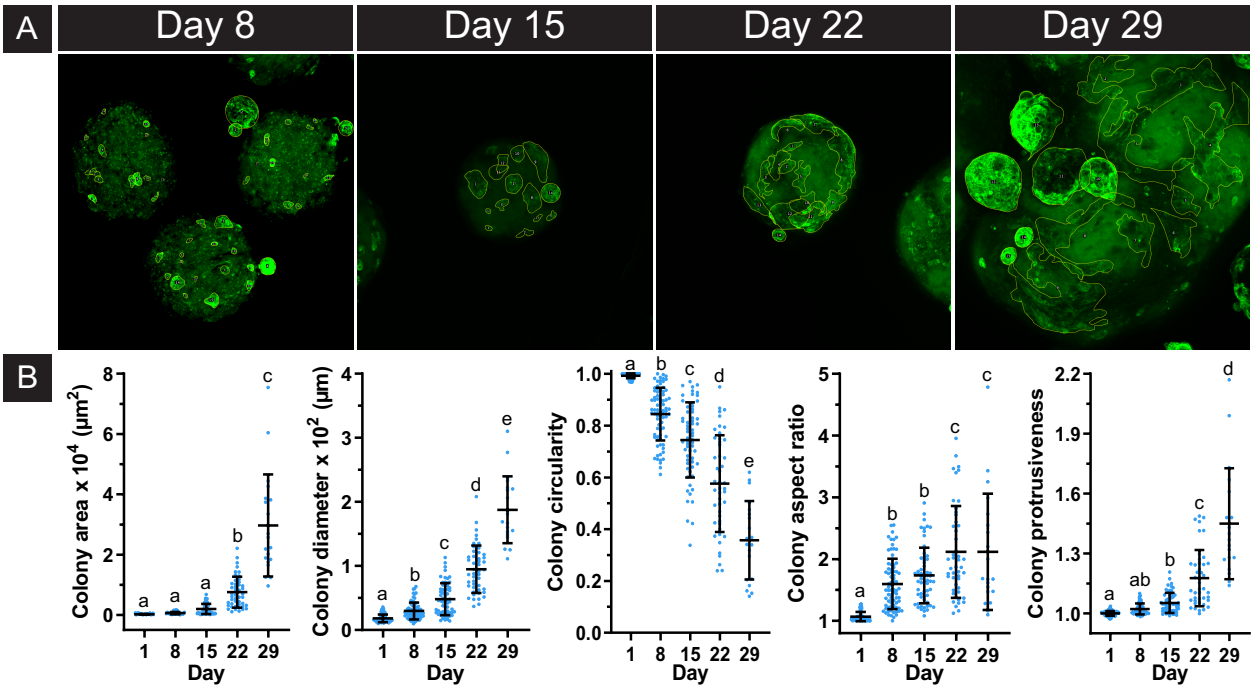

Figure 5.5. CRC-PDX cell colonies grew in microspheres. (A) Representative confocal images of CRC-PDX cells in microspheres on different time points. (B) Both cell colony area and diameter of CRC-PDX cells in microspheres increased significantly over time. Colony circularity exhibited an approximately 64% significant decrease, whereas colony aspect ratio showed an approximately 98% significant increase from Day 1 to Day 29. The colony protrusiveness also demonstrated an approximately 50% significant increase over 29 days of culture. Decreased circularity and increased aspect ratio and protrusiveness of CRC-PDX cells in microspheres were indicative of an increased invasive phenotype. Data are mean ± SD, and each dot represents one microsphere. Means that do not share a letter are significantly different ($p \leq 0.05$; $n \geq 50$ colonies per time point).

5.3.6 Microspheres Better Maintained CRC-PDX Cell Subpopulations as Compared to 2D-eCRC-PDX Cultures

To recapitulate PDX tumors in *in vitro* platforms, it is essential to maintain both human-derived (human) and mouse-derived (mouse) cell subpopulations in *in vitro* cultures. To examine

the ability of both 3D-eCRC-PDX microspheres and 2D-eCRC-PDX cultures in maintaining different cell subpopulations of the originating CRC-PDX tumors in *in vitro* cultures over 29 days, flow cytometry cell quantification was employed. To quantify the percentage of human cell and $CK20^+$ cell subpopulations, B2M marker was used in tandem with CK20 marker. Approximately, 25%, 27%, and 48% of the cells from originating CRC-PDX tumor were $B2M^+$ $CK20^+$ (human $CK20^+$ cells) $B2M^+$ $CK20^-$ (human $CK20^-$ cells), and $B2M^-$ $CK20^-$ (mouse cells) respectively (Figure 5.6 A). In addition, approximately 18% and 4% of the cells were $B2M^+$ $Ki67^+$ (human proliferative cells) $B2M^-$ $Ki67^+$ (mouse proliferative cells), respectively, meaning that a higher percentage of proliferative cell subpopulation was human cells (Figure 5.6 B). The percentages of these cell subpopulations in 3D-ePDX-CRC microspheres were fairly similar to those found in the originating CRC-PDX tumors. In sharp contrast, in 2D-CRC-PDX cultures, most of the proliferating cell subpopulations were mouse cells, meaning that the mouse cells grow faster and overtook human cells in culture (Figure 5.6 B). Cluster analysis of all cell subpopulations demonstrated that the 3D-eCRC-PDX microspheres from all time points clustered in a group with the CRC-PDX tumors, with Day 15 of the 3D-eCRC-PDX microspheres clustering closest (Figure 5.6 C). In contrast, the 2D-CRC-PDX cells clustered separately from both the CRC-PDX tumors and 3D-eCRC-PDX microspheres.

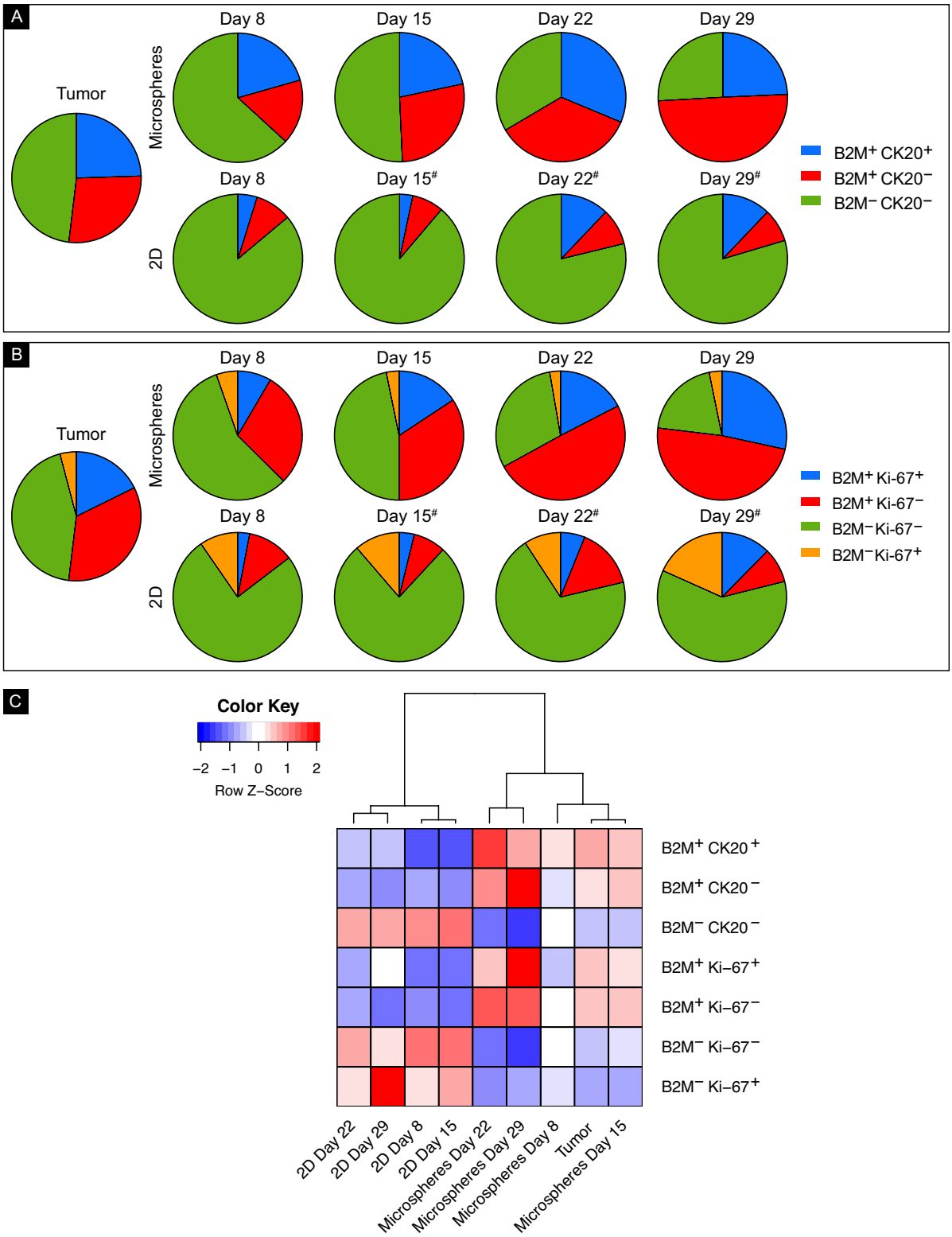

Figure 5.6. Microspheres better maintained CRC-PDX cell subpopulations as compared to 2D-eCRC-PDX cultures. (A, B) Pie charts showing the portion of each cell subpopulation in 3D-

eCRC-PDX microsphere and 2D-CRC-PDX cultures. In sharp contrast to 2D-CRC-PDX cultures, cell subpopulations in 3D-ePDX-CRC microspheres were fairly similar to those found in the originating CRC-PDX tumors. (C) Cluster analysis of all cell subpopulations demonstrated that the 3D-eCRC-PDX microspheres clustered in a group with the CRC-PDX tumors, whereas the 2D-CRC-PDX cultures clustered separately from both the CRC-PDX tumors and 3D-eCRC-PDX microspheres.

5.4 Discussion

To understand biology and investigate the mechanism of the disease, preclinical models with high physiological relevance are needed. Patient-derived xenograft (PDX) tumors, as a preclinical *in vivo* model, have shown high potential in clinical translatability and are able to more accurately recapitulate the key attributes of patients' tumors (Cree, Glaysher, and Harvey 2010; Chou et al. 2013; Brown et al. 2016; Lee et al. 2014; Cho et al. 2014). However, as an animal model, the use of PDX tumor models requires special facilities and typically is costly, time-consuming, and labor-intensive, thereby resulting in low throughput platforms (Day, Merlino, and Van Dyke 2015; McIntyre et al. 2015; Murayama and Gotoh 2019). A few studies have employed PDX cells, including CRC PDX cells, in *in vitro* models to produce higher-throughput platforms (Kondo et al. 2019; Boehnke et al. 2016; Verissimo et al. 2016). However, the models developed in these studies were matrix-free in the initial tissue formation. The lack of a supporting matrix typically results in tissues that include only one or some of the cell type(s) from the PDX or primary tumor, are not uniform, and can be easily damaged during assays and manipulation (Nunes et al. 2019).

Here, we have sought to develop a high-throughput microfluidic platform that rapidly generates a large number of uniform microspheres composed of a biomimetic material, poly(ethylene glycol)-fibrinogen (PEG-Fb), as a supporting matrix for CRC cells. First, we examined the ability of our microspheres to support the culture of HT-29 CRC cell line. Next, we generated microspheres using the CRC-PDX cells from a stage II patient and assessed the ability of the model to support the maintenance and expansion of mixed CRC-PDX tumor cell subpopulations.

To create functional *in vitro* tissue-engineered tumor microspheres, it was important for the cells to maintain high viability post-encapsulation and throughout long-term culture within the PEG-Fb biomimetic material. Similar to our previous findings with the breast cancer cell lines MCF-7, SK-BR-3, and MDA-MB-231 (Pradhan, Hassani, et al. 2017; Pradhan et al. 2018), high cell viability ($\geq$ 90%) was observed in the HT-29 microspheres on all time points in the PEG-Fb material. In addition, the decrease in cell viability in HT-29 microspheres over time was consistent with other cancer research studies based on tissue engineering. For example, Fong et al. (E.L. Fong et al. 2014) observed high viability of selectively chosen clusters of PDX MDA PCa 183 and PDX MDA PCa118b cells within the HA-SH/PEG-DA hydrogel-based tumoroids on day 1 post-encapsulation with decreasing trends in viability over time.

Another important factor in creating an *in vitro* cancer model that can recapitulate patients' tumors is the ability of the model to maintain all cell types in culture. Cell-cell and cell-matrix interactions play a significant role in the growth, proliferation, and migration of cancer cells (Riedl et al. 2017; Okada, Vaeteewoottacharn, and Kariya 2019; Kodack et al. 2017). As PDXs tumors are composed of both human-derived and mouse-derived cells, the maintenance of all cancer and stromal PDX cell subpopulations in culture is necessary for accurate recapitulation of the PDX

tumor microenvironment. Previous studies have reported that the culture of PDX cells in 2D monolayers led to significant changes in the ratios of cell types present in the overall population, thereby resulting in an *in vitro* model that no longer mimicked the *in vivo* PDX cell subpopulations (Okada, Vaeteewoottacharn, and Kariya 2019; Kodack et al. 2017). Other groups have employed 3D *in vitro* models to culture PDX cells; however, they included all cell types from the PDX cell population (E.L. Fong et al. 2014; E.L. Fong, Wan, et al. 2016). Thus, here we investigated the ability of 3D-eCRC-PD microspheres to maintain distinct PDX cell subpopulations in *in vitro* culture in comparison to 2D-CRC-PDX cultures. Notably, we showed that the 3D-eCRC-PDX microspheres better maintained the key cell subpopulations of the originating CRC-PDX tumor, whereas 2D-CRC-PDX cultures did not. The changes in cell subpopulations of 2D-CRC-PDX cultures were consistent with the observations reported by Kodack et al. (Kodack et al. 2017) as they attempted to establish cancer cell lines from multiple primary patient-derived tumors; in some cases, the stromal cells, primarily fibroblasts, outgrew the cancer cells, thereby hindering the tumor cell growth and resulting in the failure of cell line generation.

Overall, we showed that the 3D-eCRC-PDX microspheres maintained the PDX cellular heterogeneity and cell subpopulations. Remarkably, this maintenance of cellular heterogeneity and cell subpopulation ratios occurred simultaneously with an increase in the size of cell colonies and cell growth.

5.5 Conclusion

In this study, we have developed a high-throughput microfluidic platform that could rapidly generate a large number of uniform microspheres for CRC cells. The microspheres supported the culture of both HT-29 CRC cells and stage II CRC-PDX cells. The cells maintained their vitality

and grew in colonies with the microspheres. The microspheres were also able to maintain the cellular heterogeneity and mimicked the cell population composition of the originating CRC-PDX tumors. This novel high-throughput platform can be used in the future to study the mechanism of the disease and for drug testing applications.

Chapter 6: Summary and Conclusion

In this research work, my main focus was on the development of an *in vitro* colorectal cancer (CRC) model with high physiological relevance for accurate recapitulation of the tumor microenvironment. The development of physiological relevant pre-clinical CRC models is vital for understanding tumor biology to identify new, effective anti-cancer therapeutics. The findings of the research work can be used for a better understanding of CRC biology and beneficial to other researchers working on CRC tissue engineering. This study includes the following projects: 1) development of an *in vitro* 3D tissue-engineered cancer model for the investigation of CRC phenotypes; 2) establishment of engineered CRC tissue model to recapitulate key attributes of a stage II patient-derived xenograft (PDX) tumor line; 3) development of engineered CRC model employing multiple PDX lines that mimicked patient-to-patient tumor variabilities; and 4) generation of CRC tissue-engineered spheroids for high-throughput studies.

In the first project, we have developed an *in vitro* 3D engineered CRC (3D-eCRC) tissue model to systematically investigate the phenotypic differences between three CRC cell lines, HCT 116, HT-29, and SW480 in a biomimetic material, PEG- fibrinogen. For several decades, *in vitro* two-dimensional (2D) cancer models have facilitated the understanding of tumor biology and the testing of anti-cancer drug candidates. However, these models are inherently unable to mimic many pathophysiological complexities of the native tumor milieu. To overcome this limitation, three-dimensional (3D) engineered cancer models using biomimetic materials have been introduced to more closely recapitulate the key attributes of the native tumors. Specifically, for CRC, a few studies have developed 3D engineered tumor models to investigate cell-cell interactions or efficacy of anti-cancer drugs as compared to 2D cell cultures. However, the recapitulation of phenotypic differences of CRC cell lines within a 3D engineered matrix has not

been investigated systematically. To this end, stage II, stage III, and stage IV CRC cell lines were encapsulated in PEG-Fb hydrogels to create 3D engineered CRC (3D-eCRC) tissues. Our 3D-eCRC model supported encapsulation of cells at higher cell density (20×10^6 cells/mL) and longer-term culture (29 days) of these cell lines as compared to other previously reported *in vitro* CRC models. The 3D-eCRCs formed using each cell line demonstrated line-dependent differences in cellular and tissue properties, including cellular growth and morphology, cell subpopulations, cell size, cell granularity, migration patterns, tissue growth, and tissue stiffness. Importantly, these differences were found to be most prominent from Day 22 to Day 29, thereby indicating the importance of long-term culture of engineered colon cancer tissues for recapitulation and investigation of mechanistic differences and drug response. Our 3D-eCRC tissue model showed high potential for supporting future *in vitro* studies of the disease progression, metastatic mechanisms, and anti-cancer drug candidates to mitigate the impact of CRC.

In the second project, an *in vitro* 3D engineered CRC model was established using cells isolated from a Stage II CRC PDX (CRC-PDX) tumor line. The development of physiologically relevant pre-clinical CRC models is vital for understanding tumor biology to identify new, effective anti-cancer therapeutics. PDXs, an *in vivo* model, demonstrate high potential in clinical translatability due to the recapitulation of key characteristics of the patient tumor; however, the use of PDXs is costly and low throughput. To create a higher throughput platform, cells isolated from a CRC-PDX tumor were encapsulated in PEG-Fb hydrogels to generate 3D engineered CRC PDX (3D-eCRC-PDX) tissues. The isolated cells from the CRC-PDX tumors remained viable and proliferated within the 3D-eCRC-PDX tissues. The CRC-PDX tumor cell subpopulations, including human cancer and mouse stromal cells, were maintained within the 3D-eCRC-PDX tissues in long-term culture (29 days) with the number of cells in each subpopulation increasing

ratiometrically over time. The 3D-eCRC-PDX tissues mimicked the mechanical stiffness of CRC-PDX tumors. Furthermore, we observed congruence in enriched gene ontology molecular functions and Hallmark gene sets in CRC-PDX tumors and 3D-eCRC-PDX tissues compared to normal colon tissue, while prognostic Kaplan-Meier plots for overall and relapse-free survival did not reveal significant differences between CRC-PDX tumors and 3D-eCRC-PDX tissues. This robust *in vitro* model of CRC demonstrates significant potential for future implementation in the study of disease progression, tumorigenic mechanisms, and drug-testing applications.

In the third project, we employed three PDX tumor lines, originated from stages II, III-B, and IV of CRC patients, in the PEG-Fb hydrogels to examine to what extent this biomimetic material is able to recapitulate key attributes of the originating CRC-PDX tumors. For all CRC stages, we demonstrated that the rates of change in CRC PDX cell colony sizes and cell numbers in 3D-eCRC-PDX tissues over time mimicked the growth rates of the originating CRC-PDX tumors. The 3D-eCRC-PDX tissues were able to better maintain the key cell subpopulations of the originating CRC-PDX tumors for all CRC stages as compared to the 2D-CRC-PDX cultures. We measured the mechanical stiffness of both CRC-PDX tumors and 3D-eCRC-PDX tissues. Remarkably, the time-dependent stiffness of the 3D-eCRC-PDX tissues mimicked both region-dependent and batch-dependent stiffness of the originating CRC-PDX tumors for a given CRC stage. In addition, the average stiffness of all batches of 3D-eCRC-PDX tissues mimicked the stage-dependent average stiffness of the CRC-PDX tumors. The ability of these 3D-eCRC-PDX tissues to recapitulate the key attributes of the originating CRC-PDX tumors provides evidence that these engineered tissues are capable of mimicking patient-to-patient and/or cancer stage-to-stage variabilities. In the future, this model can be extended to include other types of cancer for investigation of the disease mechanisms and drug testing applications.

In the last project, a microfluidic platform was utilized to rapidly generate a large number of uniform microspheres encapsulated in PEG-Fb hydrogels for high throughput studies. The microspheres supported the culture of both HT-29 CRC cells and stage II CRC-PDX cells. The cells maintained their vitality and grew in colonies with the microspheres. The microspheres were also able to maintain the cellular heterogeneity and mimicked the cell population composition of the originating CRC-PDX tumors. This novel high-throughput platform can be used in the future to study the mechanisms of the disease and for drug testing applications.

Overall, patient-derived CRC cells were incorporated into a tissue-engineered model for the better recapitulation of the originating tumor microenvironment as compared to 2D cell culture. Culturing CRC-PDX tumor-derived cells *in vitro* through the use of our 3D-eCRC-PDX tissues was found to be mutually beneficial to (1) the advancement of *in vitro* CRC-PDX tumor-derived cell culture and (2) the capacity of 3D engineered cancer tissue models to recapitulate patient tumors. Introducing the ability to culture PDX cells long-term (29 days) in an *in vitro* biomimetic environment that preserves native cell behavior overcomes 2D culture and *in vivo* testing limitations. On the other hand, implementing a more pathophysiologically relevant cell source improves 3D engineered cancer tissue model recapitulation of patient tumors, thus overcoming limitations imposed by the use of cancer cell lines. The cell encapsulation and subsequent tissue formation generated a robust platform that has the capacity for high-throughput studies. The data described in this research work are beneficial to researchers, oncologists, and pharmaceutical companies studying preclinical cancer model development and screening anti-cancer drug candidates. In conclusion, our novel *in vitro* CRC models exhibit high potential for implementation in the study of CRC disease progression, elucidation of tumorigenic mechanisms, and application in drug-testing applications to mitigate the impact of CRC. The characterization methods used in

this study can be applied to the development and investigation of *in vitro* models employing established cancer cell lines, PDX cells, and patient-derived tumor cells for both CRC and other types of cancer (breast, prostate, liver, etc.).

References

Alizadeh, A. A., V. Aranda, A. Bardelli, C. Blanpain, C. Bock, C. Borowski, C. Caldas, A. Califano, M. Doherty, M. Elsner, M. Esteller, R. Fitzgerald, J. O. Korbel, P. Lichter, C. E. Mason, N. Navin, D. Pe'er, K. Polyak, C. W. Roberts, L. Siu, A. Snyder, H. Stower, C. Swanton, R. G. Verhaak, J. C. Zenklusen, J. Zuber, and J. Zucman-Rossi. 2015. "Toward understanding and exploiting tumor heterogeneity." *Nat Med* 21 (8): 846-53. https://doi.org/10.1038/nm.3915. https://www.ncbi.nlm.nih.gov/pubmed/26248267.

Alkasalias, Twana, Lidia Moyano-Galceran, Marie Arsenian-Henriksson, and Kaisa Lehti. 2018. "Fibroblasts in the Tumor Microenvironment: Shield or Spear?" *International Journal of Molecular Sciences* 19 (5): 1532. https://doi.org/10.3390/ijms19051532. https://dx.doi.org/10.3390/ijms19051532.

Almany, L., and D. Seliktar. 2005. "Biosynthetic hydrogel scaffolds made from fibrinogen and polyethylene glycol for 3D cell cultures." *Biomaterials* 26 (15): 2467-77. https://doi.org/10.1016/j.biomaterials.2004.06.047. https://www.ncbi.nlm.nih.gov/pubmed/15585249.

Alonso, Arnald, Brittany N Lasseigne, Kelly Williams, Josh Nielsen, Ryne C Ramaker, Andrew A Hardigan, Bobbi Johnston, Brian S Roberts, Sara J Cooper, and Sara Marsal. 2017. "aRNApipe: a balanced, efficient and distributed pipeline for processing RNA-seq data in high-performance computing environments." *Bioinformatics* 33 (11): 1727-1729.

American Cancer Society. 2019. Cancer Facts & Figures 2019. Atlanta: American Cancer Society.

Aran, V., A. P. Victorino, L. C. Thuler, and C. G. Ferreira. 2016. "Colorectal Cancer: Epidemiology, Disease Mechanisms and Interventions to Reduce Onset and Mortality."

Clin Colorectal Cancer 15 (3): 195-203. https://doi.org/10.1016/j.clcc.2016.02.008. https://www.ncbi.nlm.nih.gov/pubmed/26964802.

Bager, C. L., N. Willumsen, S. N. Kehlet, H. B. Hansen, A. C. Bay-Jensen, D. J. Leeming, K. Dragsbaek, J. S. Neergaard, C. Christiansen, E. Hogdall, and M. Karsdal. 2016. "Remodeling of the Tumor Microenvironment Predicts Increased Risk of Cancer in Postmenopausal Women: The Prospective Epidemiologic Risk Factor (PERF I) Study." *Cancer Epidemiology Biomarkers & Prevention* 25 (9): 1348-1355. https://doi.org/10.1158/1055-9965.epi-16-0127. https://dx.doi.org/10.1158/1055-9965.EPI-16-0127.

Balzer, E. M., Z. Tong, C. D. Paul, W. C. Hung, K. M. Stroka, A. E. Boggs, S. S. Martin, and K. Konstantopoulos. 2012. "Physical confinement alters tumor cell adhesion and migration phenotypes." *FASEB J* 26 (10): 4045-56. https://doi.org/10.1096/fj.12-211441. https://www.ncbi.nlm.nih.gov/pubmed/22707566.

Bardou, M., A. N. Barkun, and M. Martel. 2013. "Obesity and colorectal cancer." *Gut* 62 (6): 933-47. https://doi.org/10.1136/gutjnl-2013-304701. https://www.ncbi.nlm.nih.gov/pubmed/23481261.

Bayrak, R., H. Haltas, and S. Yenidunya. 2012. "The value of CDX2 and cytokeratins 7 and 20 expression in differentiating colorectal adenocarcinomas from extraintestinal gastrointestinal adenocarcinomas: cytokeratin 7-/20+ phenotype is more specific than CDX2 antibody." *Diagn Pathol* 7: 9. https://doi.org/10.1186/1746-1596-7-9. https://www.ncbi.nlm.nih.gov/pubmed/22268990.

Beissbarth, T., L. Hyde, G. K. Smyth, C. Job, W. M. Boon, S. S. Tan, H. S. Scott, and T. P. Speed. 2004. "Statistical modeling of sequencing errors in SAGE libraries." *Bioinformatics* 20

Suppl 1: i31-9. https://doi.org/10.1093/bioinformatics/bth924. https://www.ncbi.nlm.nih.gov/pubmed/15262778.

Bell, E., B. Ivarsson, and C. Merrill. 1979. "Production of a tissue-like structure by contraction of collagen lattices by human fibroblasts of different proliferative potential in vitro." *Proc Natl Acad Sci U S A* 76 (3): 1274-8. https://doi.org/10.1073/pnas.76.3.1274. https://www.ncbi.nlm.nih.gov/pubmed/286310.

Boehnke, K., P. W. Iversen, D. Schumacher, M. J. Lallena, R. Haro, J. Amat, J. Haybaeck, S. Liebs, M. Lange, R. Schafer, C. R. Regenbrecht, C. Reinhard, and J. A. Velasco. 2016. "Assay Establishment and Validation of a High-Throughput Screening Platform for Three-Dimensional Patient-Derived Colon Cancer Organoid Cultures." *J Biomol Screen* 21 (9): 931-41. https://doi.org/10.1177/1087057116650965. https://www.ncbi.nlm.nih.gov/pubmed/27233291.

Brabletz, T., A. Jung, S. Reu, M. Porzner, F. Hlubek, L. A. Kunz-Schughart, R. Knuechel, and T. Kirchner. 2001. "Variable beta-catenin expression in colorectal cancers indicates tumor progression driven by the tumor environment." *Proc Natl Acad Sci U S A* 98 (18): 10356-61. https://doi.org/10.1073/pnas.171610498. https://www.ncbi.nlm.nih.gov/pubmed/11526241.

Bray, L. J., M. Binner, A. Holzheu, J. Friedrichs, U. Freudenberg, D. W. Hutmacher, and C. Werner. 2015. "Multi-parametric hydrogels support 3D in vitro bioengineered microenvironment models of tumour angiogenesis." *Biomaterials* 53: 609-20. https://doi.org/10.1016/j.biomaterials.2015.02.124. https://www.ncbi.nlm.nih.gov/pubmed/25890757.

Bronsert, P., K. Enderle-Ammour, M. Bader, S. Timme, M. Kuehs, A. Csanadi, G. Kayser, I. Kohler, D. Bausch, J. Hoeppner, U. T. Hopt, T. Keck, E. Stickeler, B. Passlick, O. Schilling, C. P. Reiss, Y. Vashist, T. Brabletz, J. Berger, J. Lotz, J. Olesch, M. Werner, and U. F. Wellner. 2014. "Cancer cell invasion and EMT marker expression: a three-dimensional study of the human cancer-host interface." *J Pathol* 234 (3): 410-22. https://doi.org/10.1002/path.4416. https://www.ncbi.nlm.nih.gov/pubmed/25081610.

Brown, K. M., A. Xue, A. Mittal, J. S. Samra, R. Smith, and T. J. Hugh. 2016. "Patient-derived xenograft models of colorectal cancer in pre-clinical research: a systematic review." *Oncotarget* 7 (40): 66212-66225. https://doi.org/10.18632/oncotarget.11184. https://www.ncbi.nlm.nih.gov/pubmed/27517155.

Calle, E. E., and R. Kaaks. 2004. "Overweight, obesity and cancer: epidemiological evidence and proposed mechanisms." *Nat Rev Cancer* 4 (8): 579-91. https://doi.org/10.1038/nrc1408. https://www.ncbi.nlm.nih.gov/pubmed/15286738.

Carr, I., M. Levy, and P. Watson. 1986. "The invasive edge: invasion in colorectal cancer." *Clin Exp Metastasis* 4 (2): 129-39. https://doi.org/10.1007/BF00119079. https://www.ncbi.nlm.nih.gov/pubmed/3720057.

Carvalho, M. R., D. Lima, R. L. Reis, V. M. Correlo, and J. M. Oliveira. 2015. "Evaluating Biomaterial- and Microfluidic-Based 3D Tumor Models." *Trends Biotechnol* 33 (11): 667-678. https://doi.org/10.1016/j.tibtech.2015.09.009. https://www.ncbi.nlm.nih.gov/pubmed/26603572.

Cassidy, J. W., C. Caldas, and A. Bruna. 2015. "Maintaining Tumor Heterogeneity in Patient-Derived Tumor Xenografts." *Cancer Res* 75 (15): 2963-8. https://doi.org/10.1158/0008-5472.CAN-15-0727. https://www.ncbi.nlm.nih.gov/pubmed/26180079.

Chen, J. E., S. Pedron, and B. A. C. Harley. 2017. "The Combined Influence of Hydrogel Stiffness and Matrix-Bound Hyaluronic Acid Content on Glioblastoma Invasion." *Macromol Biosci* 17 (8). https://doi.org/10.1002/mabi.201700018. https://www.ncbi.nlm.nih.gov/pubmed/28379642.

Cho, Y. B., H. K. Hong, Y. L. Choi, E. Oh, K. M. Joo, J. Jin, D. H. Nam, Y. H. Ko, and W. Y. Lee. 2014. "Colorectal cancer patient-derived xenografted tumors maintain characteristic features of the original tumors." *J Surg Res* 187 (2): 502-9. https://doi.org/10.1016/j.jss.2013.11.010. https://www.ncbi.nlm.nih.gov/pubmed/24332554.

Chou, J., M. P. Fitzgibbon, C. L. Mortales, A. M. Towlerton, M. P. Upton, R. S. Yeung, M. W. McIntosh, and E. H. Warren. 2013. "Phenotypic and transcriptional fidelity of patient-derived colon cancer xenografts in immune-deficient mice." *PLoS One* 8 (11): e79874. https://doi.org/10.1371/journal.pone.0079874. https://www.ncbi.nlm.nih.gov/pubmed/24278200.

Colaprico, Antonio, Tiago C Silva, Catharina Olsen, Luciano Garofano, Claudia Cava, Davide Garolini, Thais S Sabedot, Tathiane M Malta, Stefano M Pagnotta, and Isabella Castiglioni. 2015. "TCGAbiolinks: an R/Bioconductor package for integrative analysis of TCGA data." *Nucleic acids research* 44 (8): e71-e71. https://www.ncbi.nlm.nih.gov/pmc/articles/PMC4856967/pdf/gkv1507.pdf.

Cox, Megan C., Laura M. Reese, Lissett R. Bickford, and Scott S. Verbridge. 2015. "Toward the Broad Adoption of 3D Tumor Models in the Cancer Drug Pipeline." *ACS Biomaterials Science & Engineering* 1 (10): 877-894. https://doi.org/10.1021/acsbiomaterials.5b00172.

Cree, I. A., S. Glaysher, and A. L. Harvey. 2010. "Efficacy of anti-cancer agents in cell lines versus human primary tumour tissue." *Curr Opin Pharmacol* 10 (4): 375-9. https://doi.org/10.1016/j.coph.2010.05.001. https://www.ncbi.nlm.nih.gov/pubmed/20570561.

Dainiak, M. B., I. N. Savina, I. Musolino, A. Kumar, B. Mattiasson, and I. Y. Galaev. 2008. "Biomimetic macroporous hydrogel scaffolds in a high-throughput screening format for cell-based assays." *Biotechnol Prog* 24 (6): 1373-83. https://doi.org/10.1002/btpr.30. https://www.ncbi.nlm.nih.gov/pubmed/19194952.

Daster, S., N. Amatruda, D. Calabrese, R. Ivanek, E. Turrini, R. A. Droeser, P. Zajac, C. Fimognari, G. C. Spagnoli, G. Iezzi, V. Mele, and M. G. Muraro. 2017. "Induction of hypoxia and necrosis in multicellular tumor spheroids is associated with resistance to chemotherapy treatment." *Oncotarget* 8 (1): 1725-1736. https://doi.org/10.18632/oncotarget.13857. https://www.ncbi.nlm.nih.gov/pubmed/27965457.

Day, C. P., G. Merlino, and T. Van Dyke. 2015. "Preclinical mouse cancer models: a maze of opportunities and challenges." *Cell* 163 (1): 39-53. https://doi.org/10.1016/j.cell.2015.08.068. https://www.ncbi.nlm.nih.gov/pubmed/26406370.

DeLong, S. A., A. S. Gobin, and J. L. West. 2005. "Covalent immobilization of RGDS on hydrogel surfaces to direct cell alignment and migration." *J Control Release* 109 (1-3): 139-48. https://doi.org/10.1016/j.jconrel.2005.09.020. https://www.ncbi.nlm.nih.gov/pubmed/16290119.

Devarasetty, M., A. Skardal, K. Cowdrick, F. Marini, and S. Soker. 2017. "Bioengineered Submucosal Organoids for In Vitro Modeling of Colorectal Cancer." *Tissue Eng Part A* 23 (19-20): 1026-1041. https://doi.org/10.1089/ten.tea.2017.0397. https://www.ncbi.nlm.nih.gov/pubmed/28922975.

Devaud, C., J. A. Westwood, L. B. John, J. K. Flynn, S. Paquet-Fifield, C. P. Duong, C. S. Yong, H. J. Pegram, S. A. Stacker, M. G. Achen, T. J. Stewart, L. A. Snyder, M. W. Teng, M. J. Smyth, P. K. Darcy, and M. H. Kershaw. 2014. "Tissues in different anatomical sites can sculpt and vary the tumor microenvironment to affect responses to therapy." *Mol Ther* 22 (1): 18-27. https://doi.org/10.1038/mt.2013.219. https://www.ncbi.nlm.nih.gov/pubmed/24048441.

Dikovsky, D., H. Bianco-Peled, and D. Seliktar. 2006. "The effect of structural alterations of PEG-fibrinogen hydrogel scaffolds on 3-D cellular morphology and cellular migration." *Biomaterials* 27 (8): 1496-506. https://doi.org/10.1016/j.biomaterials.2005.09.038. https://www.ncbi.nlm.nih.gov/pubmed/16243393.

Dobbin, Z. C., A. A. Katre, A. D. Steg, B. K. Erickson, M. M. Shah, R. D. Alvarez, M. G. Conner, D. Schneider, D. Chen, and C. N. Landen. 2014. "Using heterogeneity of the patient-derived xenograft model to identify the chemoresistant population in ovarian cancer." *Oncotarget* 5 (18): 8750-64. https://doi.org/10.18632/oncotarget.2373. https://www.ncbi.nlm.nih.gov/pubmed/25209969.

Dobin, Alexander, Carrie A Davis, Felix Schlesinger, Jorg Drenkow, Chris Zaleski, Sonali Jha, Philippe Batut, Mark Chaisson, and Thomas R Gingeras. 2013. "STAR: ultrafast universal RNA-seq aligner." *Bioinformatics* 29 (1): 15-21.

Dolznig, H., C. Rupp, C. Puri, C. Haslinger, N. Schweifer, E. Wieser, D. Kerjaschki, and P. Garin-Chesa. 2011. "Modeling colon adenocarcinomas in vitro a 3D co-culture system induces cancer-relevant pathways upon tumor cell and stromal fibroblast interaction." *Am J Pathol* 179 (1): 487-501. https://doi.org/10.1016/j.ajpath.2011.03.015. https://www.ncbi.nlm.nih.gov/pubmed/21703426.

Easwaran, H., H. C. Tsai, and S. B. Baylin. 2014. "Cancer epigenetics: tumor heterogeneity, plasticity of stem-like states, and drug resistance." *Mol Cell* 54 (5): 716-27. https://doi.org/10.1016/j.molcel.2014.05.015. https://www.ncbi.nlm.nih.gov/pubmed/24905005.

Eden, Eran, Roy Navon, Israel Steinfeld, Doron Lipson, and Zohar Yakhini. 2009. "GOrilla: a tool for discovery and visualization of enriched GO terms in ranked gene lists." *BMC bioinformatics* 10 (1): 48.

Eide, Peter W, Jarle Bruun, Ragnhild A Lothe, and Anita Sveen. 2017. "CMScaller: an R package for consensus molecular subtyping of colorectal cancer pre-clinical models." *Scientific reports* 7 (1): 16618.

Estrada, M. F., S. P. Rebelo, E. J. Davies, M. T. Pinto, H. Pereira, V. E. Santo, M. J. Smalley, S. T. Barry, E. J. Gualda, P. M. Alves, E. Anderson, and C. Brito. 2016. "Modelling the tumour microenvironment in long-term microencapsulated 3D co-cultures recapitulates phenotypic features of disease progression." *Biomaterials* 78: 50-61. https://doi.org/10.1016/j.biomaterials.2015.11.030. https://www.ncbi.nlm.nih.gov/pubmed/26650685.

Fernando, A., S. Glaysher, M. Conroy, M. Pekalski, J. Smith, L. A. Knight, F. Di Nicolantonio, and I. A. Cree. 2006. "Effect of culture conditions on the chemosensitivity of ovarian

cancer cell lines." *Anticancer Drugs* 17 (8): 913-9. https://doi.org/10.1097/01.cad.0000224445.23953.d9. https://www.ncbi.nlm.nih.gov/pubmed/16940801.

Fong, E. L., D. A. Harrington, M. C. Farach-Carson, and H. Yu. 2016. "Heralding a new paradigm in 3D tumor modeling." *Biomaterials* 108: 197-213. https://doi.org/10.1016/j.biomaterials.2016.08.052. https://www.ncbi.nlm.nih.gov/pubmed/27639438.

Fong, E. L., M. Martinez, J. Yang, A. G. Mikos, N. M. Navone, D. A. Harrington, and M. C. Farach-Carson. 2014. "Hydrogel-based 3D model of patient-derived prostate xenograft tumors suitable for drug screening." *Mol Pharm* 11 (7): 2040-50. https://doi.org/10.1021/mp500085p. https://www.ncbi.nlm.nih.gov/pubmed/24779589.

Fong, E. L. S., T. B. Toh, Q. X. X. Lin, Z. Liu, L. Hooi, M. B. Mohd Abdul Rashid, T. Benoukraf, E. K. Chow, T. H. Huynh, and H. Yu. 2018. "Generation of matched patient-derived xenograft in vitro-in vivo models using 3D macroporous hydrogels for the study of liver cancer." *Biomaterials* 159: 229-240. https://doi.org/10.1016/j.biomaterials.2017.12.026. https://www.ncbi.nlm.nih.gov/pubmed/29353739.

Fong, E. L., X. Wan, J. Yang, M. Morgado, A. G. Mikos, D. A. Harrington, N. M. Navone, and M. C. Farach-Carson. 2016. "A 3D in vitro model of patient-derived prostate cancer xenograft for controlled interrogation of in vivo tumor-stromal interactions." *Biomaterials* 77: 164-72. https://doi.org/10.1016/j.biomaterials.2015.10.059. https://www.ncbi.nlm.nih.gov/pubmed/26599623.

Font-Burgada, J., B. Sun, and M. Karin. 2016. "Obesity and Cancer: The Oil that Feeds the Flame." *Cell Metab* 23 (1): 48-62. https://doi.org/10.1016/j.cmet.2015.12.015. https://www.ncbi.nlm.nih.gov/pubmed/26771116.

Forster, J. C., W. M. Harriss-Phillips, M. J. Douglass, and E. Bezak. 2017. "A review of the development of tumor vasculature and its effects on the tumor microenvironment." *Hypoxia (Auckl)* 5: 21-32. https://doi.org/10.2147/HP.S133231. https://www.ncbi.nlm.nih.gov/pubmed/28443291.

Friedl, P., and S. Alexander. 2011. "Cancer invasion and the microenvironment: plasticity and reciprocity." *Cell* 147 (5): 992-1009. https://doi.org/10.1016/j.cell.2011.11.016. https://www.ncbi.nlm.nih.gov/pubmed/22118458.

Gao, D., I. Vela, A. Sboner, P. J. Iaquinta, W. R. Karthaus, A. Gopalan, C. Dowling, J. N. Wanjala, E. A. Undvall, V. K. Arora, J. Wongvipat, M. Kossai, S. Ramazanoglu, L. P. Barboza, W. Di, Z. Cao, Q. F. Zhang, I. Sirota, L. Ran, T. Y. MacDonald, H. Beltran, J. M. Mosquera, K. A. Touijer, P. T. Scardino, V. P. Laudone, K. R. Curtis, D. E. Rathkopf, M. J. Morris, D. C. Danila, S. F. Slovin, S. B. Solomon, J. A. Eastham, P. Chi, B. Carver, M. A. Rubin, H. I. Scher, H. Clevers, C. L. Sawyers, and Y. Chen. 2014. "Organoid cultures derived from patients with advanced prostate cancer." *Cell* 159 (1): 176-187. https://doi.org/10.1016/j.cell.2014.08.016. https://www.ncbi.nlm.nih.gov/pubmed/25201530.

Gill, B. J., D. L. Gibbons, L. C. Roudsari, J. E. Saik, Z. H. Rizvi, J. D. Roybal, J. M. Kurie, and J. L. West. 2012. "A synthetic matrix with independently tunable biochemistry and mechanical properties to study epithelial morphogenesis and EMT in a lung

adenocarcinoma model." *Cancer Res* 72 (22): 6013-23. https://doi.org/10.1158/0008-5472.CAN-12-0895. https://www.ncbi.nlm.nih.gov/pubmed/22952217.

Godbout, C., L. Follonier Castella, E. A. Smith, N. Talele, M. L. Chow, A. Garonna, and B. Hinz. 2013. "The mechanical environment modulates intracellular calcium oscillation activities of myofibroblasts." *PLoS One* 8 (5): e64560. https://doi.org/10.1371/journal.pone.0064560. https://www.ncbi.nlm.nih.gov/pubmed/23691248.

Gonzalez-Pons, M., and M. Cruz-Correa. 2015. "Colorectal Cancer Biomarkers: Where Are We Now?" *Biomed Res Int* 2015: 149014. https://doi.org/10.1155/2015/149014. https://www.ncbi.nlm.nih.gov/pubmed/26106599.

Goswami, Chirayu Pankaj, and Harikrishna Nakshatri. 2013. "PROGgene: gene expression based survival analysis web application for multiple cancers." *Journal of clinical bioinformatics* 3 (1): 22.

---. 2014. "PROGgeneV2: enhancements on the existing database." *BMC cancer* 14 (1): 970.

Gu, L., and D. J. Mooney. 2016. "Biomaterials and emerging anticancer therapeutics: engineering the microenvironment." *Nat Rev Cancer* 16 (1): 56-66. https://doi.org/10.1038/nrc.2015.3. https://www.ncbi.nlm.nih.gov/pubmed/26694936.

Guinney, Justin, Rodrigo Dienstmann, Xin Wang, Aurélien De Reyniès, Andreas Schlicker, Charlotte Soneson, Laetitia Marisa, Paul Roepman, Gift Nyamundanda, and Paolo Angelino. 2015. "The consensus molecular subtypes of colorectal cancer." *Nature medicine* 21 (11): 1350.

Gurski, L. A., A. K. Jha, C. Zhang, X. Jia, and M. C. Farach-Carson. 2009. "Hyaluronic acid-based hydrogels as 3D matrices for in vitro evaluation of chemotherapeutic drugs using poorly

adherent prostate cancer cells." *Biomaterials* 30 (30): 6076-85. https://doi.org/10.1016/j.biomaterials.2009.07.054. https://www.ncbi.nlm.nih.gov/pubmed/19695694.

Han, X. Y., B. Wei, J. F. Fang, S. Zhang, F. C. Zhang, H. B. Zhang, T. Y. Lan, H. Q. Lu, and H. B. Wei. 2013. "Epithelial-mesenchymal transition associates with maintenance of stemness in spheroid-derived stem-like colon cancer cells." *PLoS One* 8 (9): e73341. https://doi.org/10.1371/journal.pone.0073341. https://www.ncbi.nlm.nih.gov/pubmed/24039918.

Hidalgo, M., F. Amant, A. V. Biankin, E. Budinska, A. T. Byrne, C. Caldas, R. B. Clarke, S. de Jong, J. Jonkers, G. M. Maelandsmo, S. Roman-Roman, J. Seoane, L. Trusolino, and A. Villanueva. 2014. "Patient-derived xenograft models: an emerging platform for translational cancer research." *Cancer Discov* 4 (9): 998-1013. https://doi.org/10.1158/2159-8290.CD-14-0001. https://www.ncbi.nlm.nih.gov/pubmed/25185190.

Hinz, B., G. Celetta, J. J. Tomasek, G. Gabbiani, and C. Chaponnier. 2001. "Alpha-smooth muscle actin expression upregulates fibroblast contractile activity." *Mol Biol Cell* 12 (9): 2730-41. https://doi.org/10.1091/mbc.12.9.2730. https://www.ncbi.nlm.nih.gov/pubmed/11553712.

Holt, Samantha E., E. Sally Ward, Raimund J. Ober, and Daniel L. Alge. 2017. "Shooting for the moon: using tissue-mimetic hydrogels to gain new insight on cancer biology and screen therapeutics." *MRS Communications* 7 (3): 427-441. https://doi.org/10.1557/mrc.2017.86.

Hoshiba, T., and M. Tanaka. 2016. "Decellularized matrices as in vitro models of extracellular matrix in tumor tissues at different malignant levels: Mechanism of 5-fluorouracil resistance in colorectal tumor cells." *Biochim Biophys Acta* 1863 (11): 2749-2757.

https://doi.org/10.1016/j.bbamcr.2016.08.009. https://www.ncbi.nlm.nih.gov/pubmed/27558478.

Hoshida, Yujin. 2010. "Nearest template prediction: a single-sample-based flexible class prediction with confidence assessment." *PloS one* 5 (11): e15543.

Hsiao, A. Y., Y. S. Torisawa, Y. C. Tung, S. Sud, R. S. Taichman, K. J. Pienta, and S. Takayama. 2009. "Microfluidic system for formation of PC-3 prostate cancer co-culture spheroids." *Biomaterials* 30 (16): 3020-7. https://doi.org/10.1016/j.biomaterials.2009.02.047. https://www.ncbi.nlm.nih.gov/pubmed/19304321.

Imai, Y., H. Yamagishi, K. Fukuda, T. Okamura, Y. Ono, S. Ban, T. Inoue, and Y. Ueda. 2014. "Expression of cytokeratin 20 indicates invasive histological phenotype in poorly differentiated colorectal adenocarcinoma." *Anticancer Res* 34 (1): 159-67. https://www.ncbi.nlm.nih.gov/pubmed/24403457.

Jabbari, E., S. K. Sarvestani, L. Daneshian, and S. Moeinzadeh. 2015. "Optimum 3D Matrix Stiffness for Maintenance of Cancer Stem Cells Is Dependent on Tissue Origin of Cancer Cells." *PLoS One* 10 (7): e0132377. https://doi.org/10.1371/journal.pone.0132377. https://www.ncbi.nlm.nih.gov/pubmed/26168187.

Jansen, K. A., R. G. Bacabac, I. K. Piechocka, and G. H. Koenderink. 2013. "Cells actively stiffen fibrin networks by generating contractile stress." *Biophys J* 105 (10): 2240-51. https://doi.org/10.1016/j.bpj.2013.10.008. https://www.ncbi.nlm.nih.gov/pubmed/24268136.

Jin, T., L. Li, R. C. Siow, and K. K. Liu. 2015. "A novel collagen gel-based measurement technique for quantitation of cell contraction force." *J R Soc Interface* 12 (106). https://doi.org/10.1098/rsif.2014.1365. https://www.ncbi.nlm.nih.gov/pubmed/25977960.

Kawano, S., M. Kojima, Y. Higuchi, M. Sugimoto, K. Ikeda, N. Sakuyama, S. Takahashi, R. Hayashi, A. Ochiai, and N. Saito. 2015. "Assessment of elasticity of colorectal cancer tissue, clinical utility, pathological and phenotypical relevance." *Cancer Sci* 106 (9): 1232-9. https://doi.org/10.1111/cas.12720. https://www.ncbi.nlm.nih.gov/pubmed/26083008.

Keller, A., A. I. Nesvizhskii, E. Kolker, and R. Aebersold. 2002. "Empirical statistical model to estimate the accuracy of peptide identifications made by MS/MS and database search." *Anal Chem* 74 (20): 5383-92. https://doi.org/10.1021/ac025747h. https://www.ncbi.nlm.nih.gov/pubmed/12403597.

Khaitan, D., S. Chandna, M. B. Arya, and B. S. Dwarakanath. 2006. "Establishment and characterization of multicellular spheroids from a human glioma cell line; Implications for tumor therapy." *J Transl Med* 4: 12. https://doi.org/10.1186/1479-5876-4-12. https://www.ncbi.nlm.nih.gov/pubmed/16509995.

Kim, D. H., A. J. Ewald, J. Park, Kshitiz, M. Kwak, R. S. Gray, C. Y. Su, J. Seo, S. S. An, and A. Levchenko. 2018. "Biomechanical interplay between anisotropic re-organization of cells and the surrounding matrix underlies transition to invasive cancer spread." *Sci Rep* 8 (1): 14210. https://doi.org/10.1038/s41598-018-32010-3. https://www.ncbi.nlm.nih.gov/pubmed/30242256.

Kim, J. H., Y. Y. Rhee, J. M. Bae, N. Y. Cho, and G. H. Kang. 2013. "Loss of CDX2/CK20 expression is associated with poorly differentiated carcinoma, the CpG island methylator phenotype, and adverse prognosis in microsatellite-unstable colorectal cancer." *Am J Surg Pathol* 37 (10): 1532-41. https://doi.org/10.1097/PAS.0b013e31829ab1c1. https://www.ncbi.nlm.nih.gov/pubmed/24025523.

Kodack, D. P., A. F. Farago, A. Dastur, M. A. Held, L. Dardaei, L. Friboulet, F. von Flotow, L. J. Damon, D. Lee, M. Parks, R. Dicecca, M. Greenberg, K. E. Kattermann, A. K. Riley, F. J. Fintelmann, C. Rizzo, Z. Piotrowska, A. T. Shaw, J. F. Gainor, L. V. Sequist, M. J. Niederst, J. A. Engelman, and C. H. Benes. 2017. "Primary Patient-Derived Cancer Cells and Their Potential for Personalized Cancer Patient Care." *Cell Rep* 21 (11): 3298-3309. https://doi.org/10.1016/j.celrep.2017.11.051. https://www.ncbi.nlm.nih.gov/pubmed/29241554.

Kondo, J., T. Ekawa, H. Endo, K. Yamazaki, N. Tanaka, Y. Kukita, H. Okuyama, J. Okami, F. Imamura, M. Ohue, K. Kato, T. Nomura, A. Kohara, S. Mori, S. Dan, and M. Inoue. 2019. "High-throughput screening in colorectal cancer tissue-originated spheroids." *Cancer Sci* 110 (1): 345-355. https://doi.org/10.1111/cas.13843. https://www.ncbi.nlm.nih.gov/pubmed/30343529.

Kopetz, S., R. Lemos, and G. Powis. 2012. "The promise of patient-derived xenografts: the best laid plans of mice and men." *Clin Cancer Res* 18 (19): 5160-2. https://doi.org/10.1158/1078-0432.CCR-12-2408. https://www.ncbi.nlm.nih.gov/pubmed/22912394.

Kraning-Rush, C. M., S. P. Carey, M. C. Lampi, and C. A. Reinhart-King. 2013. "Microfabricated collagen tracks facilitate single cell metastatic invasion in 3D." *Integr Biol (Camb)* 5 (3): 606-16. https://doi.org/10.1039/c3ib20196a. https://www.ncbi.nlm.nih.gov/pubmed/23388698.

Kraning-Rush, C. M., and C. A. Reinhart-King. 2012. "Controlling matrix stiffness and topography for the study of tumor cell migration." *Cell Adh Migr* 6 (3): 274-9. https://doi.org/10.4161/cam.21076. https://www.ncbi.nlm.nih.gov/pubmed/22863740.

Larson, Brad. 2015. "3D cell culture: A review of current techniques." *BioTek* 6: 1-10.

Lee, W. S., H. Y. Kim, J. Y. Seok, H. H. Jang, Y. H. Park, S. Y. Kim, D. B. Shin, and S. Hong. 2014. "Genomic profiling of patient-derived colon cancer xenograft models." *Medicine (Baltimore)* 93 (28): e298. https://doi.org/10.1097/MD.0000000000000298. https://www.ncbi.nlm.nih.gov/pubmed/25526474.

Liberzon, Arthur, Chet Birger, Helga Thorvaldsdóttir, Mahmoud Ghandi, Jill P Mesirov, and Pablo Tamayo. 2015. "The Molecular Signatures Database Hallmark Gene Set Collection." *Cell Systems* 1 (6): 417-425. https://doi.org/https://doi.org/10.1016/j.cels.2015.12.004. http://www.sciencedirect.com/science/article/pii/S2405471215002185.

Libutti, Steven K., Leonard B. Saltz, Christopher G. Willett, and Rebecca Levine. 2015. "Chapter 57 - Cancer of the colon." In *DeVita, Hellman, and Rosenberg's Cancer: Principles & Practice of Oncology: Tenth Edition*, edited by Vincent T DeVita, Theodore S Lawrence and Steven A Rosenberg. Wolters Kluwer Health Adis (ESP).

Liu, H., R. G. Sadygov, and J. R. Yates, 3rd. 2004. "A model for random sampling and estimation of relative protein abundance in shotgun proteomics." *Anal Chem* 76 (14): 4193-201. https://doi.org/10.1021/ac0498563. https://www.ncbi.nlm.nih.gov/pubmed/15253663.

Long, T. J., M. Takeno, C. C. Sprenger, S. R. Plymate, and B. D. Ratner. 2013. "Capillary force seeding of sphere-templated hydrogels for tissue-engineered prostate cancer xenografts." *Tissue Eng Part C Methods* 19 (9): 738-44. https://doi.org/10.1089/ten.TEC.2012.0388. https://www.ncbi.nlm.nih.gov/pubmed/23373788.

Love, Michael I, Wolfgang Huber, and Simon Anders. 2014. "Moderated estimation of fold change and dispersion for RNA-seq data with DESeq2." *Genome biology* 15 (12): 550.

Luca, A. C., S. Mersch, R. Deenen, S. Schmidt, I. Messner, K. L. Schafer, S. E. Baldus, W. Huckenbeck, R. P. Piekorz, W. T. Knoefel, A. Krieg, and N. H. Stoecklein. 2013. "Impact of the 3D microenvironment on phenotype, gene expression, and EGFR inhibition of colorectal cancer cell lines." *PLoS One* 8 (3): e59689. https://doi.org/10.1371/journal.pone.0059689. https://www.ncbi.nlm.nih.gov/pubmed/23555746.

Ludwig, M. R., K. Kojima, G. J. Bowersock, D. Chen, N. C. Jhala, D. J. Buchsbaum, W. E. Grizzle, C. A. Klug, and J. A. Mobley. 2016. "Surveying the serologic proteome in a tissue-specific kras(G12D) knockin mouse model of pancreatic cancer." *Proteomics* 16 (3): 516-31. https://doi.org/10.1002/pmic.201500133. https://www.ncbi.nlm.nih.gov/pubmed/26572242.

Lyons, S. M., E. Alizadeh, J. Mannheimer, K. Schuamberg, J. Castle, B. Schroder, P. Turk, D. Thamm, and A. Prasad. 2016. "Changes in cell shape are correlated with metastatic potential in murine and human osteosarcomas." *Biol Open* 5 (3): 289-99. https://doi.org/10.1242/bio.013409. https://www.ncbi.nlm.nih.gov/pubmed/26873952.

Magdeldin, T., V. Lopez-Davila, J. Pape, G. W. Cameron, M. Emberton, M. Loizidou, and U. Cheema. 2017. "Engineering a vascularised 3D in vitro model of cancer progression." *Sci Rep* 7: 44045. https://doi.org/10.1038/srep44045. https://www.ncbi.nlm.nih.gov/pubmed/28276469.

Magdeldin, T., V. Lopez-Davila, C. Villemant, G. Cameron, R. Drake, U. Cheema, and M. Loizidou. 2014. "The efficacy of cetuximab in a tissue-engineered three-dimensional in vitro model of colorectal cancer." *J Tissue Eng* 5: 2041731414544183.

https://doi.org/10.1177/2041731414544183. https://www.ncbi.nlm.nih.gov/pubmed/25383169.

Marquez, J. P., E. L. Elson, and G. M. Genin. 2010. "Whole cell mechanics of contractile fibroblasts: relations between effective cellular and extracellular matrix moduli." *Philos Trans A Math Phys Eng Sci* 368 (1912): 635-54. https://doi.org/10.1098/rsta.2009.0240. https://www.ncbi.nlm.nih.gov/pubmed/20047943.

Marquez, J. P., G. M. Genin, K. M. Pryse, and E. L. Elson. 2006. "Cellular and matrix contributions to tissue construct stiffness increase with cellular concentration." *Ann Biomed Eng* 34 (9): 1475-82. https://doi.org/10.1007/s10439-006-9160-2. https://www.ncbi.nlm.nih.gov/pubmed/16874557.

Marusyk, A., and K. Polyak. 2010. "Tumor heterogeneity: causes and consequences." *Biochim Biophys Acta* 1805 (1): 105-17. https://doi.org/10.1016/j.bbcan.2009.11.002. https://www.ncbi.nlm.nih.gov/pubmed/19931353.

Maykel, J., J. H. Liu, H. Li, L. D. Shultz, D. L. Greiner, and J. Houghton. 2014. "NOD-scidIl2rg (tm1Wjl) and NOD-Rag1 (null) Il2rg (tm1Wjl) : a model for stromal cell-tumor cell interaction for human colon cancer." *Dig Dis Sci* 59 (6): 1169-79. https://doi.org/10.1007/s10620-014-3168-5. https://www.ncbi.nlm.nih.gov/pubmed/24798995.

Mazzoleni, G., D. Di Lorenzo, and N. Steimberg. 2009. "Modelling tissues in 3D: the next future of pharmaco-toxicology and food research?" *Genes Nutr* 4 (1): 13-22. https://doi.org/10.1007/s12263-008-0107-0. https://www.ncbi.nlm.nih.gov/pubmed/19104883.

McGranahan, N., and C. Swanton. 2015. "Biological and therapeutic impact of intratumor heterogeneity in cancer evolution." *Cancer Cell* 27 (1): 15-26. https://doi.org/10.1016/j.ccell.2014.12.001. https://www.ncbi.nlm.nih.gov/pubmed/25584892.

McIntyre, R. E., S. J. Buczacki, M. J. Arends, and D. J. Adams. 2015. "Mouse models of colorectal cancer as preclinical models." *Bioessays* 37 (8): 909-20. https://doi.org/10.1002/bies.201500032. https://www.ncbi.nlm.nih.gov/pubmed/26115037.

Murayama, T., and N. Gotoh. 2019. "Patient-Derived Xenograft Models of Breast Cancer and Their Application." *Cells* 8 (6). https://doi.org/10.3390/cells8060621. https://www.ncbi.nlm.nih.gov/pubmed/31226846.

Muzny, Donna M., Matthew N. Bainbridge, Kyle Chang, Huyen H. Dinh, Jennifer A. Drummond, Gerald Fowler, Christie L. Kovar, Lora R. Lewis, Margaret B. Morgan, Irene F. Newsham, Jeffrey G. Reid, Jireh Santibanez, Eve Shinbrot, Lisa R. Trevino, Yuan-Qing Wu, Min Wang, Preethi Gunaratne, Lawrence A. Donehower, Chad J. Creighton, David A. Wheeler, Richard A. Gibbs, Michael S. Lawrence, Douglas Voet, Rui Jing, Kristian Cibulskis, Andrey Sivachenko, Petar Stojanov, Aaron McKenna, Eric S. Lander, Stacey Gabriel, Gad Getz, Li Ding, Robert S. Fulton, Daniel C. Koboldt, Todd Wylie, Jason Walker, David J. Dooling, Lucinda Fulton, Kim D. Delehaunty, Catrina C. Fronick, Ryan Demeter, Elaine R. Mardis, Richard K. Wilson, Andy Chu, Hye-Jung E. Chun, Andrew J. Mungall, Erin Pleasance, A. Gordon Robertson, Dominik Stoll, Miruna Balasundaram, Inanc Birol, Yaron S. N. Butterfield, Eric Chuah, Robin J. N. Coope, Noreen Dhalla, Ranabir Guin, Carrie Hirst, Martin Hirst, Robert A. Holt, Darlene Lee, Haiyan I. Li, Michael Mayo,

Richard A. Moore, Jacqueline E. Schein, Jared R. Slobodan, Angela Tam, Nina Thiessen, Richard Varhol, Thomas Zeng, Yongjun Zhao, Steven J. M. Jones, Marco A. Marra, Adam J. Bass, Alex H. Ramos, Gordon Saksena, Andrew D. Cherniack, Stephen E. Schumacher, Barbara Tabak, Scott L. Carter, Nam H. Pho, Huy Nguyen, Robert C. Onofrio, Andrew Crenshaw, Kristin Ardlie, Rameen Beroukhim, Wendy Winckler, Gad Getz, Matthew Meyerson, Alexei Protopopov, Juinhua Zhang, Angela Hadjipanayis, Eunjung Lee, Ruibin Xi, Lixing Yang, Xiaojia Ren, Hailei Zhang, Narayanan Sathiamoorthy, Sachet Shukla, Peng-Chieh Chen, Psalm Haseley, Yonghong Xiao, Semin Lee, Jonathan Seidman, Lynda Chin, Peter J. Park, Raju Kucherlapati, J. Todd Auman, Katherine A. Hoadley, Ying Du, Matthew D. Wilkerson, Yan Shi, Christina Liquori, Shaowu Meng, Ling Li, Yidi J. Turman, Michael D. Topal, Donghui Tan, Scot Waring, Elizabeth Buda, Jesse Walsh, Corbin D. Jones, Piotr A. Mieczkowski, Darshan Singh, Junyuan Wu, Anisha Gulabani, Peter Dolina, Tom Bodenheimer, Alan P. Hoyle, Janae V. Simons, Matthew Soloway, Lisle E. Mose, Stuart R. Jefferys, Saianand Balu, Brian D. O'Connor, Jan F. Prins, Derek Y. Chiang, D. Neil Hayes, Charles M. Perou, Toshinori Hinoue, Daniel J. Weisenberger, Dennis T. Maglinte, Fei Pan, Benjamin P. Berman, David J. Van Den Berg, Hui Shen, Timothy Triche Jr, Stephen B. Baylin, Peter W. Laird, Gad Getz, Michael Noble, Doug Voet, Gordon Saksena, Nils Gehlenborg, Daniel DiCara, Juinhua Zhang, Hailei Zhang, Chang-Jiun Wu, Spring Yingchun Liu, Sachet Shukla, Michael S. Lawrence, Lihua Zhou, Andrey Sivachenko, Pei Lin, Petar Stojanov, Rui Jing, Richard W. Park, Marc-Danie Nazaire, Jim Robinson, Helga Thorvaldsdottir, Jill Mesirov, Peter J. Park, Lynda Chin, Vesteinn Thorsson, Sheila M. Reynolds, Brady Bernard, Richard Kreisberg, Jake Lin, Lisa Iype, Ryan Bressler, Timo Erkkilä, Madhumati Gundapuneni, Yuexin Liu, Adam Norberg,

Tom Robinson, Da Yang, Wei Zhang, Ilya Shmulevich, Jorma J. de Ronde, Nikolaus Schultz, Ethan Cerami, Giovanni Ciriello, Arthur P. Goldberg, Benjamin Gross, Anders Jacobsen, Jianjiong Gao, Bogumil Kaczkowski, Rileen Sinha, B. Arman Aksoy, Yevgeniy Antipin, Boris Reva, Ronglai Shen, Barry S. Taylor, Timothy A. Chan, Marc Ladanyi, Chris Sander, Rehan Akbani, Nianxiang Zhang, Bradley M. Broom, Tod Casasent, Anna Unruh, Chris Wakefield, Stanley R. Hamilton, R. Craig Cason, Keith A. Baggerly, John N. Weinstein, David Haussler, Christopher C. Benz, Joshua M. Stuart, Stephen C. Benz, J. Zachary Sanborn, Charles J. Vaske, Jingchun Zhu, Christopher Szeto, Gary K. Scott, Christina Yau, Sam Ng, Ted Goldstein, Kyle Ellrott, Eric Collisson, Aaron E. Cozen, Daniel Zerbino, Christopher Wilks, Brian Craft, Paul Spellman, Robert Penny, Troy Shelton, Martha Hatfield, Scott Morris, Peggy Yena, Candace Shelton, Mark Sherman, Joseph Paulauskis, Julie M. Gastier-Foster, Jay Bowen, Nilsa C. Ramirez, Aaron Black, Robert Pyatt, Lisa Wise, Peter White, Monica Bertagnolli, Jen Brown, Timothy A. Chan, Gerald C. Chu, Christine Czerwinski, Fred Denstman, Rajiv Dhir, Arnulf Dörner, Charles S. Fuchs, Jose G. Guillem, Mary Iacocca, Hartmut Juhl, Andrew Kaufman, Bernard Kohl Iii, Xuan Van Le, Maria C. Mariano, Elizabeth N. Medina, Michael Meyers, Garrett M. Nash, Phillip B. Paty, Nicholas Petrelli, Brenda Rabeno, William G. Richards, David Solit, Pat Swanson, Larissa Temple, Joel E. Tepper, Richard Thorp, Efsevia Vakiani, Martin R. Weiser, Joseph E. Willis, Gary Witkin, Zhaoshi Zeng, Michael J. Zinner, Network The Cancer Genome Atlas, Medicine Genome Sequencing Center Baylor College of, Institute Genome Sequencing Center Broad, Louis Genome Sequencing Center Washington University in St, B. C. Cancer Agency Genome Characterization Center, Institute Genome-Characterization Center Broad, Brigham Genome-Characterization Center, Hospital

Women's, School Harvard Medical, Chapel Hill Genome-Characterization Center University of North Carolina, California Genome-Characterization Centers University of Southern, University Johns Hopkins, Institute Genome Data Analysis Center Broad, Biology Genome Data Analysis Center Institute for Systems, Center Genome Data Analysis Center Memorial Sloan-Kettering Cancer, M. D. Anderson Cancer Center Genome Data Analysis Center University of Texas, University of California Santa Cruz Genome Data Analysis Centers, Institute the Buck, Consortium Biospecimen Core Resource International Genomics, Resource Nationwide Children's Hospital Biospecimen Core, sites Tissue source, and group disease working. 2012. "Comprehensive molecular characterization of human colon and rectal cancer." *Nature* 487 (7407): 330-337. https://doi.org/10.1038/nature11252. https://doi.org/10.1038/nature11252.

Naba, A., K. R. Clauser, S. Hoersch, H. Liu, S. A. Carr, and R. O. Hynes. 2012. "The matrisome: in silico definition and in vivo characterization by proteomics of normal and tumor extracellular matrices." *Mol Cell Proteomics* 11 (4): M111 014647. https://doi.org/10.1074/mcp.M111.014647. https://www.ncbi.nlm.nih.gov/pubmed/22159717.

Naba, A., K. R. Clauser, and R. O. Hynes. 2015. "Enrichment of Extracellular Matrix Proteins from Tissues and Digestion into Peptides for Mass Spectrometry Analysis." *J Vis Exp* (101): e53057. https://doi.org/10.3791/53057. https://www.ncbi.nlm.nih.gov/pubmed/26273955.

Naba, A., K. R. Clauser, C. A. Whittaker, S. A. Carr, K. K. Tanabe, and R. O. Hynes. 2014. "Extracellular matrix signatures of human primary metastatic colon cancers and their

metastases to liver." *BMC Cancer* 14: 518. https://doi.org/10.1186/1471-2407-14-518. https://www.ncbi.nlm.nih.gov/pubmed/25037231.

Naba, A., O. M. T. Pearce, A. Del Rosario, D. Ma, H. Ding, V. Rajeeve, P. R. Cutillas, F. R. Balkwill, and R. O. Hynes. 2017. "Characterization of the Extracellular Matrix of Normal and Diseased Tissues Using Proteomics." *J Proteome Res* 16 (8): 3083-3091. https://doi.org/10.1021/acs.jproteome.7b00191. https://www.ncbi.nlm.nih.gov/pubmed/28675934.

Nabeshima, K., T. Inoue, Y. Shimao, H. Kataoka, and M. Koono. 1999. "Cohort migration of carcinoma cells: differentiated colorectal carcinoma cells move as coherent cell clusters or sheets." *Histol Histopathol* 14 (4): 1183-97. https://doi.org/10.14670/HH-14.1183. https://www.ncbi.nlm.nih.gov/pubmed/10506935.

Nagle, R. B. 2004. "Role of the extracellular matrix in prostate carcinogenesis." *J Cell Biochem* 91 (1): 36-40. https://doi.org/10.1002/jcb.10692. https://www.ncbi.nlm.nih.gov/pubmed/14689579.

Nesvizhskii, A. I., A. Keller, E. Kolker, and R. Aebersold. 2003. "A statistical model for identifying proteins by tandem mass spectrometry." *Anal Chem* 75 (17): 4646-58. https://doi.org/10.1021/ac0341261. https://www.ncbi.nlm.nih.gov/pubmed/14632076.

Nguyen, D. X., P. D. Bos, and J. Massague. 2009. "Metastasis: from dissemination to organ-specific colonization." *Nat Rev Cancer* 9 (4): 274-84. https://doi.org/10.1038/nrc2622. https://www.ncbi.nlm.nih.gov/pubmed/19308067.

Nunes, A. S., A. S. Barros, E. C. Costa, A. F. Moreira, and I. J. Correia. 2019. "3D tumor spheroids as in vitro models to mimic in vivo human solid tumors resistance to therapeutic drugs."

Biotechnol Bioeng 116 (1): 206-226. https://doi.org/10.1002/bit.26845. https://www.ncbi.nlm.nih.gov/pubmed/30367820.

Nyga, A., M. Loizidou, M. Emberton, and U. Cheema. 2013. "A novel tissue engineered three-dimensional in vitro colorectal cancer model." *Acta Biomater* 9 (8): 7917-26. https://doi.org/10.1016/j.actbio.2013.04.028. https://www.ncbi.nlm.nih.gov/pubmed/23624217.

Okada, S., K. Vaeteewoottacharn, and R. Kariya. 2019. "Application of Highly Immunocompromised Mice for the Establishment of Patient-Derived Xenograft (PDX) Models." *Cells* 8 (8). https://doi.org/10.3390/cells8080889. https://www.ncbi.nlm.nih.gov/pubmed/31412684.

Old, W. M., K. Meyer-Arendt, L. Aveline-Wolf, K. G. Pierce, A. Mendoza, J. R. Sevinsky, K. A. Resing, and N. G. Ahn. 2005. "Comparison of label-free methods for quantifying human proteins by shotgun proteomics." *Mol Cell Proteomics* 4 (10): 1487-502. https://doi.org/10.1074/mcp.M500084-MCP200. https://www.ncbi.nlm.nih.gov/pubmed/15979981.

Pandya, P., J. L. Orgaz, and V. Sanz-Moreno. 2017. "Modes of invasion during tumour dissemination." *Mol Oncol* 11 (1): 5-27. https://doi.org/10.1002/1878-0261.12019. https://www.ncbi.nlm.nih.gov/pubmed/28085224.

Pape, J., T. Magdeldin, M. Ali, C. Walsh, M. Lythgoe, M. Emberton, and U. Cheema. 2019. "Cancer invasion regulates vascular complexity in a three-dimensional biomimetic model." *Eur J Cancer* 119: 179-193. https://doi.org/10.1016/j.ejca.2019.07.005. https://www.ncbi.nlm.nih.gov/pubmed/31470251.

Park, J., D. H. Kim, H. N. Kim, C. J. Wang, M. K. Kwak, E. Hur, K. Y. Suh, S. S. An, and A. Levchenko. 2016. "Directed migration of cancer cells guided by the graded texture of the underlying matrix." *Nat Mater* 15 (7): 792-801. https://doi.org/10.1038/nmat4586. https://www.ncbi.nlm.nih.gov/pubmed/26974411.

Park, J. S., J. S. Chu, A. D. Tsou, R. Diop, Z. Tang, A. Wang, and S. Li. 2011. "The effect of matrix stiffness on the differentiation of mesenchymal stem cells in response to TGF-beta." *Biomaterials* 32 (16): 3921-30. https://doi.org/10.1016/j.biomaterials.2011.02.019. https://www.ncbi.nlm.nih.gov/pubmed/21397942.

Paul, C. D., P. Mistriotis, and K. Konstantopoulos. 2017. "Cancer cell motility: lessons from migration in confined spaces." *Nat Rev Cancer* 17 (2): 131-140. https://doi.org/10.1038/nrc.2016.123. https://www.ncbi.nlm.nih.gov/pubmed/27909339.

Pedron, S., J. S. Hanselman, M. A. Schroeder, J. N. Sarkaria, and B. A. C. Harley. 2017. "Extracellular Hyaluronic Acid Influences the Efficacy of EGFR Tyrosine Kinase Inhibitors in a Biomaterial Model of Glioblastoma." *Adv Healthc Mater* 6 (21). https://doi.org/10.1002/adhm.201700529. https://www.ncbi.nlm.nih.gov/pubmed/28766870.

Pedron, S., H. Polishetty, A. M. Pritchard, B. P. Mahadik, J. N. Sarkaria, and B. A. C. Harley. 2017. "Spatially graded hydrogels for preclinical testing of glioblastoma anticancer therapeutics." *MRS Commun* 7 (3): 442-449. https://doi.org/10.1557/mrc.2017.85. https://www.ncbi.nlm.nih.gov/pubmed/29230350.

Pedron, S., G. L. Wolter, J. E. Chen, S. E. Laken, J. N. Sarkaria, and B. A. C. Harley. 2019. "Hyaluronic acid-functionalized gelatin hydrogels reveal extracellular matrix signals temper the efficacy of erlotinib against patient-derived glioblastoma specimens."

Biomaterials 219: 119371. https://doi.org/10.1016/j.biomaterials.2019.119371. https://www.ncbi.nlm.nih.gov/pubmed/31352310.

Peng, Li, Xiu Wu Bian, Di Kang Li, Chuan Xu, Guang Ming Wang, Qing You Xia, and Qing Xiong. 2015. "Large-scale RNA-Seq Transcriptome Analysis of 4043 Cancers and 548 Normal Tissue Controls across 12 TCGA Cancer Types." *Scientific Reports* 5 (1): 13413. https://doi.org/10.1038/srep13413. https://doi.org/10.1038/srep13413.

Petit, V., G. Massonnet, Z. Maciorowski, J. Touhami, A. Thuleau, F. Nemati, J. Laval, S. Chateau-Joubert, J. L. Servely, D. Vallerand, J. J. Fontaine, N. Taylor, J. L. Battini, M. Sitbon, and D. Decaudin. 2013. "Optimization of tumor xenograft dissociation for the profiling of cell surface markers and nutrient transporters." *Lab Invest* 93 (5): 611-21. https://doi.org/10.1038/labinvest.2013.44. https://www.ncbi.nlm.nih.gov/pubmed/23459372.

Pradhan, S., C. S. Chaudhury, and E. A. Lipke. 2014. "Dual-phase, surface tension-based fabrication method for generation of tumor millibeads." *Langmuir* 30 (13): 3817-25. https://doi.org/10.1021/la500402m. https://www.ncbi.nlm.nih.gov/pubmed/24617794.

Pradhan, S., J. M. Clary, D. Seliktar, and E. A. Lipke. 2017. "A three-dimensional spheroidal cancer model based on PEG-fibrinogen hydrogel microspheres." *Biomaterials* 115: 141-154. https://doi.org/10.1016/j.biomaterials.2016.10.052. https://www.ncbi.nlm.nih.gov/pubmed/27889665.

Pradhan, S., I. Hassani, J. M. Clary, and E. A. Lipke. 2016. "Polymeric Biomaterials for In Vitro Cancer Tissue Engineering and Drug Testing Applications." *Tissue Eng Part B Rev* 22 (6): 470-484. https://doi.org/10.1089/ten.TEB.2015.0567. https://www.ncbi.nlm.nih.gov/pubmed/27302080.

Pradhan, S., I. Hassani, W. J. Seeto, and E. A. Lipke. 2017. "PEG-fibrinogen hydrogels for three-dimensional breast cancer cell culture." *J Biomed Mater Res A* 105 (1): 236-252. https://doi.org/10.1002/jbm.a.35899. https://www.ncbi.nlm.nih.gov/pubmed/27615742.

Pradhan, S., and J. H. Slater. 2019. "Tunable hydrogels for controlling phenotypic cancer cell states to model breast cancer dormancy and reactivation." *Biomaterials* 215: 119177. https://doi.org/10.1016/j.biomaterials.2019.04.022. https://www.ncbi.nlm.nih.gov/pubmed/31176804.

Pradhan, S., A. M. Smith, C. J. Garson, I. Hassani, W. J. Seeto, K. Pant, R. D. Arnold, B. Prabhakarpandian, and E. A. Lipke. 2018. "A Microvascularized Tumor-mimetic Platform for Assessing Anti-cancer Drug Efficacy." *Sci Rep* 8 (1): 3171. https://doi.org/10.1038/s41598-018-21075-9. https://www.ncbi.nlm.nih.gov/pubmed/29453454.

Prall, F., H. Nizze, and M. Barten. 2005. "Tumour budding as prognostic factor in stage I/II colorectal carcinoma." *Histopathology* 47 (1): 17-24. https://doi.org/10.1111/j.1365-2559.2005.02161.x. https://www.ncbi.nlm.nih.gov/pubmed/15982319.

Prasetyanti, P. R., and J. P. Medema. 2017. "Intra-tumor heterogeneity from a cancer stem cell perspective." *Mol Cancer* 16 (1): 41. https://doi.org/10.1186/s12943-017-0600-4. https://www.ncbi.nlm.nih.gov/pubmed/28209166.

Prasetyanti, Pramudita R, Sander R van Hooff, Tessa van Herwaarden, Nathalie de Vries, Kieshen Kalloe, Hans Rodermond, Ronald van Leersum, Joan H de Jong, Marek Franitza, and Peter Nürnberg. 2019. "Capturing colorectal cancer inter-tumor heterogeneity in patient-derived xenograft (PDX) models." *International journal of cancer* 144 (2): 366-371.

Quail, D. F., and J. A. Joyce. 2013. "Microenvironmental regulation of tumor progression and metastasis." *Nat Med* 19 (11): 1423-37. https://doi.org/10.1038/nm.3394. https://www.ncbi.nlm.nih.gov/pubmed/24202395.

Riedl, A., M. Schlederer, K. Pudelko, M. Stadler, S. Walter, D. Unterleuthner, C. Unger, N. Kramer, M. Hengstschlager, L. Kenner, D. Pfeiffer, G. Krupitza, and H. Dolznig. 2017. "Comparison of cancer cells in 2D vs 3D culture reveals differences in AKT-mTOR-S6K signaling and drug responses." *J Cell Sci* 130 (1): 203-218. https://doi.org/10.1242/jcs.188102. https://www.ncbi.nlm.nih.gov/pubmed/27663511.

Riondino, S., M. Roselli, R. Palmirotta, D. Della-Morte, P. Ferroni, and F. Guadagni. 2014. "Obesity and colorectal cancer: role of adipokines in tumor initiation and progression." *World J Gastroenterol* 20 (18): 5177-90. https://doi.org/10.3748/wjg.v20.i18.5177. https://www.ncbi.nlm.nih.gov/pubmed/24833848.

Rios de la Rosa, J. M., J. Wubetu, N. Tirelli, and A. Tirella. 2018. "Colorectal tumor 3D in vitro models: advantages of biofabrication for the recapitulation of early stages of tumour development." *Biomedical Physics & Engineering Express* 4 (4). https://doi.org/10.1088/2057-1976/aac1c9.

Rodenhizer, D., T. Dean, E. D'Arcangelo, and A. P. McGuigan. 2018. "The Current Landscape of 3D In Vitro Tumor Models: What Cancer Hallmarks Are Accessible for Drug Discovery?" *Adv Healthc Mater* 7 (8): e1701174. https://doi.org/10.1002/adhm.201701174. https://www.ncbi.nlm.nih.gov/pubmed/29350495.

Sachs, N., and H. Clevers. 2014. "Organoid cultures for the analysis of cancer phenotypes." *Curr Opin Genet Dev* 24: 68-73. https://doi.org/10.1016/j.gde.2013.11.012. https://www.ncbi.nlm.nih.gov/pubmed/24657539.

Schaeybroeck, Sandra Van, Mark Lawler, Brian Johnston, Manuel Salto-Tellez, Jack Lee, Paula Loughlin, Richard Wilson, and Patrick G. Johnston. 2014. "Chapter 77 - Colorectal Cancer." In *Abeloff's Clinical Oncology (Fifth Edition)*, edited by John E. Niederhuber, James O. Armitage, James H. Doroshow, Michael B. Kastan and Joel E. Tepper, 1278 - 1335.e14. Philadelphia: Elsevier.

Schrader, J., T. T. Gordon-Walker, R. L. Aucott, M. van Deemter, A. Quaas, S. Walsh, D. Benten, S. J. Forbes, R. G. Wells, and J. P. Iredale. 2011. "Matrix stiffness modulates proliferation, chemotherapeutic response, and dormancy in hepatocellular carcinoma cells." *Hepatology* 53 (4): 1192-205. https://doi.org/10.1002/hep.24108. https://www.ncbi.nlm.nih.gov/pubmed/21442631.

Seol, H. S., H. J. Kang, S. I. Lee, N. E. Kim, T. I. Kim, S. M. Chun, T. W. Kim, C. S. Yu, Y. A. Suh, S. R. Singh, S. Chang, and S. J. Jang. 2014. "Development and characterization of a colon PDX model that reproduces drug responsiveness and the mutation profiles of its original tumor." *Cancer Lett* 345 (1): 56-64. https://doi.org/10.1016/j.canlet.2013.11.010. https://www.ncbi.nlm.nih.gov/pubmed/24333725.

Shakibaei, M., P. Kraehe, B. Popper, P. Shayan, A. Goel, and C. Buhrmann. 2015. "Curcumin potentiates antitumor activity of 5-fluorouracil in a 3D alginate tumor microenvironment of colorectal cancer." *BMC Cancer* 15: 250. https://doi.org/10.1186/s12885-015-1291-0. https://www.ncbi.nlm.nih.gov/pubmed/25884903.

Shin, J. H., J. H. Bae, A. Lee, C. K. Jung, H. W. Yim, J. S. Park, and K. Y. Lee. 2010. "CK7, CK20, CDX2 and MUC2 Immunohistochemical staining used to distinguish metastatic colorectal carcinoma involving ovary from primary ovarian mucinous adenocarcinoma."

Jpn J Clin Oncol 40 (3): 208-13. https://doi.org/10.1093/jjco/hyp150. https://www.ncbi.nlm.nih.gov/pubmed/19926591.

Siegel, R. L., K. D. Miller, and A. Jemal. 2020. "Cancer statistics, 2020." *CA Cancer J Clin* 70 (1): 7-30. https://doi.org/10.3322/caac.21590. https://www.ncbi.nlm.nih.gov/pubmed/31912902.

Simon, K. A., B. Mosadegh, K. T. Minn, M. R. Lockett, M. R. Mohammady, D. M. Boucher, A. B. Hall, S. M. Hillier, T. Udagawa, B. K. Eustace, and G. M. Whitesides. 2016. "Metabolic response of lung cancer cells to radiation in a paper-based 3D cell culture system." *Biomaterials* 95: 47-59. https://doi.org/10.1016/j.biomaterials.2016.03.002. https://www.ncbi.nlm.nih.gov/pubmed/27116031.

Stadler, M., M. Scherzer, S. Walter, S. Holzner, K. Pudelko, A. Riedl, C. Unger, N. Kramer, B. Weil, J. Neesen, M. Hengstschlager, and H. Dolznig. 2018. "Exclusion from spheroid formation identifies loss of essential cell-cell adhesion molecules in colon cancer cells." *Sci Rep* 8 (1): 1151. https://doi.org/10.1038/s41598-018-19384-0. https://www.ncbi.nlm.nih.gov/pubmed/29348601.

Subramanian, Aravind, Pablo Tamayo, Vamsi K. Mootha, Sayan Mukherjee, Benjamin L. Ebert, Michael A. Gillette, Amanda Paulovich, Scott L. Pomeroy, Todd R. Golub, Eric S. Lander, and Jill P. Mesirov. 2005. "Gene set enrichment analysis: a knowledge-based approach for interpreting genome-wide expression profiles." *Proceedings of the National Academy of Sciences of the United States of America* 102 (43): 15545-15550. https://doi.org/10.1073/pnas.0506580102. https://www.ncbi.nlm.nih.gov/pubmed/16199517 https://www.ncbi.nlm.nih.gov/pmc/articles/PMC1239896/.

Supek, Fran, Matko Bošnjak, Nives Škunca, and Tomislav Šmuc. 2011. "REVIGO summarizes and visualizes long lists of gene ontology terms." *PloS one* 6 (7): e21800.

Swaminathan, V., K. Mythreye, E. T. O'Brien, A. Berchuck, G. C. Blobe, and R. Superfine. 2011. "Mechanical stiffness grades metastatic potential in patient tumor cells and in cancer cell lines." *Cancer Res* 71 (15): 5075-80. https://doi.org/10.1158/0008-5472.CAN-11-0247. https://www.ncbi.nlm.nih.gov/pubmed/21642375.

Szot, C. S., C. F. Buchanan, J. W. Freeman, and M. N. Rylander. 2011. "3D in vitro bioengineered tumors based on collagen I hydrogels." *Biomaterials* 32 (31): 7905-12. https://doi.org/10.1016/j.biomaterials.2011.07.001. https://www.ncbi.nlm.nih.gov/pubmed/21782234.

Thomlinson, R. H., and L. H. Gray. 1955. "The histological structure of some human lung cancers and the possible implications for radiotherapy." *Br J Cancer* 9 (4): 539-49. https://doi.org/10.1038/bjc.1955.55. https://www.ncbi.nlm.nih.gov/pubmed/13304213.

Tian, Yuan, and Elizabeth A. Lipke. 2020. "Microfluidic Production of Cell-Laden Microspheroidal Hydrogels with Different Geometric Shapes." *ACS Biomaterials Science & Engineering*. https://doi.org/10.1021/acsbiomaterials.0c00980.

Toyoshima, M., Y. Momono, H. Makino, T. Kudo, N. Oka, J. Sakurada, H. Suzuki, H. Kodama, and K. Yoshinaga. 2016. "Cytokeratin 7-positive/cytokeratin 20-negative cecal adenocarcinoma metastatic to the uterine cervix: a case report." *World J Surg Oncol* 14 (1): 22. https://doi.org/10.1186/s12957-016-0774-z. https://www.ncbi.nlm.nih.gov/pubmed/26810414.

Truong, D. D., A. Kratz, J. G. Park, E. S. Barrientos, H. Saini, T. Nguyen, B. Pockaj, G. Mouneimne, J. LaBaer, and M. Nikkhah. 2019. "A Human Organotypic Microfluidic

Tumor Model Permits Investigation of the Interplay between Patient-Derived Fibroblasts and Breast Cancer Cells." *Cancer Res* 79 (12): 3139-3151. https://doi.org/10.1158/0008-5472.CAN-18-2293. https://www.ncbi.nlm.nih.gov/pubmed/30992322.

Truong, D., J. Puleo, A. Llave, G. Mouneimne, R. D. Kamm, and M. Nikkhah. 2016. "Breast Cancer Cell Invasion into a Three Dimensional Tumor-Stroma Microenvironment." *Sci Rep* 6: 34094. https://doi.org/10.1038/srep34094. https://www.ncbi.nlm.nih.gov/pubmed/27678304.

Vaz, M. A., J. C. Martinez, J. M. Devesa, J. D. Trill, V. Abraira, A. Riquelme, and A. Carrato. 2014. "Prognostic value of stem cell quantification in stage II colon cancer." *PLoS One* 9 (2): e88480. https://doi.org/10.1371/journal.pone.0088480. https://www.ncbi.nlm.nih.gov/pubmed/24586330.

Verissimo, C. S., R. M. Overmeer, B. Ponsioen, J. Drost, S. Mertens, I. Verlaan-Klink, B. V. Gerwen, M. van der Ven, M. V. Wetering, D. A. Egan, R. Bernards, H. Clevers, J. L. Bos, and H. J. Snippert. 2016. "Targeting mutant RAS in patient-derived colorectal cancer organoids by combinatorial drug screening." *Elife* 5. https://doi.org/10.7554/eLife.18489. https://www.ncbi.nlm.nih.gov/pubmed/27845624.

Walrath, J. C., J. J. Hawes, T. Van Dyke, and K. M. Reilly. 2010. "Genetically engineered mouse models in cancer research." *Adv Cancer Res* 106: 113-64. https://doi.org/10.1016/S0065-230X(10)06004-5. https://www.ncbi.nlm.nih.gov/pubmed/20399958.

Weatherly, D. B., J. A. Atwood, 3rd, T. A. Minning, C. Cavola, R. L. Tarleton, and R. Orlando. 2005. "A Heuristic method for assigning a false-discovery rate for protein identifications from Mascot database search results." *Mol Cell Proteomics* 4 (6): 762-72.

https://doi.org/10.1074/mcp.M400215-MCP200. https://www.ncbi.nlm.nih.gov/pubmed/15703444.

Wei, B., X. Y. Han, C. L. Qi, S. Zhang, Z. H. Zheng, Y. Huang, T. F. Chen, and H. B. Wei. 2012. "Coaction of spheroid-derived stem-like cells and endothelial progenitor cells promotes development of colon cancer." *PLoS One* 7 (6): e39069. https://doi.org/10.1371/journal.pone.0039069. https://www.ncbi.nlm.nih.gov/pubmed/22745705.

Welte, Y., C. Davies, R. Schafer, and C. R. Regenbrecht. 2013. "Patient derived cell culture and isolation of CD133(+) putative cancer stem cells from melanoma." *J Vis Exp* (73): e50200. https://doi.org/10.3791/50200. https://www.ncbi.nlm.nih.gov/pubmed/23525090.

Wong, C. H., K. W. Siah, and A. W. Lo. 2019. "Estimation of clinical trial success rates and related parameters." *Biostatistics* 20 (2): 273-286. https://doi.org/10.1093/biostatistics/kxx069. https://www.ncbi.nlm.nih.gov/pubmed/29394327.

Xu, K., K. Ganapathy, T. Andl, Z. Wang, J. A. Copland, R. Chakrabarti, and S. J. Florczyk. 2019. "3D porous chitosan-alginate scaffold stiffness promotes differential responses in prostate cancer cell lines." *Biomaterials* 217: 119311. https://doi.org/10.1016/j.biomaterials.2019.119311. https://www.ncbi.nlm.nih.gov/pubmed/31279100.

Yang, L., S. Wang, J. J. Lee, S. Lee, E. Lee, E. Shinbrot, D. A. Wheeler, R. Kucherlapati, and P. J. Park. 2019. "An enhanced genetic model of colorectal cancer progression history." *Genome Biol* 20 (1): 168. https://doi.org/10.1186/s13059-019-1782-4. https://www.ncbi.nlm.nih.gov/pubmed/31416464.

Yang, X., S. K. Sarvestani, S. Moeinzadeh, X. He, and E. Jabbari. 2013. "Three-dimensional-engineered matrix to study cancer stem cells and tumorsphere formation: effect of matrix modulus." *Tissue Eng Part A* 19 (5-6): 669-84. https://doi.org/10.1089/ten.TEA.2012.0333. https://www.ncbi.nlm.nih.gov/pubmed/23013450.

Yuan, Yao, Yu-Chen Jiang, Chong-Kui Sun, and Qian-Ming Chen. 2016. "Role of the tumor microenvironment in tumor progression and the clinical applications (Review)." *Oncology Reports* 35 (5): 2499-2515. https://doi.org/10.3892/or.2016.4660. https://dx.doi.org/10.3892/or.2016.4660.

Zaman, M. H., L. M. Trapani, A. L. Sieminski, D. Mackellar, H. Gong, R. D. Kamm, A. Wells, D. A. Lauffenburger, and P. Matsudaira. 2006. "Migration of tumor cells in 3D matrices is governed by matrix stiffness along with cell-matrix adhesion and proteolysis." *Proc Natl Acad Sci U S A* 103 (29): 10889-94. https://doi.org/10.1073/pnas.0604460103. https://www.ncbi.nlm.nih.gov/pubmed/16832052.

Zhou, J., L. Belov, M. J. Solomon, C. Chan, S. J. Clarke, and R. I. Christopherson. 2011. "Colorectal cancer cell surface protein profiling using an antibody microarray and fluorescence multiplexing." *J Vis Exp* (55). https://doi.org/10.3791/3322. https://www.ncbi.nlm.nih.gov/pubmed/21968569.

Appendix A: Method Details

A.1 Fabrication of PDMS Molds

Polydimethylsiloxane (PDMS) molds were fabricated using the SYLGARD® 184 Silicone Elastomer Kit (Dow Corning). SYLGARD® 184 Silicone Elastomer base and SYLGARD® 184 Silicone Elastomer curing agent were mixed thoroughly at a ratio of 10:1 (w/w). The mixture was then degassed using a desiccator equipped with a vacuum pump for 15 minutes to remove any air bubbles. The liquid PDMS was poured onto a glass piece, sandwiched by another glass, and cured in an oven at 70 °C for 1 hour. The PDMS layer was then separated from the glasses, and 1-inch PDMS disks, each with ten 4 mm diameter wells were made using a hole-punch kit.

A.2 CRC-PDX Tumor Dissociation and Cell Isolation

Using an optimized method adapted from previous publications (Chou et al. 2013; Devaud et al. 2014; Seol et al. 2014; Welte et al. 2013; Zhou et al. 2011), a portion of the excised tumor was dissociated to isolate the cells for subsequent *in vitro* culture as 2D-CRC-PDX cells and 3D-eCRC-PDX tissues. A dissociation solution with a final concentration of 250 U/mL collagenase IV (Worthington) and 100 U/mL deoxyribonuclease I (DNase I) (Worthington) in Hank's Buffered Saline Solution (HBSS) (Lonza) was prepared with gentle mixing and sterile-filtered using a 0.2 µm syringe filter (VWR). Fresh CRC PDX tissues were collected and placed on a sterile Petri dish. The tissues were washed with 1X phosphate-buffered saline (PBS) (Lonza), and 10 mL of dissociation solution per 1 g of tissue was added to the Petri dish. The tumor was minced into small pieces between 2-4 mm using sterile surgical scissors. Minced CRC-PDX tumor (500 mg) was transferred into a 50 mL centrifuge tube, along with 5 mL of fresh dissociation solution, and incubated at 37 °C. The tube was manually swirled every 5 minutes to resuspend settled tissue

fragments. The supernatant containing the dissociated cells was collected in a 50 mL centrifuge tube every 10 minutes, and 5 mL of fresh, pre-warmed (37 °C) dissociation solution was added to the minced tissue. When all tissue segments were dissociated (approximately 1 hour of incubation), the total collected supernatant containing CRC PDX cells was passed through a 40-μm cell strainer (Corning) and the strainer was rinsed with 20 mL of HBSS. The cell suspension was centrifuged at 300 ×g for 5 min without the brake, the supernatant was removed, and the cell pellets were resuspended in 10 mL of cell culture media. Media for all experiments was composed of DMEM (Lonza) containing 10% (v/v) fetal bovine serum (FBS) (Atlanta Biologicals™), 1% (v/v) penicillin:streptomycin solution (pen/strep) (HyClone™), and 2 mM glutagro™ Supplement (Corning). The centrifugation was repeated for a total of six times to remove dead cells and extracellular matrix (ECM) debris from the cell suspension as much as possible. Finally, the viable cells were labeled with trypan blue (Lonza) and manually counted using a hemocytometer.

A.3 Formation and Culture of 3D-eCRC-PDX Tissues

To create the 3D-eCRC-PDX tissues, the isolated CRC PDX cells were mixed with a polymer precursor solution containing poly(ethylene glycol)-fibrinogen (PEG-Fb) with a final concentration of 1.5% (v/v) triethanolamine (TEOA) (Acros Organics), 37 mM 1-vinyl-2-pyrrolidinone (NVP) (Sigma-Aldrich), and 0.1 mM Eosin Y in PBS at a density of 20×10^6 cells/mL. The cell-laden precursor solution was gently added to the PDMS mold wells (10 μl/well) and photocrosslinked with visible light for 2 minutes. Molds were then removed, and cell culture media was added. The 3D-eCRC-PDX tissues were maintained in long-term culture (29 days) in a standard incubator with a temperature of 37 °C and 5% CO_2 with media refreshes every 2-3 days.

A.4 2D CRC PDX Cell Culture

CRC cells isolated from the CRC-PDX tumors were cultured in T-75 standard cell culture flasks using the same cell culture media as was employed for the 3D-eCRC-PDX tissues. These 2D cultured CRC PDX (2D-CRC-PDX) cells were passaged after 8 days of culture and subsequently passaged every 7 days up to a total of 29 days. Importantly, since non-adherent cell types (mostly cell aggregates) were present, the spent media containing the 2D-CRC2D-CRC-PDX cells was also collected and centrifuged at 300 ×g. The non-adherent cell pellets were then resuspended in fresh media and recombined with the seeded adherent cells. All of the cultured cells were maintained in a standard incubator with a temperature of 37 °C and 5% CO_2, with media changes every 2-3 days.

A.5 Cell Viability Assay and Image Analysis

A cell viability assay was performed using the LIVE/DEAD® Viability/Cytotoxicity Kit (ThermoFisher Scientific) according to the manufacturer's protocol. Briefly, the optimal dye concentration was determined and accordingly, a viability solution was prepared by mixing the 4 mM calcein AM stock solution (live dye) and 2 mM ethidium homodimer-1 (EthD-1) stock solution (dead dye) at ratios of 1:2000 and 1:500 in PBS, respectively. To quantify the percentage of live cells, a viability working solution was made by adding Hoechst 33342 (Calbiochem) (20 µg/mL) to the viability solution to counterstain the cell nuclei. The 3D-eCRC-PDX tissues were washed thoroughly with PBS (3 times over 15 minutes) and incubated in the viability working solution at room temperature for 30 minutes in the dark. For the 2D-CRC-PDX cell viability assay on Day 1, the cells previously cultured on a 24-well plate were washed thoroughly with PBS three times prior to adding the working solution. Since most of the cell colonies did not adhere to the

tissue culture surface, the cell culture media containing these non-adherent cell colonies was also collected, placed into a centrifuge tube, centrifuged at 300 ×g for 5 minutes, and then washed three times with PBS. After the final washing step, the cell colonies were resuspended in the viability assay working solution and added to the adherent 2D-CRC-PDX cells. The confocal viability images presented in Figure A.1 B were processed using ImageJ software (version: 2.0.0-rc-68/1.52e) as Z-Projection, meaning that the captured Z-stack of images for each 3D-eCRC-PDX tissue was flatted into one layer of image.

A.6 Flow Cytometry

Here, we present a comprehensive protocol for cell immunolabeling and flow cytometry analysis of the cells from the CRC-PDX tumors, 3D-eCRC-PDX tissues, and 2D-CRC-PDX cultures. It must be noted that the centrifuge brake was turned off throughout the entire process to minimize cell loss. Moreover, centrifugation was performed at 300 ×g for 5 minutes throughout the process unless otherwise stated. Cell preparation, antibody-Zenon™ labeling conjugate preparation, cell labeling, compensation controls, unstained controls, viability controls, and flow cytometer and data analysis are described.

Cell Preparation: For the CRC-PDX tumors, the cells were cultured on T-75 standard tissue culture flasks in CRC-PDX media and maintained in a standard incubator with a temperature of 37 °C and 5% CO2. Cells were given 12 hours to retrieve surface proteins that may have been damaged during the process of dissociation. After 12-hours of surface protein retrieval, the media containing non-adherent cells (mostly cell colonies) was collected into a centrifuge tube, centrifuged, and washed twice with PBS (the adherent cells were washed with PBS twice as well). After the final washing step, the cells were resuspended in Accumax (Innovative Cell Technology,

Inc.) and placed back into the culture flask alongside the adherent cells. All cells were then incubated in a total amount of 3 mL Accumax at room temperature. The cell suspension in the flask was mixed using a pipette every 5 minutes to help dissociate the cells and examined under a microscope to check for single cells. When single cells were achieved (typically after 30 minutes of incubation), the cell suspension was collected into a centrifuge tube and washed with PBS once to remove Accumax from the suspension, and the cells were resuspended in PBS for labeling.

To begin 3D-eCRC-PDX cell preparation for flow cytometry, a dissociation solution was prepared by gently mixing 250 U/mL collagenase IV in PBS, followed by filter sterilization. The desired number of 3D-eCRC-PDX tissues (typically 3 to 5) were placed in a 1.5 mL centrifuge tube and washed with PBS twice over 10 minutes. The PBS was removed, and the dissociation solution was added to the 3D-eCRC-PDX tissues. The 3D-eCRC-PDX tissues were then incubated for 30 minutes at 37 °C, and the suspension was mixed every 10 minutes using a micropipette. The cell suspension was then centrifuged, and the cells were resuspended in Accumax and incubated at room temperature with mixing every 5 minutes until single cells were achieved (typically for 30 minutes). The dissociated single cells were centrifuged to remove Accumax and resuspended in PBS. The dissociated single cells from 3D-eCRC-PDX tissues were ready for labeling at this point.

For 2D-CRC-PDX cell preparation for flow cytometry, the process of cell preparation was similar to that of the isolated cells from CRC-PDX tumors; however, the 12-hour surface protein retrieval was not necessary because the 2D-CRC-PDX cells had been maintained in culture for 7 days.

Antibody-Zenon™ Labeling Conjugate Preparation: To label the cells, β-2-microglobulin (B2M) mouse IgG2a mAb, MHC Class I H-2 Db antibody (H2Db) mouse IgG2a mAb, cytokeratin 20 (CK20) rabbit IgG mAb, and Ki-67 rabbit IgG pAb were used to mark human-derived cells,

mouse cells, CRC cells, and proliferative cells, respectively. All primary antibodies were conjugated to Zenon™ Labeling Kits. B2M mouse IgG2a mAb, H2Db mouse IgG2a mAb, CK20 rabbit IgG mAb, and Ki-67 rabbit IgG pAb were conjugated to Zenon™ R-phycoerythrin (PE) mouse IgG2a, Zenon™ R-phycoerythrin (PE) mouse IgG2a, Zenon™ Alexa Fluor™ 647 rabbit IgG, and Zenon™ Alexa Fluor™ 647 rabbit IgG Labeling Kits, respectively, according to the manufacturer protocol. As such, a required amount (calculated based on the number of samples) of primary antibody solution with a concentration of 50 µg/mL in PBS (the corresponding volume of the primary antibody was calculated based on the antibody concentration) was prepared in a microcentrifuge tube. One volume of Zenon™ labeling reagent (Component A) was added to 4 volumes of primary antibody solution, mixed gently, and incubated for 5 minutes at room temperature, protected from light. Then, an equal amount of Zenon™ blocking reagent (Component B) was added to the mixture, mixed gently, and incubated for 5 minutes at room temperature, protected from light. The antibody-Zenon™ labeling conjugate was ready at this point and applied to the samples within 30 minutes.

To distinguish nonspecific background signal from a particular antibody, isotype controls that matched the class and type of the primary antibodies were used. Mouse IgG2a isotype control (ThermoFisher Scientific) and rabbit IgG isotype control (ThermoFisher Scientific) with sat the same concentration as the corresponding primary antibodies were conjugated to Zenon™ R-phycoerythrin (PE) mouse IgG2a and Zenon™ Alexa Fluor™ 647 rabbit IgG labeling kit according to the above protocol.

Cell Labeling: After the cell preparation step, the cells were transferred to 1.5 mL centrifuge tubes, washed with cold protein-free PBS, and centrifuged. To exclude dead cells and debris from the analysis, 100 µL viability solution was prepared for each sample tube by mixing

Zombie Green™ dye in PBS at a ratio of 1:1000 (based on titration). The viability solution was added to the cells, and cells were incubated at 4 °C for 30 minutes in the dark. The cells were then washed by adding 1.3 mL of cold blocking buffer (0.5 % (w/v) BSA and 10 % (v/v) FBS in 1X PBS) to the sample tube and mixing gently, centrifuged, and the supernatant was decanted. To block nonspecific binding on the cell surface, 90 µL of cold blocking buffer containing Human BD Fc Block™ (12 mg/L) and Mouse BD Fc Block™ (5 mg/L) was added to the cells, and the cells were vortexed briefly and incubated at 4 °C for 30 minutes, protected from light. For surface staining, B2M antibody conjugated to Zenon™ PE was added directly to cells with a final primary antibody (B2M) concentration of 0.4 mg/L. The cells were incubated at 4 °C for 30 minutes in the dark. After the incubation, the cells were fixed and permeabilized by adding 0.5 mL of cold Foxp3 Fixation/Permeabilization (eBioscience™) working solution (prepared according to manufacturer protocol by mixing 1 part of Foxp3 Fixation/Permeabilization Concentrate with 3 parts of Foxp3 Fixation/Permeabilization Diluent) to each sample tube, pulse vortexing, and incubating at 4 °C for 30 minutes in the dark. The cells were then centrifuged to remove the Foxp3 Fixation/Permeabilization solution and washed with 1.3 mL of 1X Permeabilization Buffer (eBioscience™) once. To block nonspecific binding for intracellular staining, 90 µL of FACS buffer (0.5 % (w/v) BSA and 10 % (v/v) FBS in 1X Permeabilization Buffer) was added to the cells, and the cells were vortexed briefly and incubated at room temperature for 30 minutes in the dark. For intracellular staining, the conjugated antibodies were directly added to the cells, and the cells were vortexed briefly and incubated at room temperature for 30 minutes in the dark. It should be noted that we had to use separate samples for each primary antibody-Zenon™ conjugate as a similar Zenon™ labeling kit (Zenon™ Alexa Fluor™ 647) was used to create CK20-Zenon™ conjugate and Ki-67-Zenon™ conjugate. After a 30-minute incubation, 1.3 mL of 1X

Permeabilization Buffer was added to each tube and the cells were incubated for 10 minutes at room temperature in the dark and centrifuged to remove unbound antibodies. The washing step was repeated once more, and the cells were resuspended in the blocking buffer and filtered using 40 μm Scienceware® Flowmi™ Cell Strainers before analyzing via a BD Accuri C6 cytometer (BD Biosciences).

Compensation Controls: Compensation beads (ThermoFisher Scientific) were used according to the manufacturer protocol to ensure that the fluorescent signal measured by each flow cytometer filter is merely due to the fluorochrome of interest and to accurately set the compensation if there was any overlap between the fluorochromes. Briefly, AbCTM Total Compensation capture beads (Component A) and negative beads (Component B) were resuspended thoroughly by vortexing for 10 seconds. One drop of Component A was added to a 1.5 mL centrifuge tube for each fluorochrome-conjugated antibody. Each antibody-Zenon™ labeling conjugate was added to the designated tube, mixed, and incubated for 15 minutes at room temperature in the dark. PBS (1.3 mL) was then added to the beads, and the beads were centrifuged and resuspended by adding 0.5 mL of PBS. One drop of Component B was then added to the tubes, and the beads were mixed thoroughly and vortexed before analyzing by flow cytometry.

Unstained Controls: To check for cell autofluorescence, unstained cells were used. The unstained cells underwent the entire flow cytometry protocol with the exception of adding Zombie Green™ and the antibody-Zenon™ labeling conjugates.

Viability Controls: To set an accurate compensation for Zombie Green™ dye, some cells were killed using pure ethanol. Briefly, 2×10^5 of prepared cells in PBS were transferred in a 1.5 mL centrifuge tube and centrifuged at 200 ×g for 5 minutes. The supernatant was then removed, and 1 mL of pure ethanol was added to the cells. The cells were incubated at room temperature for

5 minutes and immediately centrifuged at 200 ×g for 5 minutes. After centrifugation, the ethanol was removed thoroughly, and the cells were washed once with PBS, resuspended in 100 µL viability solution, and incubated at 4 °C for 20 minutes in the dark. The cells were washed by adding 1.3 mL of cold blocking buffer to the sample tube and mixing gently, centrifuged at 200 ×g for 5 minutes, resuspended in the blocking buffer and filtered using 40 µm Scienceware® Flowmi™ Cell Strainers before analyzing via BD Accuri C6 cytometer.

Flow Cytometer and Data Analysis: A BD Accuri C6 cytometer was used to analyze the labeled cells. The cytometer was equipped with two excitation lasers, 488nm (blue) and 635nm (red), and four filters, FL1 533/30, FL2 585/40, FL3 670/LP, and FL4 675/25. The Zombie Green™ dye and Zenon™ PE were excited by the blue laser and captured by FL1 and FL2, respectively, and the Zenon™ Alexa Fluor™ 647 was excited by the red laser and captured by FL4. Twenty thousand events were counted for compensation, unstained, and viability controls. For the labeled cells, twenty thousand viable cells were counted from each sample tube.

FlowJo software (version 10.0.7) was employed for flow cytometry data analysis. Briefly, a compensation matrix was created based on compensation beads and dead cell control. Small debris and particles were gated out using the side scattering-area (SSC-A) vs. forward scattering-area (FSC-A) graph. By excluding the small debris and particles and only looking at the cells, the singlets were gated on using forward scattering-height (FSC-H) vs. FSC-A graph. Then the dead cells were gated out from the singlets using FSC-H vs. Compensated FL1-Height (Comp-FL1-H) (Zombie Green™ dye). By looking at the viable singlets, the Comp-FL4-H vs. Comp-FL3-H graph was used to analyzed $B2M^{+/-}$ and $CK20^{+/-}$ cells or the $B2M^{+/-}$ and $Ki\text{-}67^{+/-}$ cells. Furthermore, the Comp-FL4-H vs. Comp-FL3-H graph was used to check whether unstained cells were autofluorescent and whether there was nonspecific binding on isotype control.

A.7 Immunostaining for Examination of Cell Morphology

To study the cell morphology within both 3D-eCRC-PDX tissues and the 2D-CRC-PDX cultures, the cells were labeled with Hoechst 33342, B2M, Phalloidin, and CK20 to observe the cell nuclei, human-derived cells, f-Actin filaments, and CRC cells, respectively. Briefly, the 3D-eCRC-PDX tissues and 2D-CRC-PDX cells were separately washed 3 times with 1X PBS over a period of 10 minutes. The PBS was then removed, and the cells were fixed using 4% paraformaldehyde (Electron Microscopy Sciences, 15710) (diluted in PBS) for 1 hour at room temperature. Next, samples were rinsed with PBS 2 times over a period of 10 minutes and subsequently permeabilized using sterile-filtered PBS-T (1% w/v BSA and 0.2% v/v TritonX (Sigma-Aldrich) in PBS) for 30 minutes on an Orbitron. The PBS-T was removed, and the samples were incubated in blocking buffer (0.5 % (w/v) BSA and 10 % (v/v) FBS in 1X PBS) for 2 hours at room temperature. The blocking buffer was discarded and a solution of B2M primary antibody in blocking buffer (5 μg/mL) was added to the cells and the cells were again incubated at room temperature for 2 hours. Next, cells were washed with PBS-T 3 times over a period of 15 minutes; PBS-T was removed, a blocking buffer solution containing goat anti-mouse IgG Alexa Fluor™ 488 (ThermoFisher Scientific) (1:100 ratio), Alexa Fluor™ 568 Phalloidin (ThermoFisher Scientific) (1:100 ratio), and CK20 rabbit IgG mAb conjugated to Zenon™ Alexa Fluor™ 647 rabbit IgG (1.25 μg/mL) was added and samples were then incubated for 2 hours at room temperature. Finally, cells were washed with PBS-T 3 times over a period of 15 minutes, counterstained using Hoechst 33342 (20 μg/mL) for 30 minutes.

A.8 Histological Examination of CRC-PDX Tumors and 3D-eCRC-PDX Tissues

To stain the samples, the CRC-PDX tumors and 3D-eCRC-PDX tissues were washed with 1X PBS, fixed with 4% paraformaldehyde, dehydrated with increasing grades of ethanol (70% to 100%), cleared in Hemo-De, soaked in wax, embedded in paraffin, and sectioned. The sections (6 μm) were cleared using Hemo-De (3 washes; 8 minutes each), rehydrated with decreasing grades of ethanol (100% to 80%) and rinsed with distilled water, stained with Mayers Hematoxylin for 8 minutes, rinsed with tap water for 20 minutes and 80% ethanol for 2 minutes, stained with eosin-phloxine B solution for 2 minutes, dehydrated by increasing grades of ethanol (70% to 100%), and finally cleared using Hemo-De (3 washes; 8 minutes each). A thin layer of Eukitt™ mounting medium was applied and the slides were covered with clean coverslips. The stained sections were scanned using an Aperio CS2 scanner (Leica Biosystems) at 40x magnification. The digital images were viewed using Aperio ImageScope (Ver. 12.3.2.8013).

A.9 Mechanical Stiffness

The mechanical stiffness of CRC-PDX tumors and 3D-eCRC-PDX tissues was evaluated using a CellScale MicroSquisher system and the associated SquisherJoy software. Briefly, the geometric core, midpoint, and periphery of CRC-PDX tumors were cut into disk-shaped slices with a diameter of approximately 3 mm and a thickness of approximately 1 mm (thus resembling the 3D-eCRC-PDX tissue geometry) using a sterile scalpel (Bard-Parker®) and a surgical punch (Sklar). All tumors and tissues were subjected to parallel compression testing under physiological temperatures in a PBS bath using the MicroSquisher apparatus. The compression system was equipped with a 558.8 μm gauge cantilever beam and a square microplate. All samples were preconditioned to 30% deformation for 3 compressions before data were collected. The force

versus displacement data were then obtained via compression and relaxation cycles at a rate of 10 μm/s to 30% deformation. The data were then converted to stress-strain curves, linear least-squares fitting was performed on the linear portion of the curves, and Young's moduli of the tissue samples were calculated.

A.10 Proteomics Analysis

Sample Preparation: CRC-PDX tumors and 3D-eCRC-PDX tissues were processed via Millipore Compartmental Protein Extraction Kit following the manufacturer's instruction. Of note, tissues were weighed prior to processing, and buffer volume was adjusted appropriately based on the sample weight. Following sequential extraction of cytoplasmic, nuclear, membrane, and cytoskeletal proteins via the kit (Naba et al. 2012; Naba, Clauser, and Hynes 2015), the remaining pellet was washed once with 500 μL of PBS and reconstituted in 2x Novex NuPAGE LDS sample buffer (Invitrogen) supplemented with 2x NuPAGE sample reducing agent (Invitrogen). ECM-enriched fractions were then sonicated in an ultrasonic water bath for 20min. at ambient temperature. Debris was removed by centrifugation for 20min. at 16,000×g, 4°C. Proteomics analysis was carried out as previously referenced with minor changes (Ludwig et al. 2016). The ECM-enriched fraction was quantified using an EZQ Protein Quantitation Kit (Invitrogen). Twenty micrograms of protein per sample were then diluted to 35 μL using NuPAGE LDS sample buffer (1x final conc.) and denatured at 70°C for 10min. prior to loading onto a Novex NuPAGE 10% Bis-Tris Protein gel (Invitrogen) and separated for its full-length (35min. at 200 constant V). The gels were stained overnight with Novex Colloidal Blue Staining Kit (Invitrogen). Following de-staining, each lane was cut into four MW fractions and equilibrated in 100 mM ammonium bicarbonate (AmBc). Each gel plug was then digested overnight with Trypsin Gold, Mass

Spectrometry Grade (Promega) following manufacturer's instruction. Peptide extracts were reconstituted in 0.1% Formic Acid/ ddH_2O at 0.1 µg/µL.

Mass Spectrometry: Peptide digests (8 µL each) were injected onto a 1260 Infinity nHPLC stack (Agilent Technologies), and separated using a 75 micron I.D. x 15 cm pulled tip C-18 column (Jupiter C-18 300 Å, 5 microns, Phenomenex). This system runs in-line with a Thermo Orbitrap Velos Pro hybrid mass spectrometer, equipped with a nano-electrospray source (Thermo Fisher Scientific), and all data were collected in CID mode. The nHPLC was configured with binary mobile phases that included solvent A (0.1%FA in ddH_2O), and solvent B (0.1%FA in 15% ddH_2O / 85% ACN), programmed as follows; 10min @ 5%B (2 µL/min, load), 90min @ 5%-40%B (linear: 0.5 nL/min, analyze), 5min @ 70%B (2 µL/min, wash), 10min @ 0%B (2 µL/min, equilibrate). Following each parent ion scan (300-1200 m/z @ 60k resolution), fragmentation data (MS2) was collected on the top most intense 15 ions. For data-dependent scans, charge state screening and dynamic exclusion were enabled with a repeat count of 2, repeat duration of 30s, and exclusion duration of 90s.

MS Data Conversion and Searches: The XCalibur RAW files were collected in profile mode, centroided, and converted to MzXML using ReAdW v. 3.5.1. The mgf files were then be created using MzXML2Search (included in TPP v. 3.5) for all scans. The data were searched using SEQUEST, which was set for two maximum missed cleavages, a precursor mass window of 20 ppm, trypsin digestion, variable modification C @ 57.0293, and M @ 15.9949. Searches were performed with species-specific subsets of the UniProtKB database (ex: Homo sapiens, Mus musculus).

Peptide Filtering, Grouping, and Quantification: The list of peptide IDs generated based on SEQUEST (Thermo Fisher Scientific) search results were filtered using Scaffold (Protein Sciences, Portland, Oregon). Scaffold filters and groups all peptides to generate and retain only high confidence IDs while also generating normalized spectral counts (N-SC's) across all samples for the purpose of relative quantification. The filter cut-off values were set with a minimum peptide length of >5 AA's, with no MH+1 charge states, with peptide probabilities of >80% C.I., and with the number of peptides per protein ≥2. The protein probabilities were then set to a >99.0% C.I., and an FDR<1.0. Scaffold incorporates the two most common methods for statistical validation of large proteome datasets, the false discovery rate (FDR) and protein probability (Keller et al. 2002; Nesvizhskii et al. 2003; Weatherly et al. 2005). Relative quantifications across experiments were then performed via spectral counting (Old et al. 2005; Liu, Sadygov, and Yates 2004), and when relevant, spectral count abundances were then normalized between samples (Beissbarth et al. 2004).

A.11 Method Validation

In-depth characterization of the models presented in this article can be found in Chapter 3 and Appendix C. Here, we present representative images and data for several described methods. Figure A.1 demonstrates representative images of 3D-eCRC-PDX tissues and 2D-CRC-PDX cells. Figure A.2 displays the cell viability assay for 3D-eCRC-PDX tissues. Figure A.3 exhibits representative flow cytometry graphs used for quantification of cell subpopulations. Figure A.4 presents the images of immunostained cells within the 3D-eCRC-PDX tissues. Figure A.5 shows representative stress vs. strain graph used to calculate Young's modulus of tissues.

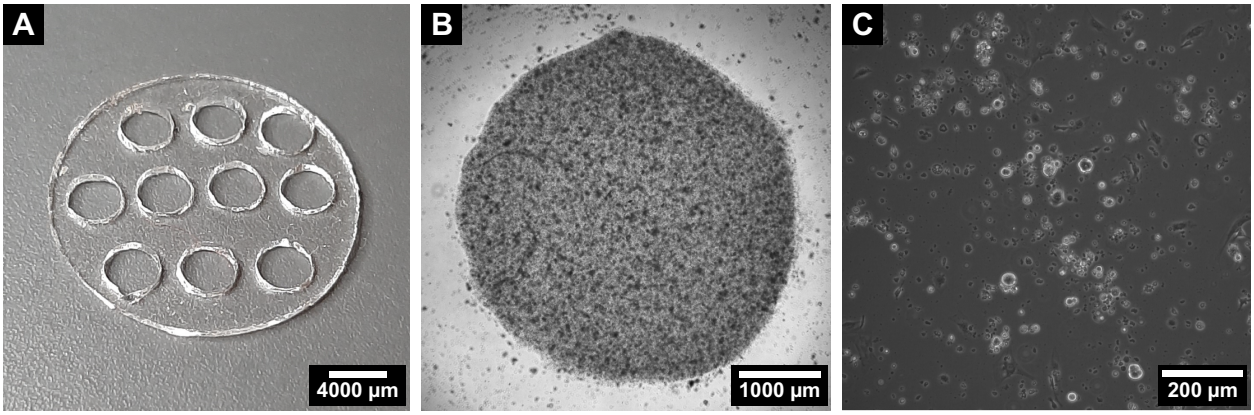

Figure A.1. Representative images of (A) the PDMS mold used to generate 3D-eCRC-PDX tissues, (B) the generated 3D-eCRC-PDX tissues, and (C) 2D-CRC-PDX cells.

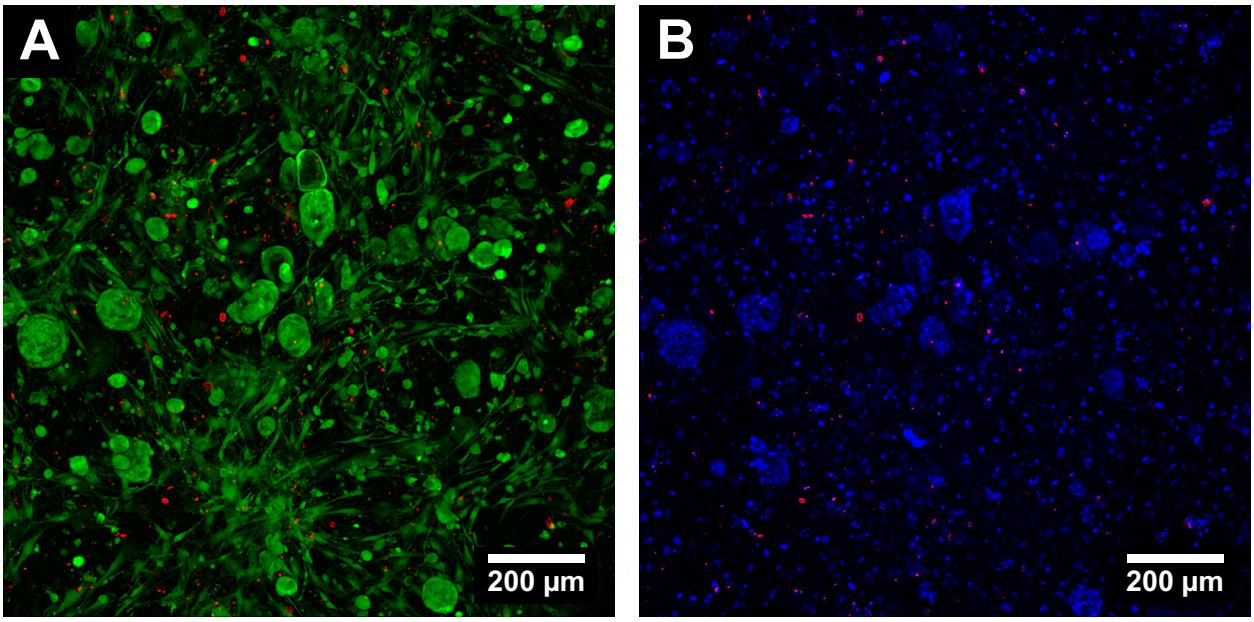

Figure A.2. Representative fluorescent images of cell viability assay for the 3D-eCRC-PDX tissues. (A) The cells were labeled with calcein AM to visualize viable cells (green). (B) The cells were simultaneously labeled with Hoechst 33342 (cell nuclei; blue) and ethidium homodimer-1 (dead cells; red) to count the total number of cells and number of dead cells, respectively, for viability percentage calculation.

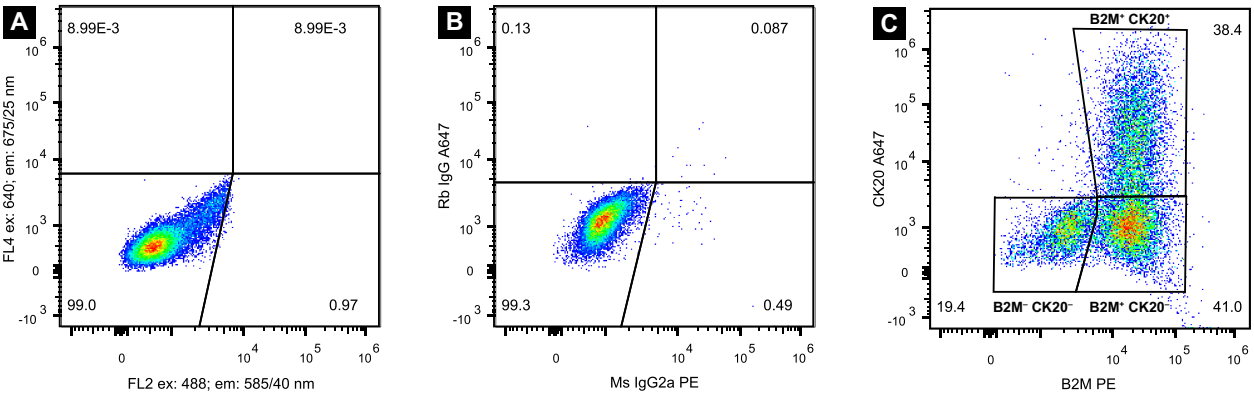

Figure A.3. Quantification of cell subpopulations. Representative flow cytometry graphs demonstrating (A) the unstained CRC-PDX cell control, (B) isotype control, and (C) CRC-PDX cells labeled with B2M and CK20.

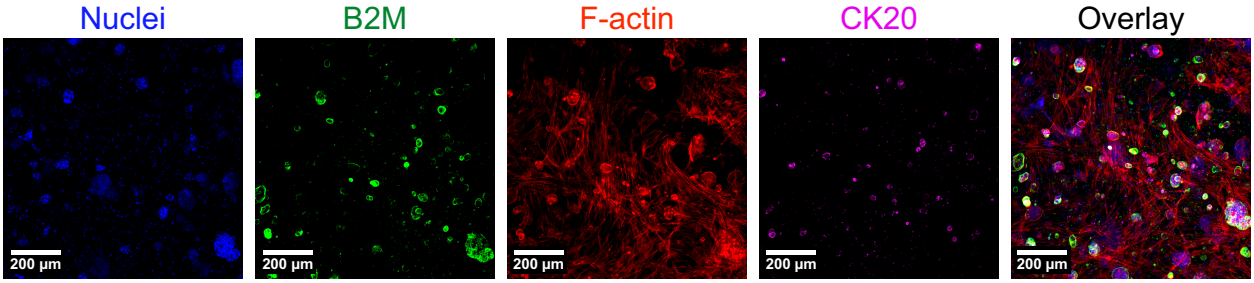

Figure A.4. Immunostaining of the CRC-PDX cells within the 3D-eCRC-PDX tissues. The cells were labeled with Hoechst 33342 (blue), B2M (green), phalloidin (red), and CK20 (magenta) to visualize the morphology of human- and mouse-derived cells.

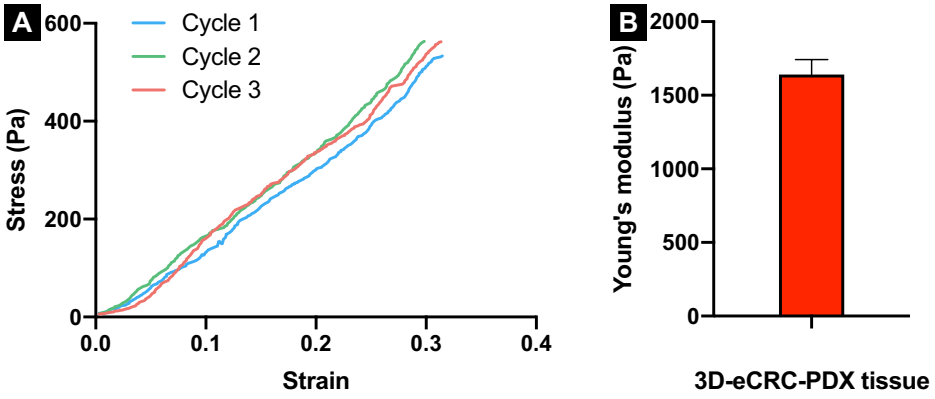

Figure A.5. Mechanical stiffness measurements. (A) A representative graph demonstrating stress vs. strain curves for a 3D-eCRC-PDX tissue. Each tissue was undergone three cycles of compression and relaxation. The average of three slopes was reported as (B) Young's modulus for each 3D-eCRC-PDX tissue.

Appendix B: Supporting Information for Chapter 2

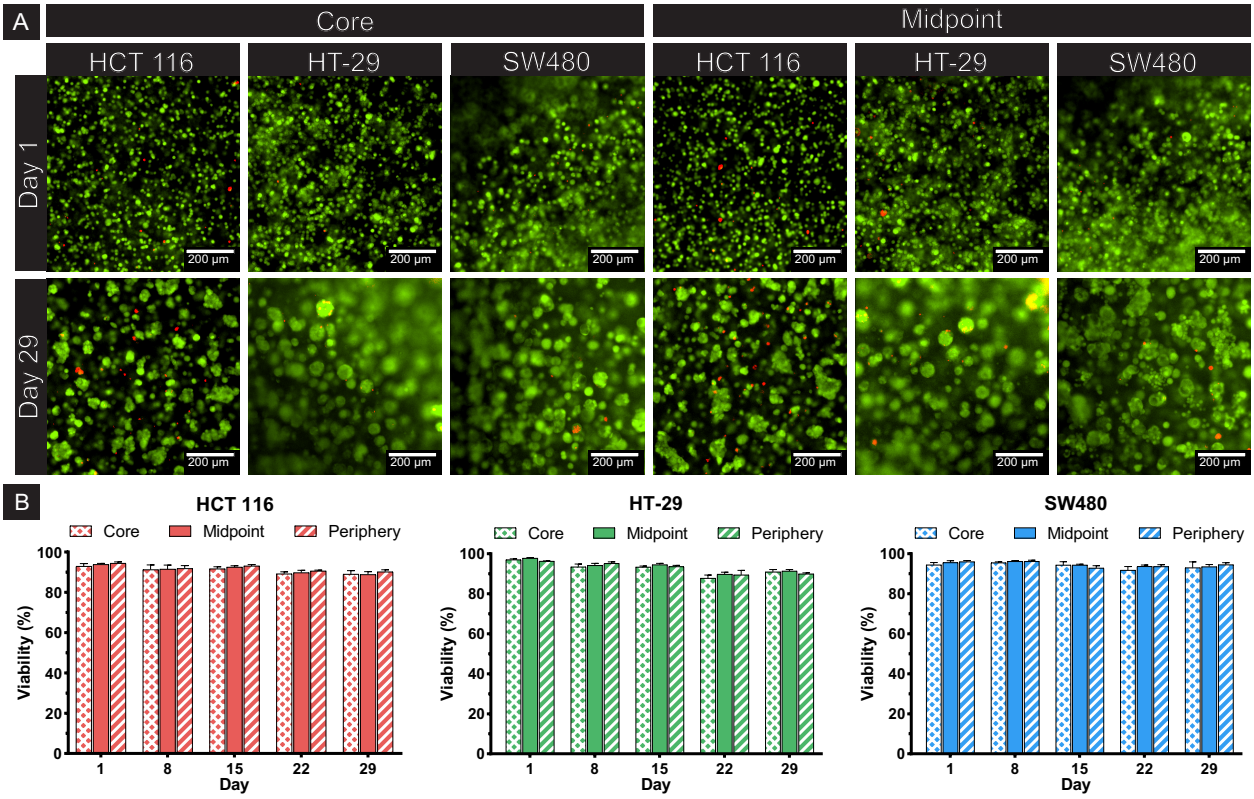

Figure B.1. Cell viability was similar in the core, midpoint, and periphery regions. (A) Representative confocal images of live (green) and dead (red) cells in the core and midpoint regions of 3D-eCRC tissues (scale bar = 200 µm). (B) Cell viability quantification. Cell viability was approximately higher than 90% for all CRC cells at all time points; no significant difference was found between regions at a given time point. Bar = mean ± SD ($p \leq 0.05$; n = 3 tissues).

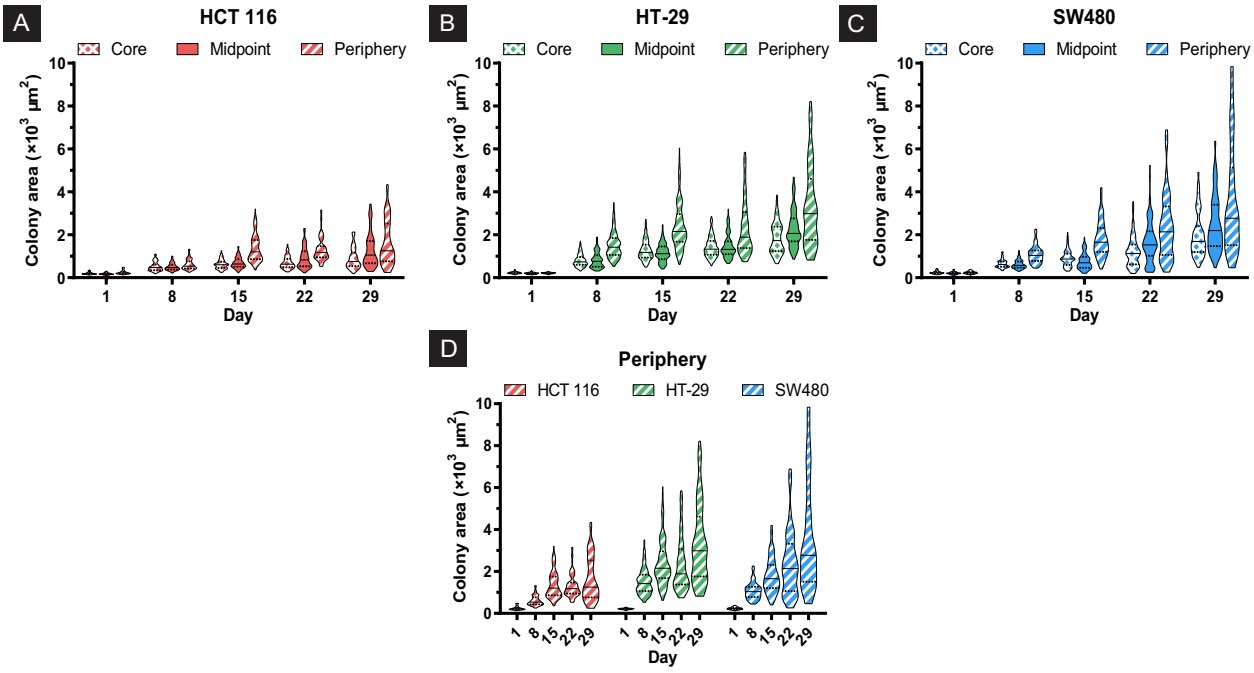

Figure B.2. Temporal changes in the cell colony area were both region- and line-dependent. (A-C) As time progressed, the periphery region showed larger colony areas, followed by midpoint and core regions for all CRC cell lines. (D) In the periphery, HCT-116 tissues showed smaller cell colony areas than HT-29 and SW480 tissues as time progressed ($p \leq 0.05$; $n \geq 100$ cell colonies from at least 3 tissues).

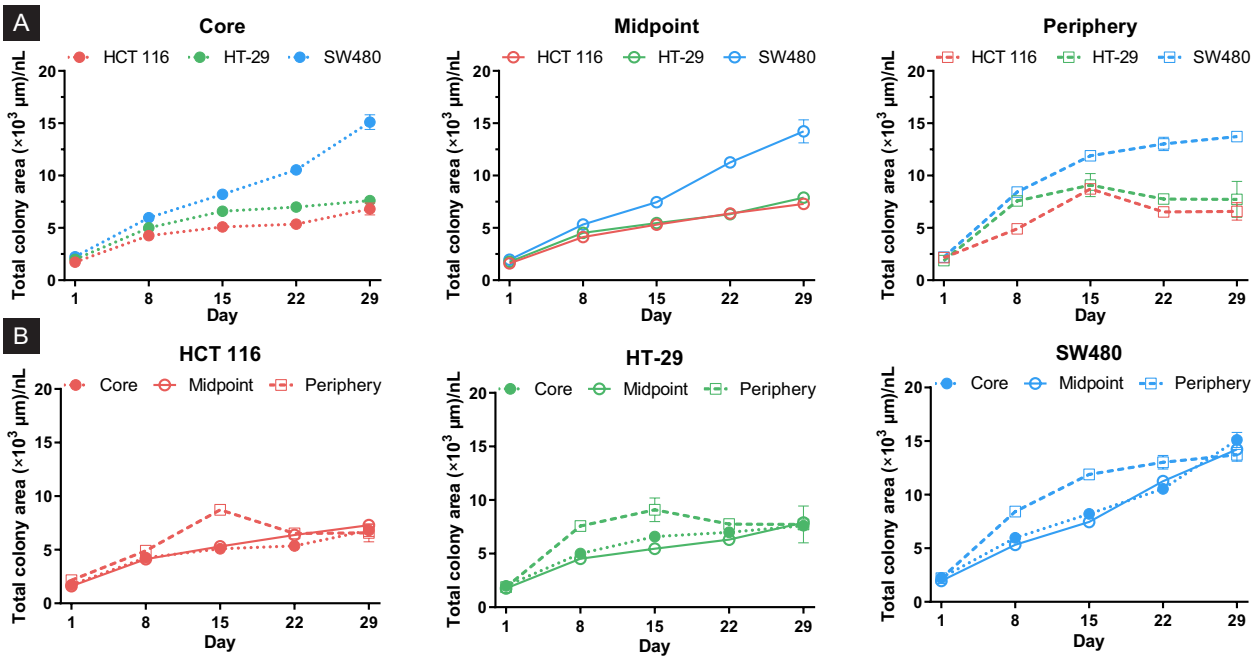

Figure B.3. Total colony area per tissue volume was both region- and line-dependents. (A) The rate of increase in total colony area per nL tissue volume was higher for SW480 as compared to those for HT-29, and HCT 116 tissues for a given region. (B) This rate was also higher for the periphery as compared to those for the midpoint and core regions for a given cell line. Data are mean ± SD ($p \leq 0.05$; n = 3 tissues).

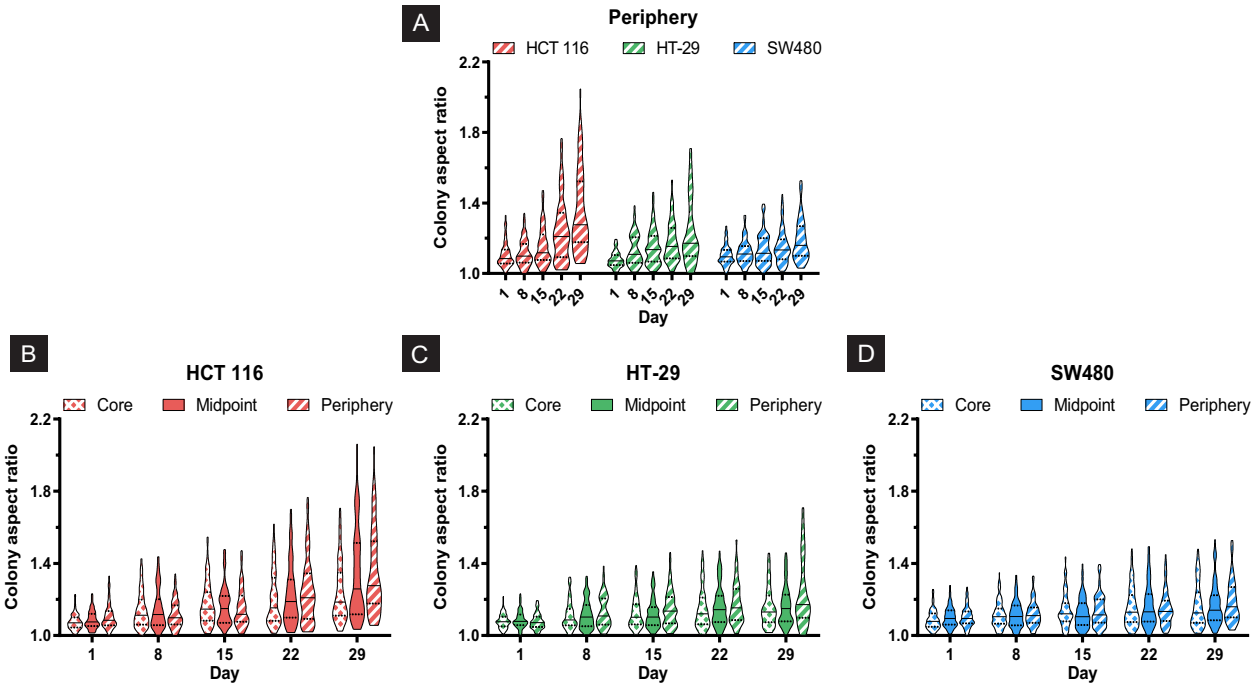

Figure B.4. Temporal changes in cell colony aspect ratio were both line- and region-dependent. (A) As time progressed, HCT 116 tissues showed higher cell colony aspect ratios in the periphery region, followed by HT-29 and SW480 tissues. (B-D) Similarly, HCT 116 exhibited higher cell colony aspect ratios in both midpoint and periphery as compared to the core region. HT-29 tissues showed higher cell colony aspect ratios in the periphery as compared to midpoint and core regions. For the SW480 cell colony aspect ratio, no significant difference between core, midpoint, and periphery regions was observed for a given time point ($p \leq 0.05$; n $\geq$ 100 cell colonies from at least 3 tissues).

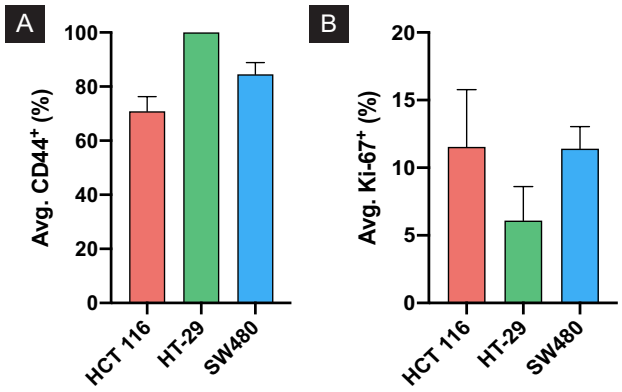

Figure B.5. 3D-eCRC tissues demonstrated line-dependent changes in cell subpopulations. The average percentages of $CD44^+$ and $Ki\text{-}67^+$ cell subpopulations in the 3D-eCRC tissues were calculated from Day 1 to Day 29. (A) HT-29 tissues had the highest average percentage of $CD44^+$ cell subpopulation, followed by SW480, and then HCT 116 tissues. (B) Average percentages of proliferative cell subpopulation in HCT 116 and SW480 tissues were equivalent, whereas HT-29 tissues had a significantly lower value ($p \leq 0.05$, n = 5 time points. Bar = mean ± SD. Means that do not share a letter are significantly different)

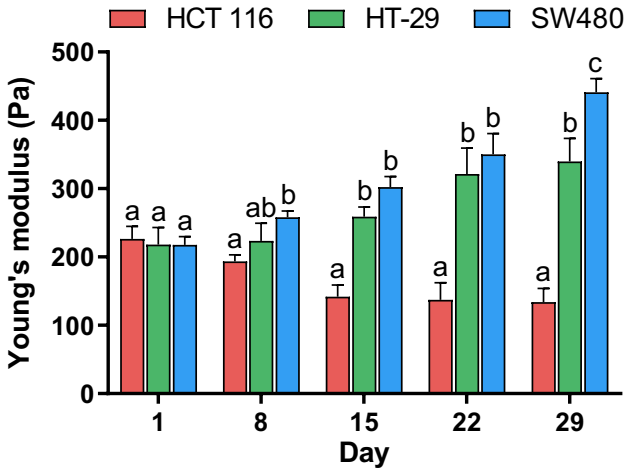

Figure B.6. Changes in mechanical stiffness of the 3D-eCRC tissues over time were cell line-dependent. Although, as expected, the stiffness of 3D-eCRC tissues from the three cells was similar on Day 1, temporal changes resulted in significantly higher stiffness for SW480 and HT-

29 compared to HCT 116 beginning from Day 15. On Day 29, SW480 tissues showed the highest stiffness, followed by that for HT-29, and then HCT 116 tissues ($p \leq 0.05$, n = 3 tissues of 3D-eCRC per time point. Bar = mean ± SD. Means that do not share a letter are significantly different. Statistical significance was calculated between cell lines for a given time point).

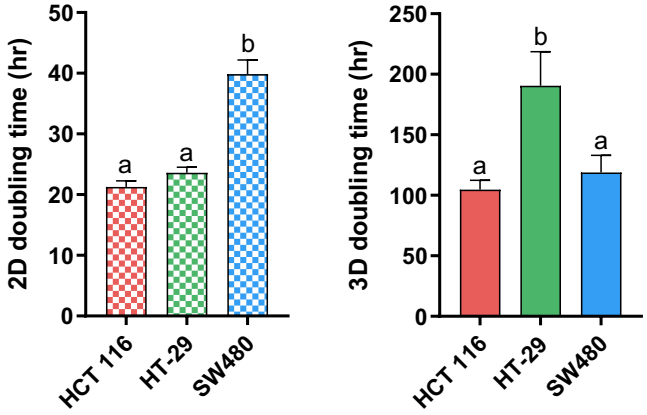

Figure B.7. Doubling time of the cell lines in 2D-CRC cultures and 3D-eCRC tissues. The doubling times for HCT 116 and HT-29 cells in 2D-CRC cultures were equivalent whereas that for SW480 was significantly higher. These numbers were consistent with ATCC (Manassas, VA) protocols for each cell line. However, in 3D-eCRC tissues, the doubling times for HCT 116 and SW480 were equivalent whereas that for HT-29 was significantly higher over 15 days of culture ($p \leq 0.05$, n = 5 cultures of 2D-CRC or 3 tissues of 3D-eCRC. Bar = mean ± SD. Means that do not share a letter are significantly different).

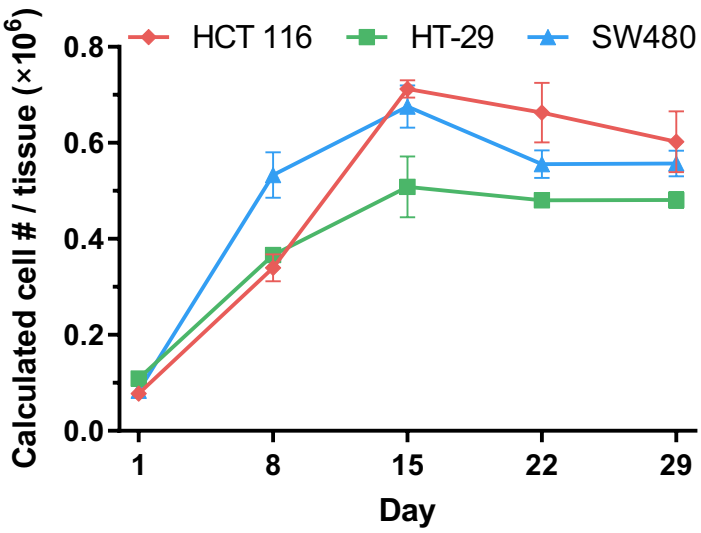

Figure B.8. Calculated cell numbers for the 3D-eCRC correlated with direct cell count. The total cell numbers were calculated based on the number of colonies per tissue, cell colony area, cell area, and cell viability and compared to the direct cell count. Interestingly, the calculated cell numbers per tissue showed an increasing trend similar to direct cell count for each cell line (Figure 2.8 A). Data are mean ± SD ($p \leq 0.05$; n = 3 tissues).

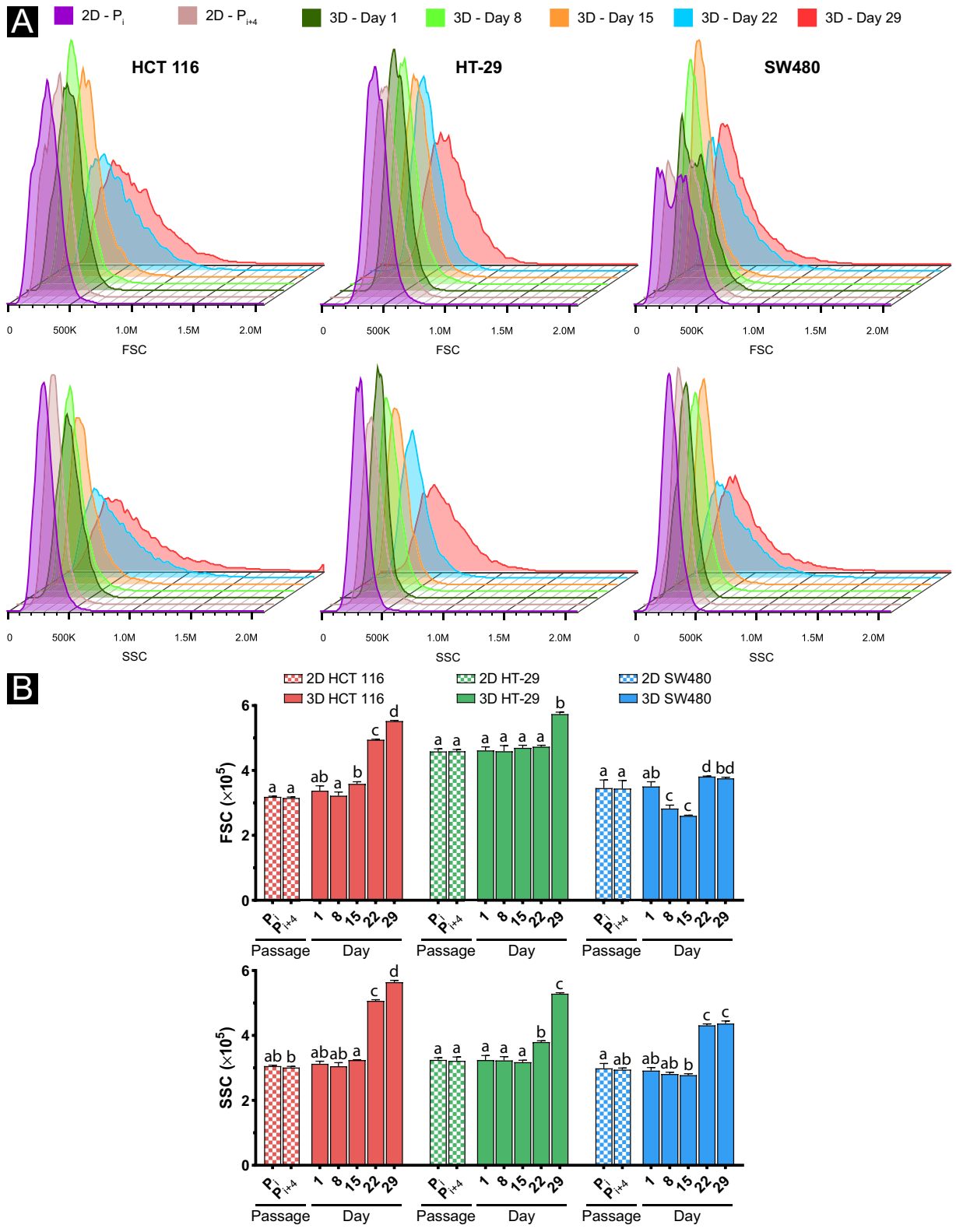

Figure B.9. Forward Scatter (FSC) and Side Scatter (SSC) were line- and time-dependent.

(A) The histograms obtained from flow cytometry analysis display FSC and SSC distribution for

2D-eCRC cultures and 3D-eCRC tissues. These data were used to calculate the average FSC and SCC. (B) The average FSC began to increase on Day 15 for HCT 116 and Day 29 for HT-29 tissues, whereas it decreased for SW480 tissues from Day 1 to Day 15 and then increased. The average SSC began to increase on Day 22 for all cell lines with the 3De-CRC tissues. Overall, the changes in FSC and SSC were more evident on Day 22 and Day 29 ($p \leq 0.05$, n = 3 tissue culture flasks for 2D or tissues for 3D. Bar = mean ± SD. Means that do not share a letter are significantly different).

Appendix C: Supporting Information for Chapter 3

C.1 Data

The dataset in this article describes the in-depth characterization of *in vitro* 3D engineered CRC-PDX (3D-eCRC-PDX) tissues that accurately recapitulated key features of the originating CRC-PDX tumors, thereby providing a novel platform for future investigation of CRC disease mechanisms and drug testing. These data also characterize 2D-CRC-PDX cell cultures for comparison with 3D-eCRC-PDX tissues and the originating CRC-PDX tumors. Figure C.1 demonstrates the viability of cells in 2D-CRC-PDX cell cultures and 3D-eCRC-PDX tissues. Figure C.2 and Figure C.3 show temporal changes in cell numbers for 2D-CRC-PDX cultures and 3D-eCRC-PDX tissues, respectively. Figure C.4, Figure C.5, Figure C.6, and Figure C.7 provide flow cytometry data examining temporal changes in the multiple PDX CRC-derived cell subpopulations for the CRC-PDX tumors, 3D-eCRC-PDX tissues, and 2D-CRC-PDX cultures. Figure C.8 and Figure C.9 present confocal microscopy images of the labeled cells in the 3D-eCRC-PDX tissues and 2D-CRC-PDX cultures, respectively. Figure C.10 and Figure C.11 provide the size and shape and machinal stiffness data for acellular poly(ethylene glycol)-fibrinogen (PEG-Fb) hydrogels. Figure C.12, Figure C.13, and Figure C.14 present the proteomics data. Figure C.15, Figure C.16, and Figure C.17 provide comparison data obtained through analysis of the RNA seq results. Full description of each figure is provided in the relevant figure legend. All flow cytometry data are available in the supplementary material. RNA seq data (GSE151069) for the CRC-PDX tumors and 3D-eCRC-PDX tissues are available from the NCBI Gene Expression Omnibus database (www.ncbi.nlm.nih.gov/geo). Proteomics data for the CRC-PDX tumors and 3D-eCRC-PDX tissues will be uploaded to the PRIDE - Proteomics Identification Database - EMBL-EBI upon acceptance of the manuscript.

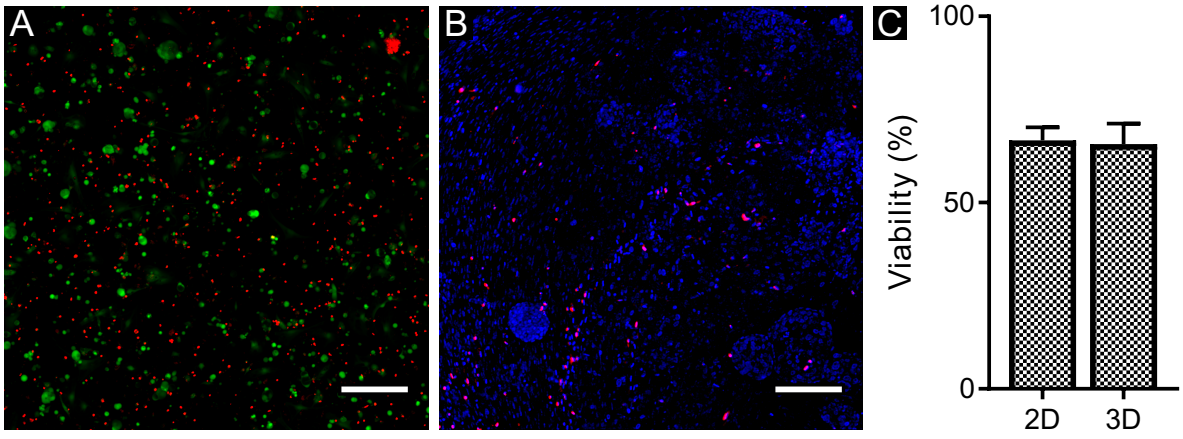

Figure C.1. Live/Dead assay quantification of cell viability. (A) Representative confocal microscopy images of live (green) and dead (red) cells in 2D-CRC-PDX cultures on Day 1 (Scale bar=200 µm). (B) Representative confocal microscopy images of cell nuclei (blue) counterstained with Hoechst 33342 and dead cells (red) within the 3D-eCRC-PDX tissues employed for cell viability quantification purposes (Scale bar=200 µm). (C) Approximately, 67 ± 4 percent of the 2D-CRC-PDX cells and 66 ± 6 percent of the cells within the 3D-eCRC-PDX tissues were viable on Day 1; there was no significant difference between conditions. Bars are mean ± SD ($p \leq 0.05$, n = 3 tissues or 2D-CRC-PDX cultures).

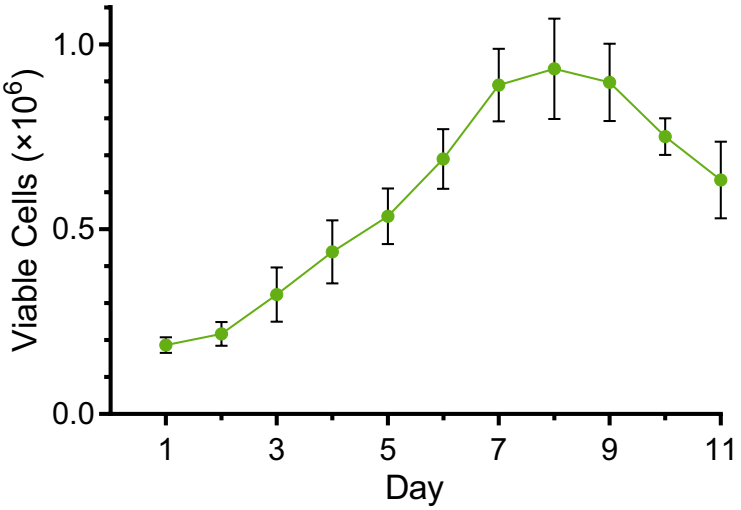

Figure C.2. CRC-PDX cell growth rate in 2D-CRC-PDX cultures without cell passaging. The total number of viable CRC-PDX cells, cultured in T25 flasks, increased from Day 1 to Day 8, at which point confluency was reached. A decrease in cell number was observed thereafter. Therefore, the 2D-CRC-PDX cells were passaged every 7 days for experiments comparing them to the 3D-eCRC-PDX tissues. Data are mean ± SD (n= 3 separate batches of cell cultures).

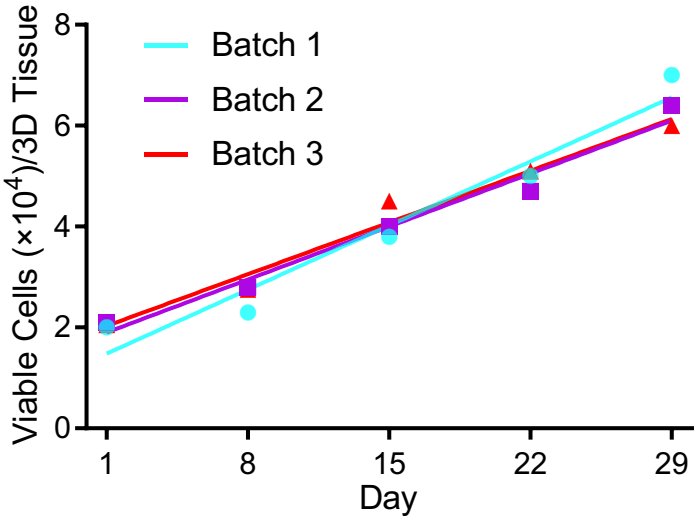

Figure C.3. Viable CRC-PDX cell numbers within the 3D-eCRC-PDX tissues. Following 3D-eCRC-PDX tissue dissociation and trypan blue staining, the viable cells were counted using a hemocytometer. The numbers of viable cells within the 3D-eCRC-PDX tissues increased from

Day 1 to Day 29 for all 3 batches of cell culture. No significant difference was observed between the rates of increase (slopes) based on linear regression analysis ($p \leq 0.05$, n = 3 separately prepared batches).

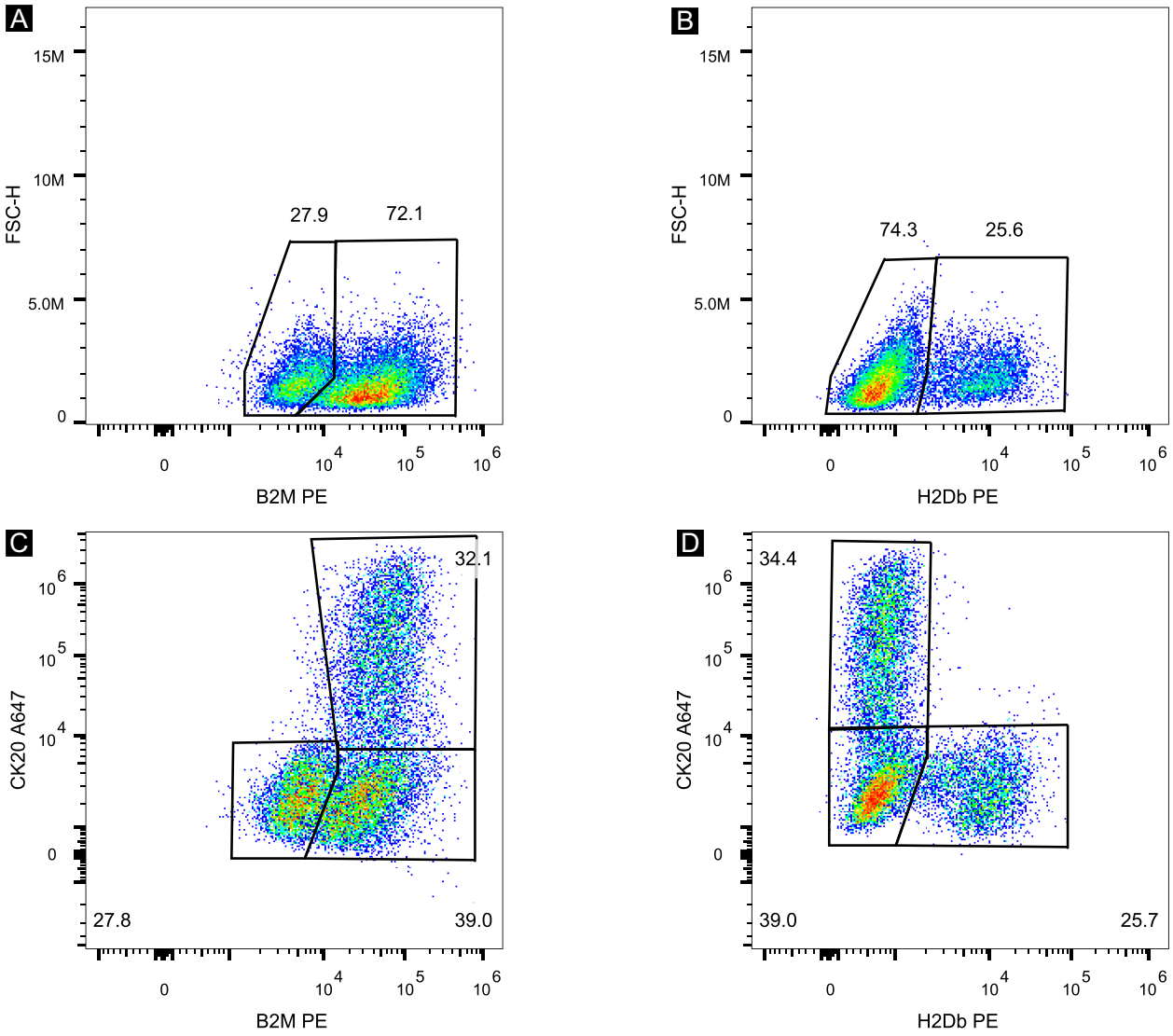

Figure C.4. Examination of human (B2M$^+$), mouse (H2Db$^+$), and CK20$^+$ cell subpopulations. One sample containing CRC-PDX cells was divided equally into two samples and the cells were labeled with β-2 microglobulin (B2M) and cytokeratin 20 (CK20) or H2Db and CK20. The

percentage of (A) B2M$^-$ cells in sample 1 was approximately equal to that of (B) H2Db$^+$ cells in sample 2. Furthermore, all CK20$^+$ cells were also positive for (C) B2M and negative for (D) H2Db.

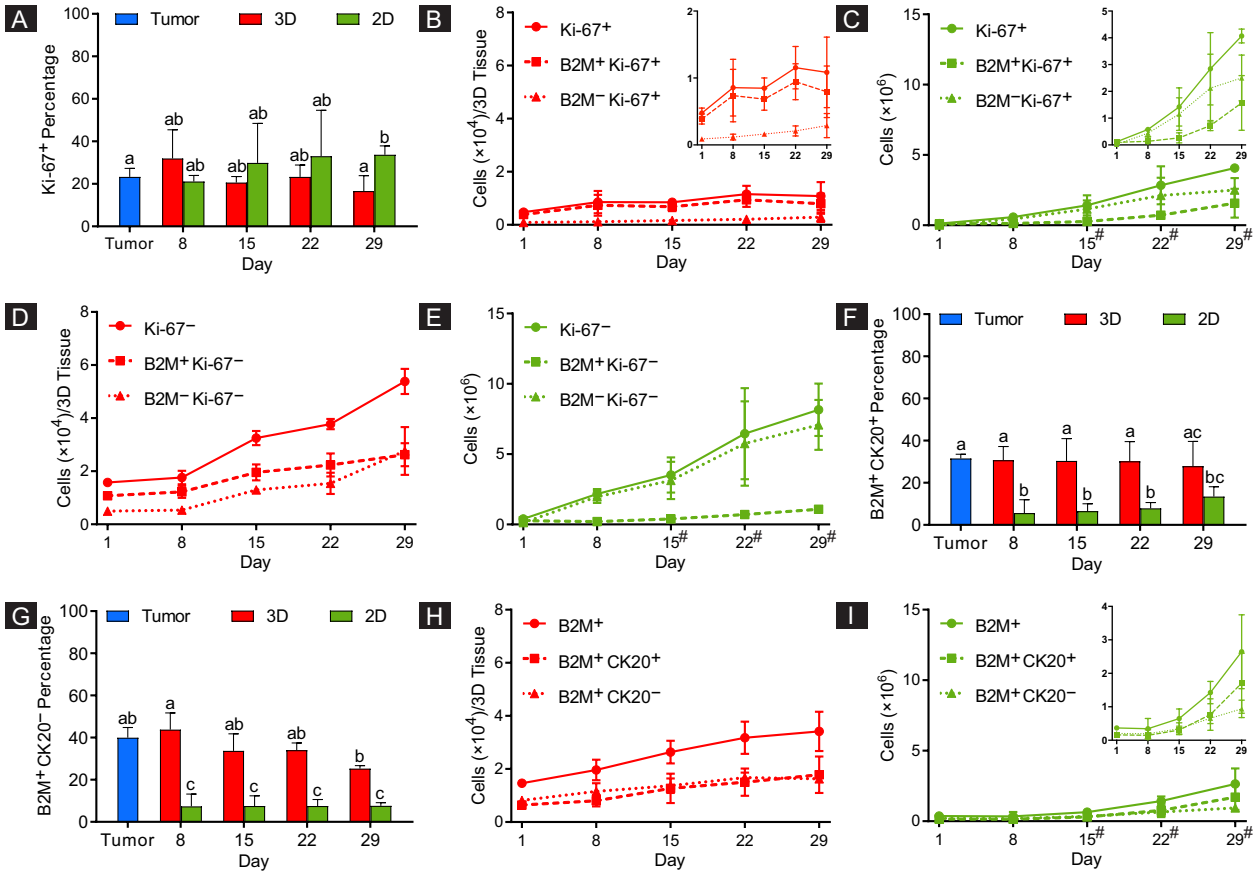

Figure C.5. Quantification of CRC PDX cell subpopulations through flow cytometry. (A) The total percentages of Ki-67$^+$ cells (B2M$^+$ and B2M$^-$) in the 3D-eCRC-PDX tissues and 2D-CRC-PDX cultures were similar to that in the CRC-PDX tumors, except for 2D-CRC-PDX cells on Day 29, which had a significantly higher percentage of proliferating cells (Ki-67$^+$) than the original CRC-PDX tumors. For 3D-eCRC-PDX tissues, the rates of increase in (B) human proliferative (B2M$^+$ Ki67$^+$) and mouse proliferative (B2M$^-$ Ki-67$^+$) cell numbers were similar, maintaining a ratio equivalent to the original tumor. In sharp contrast, (C) for 2D-CRC-PDX cultures, mouse cells were the major contributor to the total proliferative cell number increase, whereas human

proliferative cell number increased at significantly lower rates (0.53±0.07 fold). Similarly, the (D) human non-proliferative ($B2M^+$ $Ki\text{-}67^-$) and mouse non-proliferative ($B2M^-$ $Ki\text{-}67^-$) cell numbers increased with similar rates in the 3D-eCRC-PDX tissues, whereas (E) in 2D-CRC-PDX cultures, human non-proliferative cell number increased at significantly lower rates compared to mouse non-proliferative cells (0.12±0.01 fold). (F, G) The 3D-eCRC-PDX tissues maintained $B2M^+$ $CK20^+$ and $B2M^+$ $CK20^-$ cell subpopulations over time, whereas in 2D-CRC-PDX cultures, these cell subpopulations decreased significantly after 8 days of culture and remained unchanged thereafter. (H, I) $B2M^+$ $CK20^+$ and $B2M^+$ $CK20^-$ cell subpopulations increased ratiometrically in the 3D-eCRC-PDX tissues whereas the rates of increase in 2D-CRC-PDX cultures were lower during initial days of culture compared to later time points. Data are mean ± SD. Means that do not share a letter are significantly different ($p \leq 0.05$, n=3 separate batches of cell culture). # indicates that the 2D-CRC-PDX cells were passaged at the previous time point.

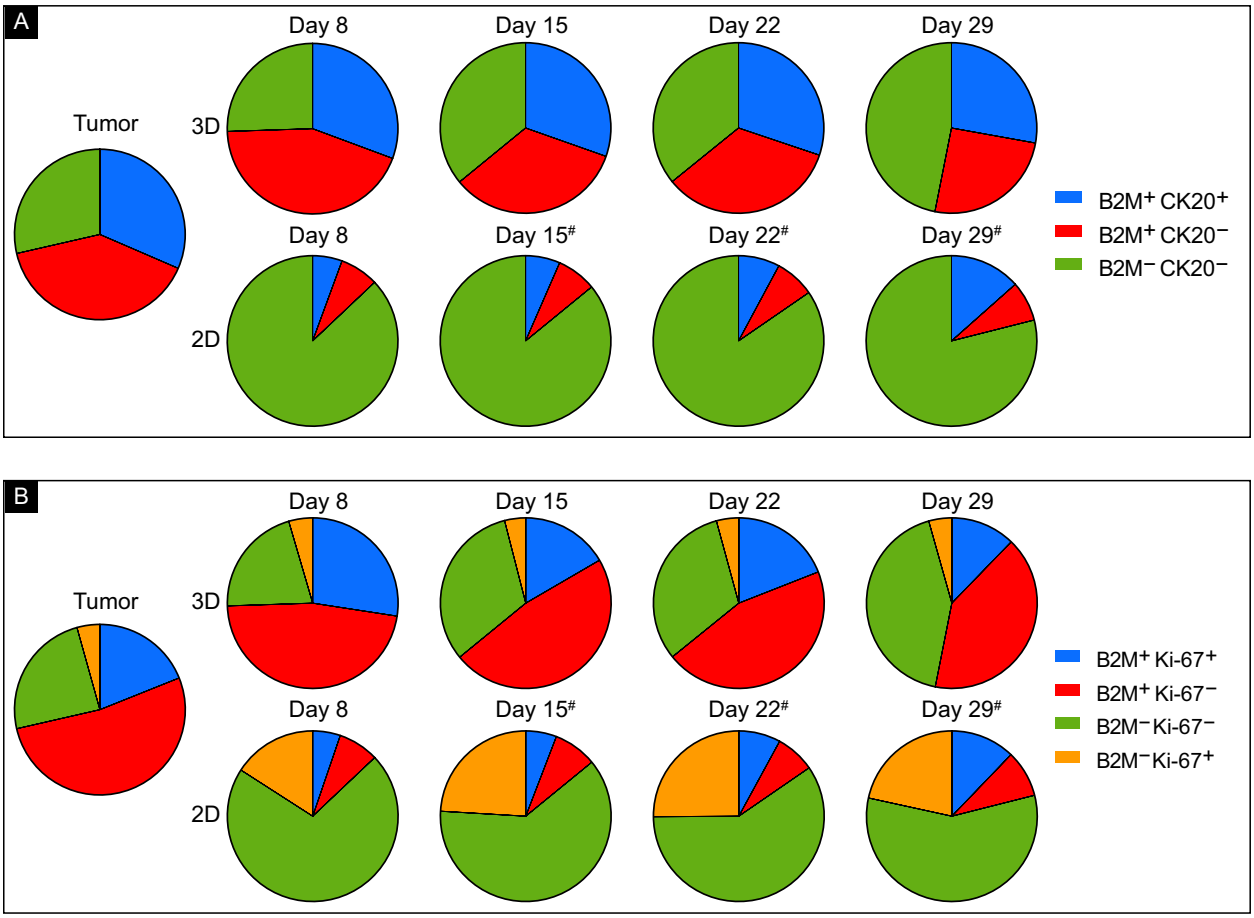

Figure C.6. Cell subpopulations within the CRC-PDX tumors, 3D-eCRC-PDX tissues, and 2D-CRC-PDX cultures. Flow cytometry analysis using B2M, CK20, and Ki-67 markers showed that different CRC-PDX cell subpopulations within 3D-eCRC-PDX tissues were similar to the CRC-PDX tumors over time, whereas the 2D-CRC-PDX cell subpopulations displayed a significant deviation from the CRC-PDX tumors. # indicates that the 2D-CRC-PDX cells were passaged at the previous time point.

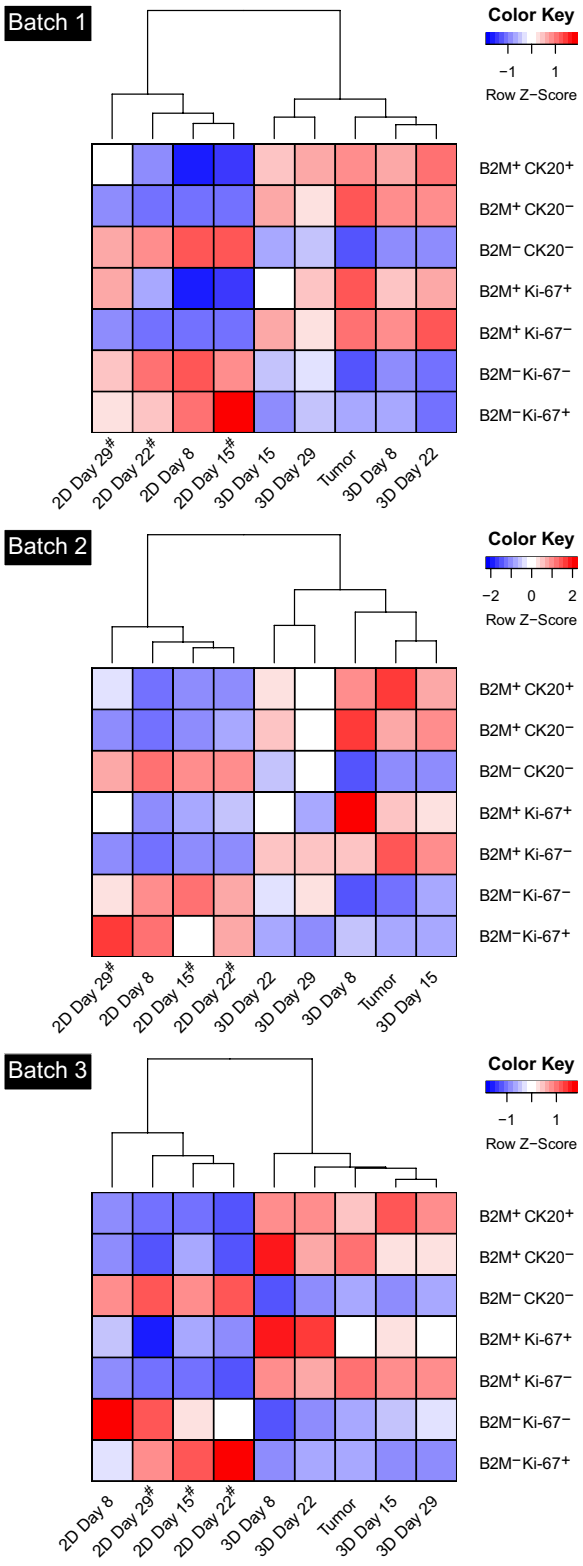

Figure C.7. Cluster analysis of the cell subpopulations obtained from flow cytometry results.

For three separate batches of cell culture, the 3D-eCRC-PDX tissues clustered with the CRC-PDX

tumors whereas the 2D-CRC-PDX cells clustered separately from both the 3D-eCRC-PDX tissues and CRC-PDX tumors. # indicates that the 2D-CRC-PDX cells were passaged at the previous time point.

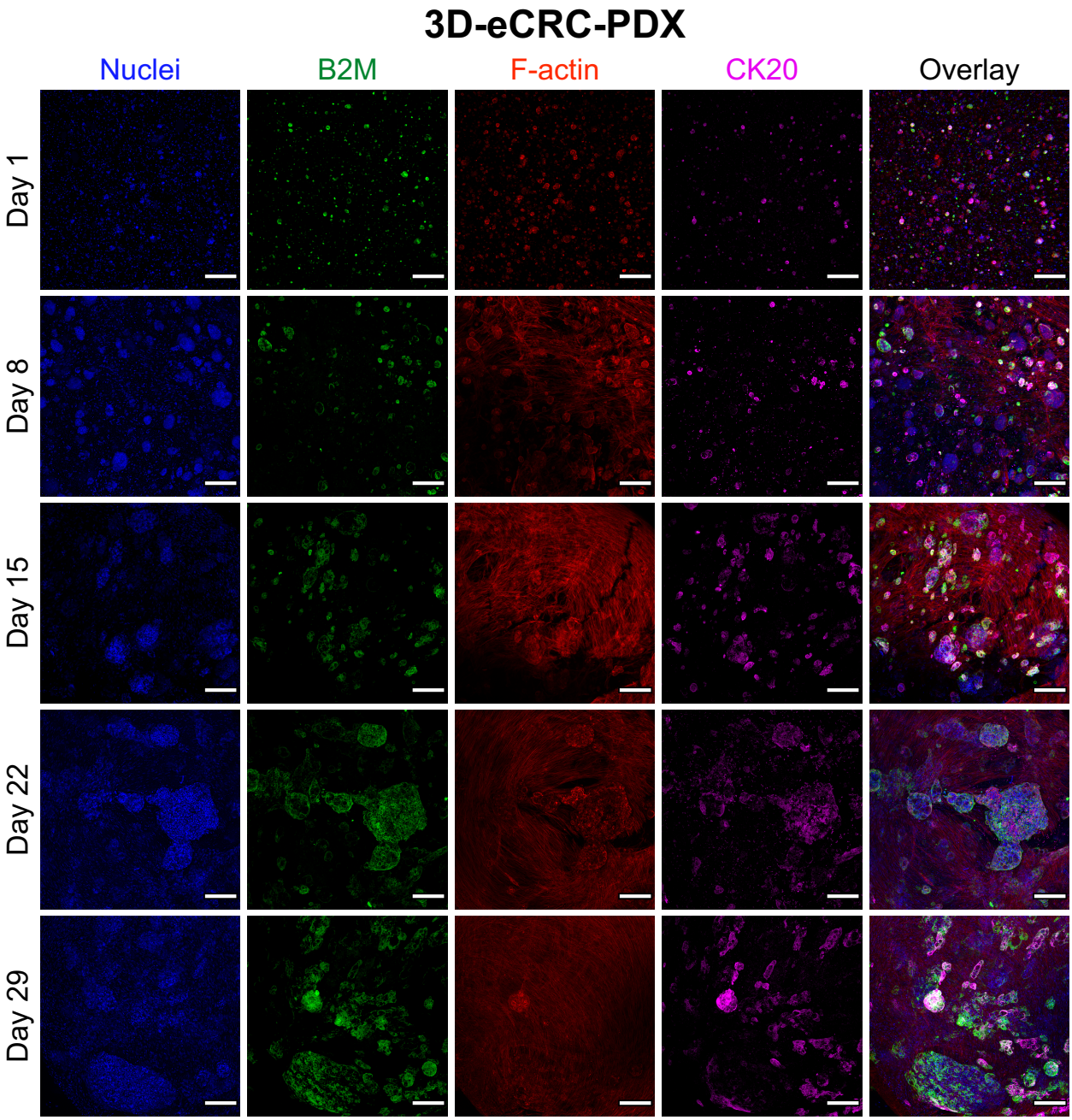

Figure C.8. Staining of cells within the 3D-eCRC-PDX tissues. Cells within the 3D-eCRC-PDX tissues were labeled with Hoechst 33342 (blue), B2M (green), phalloidin (red), and CK20 (magenta). Human ($B2M^+$) and $CK20^+$ formed colonies whereas mouse ($B2M^-$) cells exhibited elongation. The size of cell colonies and the density of elongated cells increased from Day 1 to Day 29 (scale bar = 200 μm).

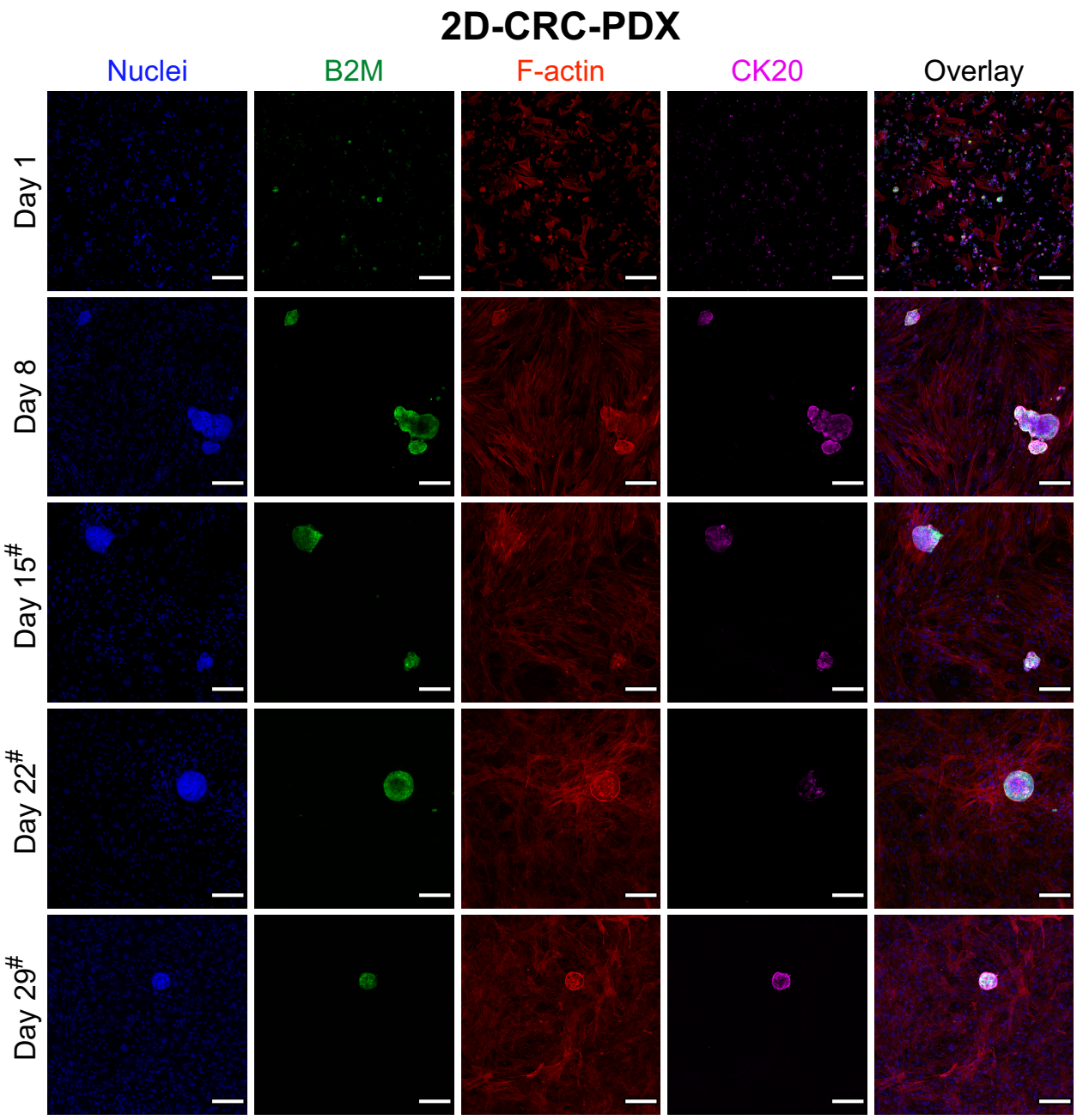

Figure C.9. Staining of 2D-CRC-PDX cells. The 2D-CRC-PDX cells were labeled with Hoechst 33342 (blue), B2M (green), phalloidin (red), and CK20 (magenta). Human ($B2M^+$) and $CK20^+$ cells formed colonies whereas mouse ($B2M^-$) cells exhibited elongation (scale bar = 200 μm). # indicates that the 2D-CRC-PDX cells were passaged at the previous time point.

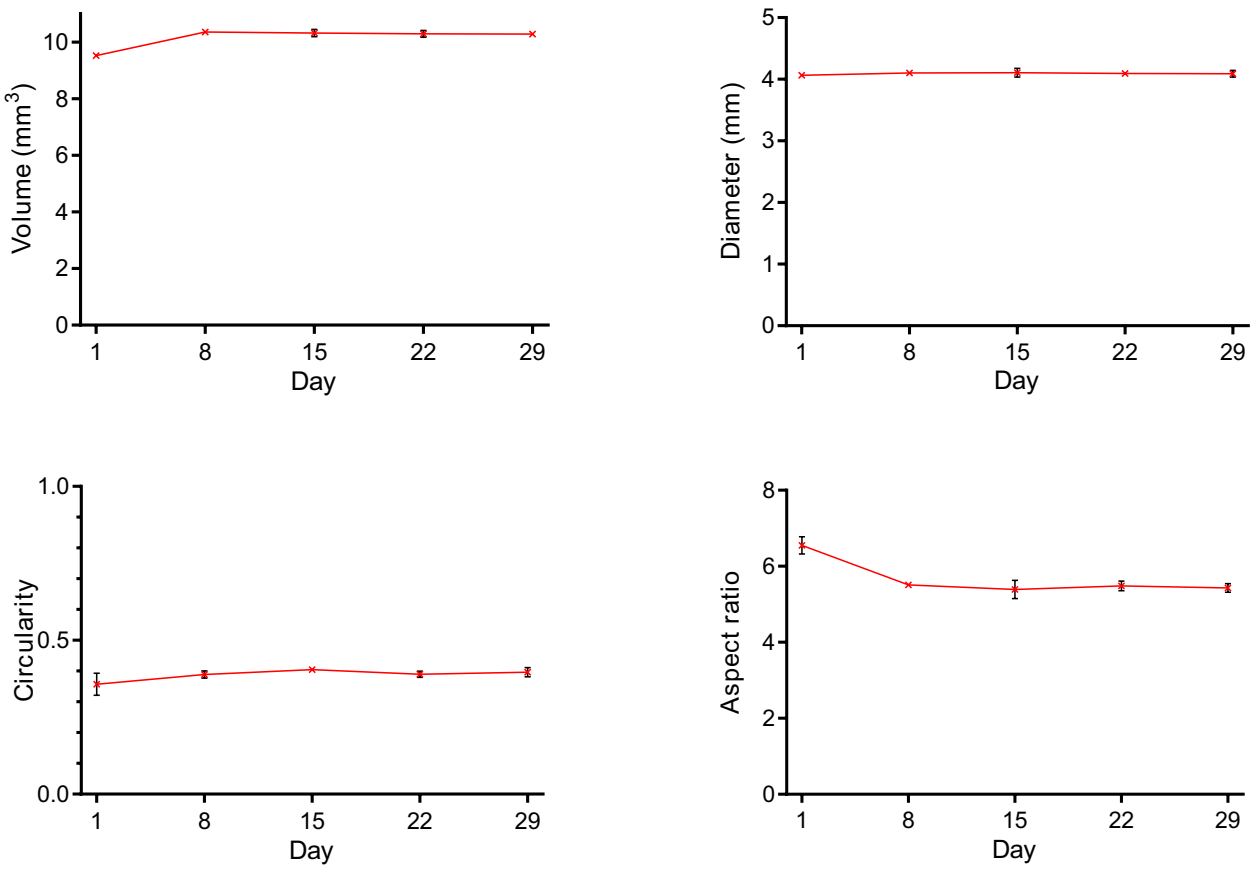

Figure C.10. Size and shape of acellular PEG-Fb hydrogels over time. The volume of acellular hydrogels increased slightly from Day 1 to Day 8 and remained constant thereafter. The diameter and circularity of the acellular hydrogels remained constant over time. The aspect ratio of the acellular hydrogels decreased from Day 1 to Day 8 and remained constant thereafter. Data are mean ± SD (n=3 acellular hydrogels).

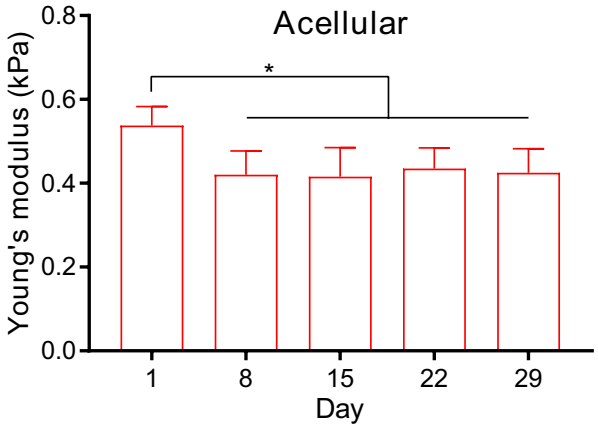

Figure C.11. Mechanical stiffness of the acellular hydrogels. The stiffness of acellular hydrogels was found to decrease from Day 1 to Day 8 and remained constant thereafter. Data are mean ± SD ($p \leq 0.05$, n=3 acellular hydrogels).



Figure C.12. Comparison of identified extracellular matrix (ECM) proteins in CRC-PDX tumors and 3D-eCRC-PDX tissues. The numbers of shared, CRC-PDX tumor-specific and 3D-

eCRC-PDX tissue-specific proteins for Batch 1, 2, and 3 are shown. (A) In batch 1, approximately 61% of identified ECM proteins were observed in both CRC-PDX tumors and 3D-eCRC-PDX tissues. Similarly, (B) in batch 2 approximately 54% of identified ECM proteins were observed in both the CRC-PDX tumor and the 3D-eCRC-PDX tissues, while (C) in batch 3, approximately 47% of proteins were found in both CRC-PDX tumors and 3D-eCRC-PDX tissues.

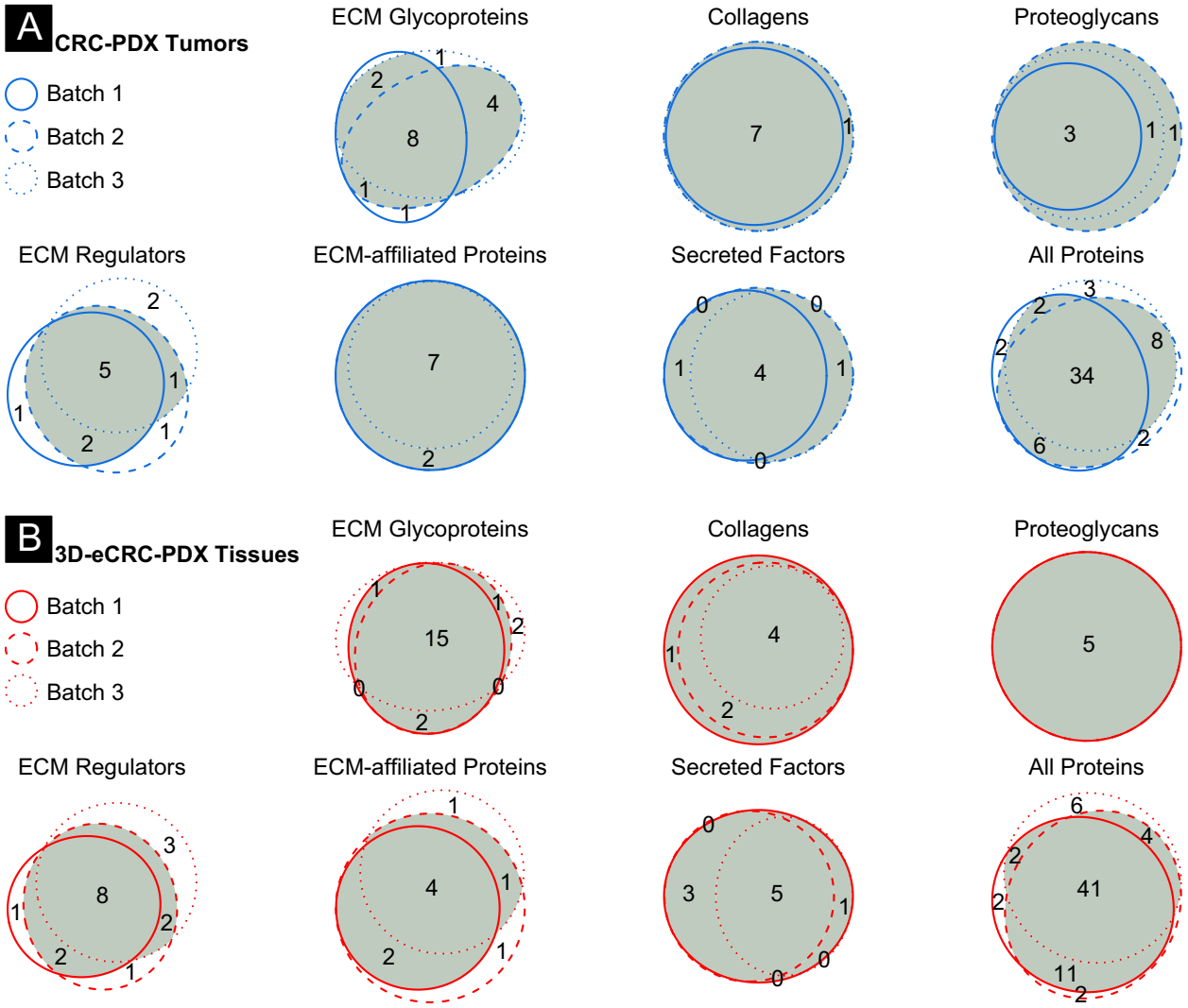

Figure C.13. Protein batch-to-batch consistency between CRC-PDX tumors or 3D-eCRC-PDX tissues. (A) Approximately 60% of ECM proteins within CRC-PDX tumors were the same for all three batches, 28% of the ECM proteins were present in at least two batches, and 12% of

the ECM proteins were specific to each batch. (B) For 3D-eCRC-PDX tissues, 60% of ECM proteins were found to be the same for all batches, 25% were present in at least two batches, and 15% were batch-specific.

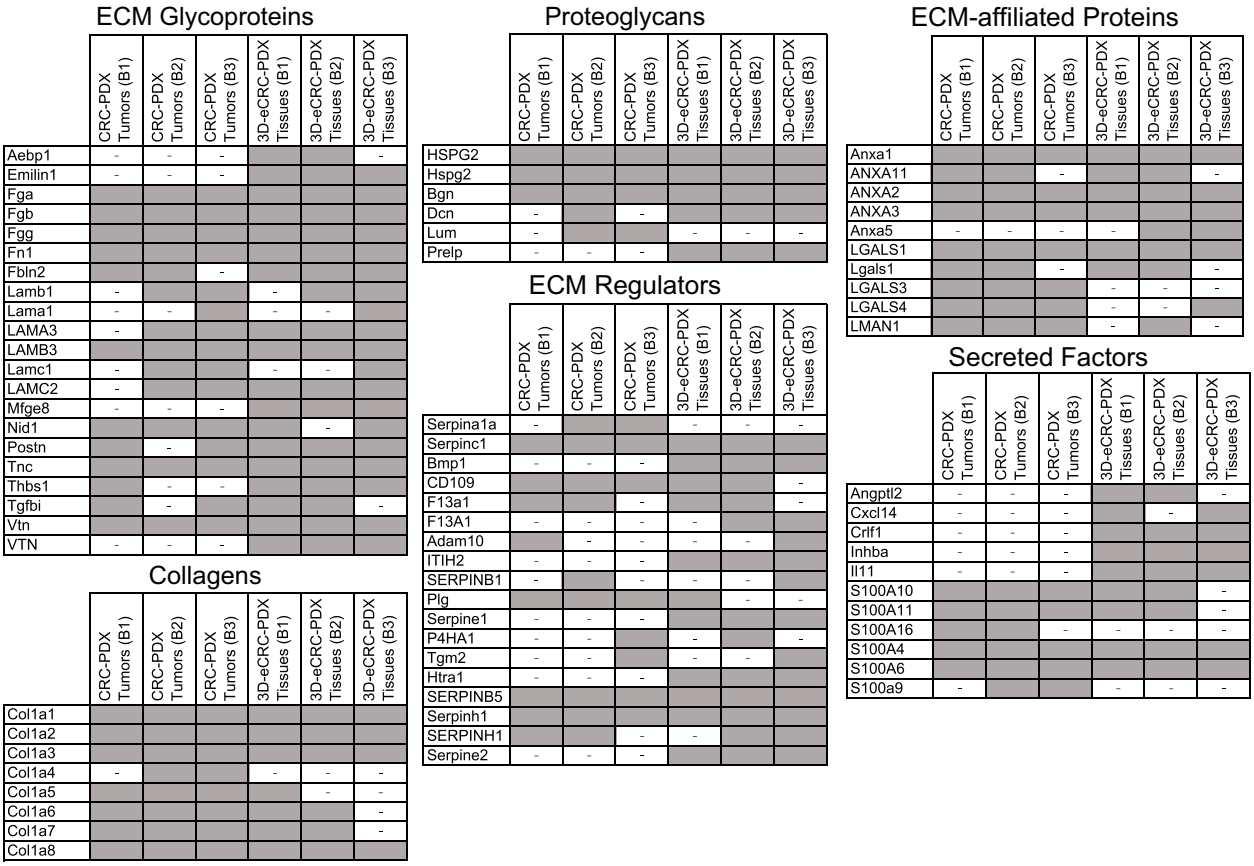

Figure C.14. Comparison between the identified ECM proteins in CRC-PDX tumors and 3D-eCRC-PDX tissues from Batch 1 (B1), Batch 2 (B2), and Batch 3 (B3). The ECM proteins identified in only one out of six samples (CRC-PDX tumors and 3D-eCRC-PDX tissues) were removed from the analysis. A protein was indicated as present (gray cell) when the protein was detected in at least two out three samples and as absent (cell with a minus sign) when the protein was detected in only one sample or was not detected at all. Proteins presented in uppercase and lowercase letters are from human and mouse databases, respectively.

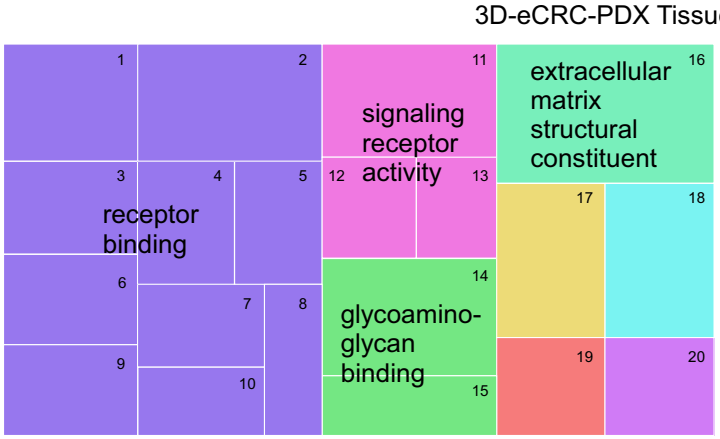

	term_ID	description	log10 FDR pvalue
1	GO:0005102	receptor binding	-8.9318
2	GO:0019955	cytokine binding	-5.3595
3	GO:0008009	chemokine activity	-4.757
4	GO:0048018	receptor agonist activity	-4.5544
5	GO:0005125	cytokine activity	-4.1325
6	GO:0019838	growth factor binding	-4.6635
7	GO:0005518	collagen binding	-3.9788
8	GO:0019956	chemokine binding	-3.3098
9	GO:0038085	VEGF binding	-4.6364
10	GO:0001968	fibronectin binding	-3.3279
11	GO:0038023	signaling receptor activity	-7.5719
12	GO:0015026	coreceptor activity	-3.6162
13	GO:0005044	scavenger receptor activity	-3.1325
14	GO:0005539	glycosaminoglycan binding	-7.8477
15	GO:0008201	heparin binding	-3.9957
16	GO:0005201	ECM structural constituent	-11.385
17	GO:0030246	carbohydrate binding	-6.3788
18	GO:0060089	molecular transducer activity	-6.2716
19	GO:0005509	calcium ion binding	-4.0278
20	GO:0030545	receptor regulator activity	-3.983

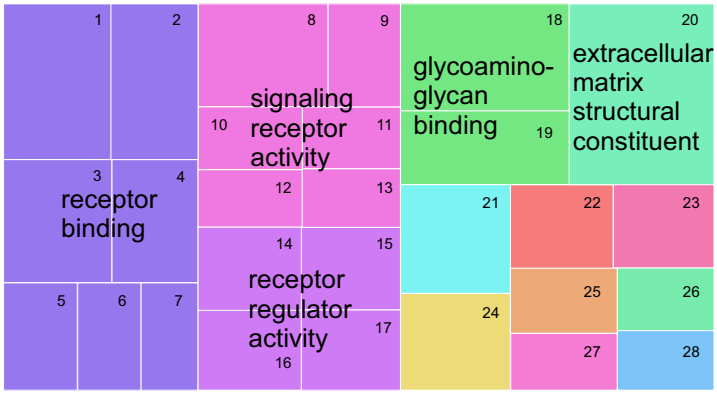

	term_ID	description	log10 FDR pvalue
1	GO:0005102	receptor binding	-9.1555
2	GO:0019838	growth factor binding	-7.4949
3	GO:0019955	cytokine binding	-7.3279
4	GO:0005518	collagen binding	-5.7986
5	GO:0038085	VEGF binding	-4.4023
6	GO:0043394	proteoglycan binding	-3.8097
7	GO:0019956	chemokine binding	-3.3468
8	GO:0038023	signaling receptor activity	-7.4112
9	GO:0038024	cargo receptor activity	-4.1415
10	GO:0004955	prostaglandin receptor activity	-3.585
11	GO:0005044	scavenger receptor activity	-3.3696
12	GO:0030545	receptor regulator activity	-4.5229
13	GO:0015026	coreceptor activity	-3.1979
14	GO:0048018	receptor agonist activity	-4.6861
15	GO:0030545	receptor regulator activity	-4.5229
16	GO:0005125	cytokine activity	-4.5969
17	GO:0042379	chemokine receptor binding	-4.4012
18	GO:0005539	glycosaminoglycan binding	-10.004
19	GO:0008201	heparin binding	-6.8041
20	GO:0005201	ECM structural constituent	-14.248
21	GO:0060089	molecular transducer activity	-6.5784
22	GO:0005509	calcium ion binding	-4.6882
23	GO:1901681	sulfur compound binding	-4.5017
24	GO:0030246	carbohydrate binding	-5.7905
25	GO:0050840	extracellular matrix binding	-3.8633
26	GO:0098772	molecular function regulator	-3.2874
27	GO:0005198	structural molecule activity	-3.3536
28	GO:0005515	protein binding	-3.1085

Figure C.15. Gene ontology analysis of molecular functions enriched in CRC-PDX tumor and 3D-eCRC-PDX tissue samples. Enriched gene molecular function ontologies between CRC-PDX tumor (n=3) and 3D-eCRC-PDX tissue samples (n=3) and tumor-adjacent (normal) colon tissue (n=41) from The Cancer Genome Atlas Colon Adenocarcinoma (TCGA-COAD) determined using the Gorilla application were analyzed for redundancy using REVIGO (Supek et al. 2011). The 'superclusters' of similar gene ontology (GO) terms are visualized with similar colors. The size of individual rectangles reflects false discovery rate (FDR) *p*-values: large

rectangles represent low log10 FDR *p*-values. Shown are GO term ID, description, and log10 FDR *p* value.

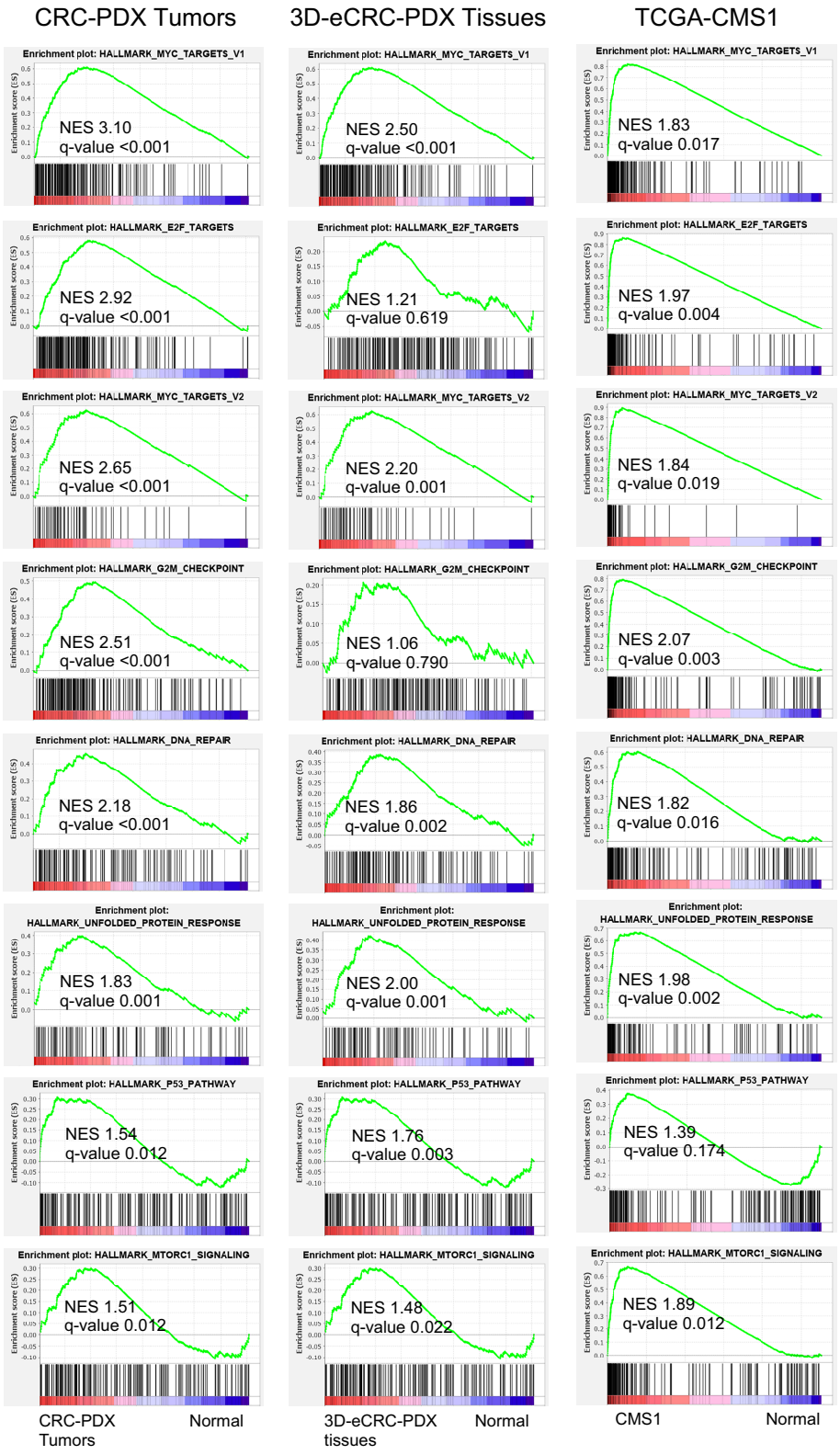

Figure C.16. Gene Set Enrichment Analysis (GSEA). The top 10 enriched gene set in the Molecular Signature Database (MSigDB) Hallmarks v7.0 gene sets in CRC-PDX tumor (n=3)

(*upper left panel*), 3D-eCRC-PDX tissue (n=3) (*middle left panel*) and patient CRC tumor TCGA-COAD samples (n=84) (*lower left panel*) compared to tumor-adjacent (normal) colon tissue (n=41) from the TCGA-COAD. Enrichment plots with the normalized enrichment score (NES) and the FDR q-value are shown.

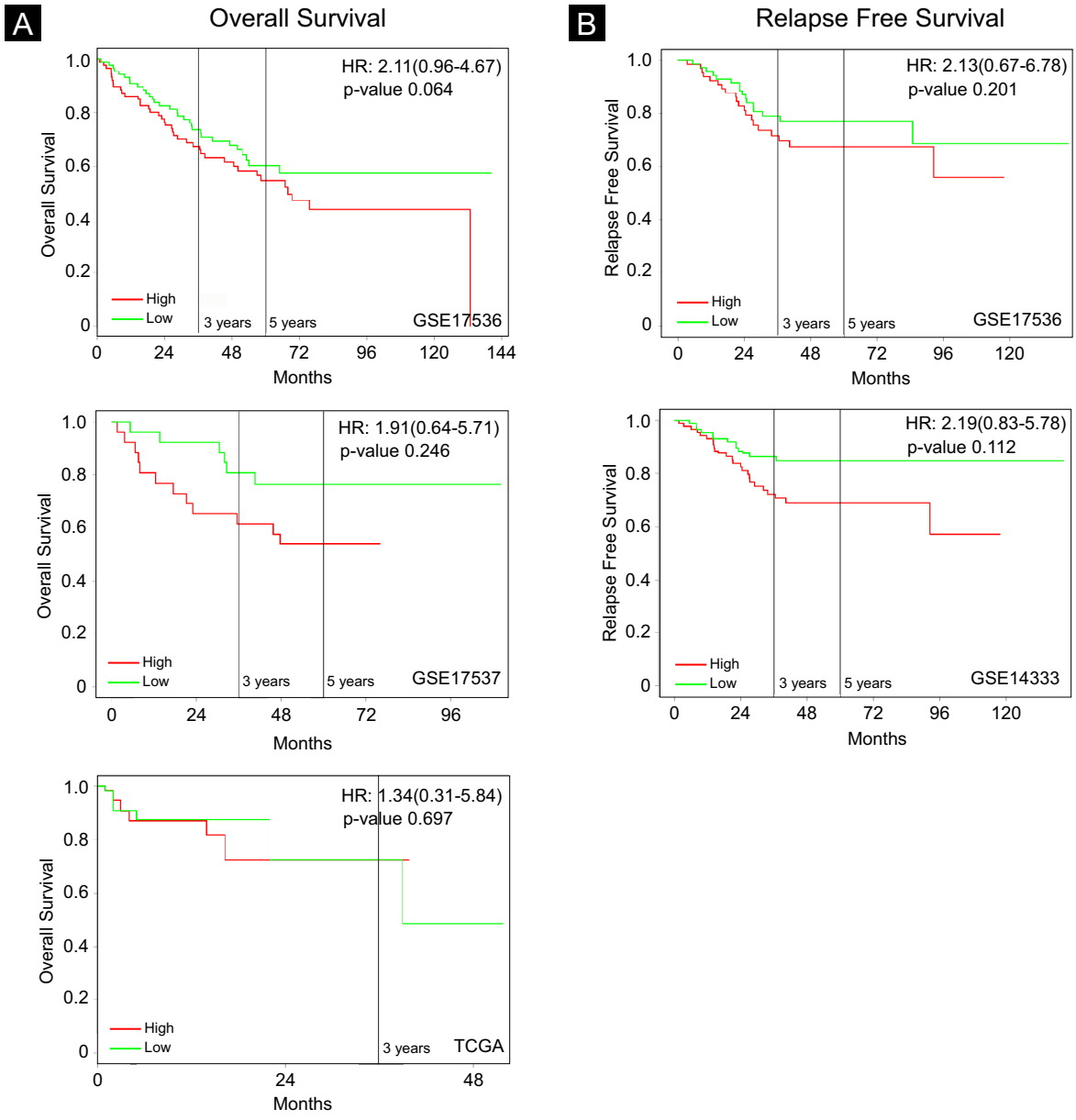

Figure C.17. Prognostic Kaplan–Meier survival analysis. Expression of the top 16 significantly upregulated genes between CRC-PDX tumors (n=3) and 3D-eCRC-PDX tissues (n=3) in the

precomputed GEO dataset GSE17536 (n=174), GSE17537 (n=54), TCGA-COAD (n=121), GSE14333 (n=187) adjusted for age, stage, and gender covariates and bifurcated based on median expression was examined for overall survival (A) and relapse-free survival (B). The hazard ratios, 95% confidence intervals, and *p*-values were shown.

Table C.1. Summary of the sequencing reads alignment to the reference genomes for the CRC-PDX

	Human		**Mouse**	
	3D[†]	**CRC-PDX**[‡]	**3D**[†]	**CRC-PDX**[‡]
All reads	180,572,171	189,200,637	180,572,171	189,200,637
All mapped reads	132,850,961	151,403,899	44,521,654	29,455,993
All mapped rate	73.6%	80.0%	24.7%	15.6%
Uniquely mapped reads	112,081,097	122,236,260	37,690,851	21,975,889
Uniquely mapped rate	62.1%	64.6%	20.9%	11.6%

[†]3D-eCRC-PDX tissues
[‡]CRC-PDX tumors

Appendix D: Supporting Information for Chapter 4

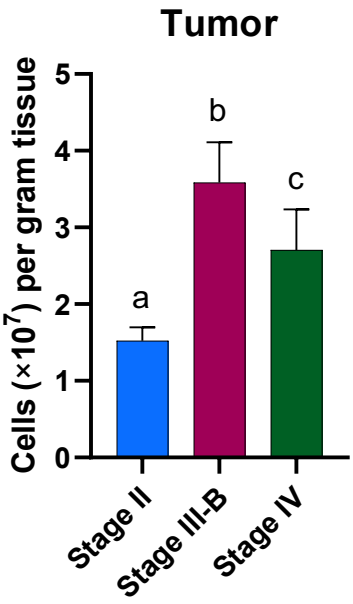

Figure D.1. Viable cell numbers isolated from CRC-PDX tumors were line-dependent. Viable cell number per gram of tumor was highest for stage III-B CRC-PDX tumors, followed by those for stage IV, and then stage II. Bar = mean ± SD. Means that do not share a letter are significantly different ($p < 0.03$; n = a minimum of 4 CRC-PDX tumors).

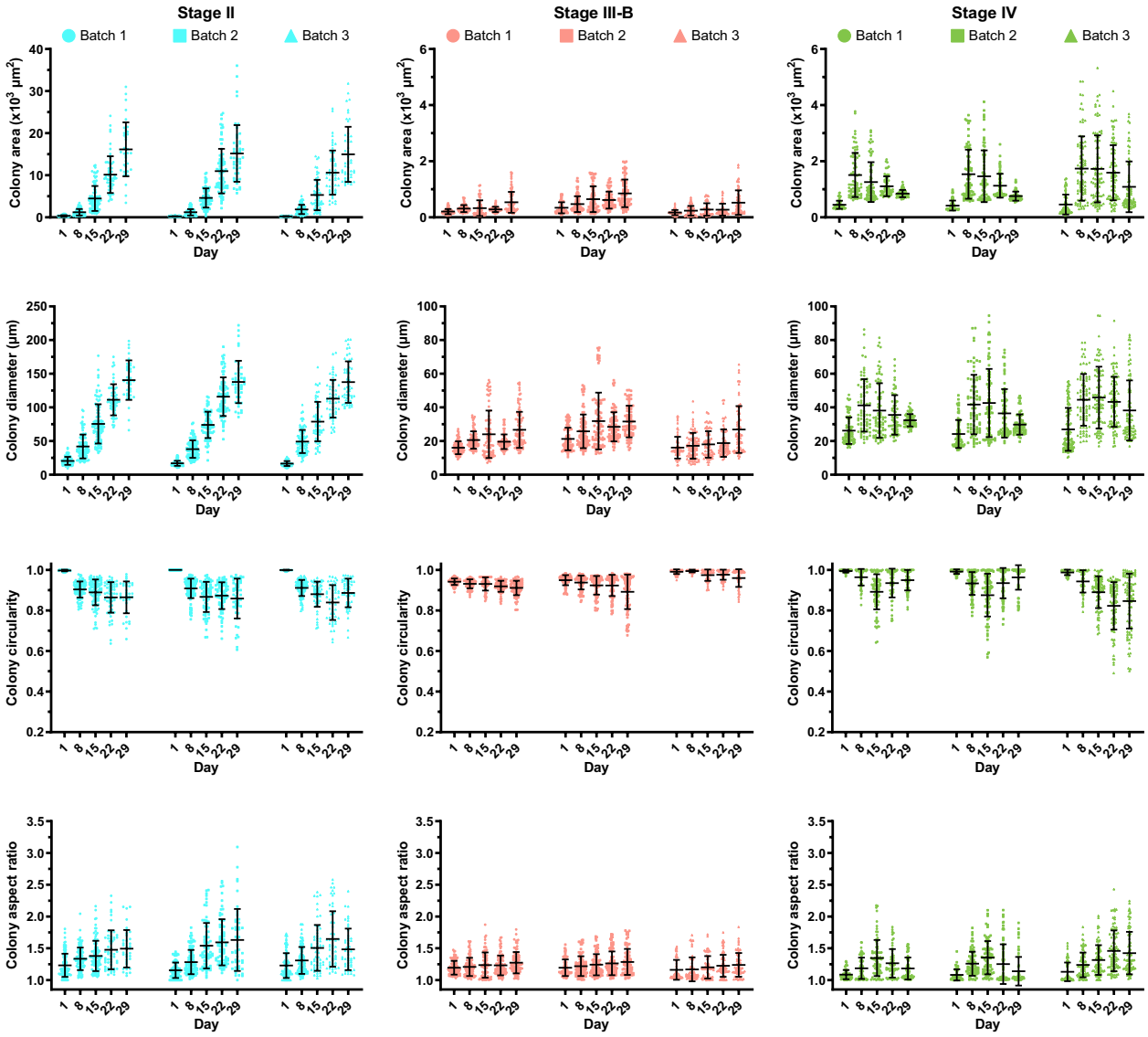

Figure D.2. Quantification of growth and morphological changes of tumor cell colonies in 3D-eCRC-PDX tissues for 3 separate batches of cultures. For each CRC stage, area, diameter, circularity, and aspect ratio of cell colonies were quantified over 29 days of culture. Data are mean ± SD, and each data point represents one colony. At least 80 CRC cell colonies per time point were examined for each of the three separately prepared batches.

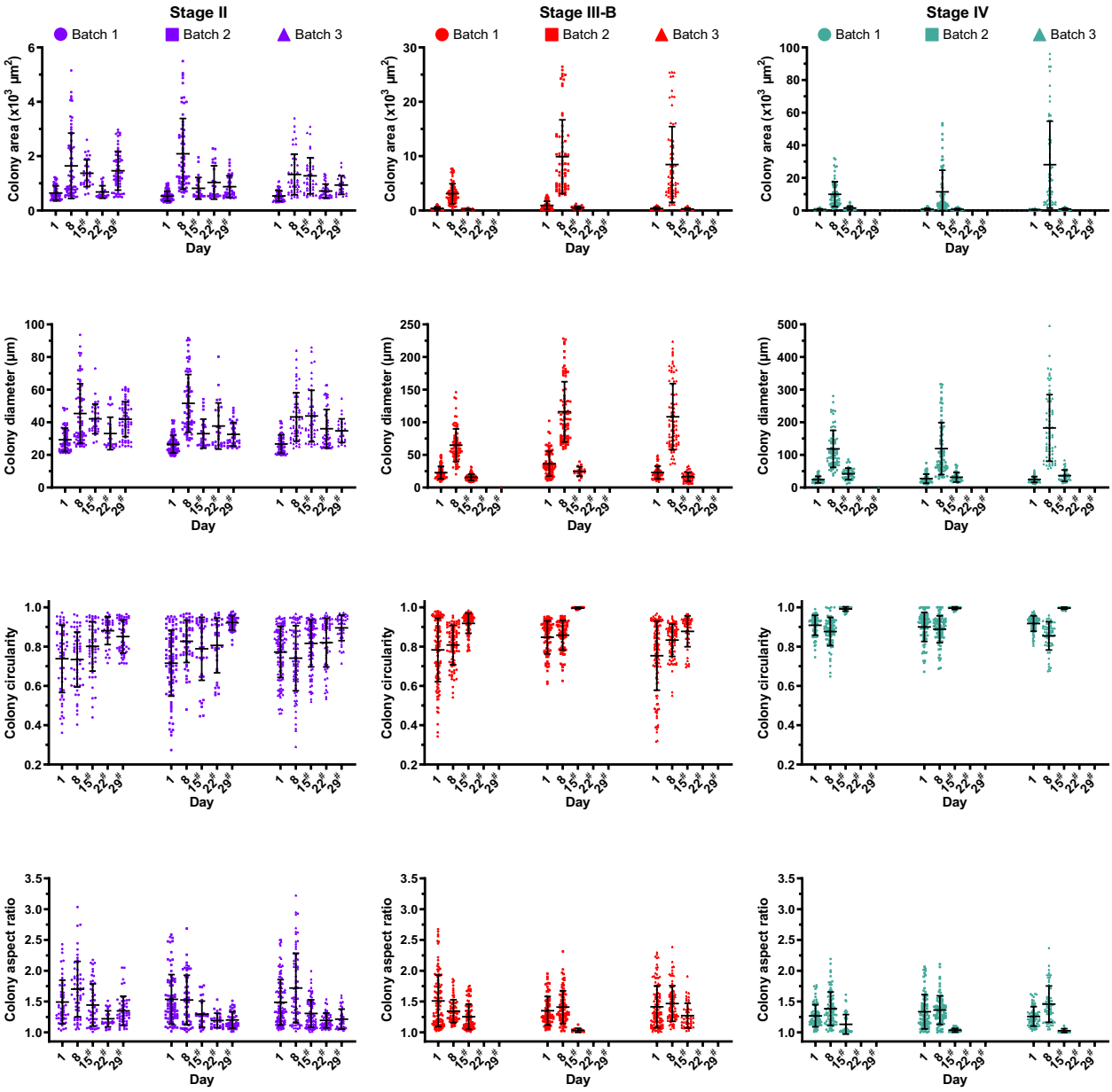

Figure D.3. Quantification of growth and morphological changes of tumor cell colonies in 2D-CRC-PDX cultures for 3 separate batches of cultures. For each CRC stage, area, diameter, circularity, and aspect ratio of cell colonies were quantified over 29 days of culture. Data are mean ± SD, and each data point represents one colony. At least 80 CRC cell colonies per time point were examined for each of the three separately prepared batches. # indicates that the 2D-CRC-PDX cells were passaged at the previous time point.

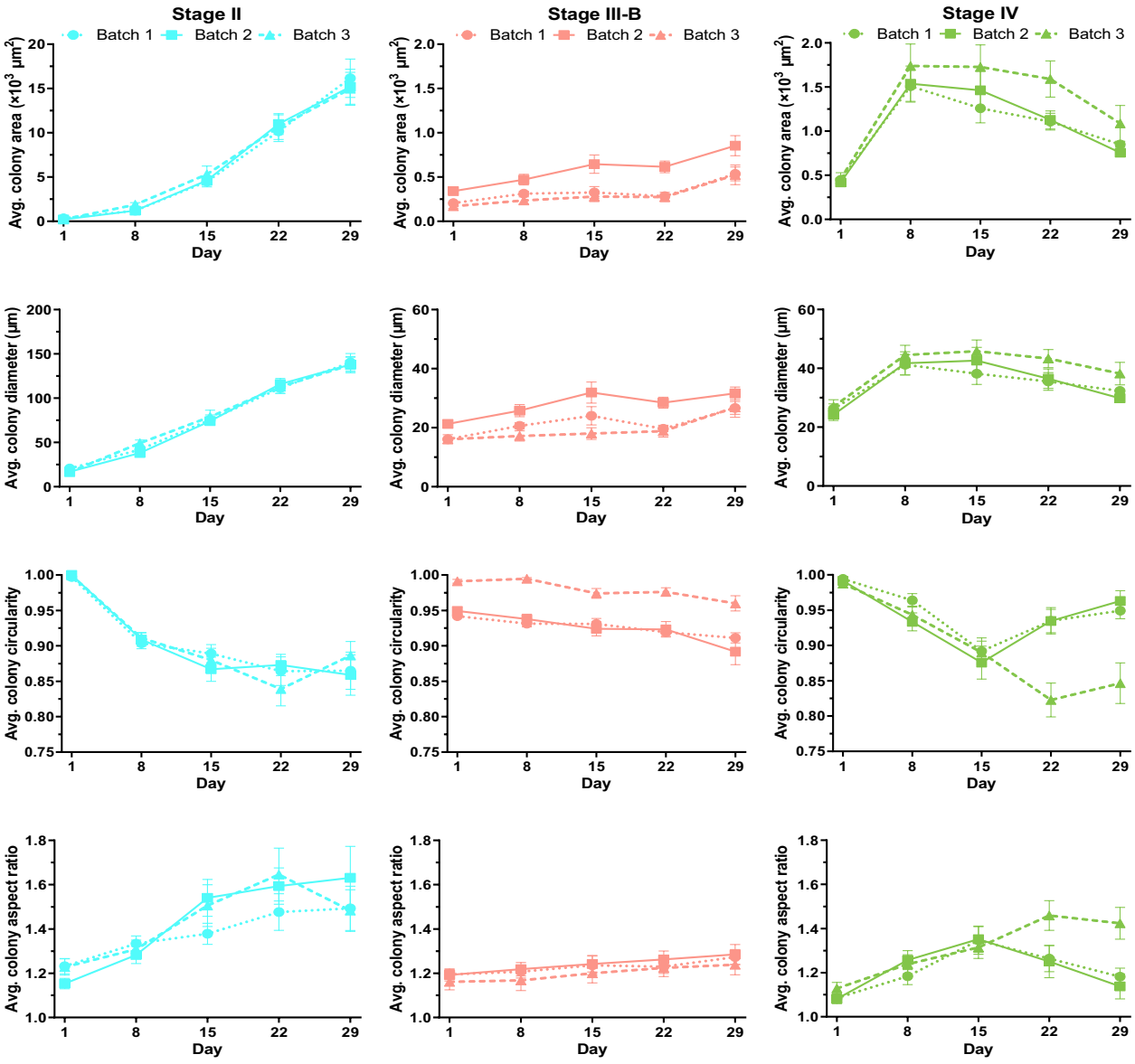

Figure D.4. Quantification of growth and morphological changes of tumor cell colonies in 3D-eCRC-PDX tissues for 3 separate batches of cultures. For each CRC stage, the averages of area, diameter, circularity, and aspect ratio of cell colonies were quantified over 29 days of culture. Data are mean ± SD and present the average values for at least 80 CRC cell colonies per time point.

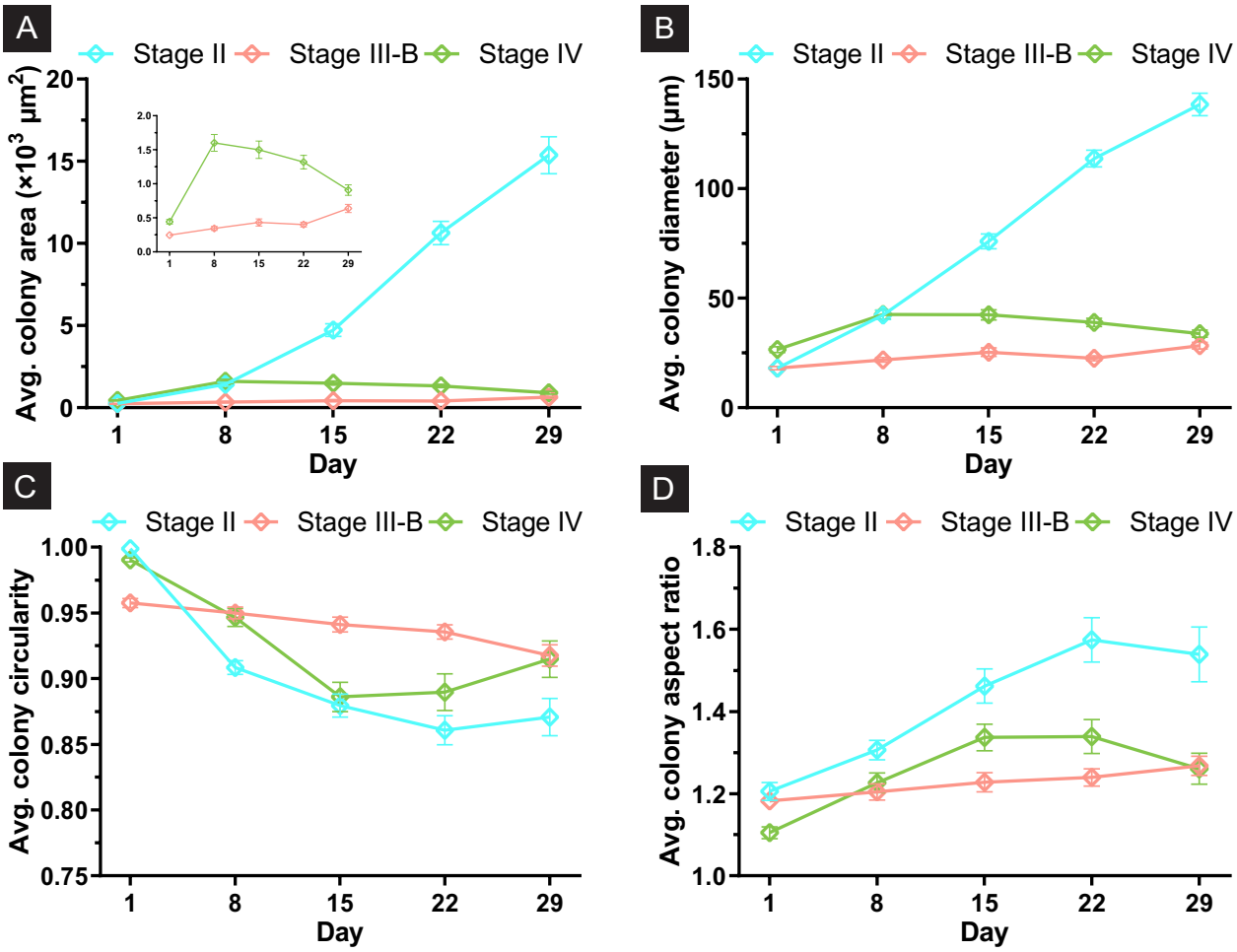

Figure D.5. Quantification of growth and morphological changes of tumor cell colonies in 3D-eCRC-PDX tissues. For each CRC stage, the averages of (A) area, (B) diameter, (C) circularity, and (D) aspect ratio of cell colonies were quantified over 29 days of culture. Data are mean ± SD and present the average values for at least 240 CRC cell colonies per time point, pooled from 3 separate batches of culture.

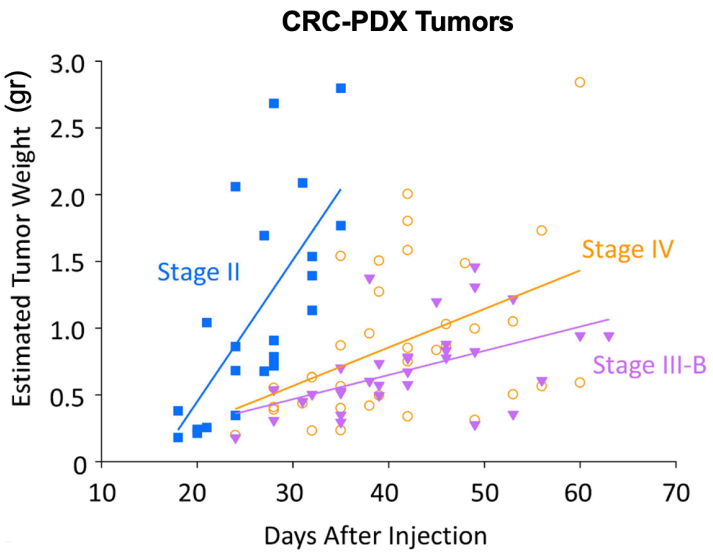

Figure D.6. Quantification of CRC-PDX tumor growth. For each CRC stage, the CRC-PDX tumors in mice were measured using a pair of calipers, and the estimated weight was calculated. Stage II CRC-PDX tumors showed a higher growth rate as compared to stage III-B and stage II CRC-PDX tumors (courtesy of Greene Lab at Auburn University).

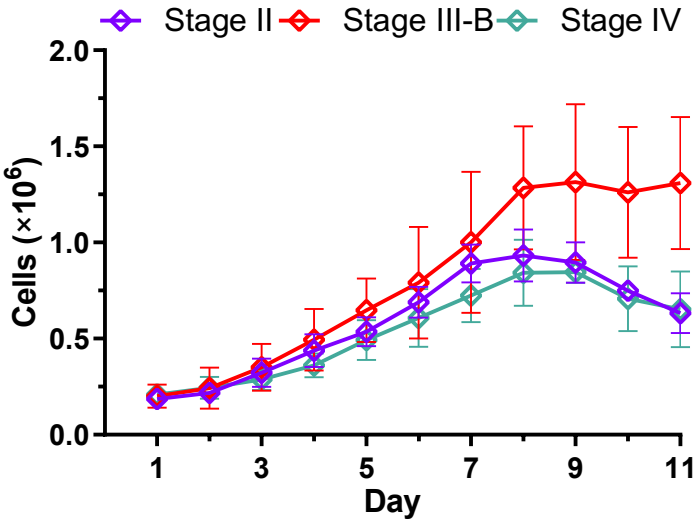

Figure D.7. CRC-PDX cell growth rate in 2D-CRC-PDX cultures without cell passaging. The total number of viable 2D-CRC-PDX cells, cultured in tissue culture flasks, increased from Day 1

to Day 8. An increase in cell number was not observed thereafter as cell confluency was reached on Day 8. Therefore, the 2D-CRC-PDX cells were passaged every 7 days for experiments comparing them to the 3D-eCRC-PDX tissues. Data are mean ± SD (n= 3 separate batches of cell cultures).

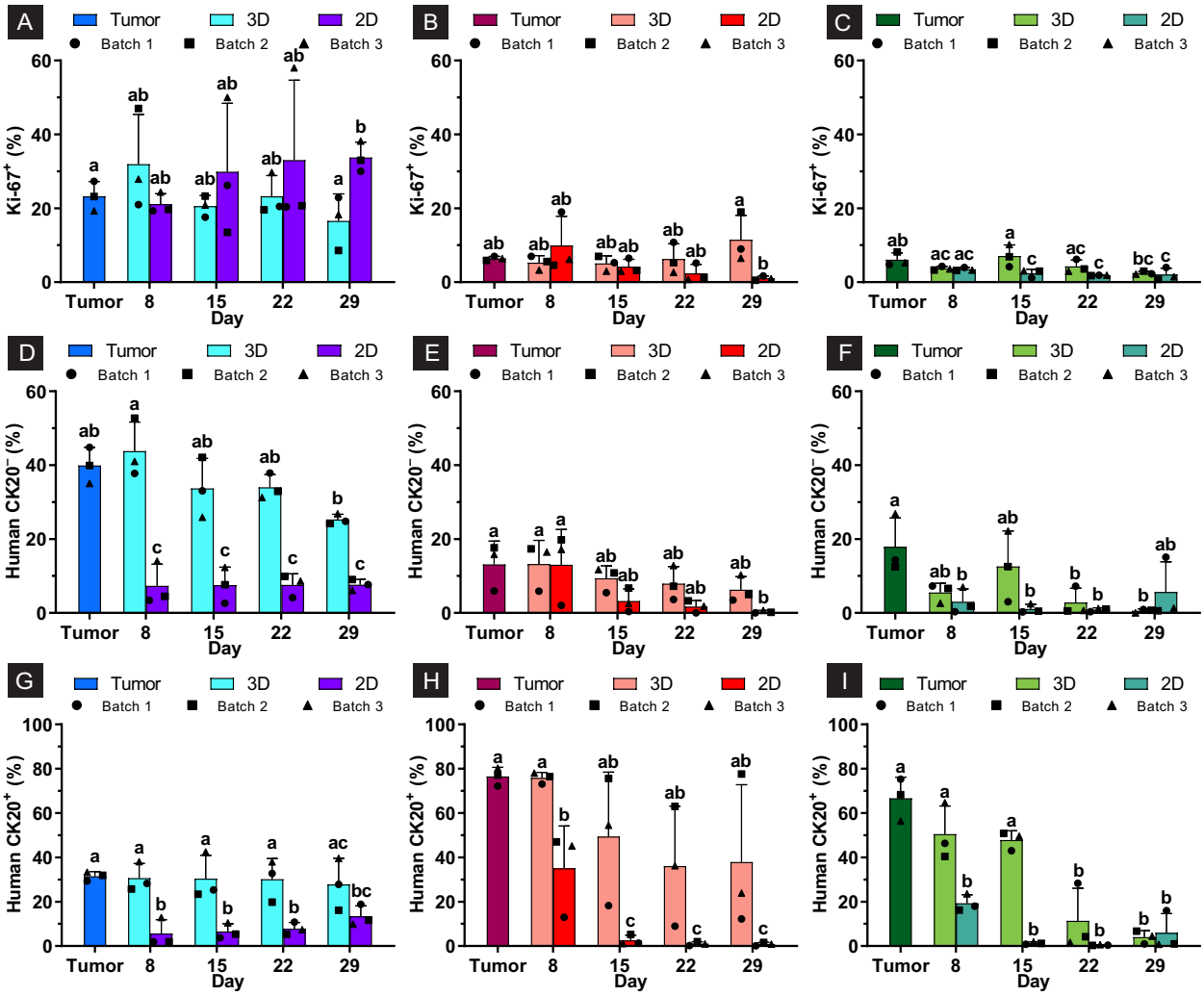

Figure D.8. The 3D-eCRC-PDX tissues better maintained the originating CRC-PDX tumor cell subpopulations as compared to 2D-CRC-PDX cultures. Consistent with their growth rate, the percentage of proliferative cells in stage (A) II 3D-eCRC-PDX tissues was higher than those in (B) stage III-B and (C) stage IV 3D-eCRC-PDX tissues. Both (D, G) stage II and (E, H) stage

III-B 3D-eCRC-PDX tissues maintained both human $CK20^+$ and human $CK20^-$ cell subpopulations over long-term culture; the (I) stage IV 3D-eCRC-PDX tissues could maintain human $CK20^+$ human cell subpopulation over 15 days. In sharp contrast, (D-I) in 2D-CRC-PDX cells, a significant decrease in these cell subpopulations was found after 8 days of culture with the percentages remaining low thereafter. Bars are mean ± SD. Means that do not share a letter are significantly different ($p \leq 0.05$, n = 3 separate batches of cell culture).

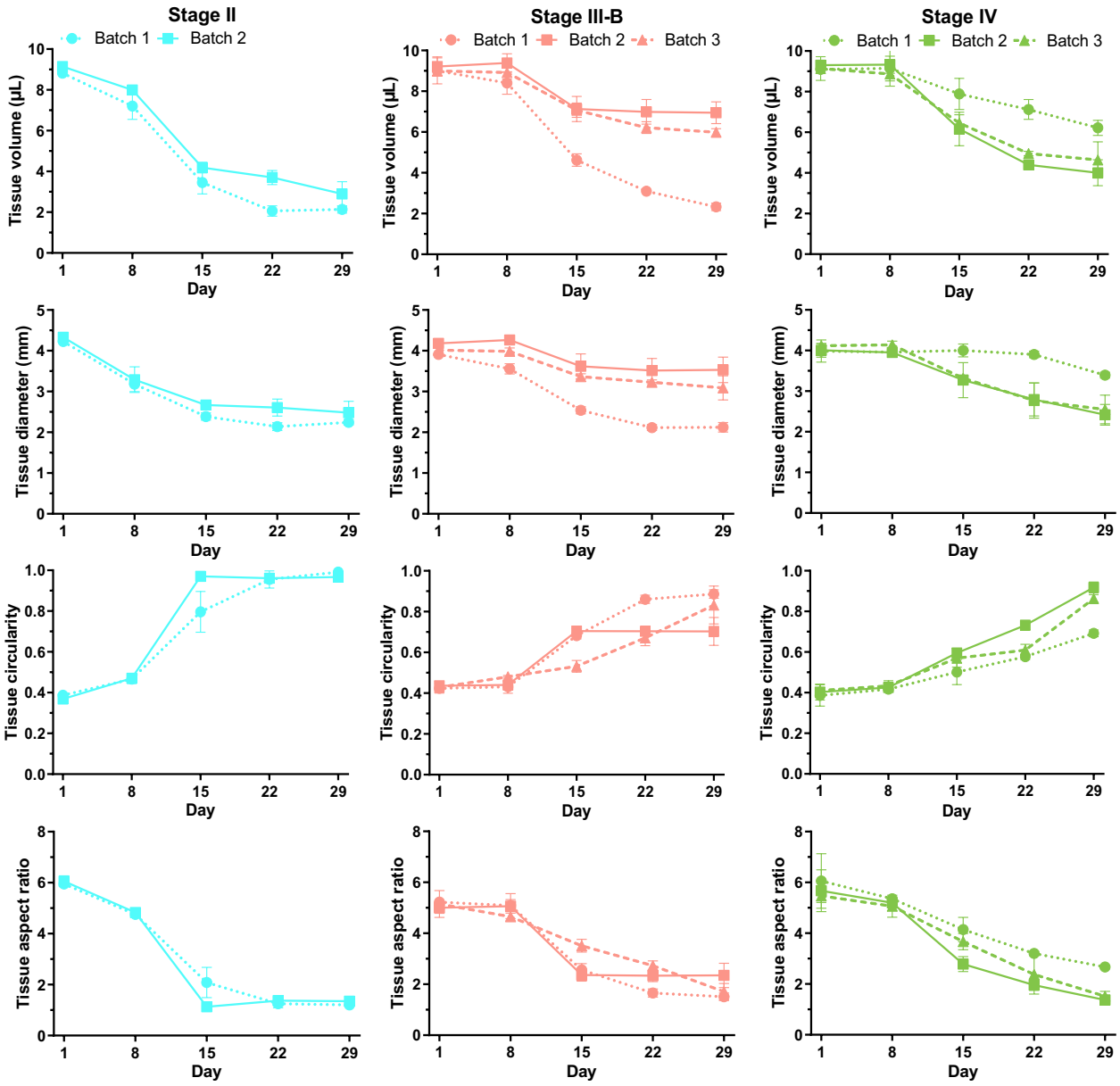

Figure D.9. Quantification of size and shape of the 3D-eCRC-PDX tissues for a minimum of two separate batches of cultures. For each CRC stage, area, diameter, circularity, and aspect ratio of the 3D-eCRC-PDX tissues were quantified over 29 days of culture. For all CRC stages, the volume, diameter, and aspect ratio (side view) decreased and circularity (side view) increased significantly over time; however, the rates of change were different among CRC stages. Data are mean ± SD (n = 3 tissues per time point per batch).

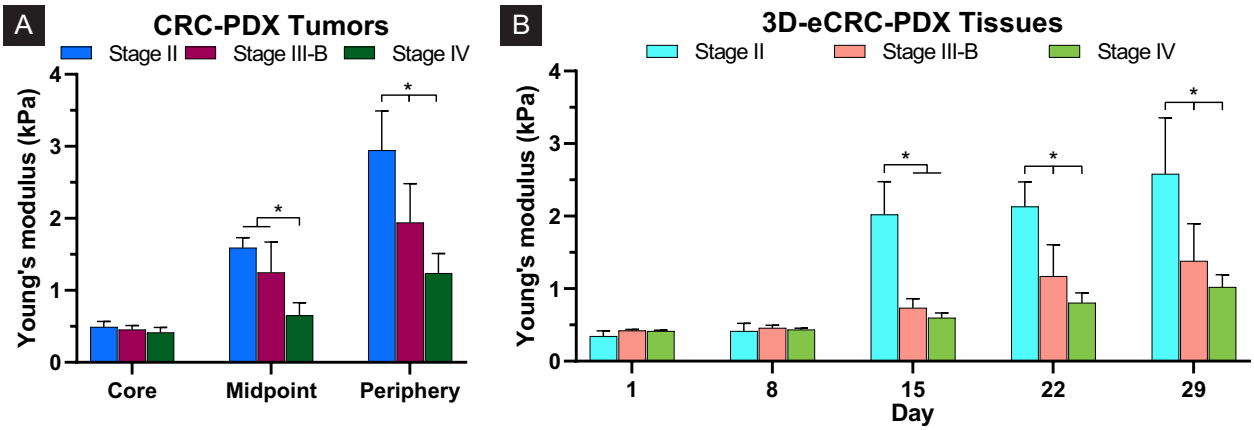

Figure D.10. The 3D-eCRC-PDX tissues mimicked the stage-dependent mechanical stiffness of CRC-PDX tumors. The average stiffness of all batches (pooled data of 3 separate batches of culture) was PDX line dependent. (A) The periphery of stage II CRC-PDX tumors had the highest stiffness, followed by those of stage III-B, and then stage IV. (B) Remarkably, the average stiffness of all batches of 3D-eCRC-PDX tissues mimicked the stage-dependent average stiffness of the CRC-PDX tumors. Bars are mean ± SD ($p \leq 0.05$, n = a minimum of 6 tissues from at least 2 separate batches of cell culture).

Appendix E: Supporting Information for Chapter 5

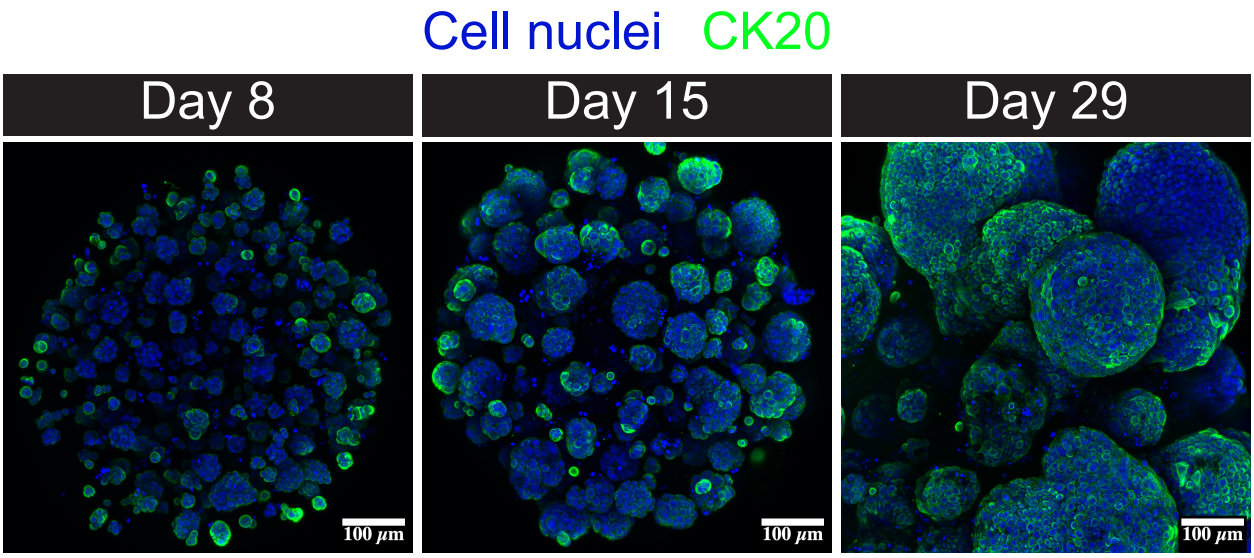

Figure E.1. HT-29 cells in microspheres were positive for CK20 marker. Representative confocal images of cell nuclei (blue) and CK20 (green) in HT-29 microspheres on Days 8, 15, and 29. All HT-29 cells were also positive for CK20 marker, indicative of their ability to express this CRC-specific protein in the microspheres.

Appendix F: Supporting Information for Figure 3.3

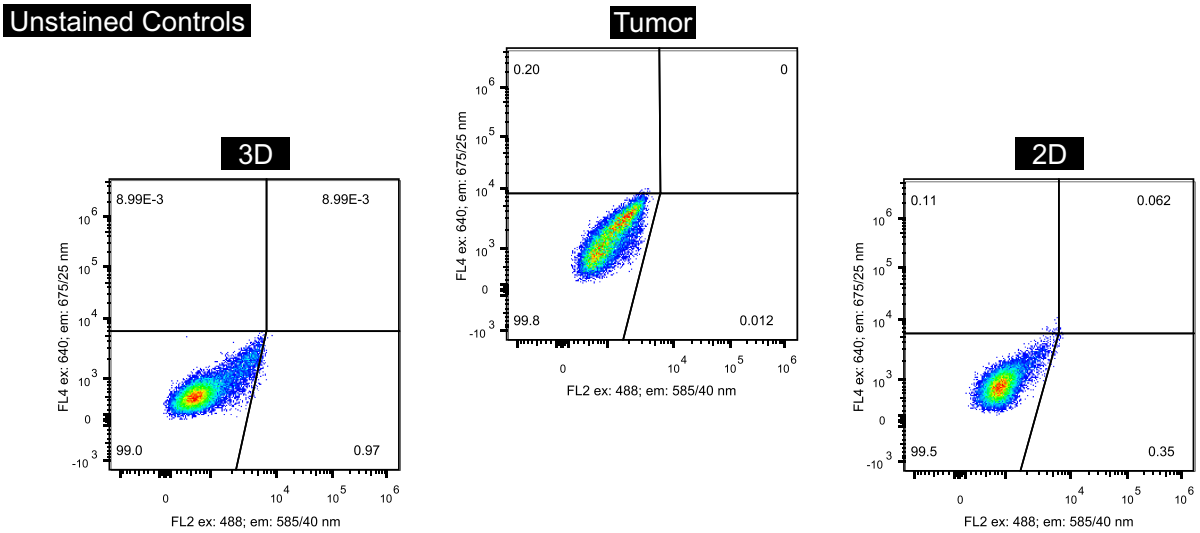

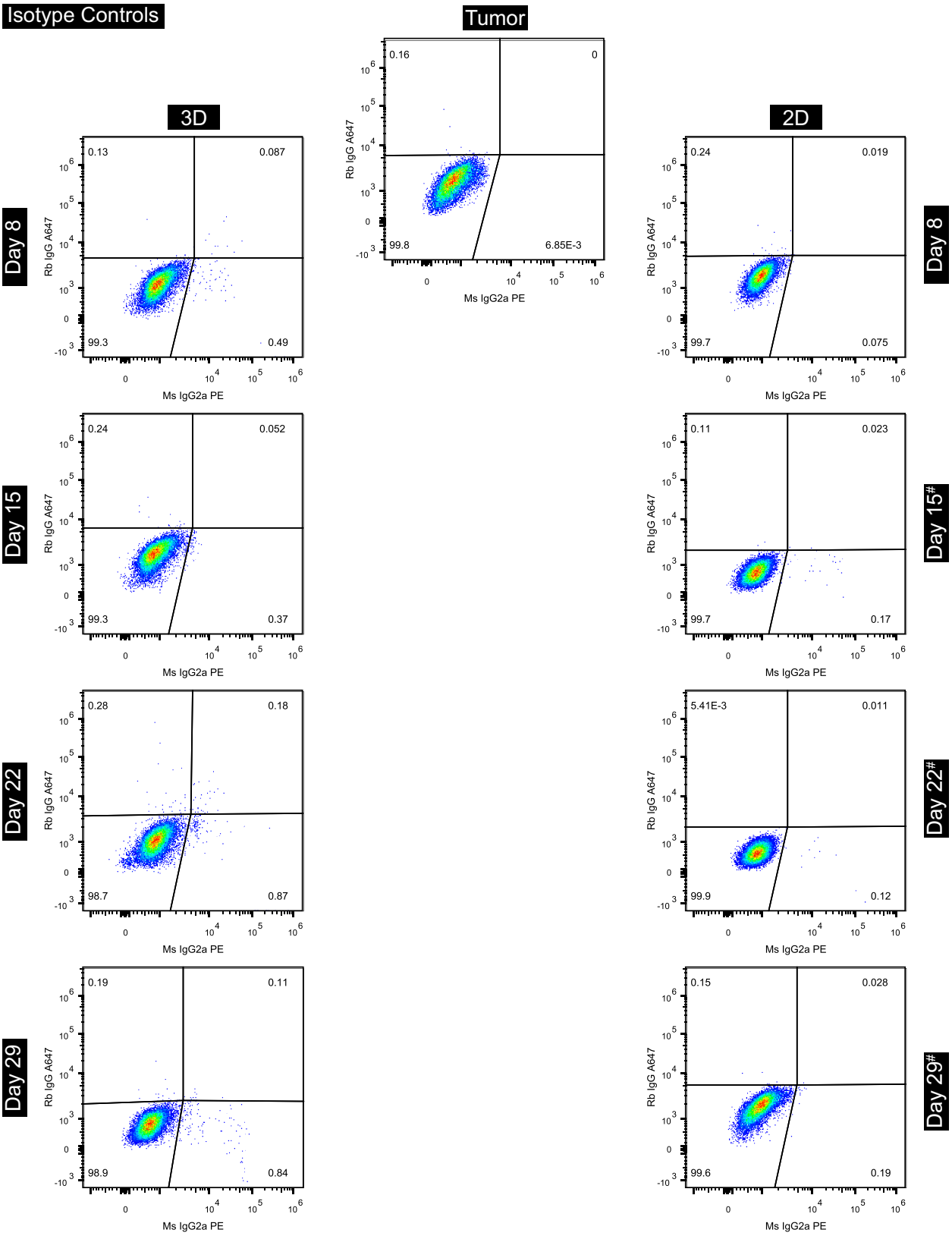
Isotype Controls
Tumor
3D
2D
Day 8
Day 15
Day 22
Day 29
Day 8
Day 15#
Day 22#
Day 29#
Rb IgG A647
Ms IgG2a PE
0.16
0
99.8
6.85E-3
0.13
0.087
99.3
0.49
0.24
0.052
99.3
0.37
0.28
0.18
98.7
0.87
0.19
0.11
98.9
0.84
0.24
0.019
99.7
0.075
0.11
0.023
99.7
0.17
5.41E-3
0.011
99.9
0.12
0.15
0.028
99.6
0.19

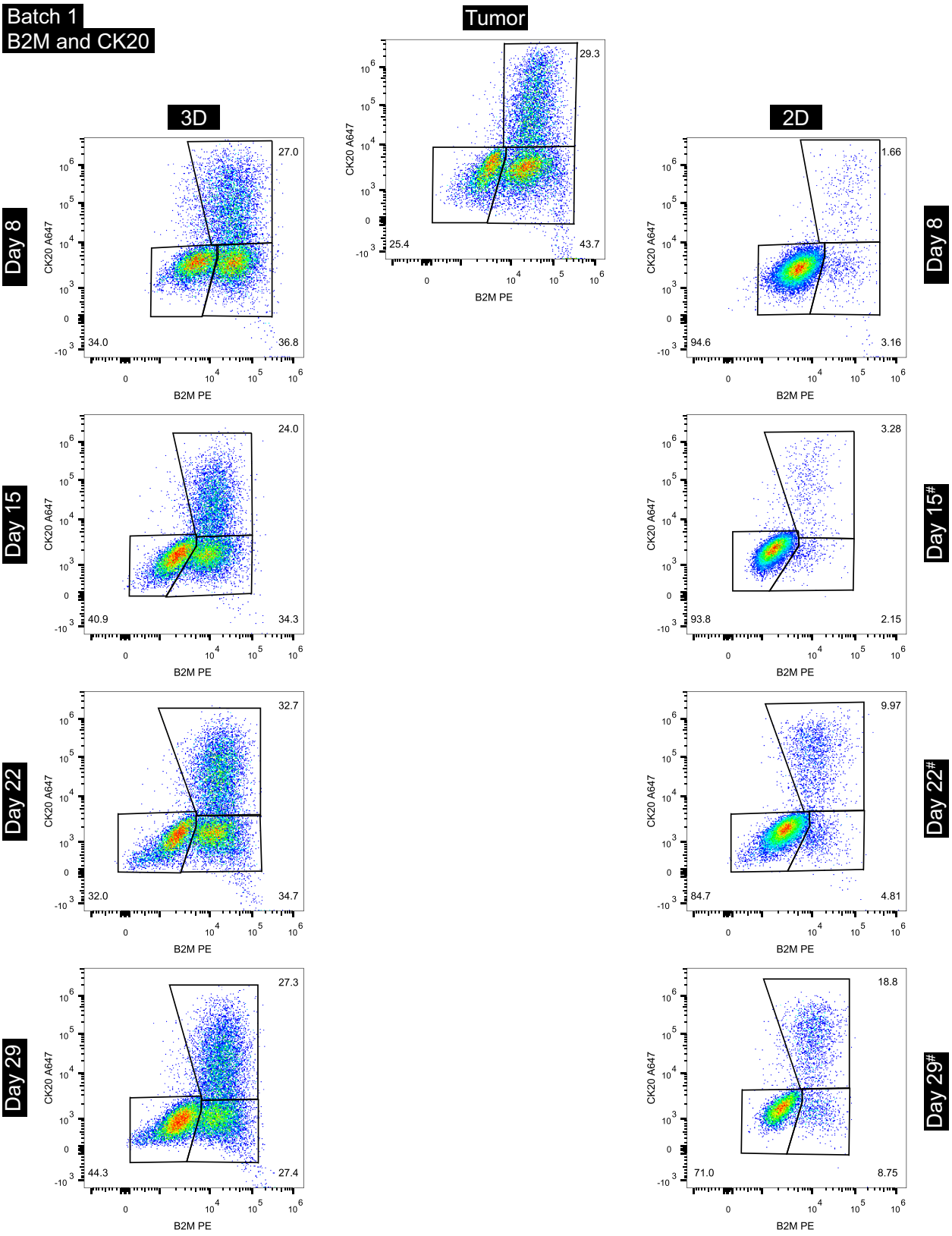
Batch 1
B2M and CK20
Tumor
3D
2D
Day 8
Day 15
Day 22
Day 29
Day 8
Day 15#
Day 22#
Day 29#
CK20 A647
B2M PE
29.3
25.4
43.7
27.0
34.0
36.8
1.66
94.6
3.16
24.0
40.9
34.3
3.28
93.8
2.15
32.7
32.0
34.7
9.97
84.7
4.81
27.3
44.3
27.4
18.8
71.0
8.75

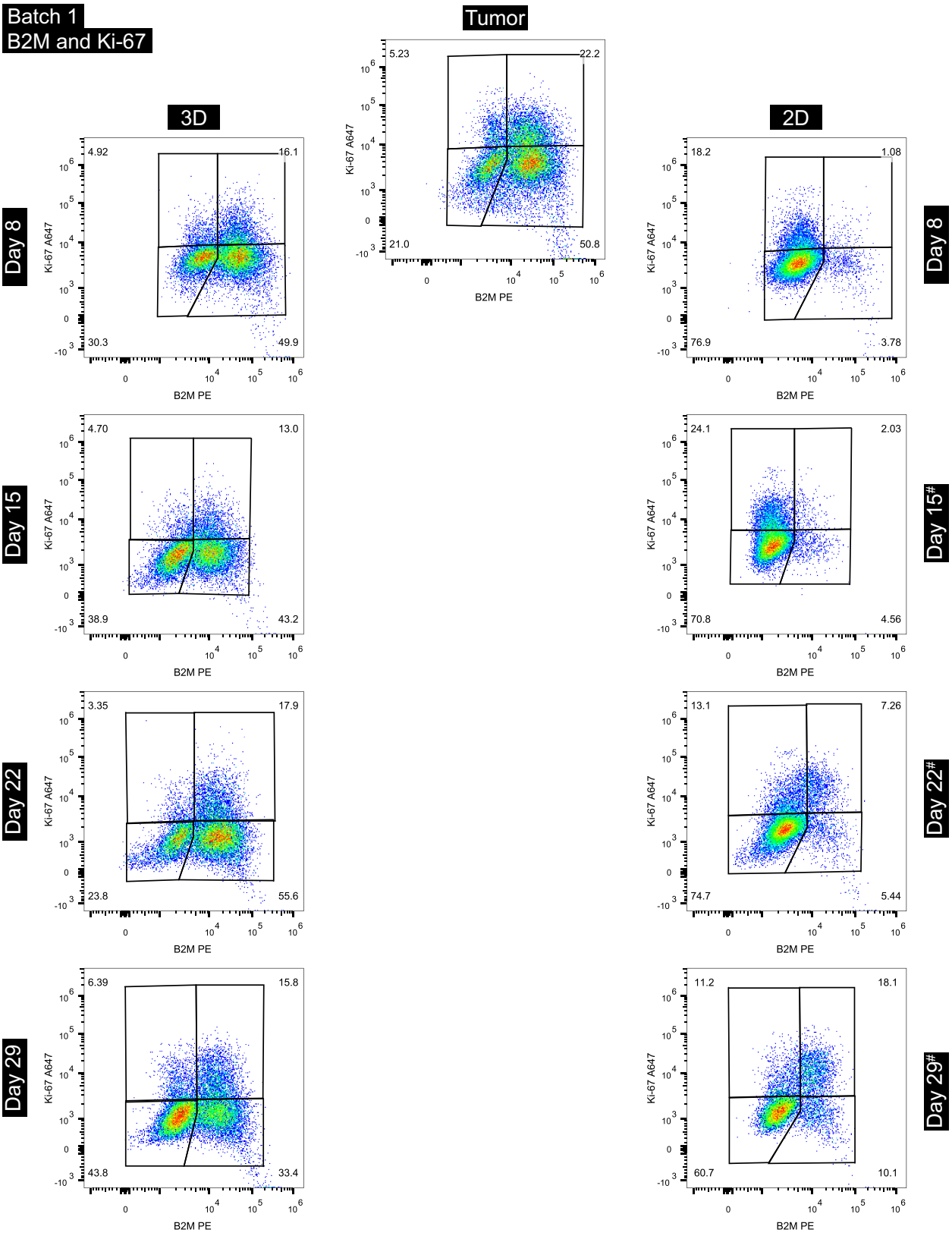
Batch 1
B2M and Ki-67
Tumor
3D
2D
Day 8
Day 15
Day 22
Day 29
Day 8
Day 15#
Day 22#
Day 29#
Ki-67 A647
B2M PE
5.23
22.2
21.0
50.8
4.92
16.1
30.3
49.9
18.2
1.08
76.9
3.78
4.70
13.0
38.9
43.2
24.1
2.03
70.8
4.56
3.35
17.9
23.8
55.6
13.1
7.26
74.7
5.44
6.39
15.8
43.8
33.4
11.2
18.1
60.7
10.1

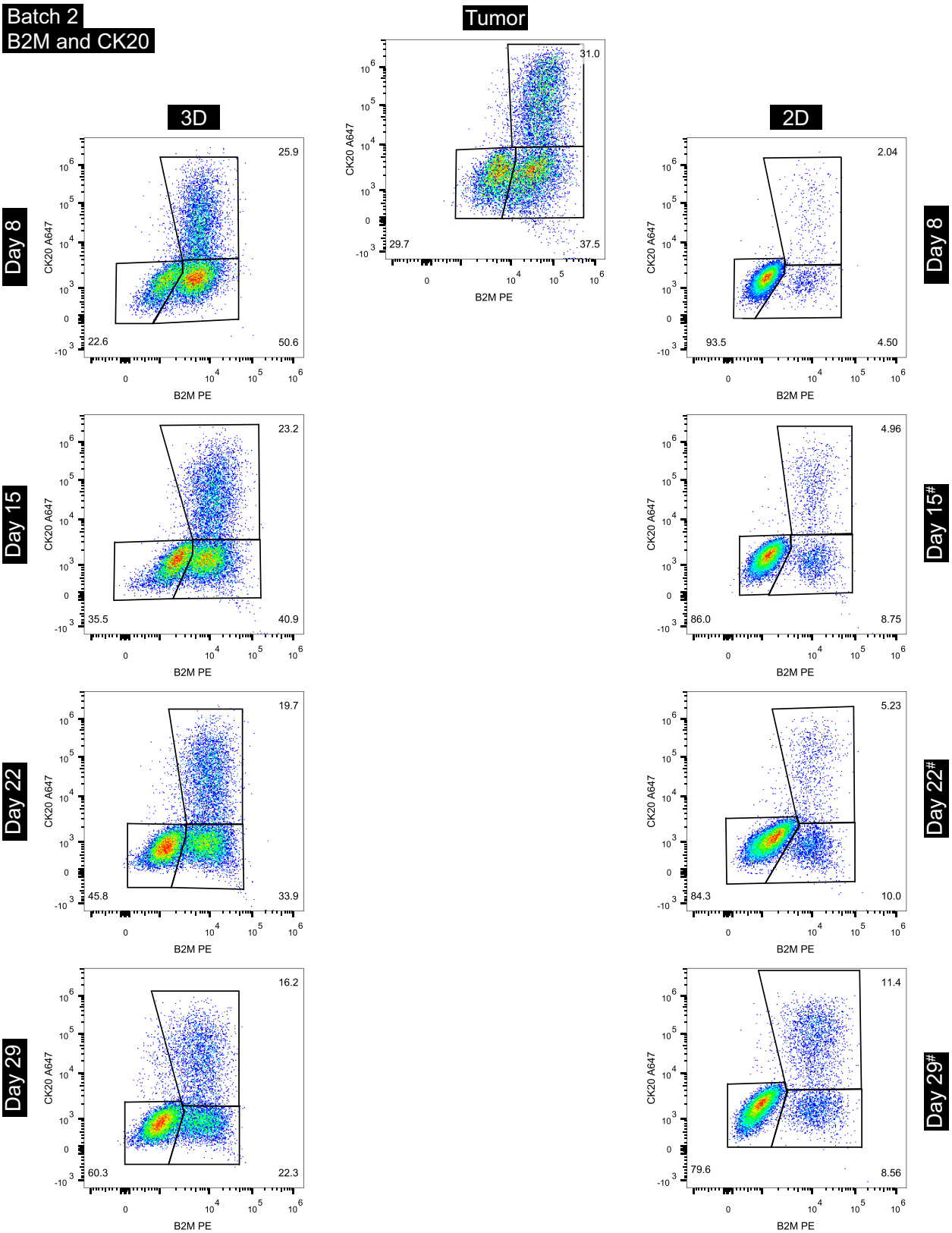
Batch 2
B2M and CK20
Tumor
3D
2D
Day 8
Day 15
Day 22
Day 29
Day 8
Day 15#
Day 22#
Day 29#
CK20 A647
B2M PE
31.0
29.7
37.5
25.9
22.6
50.6
2.04
93.5
4.50
23.2
35.5
40.9
4.96
86.0
8.75
19.7
45.8
33.9
5.23
84.3
10.0
16.2
60.3
22.3
11.4
79.6
8.56

Batch 2
B2M and Ki-67

Tumor

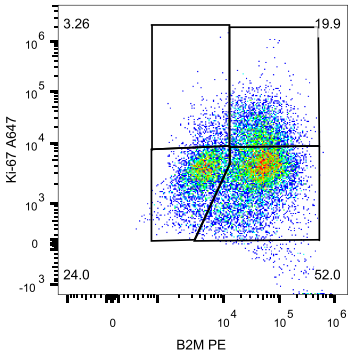

3D

2D

Day 8

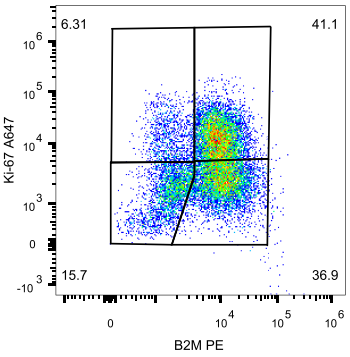

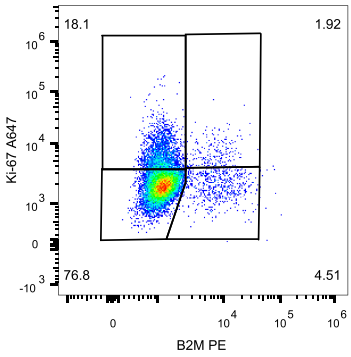

Day 8

Day 15

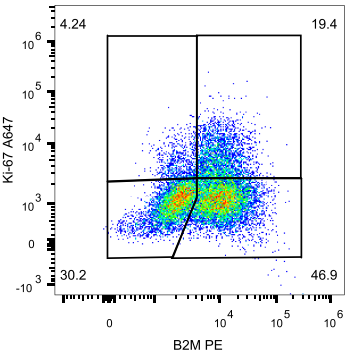

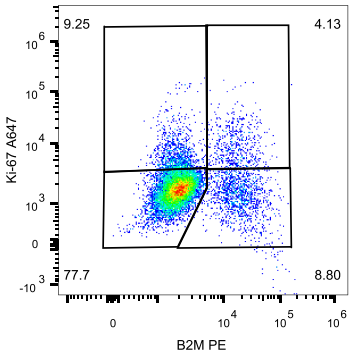

Day 15#

Day 22

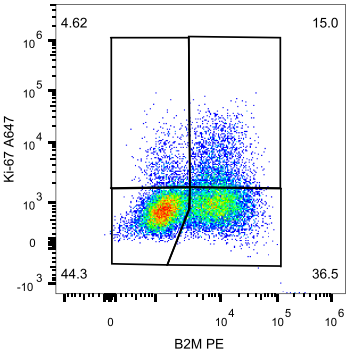

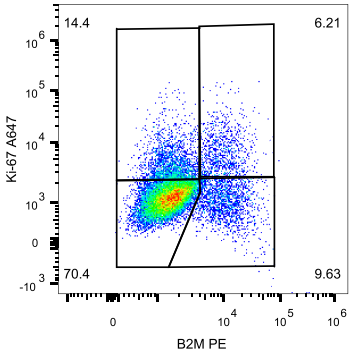

Day 22#

Day 29

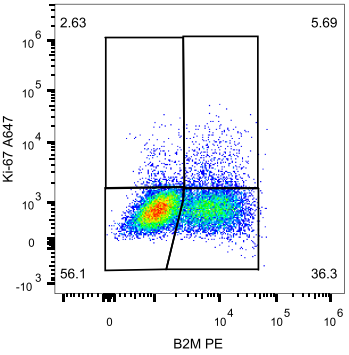

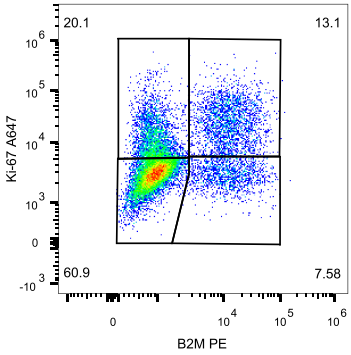

Day 29#

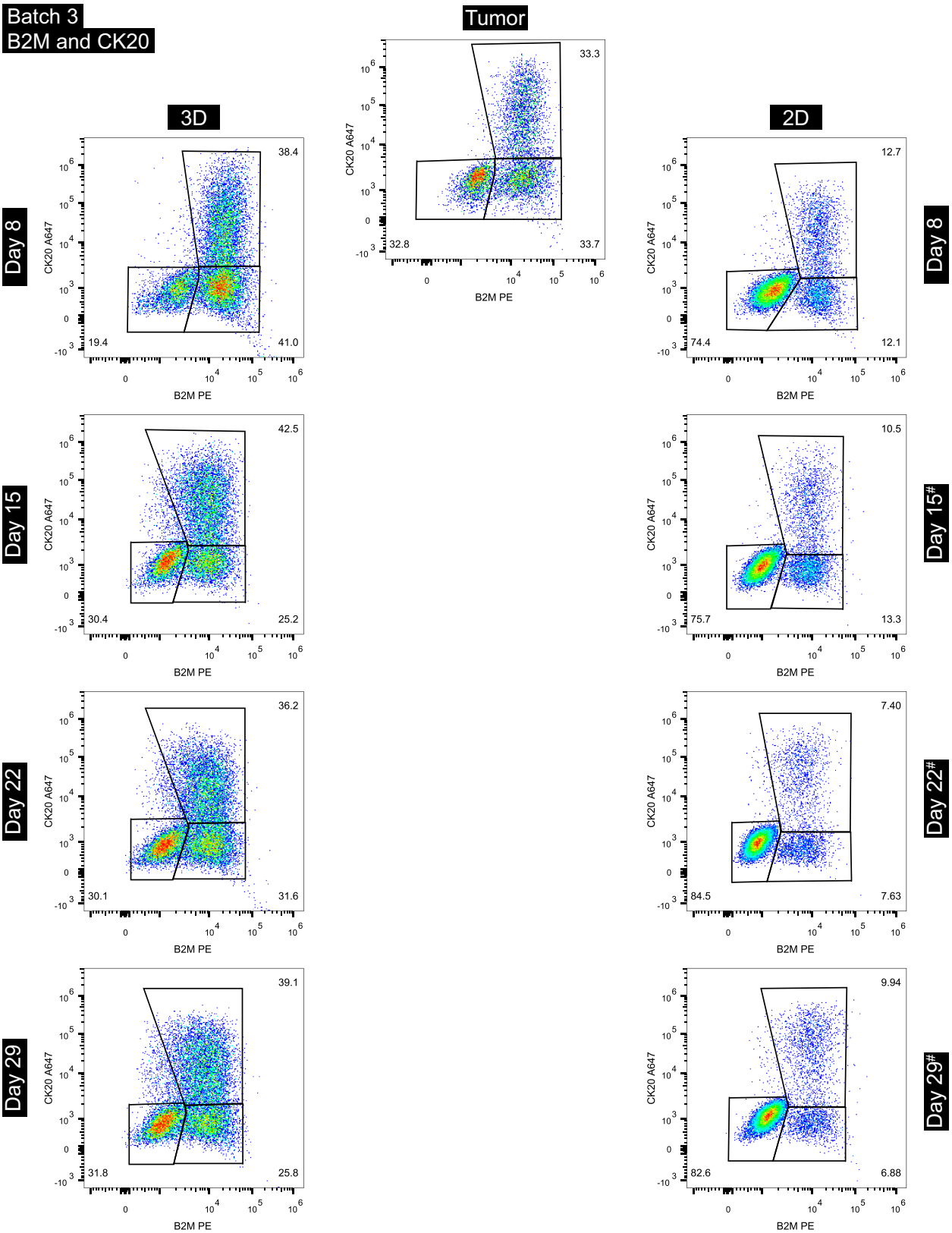
Batch 3
B2M and CK20
Tumor
3D
2D
Day 8
Day 15
Day 22
Day 29
Day 8
Day 15#
Day 22#
Day 29#
CK20 A647
B2M PE
33.3
32.8
33.7
38.4
19.4
41.0
12.7
74.4
12.1
42.5
30.4
25.2
10.5
75.7
13.3
36.2
30.1
31.6
7.40
84.5
7.63
39.1
31.8
25.8
9.94
82.6
6.88

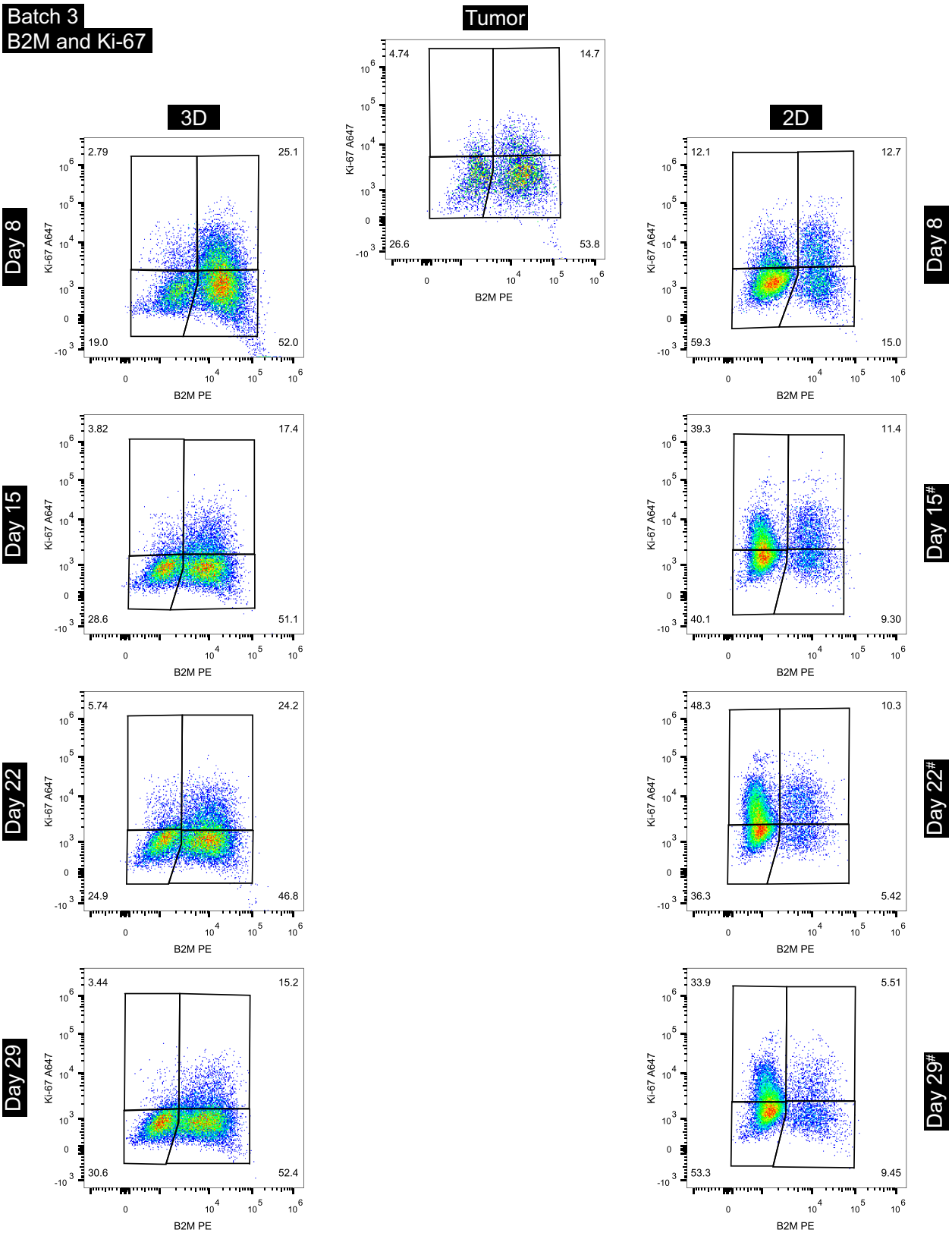
Batch 3
B2M and Ki-67
Tumor
3D
2D
Day 8
Day 15
Day 22
Day 29
Day 8
Day 15#
Day 22#
Day 29#
Ki-67 A647
B2M PE
4.74
14.7
26.6
53.8
2.79
25.1
19.0
52.0
12.1
12.7
59.3
15.0
3.82
17.4
28.6
51.1
39.3
11.4
40.1
9.30
5.74
24.2
24.9
46.8
48.3
10.3
36.3
5.42
3.44
15.2
30.6
52.4
33.9
5.51
53.3
9.45

Appendix G: Reagent Table

Table G.1. Reagents

REAGENT OR RESOUCE	SOURCE	IDENTIFIER
Matrix High Concentration, Phenol-Red free Matrigel	Corning	cat. #354262
NOD.Cg-Prkdc^{scid} Il2rg^{tm1Wjl}/SzJ (NOD-SCID) mouse	The Jackson Laboratory	cat. #005557
Collagenase IV	Worthington	cat. #LS004188
Deoxyribonuclease I (DNase I)	Worthington	cat. #LS002139
Hank's Buffered Saline Solution (HBSS)	Lonza	cat. #10-508F
Syringe Filter	VWR	cat. #28145-501
Phosphate-buffered Saline (PBS)	Lonza	cat. #17-517Q
40-µm Cell Strainer	Corning	cat. #352340
DMEM	Lonza	cat. #12-614Q
Fetal Bovine Serum	Atlanta Biologicals™	cat. #S10250
Penicillin:Streptomycin Solution	HyClone™	cat. #16777-164
Glutagro™ Supplement	Corning	REF #25-015-CI
Trypan Blue	Lonza	cat. #17-942E
1-Vinyl-2-pyrrolidinone	Sigma-Aldrich	SKU #V3409
0.25% Trypsin-EDTA	Corning	REF #25-053-CI
LIVE/DEAD® Viability/Cytotoxicity Kit	ThermoFisher Scientific	cat. #L3224
Hoechst 33342	Calbiochem	cat. #382065
Beta-2-microglobulin (B2M) mouse IgG2a mAb	OriGene Technologies	cat. #BM604S
Zenon™ R-phycoerythrin (PE) mouse IgG2a	ThermoFisher Scientific	cat. #Z25155
MHC Class I H-2 Db antibody (H2Db) mouse IgG2a mAb	OriGene Technologies	cat. #AM08082PU-N
Zenon™ PE mouse IgG2a, cytokeratin 20 (CK20) rabbit IgG mAb	Cell Signaling Technology	cat. #13063S
Zenon™ Alexa Fluor™ 647 rabbit IgG	ThermoFisher Scientific	cat. #Z25308
Ki-67 mouse IgG1 mAb	abcam	cat. #ab15580
Zombie Green™ Fixable Viability Kit, dye	BioLegend	cat. #423111
Bovine Serum Albumin (BSA)	Sigma-Aldrich	SKU #A2153
Human BD Fc Block™	BD Biosciences	cat. #564220
Mouse BD Fc Block™	BD Biosciences	cat. #553141
Foxp3	eBioscience™	cat. #00-5523-00
AbC™ Total Antibody Compensation Bead Kit	ThermoFisher Scientific	REF #A10513

B2M mouse IgG2a mAb with goat anti-mouse IgG Alexa Fluor™ 488	ThermoFisher Scientific	cat. #A-11001
Alexa Fluor™ 568 Phalloidin	ThermoFisher Scientific	cat. # A12380
RNeasy Plus Micro Kit	Qiagen	cat. #74034
SuperScript™ IV First-Strand Synthesis System	Invitrogen	cat. #18091050
RT2 SYBR Green qPCR Mastermix	Qiagen	cat. #330503
Poly(ethylene glycol) (PEG)	Sigma-Aldrich	SKU #81280
Acryloyl chloride	Alfa Aesar	STK #L10363-09
Anhydrous dichloromethane	Honeywell Research Chemicals	cat. #AS299-1
Triethylamine (TEA)	Sigma-Aldrich	SKU #471283
NaCl	Sigma-Aldrich	SKU #S5886
KCl	Sigma-Aldrich	SKU #P5405
Na_2HPO_4	Sigma-Aldrich	SKU #71643
KH_2PO_4	Sigma-Aldrich	SKU P5655
Bovine fibrinogen	Sigma-Aldrich	SKU #F8630
Urea	Sigma-Aldrich	SKU #51456
Acetone	VWR	cat. #BDH1101-4LP
Eosin Y	Fisher Scientific	cat. #E511-25
Pierce™ BCA Protein Assay Kit	ThermoFisher Scientific	cat. #23225
SYLGARD® 184 Silicone Elastomer Kit	Dow Corning	SKU #4019862
Accumax	Innovative Cell Technology, Inc.	cat. #AM105-500
Triton™ X-100	Sigma-Aldrich	SKU # X100-500ML
Safety scalpel	Bard-Parker®	REF #372611
Compartmental Protein Extraction Kit	Millipore	cat. #2145
NuPAGE™ LDS Sample Buffer	Invitrogen	cat. #NP0007
NuPAGE™ Sample Reducing Agent	Invitrogen	cat. #NP0009
EZQ™ Protein Quantitation Kit	Invitrogen	cat. #R33200
NuPAGE™ 10% Bis-Tris Protein Gels	Invitrogen	cat. #NP0315BOX
Colloidal Blue Staining Kit	Invitrogen	cat. #LC6025
Trypsin Gold, Mass Spectrometry Grade	Promega	cat. #V5280